Growth and Characterisation of Group-III Nitride-based Nanowires for Devices

Von der Fakultät für Mathematik, Informatik und Naturwissenschaften der Rheinisch-Westfälischen Technischen Hochschule Aachen zur Erlangung des akademischen Grades eines Doktors der Naturwissenschaften genehmigte Dissertation

vorgelegt von

Diplom-Physiker

Ralph Joseph Meijers

aus Kerkrade, die Niederlande

Berichter: Universitätsprofessor Dr. Dr. h.c. H. Lüth
Universitätsprofessor Dr. G. Güntherodt

Tag der mündlichen Prüfung: 30. August 2007

Mit jedem einfachen Denkakt

tritt etwas Bleibendes,

Substantielles in unsere Seele ein.

Bernhard Riemann

Table of Contents

Chapter 1

Introduction

The continuous strive to decrease the size of devices is accompanied by an enormous increase of the costs especially for lithography steps. In addition conventional device concepts might not work when quantum mechanical effects govern the behaviour of the device. Therefore it is necessary to fabricate nanosystems in a low-cost way with sizes smaller than the actual lithographic resolution. An interesting example is offered by the growth of nanowires. For some applications this approach could replace conventional device processing, but its main advantage is the possibility to investigate small device sizes which conventional device processing will probably only be able to produce in a few years. Thus, in advance of industrial production, one can already address fundamental issues and possible 'Red Brick Walls' [1] in semiconductor roadmaps for very small device sizes and try to find solutions.

In recent years nanowires have attracted a lot of interest in the research community, but also commercial companies like Intel, IBM, HP and Philips have shown their interest for these structures with very small dimensions. They can be produced in various ways, sometimes also very cost-effective. Chemically synthesised semiconductor nanowires are interesting building blocks for nanoscale devices. Although sophisticated device structures have already been realised [1–6], many fundamental questions dealing with the internal electronic structure and size dependent transport phenomena remain, but are starting to be addressed. Another subject of special interest is the extremely large surface in respect to the bulk. In this regard nanowires are expected to be suitable for the purpose of studying surface related topics, which in turn have a strong influence on the physical behaviour of the nanosystem itself. Due to the limited size, the de Broglie wavelength of electrons is of the same order as the nanowire diameter and quantum mechanical effects can be expected. This makes them very suitable for the study of fundamental quantum transport phenomena.

In addition, nanowires offer the unique capability to realise highly lattice mismatched heterostructures with much more flexibility than in planar films and with a broad variety of material combinations. Hence, one can expect to cover an extended frequency range of electromagnetic fields, in particular the intermediate (THz to far-infrared) wavelength regime,

[1] 'Red Brick Walls' in semiconductor roadmaps mark technical areas where further development is expected to be restricted by fundamental physical or technical limitations and for which no manufacturable solution is known at present.

which is a key point for optical as well as communication applications. In addition nanowires can be fabricated on a wide variety of substrates, including silicon, which make them suitable for future CMOS integration. The employment of a grown nanowire structure offers a superior one-dimensional electronic system (as compared to top-down concepts), being suitable for classical device layouts as well as quantum structures.

Nitrides have been used in many device applications lately, because they are very well suited for optoelectronics. They feature a direct band gap and cover the visible range of the electromagnetic spectrum as well as reaching into the ultra-violet allowing for very high data densities in storage applications [7]. Despite high defect densities nitrides are highly luminescent and nanowires, which can be grown with more crystalline perfection than planar films are expected to further improve the performance of optical devices.

GaN nanowires have been grown catalyst-free by molecular beam epitaxy (MBE) in the group of Calleja [8]. However, the understanding of the growth mechanism, which is essential to have good control over the growth, has not been thoroughly investigated. A vapour-liquid-solid (VLS) model has been suggested, but no evidence for a droplet formation has been presented. Also the physical properties of the nanowires have not been fully explored. Since nitrides and especially nanowires are predicted to be very good candidates for optoelectronic applications a good understanding of the material properties as for instance the influence of doping is required.

Position control of nanowires is an important task for densely-packed device applications and is usually obtained by patterning the catalyst particle employed in VLS growth of nanowires. For catalyst-free growth as in the case of nitride nanowires, however, alternative approaches to position control have to be investigated and also therefore a thorough understanding of the growth mechanism is required.

Another important issue in nanowire growth, especially for nitrides where no homosubstrates are available, is the influence of the substrate and the epitaxial relation to it. The substrate of choice in the semiconductor industry is Si(100), but to comply with the hexagonal structure of nitrides Si(111) is often used. The interface between nanowires and substrate is important for devices where the substrate is used as a bottom contact. In this respect determination of strain which can be relieved by dislocation formation is of crucial importance. Dislocations usually reduce the mobility of charge carriers and thus the performance of a device.

Among III-nitrides InN is of great interest. The physical properties reported for InN scatter a lot and recently there is a lot of scientific interest for the material as a result of significant improvements in its crystalline quality. InN nanowires could further increase the obtained material quality and give more reliable values for fundamental physical properties like the band gap, which is very important for all kinds of optical applications (light emitting diodes, lasers, solar cells).

The aim of this thesis is to address some of the issues mentioned above. The understanding of the growth mechanism for nitride nanowires and the influence of the growth parameters and the substrate is one of the central points. In addition the quality of the nanowires is studied and optimised. Furthermore, the electrical properties and influence of technological processing on nitride nanowires are determined.

In Chapter 2 the properties of nitrides are reviewed and there is special attention for the

properties of InN, because of the aforementioned active research in this field. In Chapter 3 an overview of the current status of nanowire research is presented as well as models to explain the one-dimensional growth. Promising features of nanowires are discussed as well as requirements to integrate them in devices. Chapter 4 describes the basics of growth by molecular beam epitaxy and the MBE system, which was employed to grow the samples for this thesis.

Experimental results on nitride nanowires are presented in Chapter 5, Chapter 6, Chapter 7, Chapter 8 and Chapter 9. Firstly, the nucleation, kinetics and growth mechanism is studied in Chapter 5. In Chapter 6 the morphology, crystal structure and epitaxial relation to the substrate as well as the optical properties are determined for GaN nanowires. The same studies are performed for InN nanowires in Chapter 8. Chapter 7 deals with the doping of GaN nanowires and the influence on the morphology as well as the optical properties. Finally, in Chapter 9 the influence of processing steps on nanowires is studied and results of electrical measurements and deduced physical properties are discussed.

Chapter 10 presents a summary with important conclusions of this thesis and an outlook on future interesting studies.

Chapter 2

Material Properties

2.1 General Group-III Nitride properties

This first section will describe some general properties of the group-III nitrides AlN, GaN and InN. An extensive overview of nitride properties can be found in the book of Morkoç [9] or on the website of the Ioffe institute [10]. Only a selection of properties relevant for this thesis will be given here. In the second section properties which are specific for InN will be discussed. A lot of uncertainty still exists about the properties of this material and therefore a separate section has been devoted to it.

Relevance of Group-III nitrides for applications

Silicon is the workhorse for the semiconductor industry due to its excellent properties for device applications. It is available on earth in large quantities and therefore relatively cheap and can be produced with excellent quality. Wafers are commercially available in very large sizes up to 300 mm reducing the cost per chip in the production process. It is the best investigated semiconductor material, also driven of course by the industrial interest, and the technology to process silicon is at a very high level. Other semiconductors have to show a considerable improvement in device performance to be a viable alternative to silicon.

A major disadvantage of silicon and also germanium is their indirect band gap. Ge has similar physical properties as Si, is compatible to its technology up to a certain extent and is increasingly employed in combination with Si. The indirect band gap limits the efficiency of these materials in optical applications and as a result other materials like arsenides and phosphides have acquired an important position in this field. In the spectral range of Si and Ge these materials have a direct band gap and are thus more efficient. They also span a larger part of the electromagnetic spectrum and go into the visible range. GaP emits green light at 570 nm and is widely used in green LEDs, although it has an indirect band gap. However, the spectral range of these materials is limited and does not cover the whole visible range. This is important to produce white light to be used in for instance displays and lighting. Only the spectral range from red ($\approx$ 700 nm) down to a green color of 570 nm can be addressed with these materials. Visible green light however has a wavelength of 510 nm and blue light has an even lower wavelength. To overcome this deficiency, group-III nitrides have gained significant

interest, because they span the whole visible spectral range (roughly $400 - 700\,\text{nm}$). At room temperature InN has a band gap of $\approx 0.7 - 0.8\,\text{eV}$[1]. GaN and AlN have room temperature band gaps of 3.42 eV and 6.2 eV respectively [9], so together with their alloys (InGaN, AlGaN and AlInGaN) the group-III nitrides span a very large range of the electromagnetic spectrum from the IR to the deep UV. Moreover, they are all direct band gap semiconductors. Thus, they are perfect candidates for optical applications. The large band gap of GaN, AlGaN and AlN also make them suitable for high density optical storage, because the spatial resolution of the written data scales inversely with the wavelength. An important result in this area reported very recently is the fabrication of an AlN LED, which emits light at 210 nm [7].

Crystal structure

Common III-V semiconductors like GaAs and InP crystalize in the zinc-blende (ZB) structure, which is similar to the diamond structure in which silicon crystalizes. The diamond structure consists of two interpenetrating fcc-lattices, translated over $\langle \frac{1}{4}, \frac{1}{4}, \frac{1}{4} \rangle$ relative to each other. In the ZB structure, each fcc-lattice is occupied by one element, e.g. Ga and As, respectively. The thermodynamically stable phase of bulk group-III nitrides, however, is the wurtzite (WZ) structure. Thin layers of GaN and InN have been stabilized in the ZB structure on cubic substrates such as Si(100) and GaAs(100), but thicker layers usually grow in polycrystalline form or there is a mixture of the ZB and WZ phase. For very high pressures also the rocksalt (NaCl) structure can be induced in AlN, GaN and InN.

The WZ and ZB structure are very similar. The difference is in the stacking order along the $\langle 111 \rangle$ direction, which in hexagonal crystals is also denoted by $\langle 0001 \rangle$. In the WZ structure, along the $\langle 0001 \rangle$ direction, the atoms follow the stacking sequence ... AaBbAaBb..., while in the ZB structure, along the $\langle 111 \rangle$ direction, the sequence is ... AaBbCcAaBbCc.... Capital letters correspond to group-III atoms (Al, Ga, and In) and lowercase letters to N atoms. As mentioned above, the diamond structure is a ZB structure where both atoms are the same. The stacking order for both types is shown in Fig. 2.1 along with the directions. If there is an error in the order of the layers, then this is called a stacking fault. The lowest stacking-fault formation energies per unit cell area are 10 meV and 19 meV for GaN and InN [12], so there is a probability to include them during the growth. Certain types of stacking faults can give rise to a ZB-like region [12].

Since there is no mirror plane perpendicular to the c-axis, the directions (0001) and $(000\overline{1})$ are not equal. As a matter of convention the direction for which the group-III atom is on top of the bilayer, e.g. Ga in the case of GaN, is defined as (0001) (cf. Fig. 2.2). The crystal is said to have Ga-polarity or to be Ga-face, as opposed to N-polarity (or N-face) for the $(000\overline{1})$ direction. So the polarity is related to the orientation of the crystal, whereas another property corresponds to the nature of the surface. i.e. whether the crystal ends in a Ga or N layer. In the first case, the crystal is called Ga-terminated and in the latter N-terminated. Ga- or N-polarity is determined by the choice of substrate and the growth process, especially the initial stages of it. A Ga-face layer can be both Ga- and N-terminated; this depends for

[1] There has been some controversy about the band gap value of InN and for a long time a value of 1.9 eV was assumed. Recently also a lower value of 0.7 eV [11] has been reported. The exact value depends very much on the material quality. This issue will be discussed in Sec. 2.2.

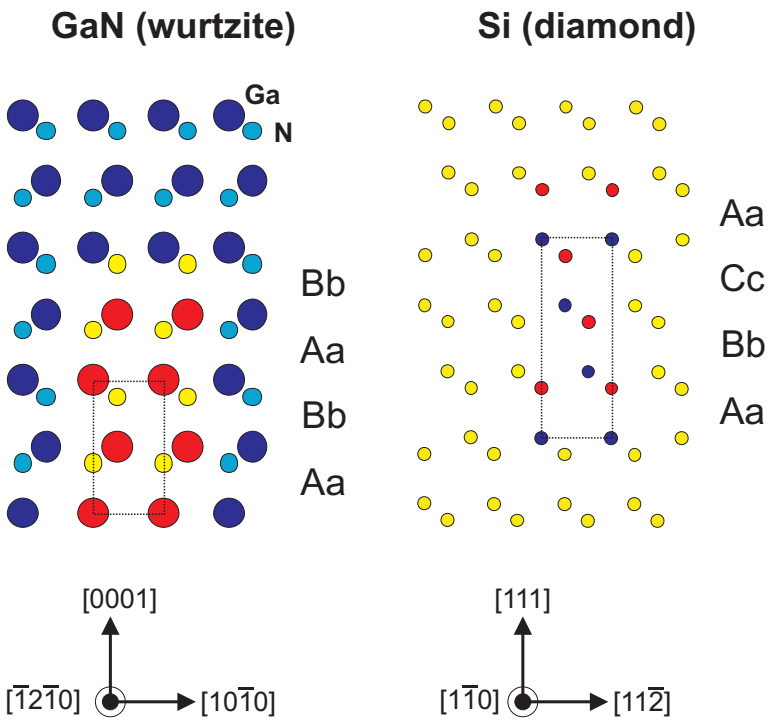

Figure 2.1: Stacking order in wurtzite (e.g. GaN) and zinc-blende/diamond structure (e.g. Si). The stacking order for the wurtzite structure is AaBbAaBb . . . and in the zinc-blende structure AaBbCcAaBbCc . . .

instance on the III-V ratio during growth [13]. Both bulk and surface properties can depend significantly on the polarity of the layer. The same conventions hold of course for InN and AlN.

Substrates for epitaxial growth

Nitride semiconductors do not enjoy native substrates of their own. The main problem to produce them is the very large vapour pressure of N, coupled with a low solubility of N in the metal melts at reasonable temperatures and pressures. The situation is most severe for InN and to a lesser extent for AlN. However, despite considerable efforts to produce nitride substrates, people usually resort to high-quality heterosubstrates. For growth in the (0001) orientation the most common substrates are Si(111), Al_2O_3(0001) (sapphire) and SiC(0001), which have the same hexagonal surface symmetry as the nitride (0001). However, in all cases there is a substantial thermal and lattice mismatch (cf. Tab. 2.1) causing tensile or compressive strain and this can result in defects in the grown layer. Quasi-substrates of very thick ($\geq 100\,\mu$m) GaN layers grown by HVPE [2] are sometimes used as an alternative.

[2]Hydride Vapour Phase Epitaxy

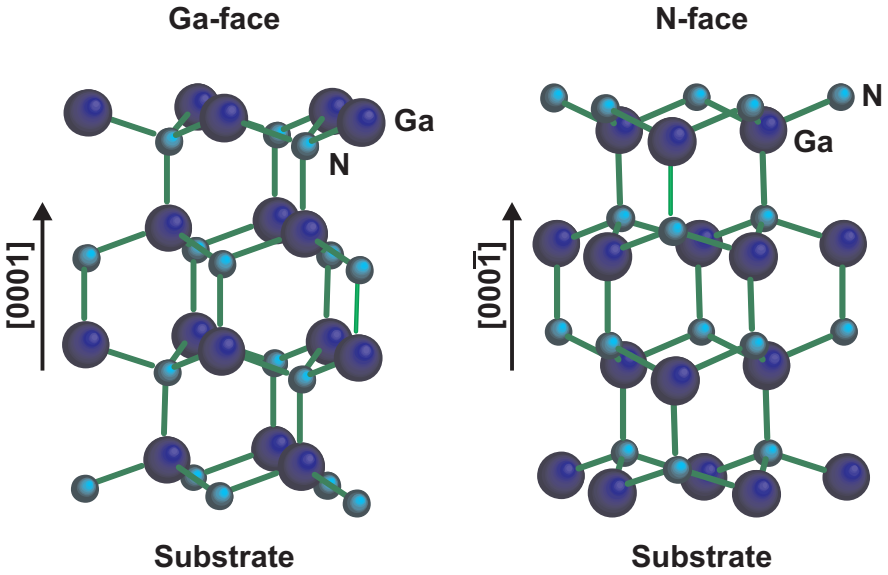

Figure 2.2: Definition of Ga- and N-face polarity in GaN. The direction for which Ga is on top of the bilayer is called Ga-face and

Table 2.1: Physical properties of group-III nitrides and some data on typical substrates for nitride growth. Data has been taken from [9, 10, 14, 15].

			GaN	**InN**	**AlN**	**Si**	Al_2O_3	**6H-SiC**
energy gap (300 K)	E_g	[eV]	3.42	0.7	6.2	1.12	9.1	3.0
lattice constant	a_0	[Å]	3.189	3.5365 [16]	3.112	5.4301	4.758	3.081
	c_0	[Å]	5.186	5.7039 [16]	4.982		12.991	15.117
internal parameter	u		0.376	0.377	0.380			
dielectric constant	ϵ_r		8.9	15.3	8.5	11.7	9.4-11.5	9.66-10.03
electron effective mass	m_e	$[m_0]$	0.20	0.11	0.4	0.19-0.98		0.42-2.0
electron mobility (300 K)	μ	$[cm^2/V \cdot s]$	1000-1350	< 3200	300	1350		< 400
thermal expansion	$\Delta a/a$	$[K^{-1}]$	$5.59 \cdot 10^{-6}$	$3.8 \cdot 10^{-6}$	$4.2 \cdot 10^{-6}$	$3.59 \cdot 10^{-6}$	$7.5 \cdot 10^{-6}$	$4.3 \cdot 10^{-6}$
	$\Delta c/c$	$[K^{-1}]$	$3.17 \cdot 10^{-6}$	$2.9 \cdot 10^{-6}$	$5.3 \cdot 10^{-6}$		$8.5 \cdot 10^{-6}$	$4.7 \cdot 10^{-6}$
thermal conductivity	κ	$[W/cm \cdot K]$	1.3	0.45	2.85	1.3	0.35	4.9
optical phonon energy	$\hbar\omega$	[meV]	91.2	73	99	62.9		104.2
melting temperature	T_m	[°C]	2500	1100	2750	1410	2040	2830
bond energy [17, 18]	E_b	[eV]	2.23	1.93	2.88			

Each of the heterosubstrates has its advantages and disadvantages. Si wafers are cheap, widely available in large wafer sizes and growth of nitrides on Si would make it compatible to standard CMOS [3] technology. However, the substrate orientation commonly employed in the

[3] Complementary Metal Oxide Semiconductor

Si industry is Si(100) and not Si(111), which is needed to grow WZ nitrides. In addition, the large thermal and lattice mismatch for Si(111) (cf. Tab. 2.1) induces tensile strain in the nitride layers and can lead to cracks for thicker layers. Sapphire wafers are also quite cheap and have a good availability, but as in the case of Si the thermal and lattice mismatch leads to strain in the epitaxial layer. The strain is however compressive. The major disadvantage of sapphire is its low thermal conductivity, which makes it unsuitable for high power applications where excessive heat has to be transferred away from the substrate. Concerning lattice mismatch and thermal conductivity, SiC is the best choice to grow nitrides, but SiC wafers are very expensive and the quality does not reach that of Si or even sapphire.

Chemical stability

The group-III nitrides (AlN, GaN and InN) have a strong chemical bond. The bonds of the nitrides are more ionic in character ($31 - 40\%$) than the other III-V semiconductors ($< 8\%$) in terms of Pauling electronegativities [19]. Pauling defined electronegativity as "the power of an atom in a molecule to attract electrons to itself" and formulated an electronegativity scale of the elements. The Pauling scale is useful for estimating bond polarities and, to some degree, the strengths of bonds between different atoms. The electronegativity differences and corresponding ionic bond character for group III nitrides are: AlN (1.41, 40%), GaN (1.23, 31%) and InN (1.26, 32%) [20]. The increased ionic character of the III-nitrides compared to other III-V semiconductors is also visible in the binary bond energies. The Ga-N bond strength is $\approx 2.23\,\mathrm{eV}$ [18] comparable to the C-C bond strength of $1.9\,\mathrm{eV}$ in diamond [19] and much larger than Ga-As or In-P bond strengths which are $\approx 1.0\,\mathrm{eV}$ [21].

The chemical stability of a material depends on its quality and especially for InN it has proven to be difficult to grow high quality material. This has only become possible by the use of molecular beam epitaxy (MBE) and chemical vapour deposition (CVD) techniques and therefore the reported physical properties scatter a lot, like for instance the value of its band gap. Nevertheless the low decomposition temperature of InN makes it less chemically stable than GaN and AlN.

From technological point of view the thermal stability of III-nitrides should allow high temperature processing steps to be performed but the chemical stability also presents a technological challenge. There have been many reports describing the resistance of nitrides to the conventional wet etching techniques used in semiconductor processing (see for instance the review by Pearton *et al.* [22]). Acid solutions are inappropriate, but alkaline etchants, such as aqueous KOH and NaOH solutions give some reasonable etching rates. Dry etching has had more success, although due to the inert nature and strong chemical bond of the group-III nitrides it is also complicated (for a review cf. [18]).

This chemical stability of the III-nitrides (especially GaN and AlN) makes them suitable for operation under harsh environments like elevated temperatures (e.g. in the automotive industry), caustic environments or outdoor applications (e.g. solar cells), where the device is exposed to the elements. In general it is also an important property for sensors. Nitrides are an excellent candidate for protective coatings due to their hardness too.

Spontaneous and piezoelectric polarisation

An interesting feature of nitrides, which can be exploited for instance to produce 2DEGs[4] without the use of modulation doping is their spontaneous polarisation due to their strong polar bonds and the lack of inversion symmetry. When the crystal is strained an additional piezoelectric polarisation is possible. This can be exploited when growing nitride heterostructures, because due to difference in polarisation of the two layers, an interface charge builds up, which combined with a bending of the conduction bend at the hetero-interface can lead to a electron accumulation in a quasi-2D layer (2DEG). The main advantage is, that there is no need for modulation doping as employed in similar heterostructures with for instance arsenides. This effect however, will not be further exploited in this work.

2.2 InN properties

At the end of the last decade, InN was the least studied material of the III-nitride alloy system (AlN, GaN and InN). Partly this was due to its band gap value, which was assumed to be around 1.89 eV and thus in the same range as well established optical materials like the group III-arsenides and -phosphides. The main interest was in connection with the other III-nitrides to cover a large range of the electromagnetic spectrum within one alloy system. It also has an important advantage over the arsenides and phosphides because it contains no poisonous elements such as arsenic and needs no toxic gases such as phosphine in the fabrication process. Of all III-nitrides it has the lowest lattice mismatch with Si(111) of only -8% (negative values correspond to tensile and positive ones to compressive strain), but the mismatch to sapphire (also commonly employed for nitride growth) is the largest amounting to 28%.

The quality of the grown InN until recently has been fair at best, which was to some extent related to the high equilibrium nitrogen pressure and a correspondingly low decomposition temperature, especially under vacuum conditions used in for instance modern deposition techniques like metalorganic vapour phase epitaxy (MOVPE) and MBE. The required low deposition temperatures limit the reactivity of the nitrogen precursor, e.g. NH_3. The low quality of the grown material is also the reason that reported values for important physical quantities scatter a lot.

In contrast to GaN and InGaN, which are very efficient light emitters despite relatively high densities of structural defects, InN has been observed to be a poor light emitter. Therefore the determination of the band gap was mainly done on the basis of absorption measurements. Recently, however, an improvement of the film quality has been obtained [23, 24] and in 2002 reports about InN grown by MBE that did have a strong luminescence started to emerge [11, 16, 25, 26]. The value of the band gap found in these experiments was below 1 eV. The reported electron concentration of InN was typically of the order of $10^{20}\,\mathrm{cm}^{-3}$, but in these recent publications they were in the mid-$10^{18}\,\mathrm{cm}^{-3}$ with mobilities of the order of $1000\,\mathrm{cm}^2/\mathrm{Vs}$ at room temperature. This is an indication of the higher quality of these MBE grown InN layers. Since the position of the photoluminescence energy correlates with an onset of strong absorption, the optical transition around 1 eV has been ascribed to the fundamental band

[4] Two-dimensional electron gas

gap of InN. The result of a low fundamental band gap of InN was supported by theoretical calculations by Bechstedt *et al.* [27].

Wu *et al.* showed that due to the so called Moss-Burstein shift [28, 29] the absorption edge of InN is greatly influenced by the free electron concentration [30, 31]. For a free electron concentration of $4.5 \times 10^{20}\,/\mathrm{cm}^3$ the absorption edge shifts to 1.7 eV, which is close to the previously accepted value of the band gap of InN ($\sim 1.9\,\mathrm{eV}$) obtained from sputter grown, degenerately doped InN films. The high electron concentration causes a band-filling of the conduction band and since absorption of a photon only occurs if an electron is excited from an occupied to an unoccupied state, the required photon energy increases with the shift of the Fermi level. Inclusions of Indium oxide have also been suggested to explain the high band gap value, despite apparently high quality material.

A report by Shubina *et al.* [32] suggested that Mie resonances[5] due to scattering or absorption of light in InN, which contains metallic In clusters could explain the 'erroneous' results of a band gap below 1 eV. They associated the emission at $0.7 - 0.8\,\mathrm{eV}$ with surface states at the metal-InN interfaces. The work was criticized by Bechstedt *et al.* (cf. [34–36]) who repeated calculations performed in [32] and showed that these pointed to a band gap value below 1 eV and not a high band gap value around 1.9 eV. Eventually the explanation of the IR emission of InN due to Mie resonances was turned down, even by some of the coauthors of Shubina [37].

Valence electron energy loss spectroscopy (VEELS) measurements in a TEM system on InN and InGaN samples performed by Specht *et al.* [38] pointed to a value of 1.7 eV, but the TEM preparation and the transmission electron spectroscopy itself probably created donor-like states lifting the Fermi level, although the quality of the original material might have been good.

So the new high quality material resulted in the revision of the value of the optical band gap of InN to $\sim 0.7\,\mathrm{eV}$ and also the value of other fundamental properties like the electron effective mass $\mathrm{m_n}$ was revised from $0.11\mathrm{m_0}$ to $0.07\mathrm{m_0}$. A lower value of $0.042\mathrm{m_0}$ proposed in [39] did not fit well to the experimental data (cf. for instance [40]).

The low value of the fundamental band gap of InN opens up a lot of exciting possibilities for the $\mathrm{In}_x\mathrm{Ga}_{1-x}\mathrm{N}$ alloy system, because it spans the whole visible spectral range, making it an ideal candidate for displays and lighting. Walukiewicz *et al.* [41] discussed the possibilities of this material for multi-junction solar cells with a higher efficiency than established Si-based photovoltaic cells, because in theory InGaN can convert the whole spectral range of the solar light into solar energy. However, the problem of the InGaN miscibility gap as reported in [27] still has to be solved.

[5] Resonant light scattering and absorption by dispersed small particles [33].

Chapter 3

Review Nanowires

3.1 Introduction and motivation

The word 'nanowire' (NW) consists of two parts: 'nano' and 'wire'. The first one describes the length scale and the second one is related to the shape of the structures. Now, intuitively from the everyday macroscopic world, one knows that a wire has two characteristic dimensions: its length and diameter, where the latter is usually considerably smaller. The word 'nano' refers to this *diameter*, which is typically of the order of $1 - 100\,\mathrm{nm}$. The length however can be up to several microns corresponding to aspect ratios (length/diameter) up to 1000 [42–44]. The nanowire cross-section is typically round, hexagonal, square or triangular depending on the material and deposition technique. Other words, which are also sometimes used instead of 'nanowire' are 'nanocolumn' or 'nanorod'. In the pioneering years of 'filamentary growth' around 1950 the word 'whisker' was often used for structures with diameters ranging from approximately 100 nm to millimeters. Currently, the word 'nanowhisker' can also still be found in publications and there is no real distinction between the different words. It is rather a personal preference. Nanotubes, however, are a different class of nanostructures. They have similar dimensions, but are hollow inside. The most prominent representatives are carbon nanotubes (CNT), which are fabricated by rolling graphite sheets into tubes. The twisting of the roll determines the electrical properties. For completeness it must be mentioned that there are also so called 'nanobelts', which have a rectangular cross-section, but still both fringes have nanometer dimensions. They have similar properties as nanowires, but will not be discussed in this chapter.

There are numerous methods to produce nanowires of which the most prominent will be discussed in Sec. 3.1.2. Most of them, however, have in common that the nanowires are deposited on some kind of substrate. The nanowires then grow either epitaxially in specific directions or in a random way, the substrate only functioning as a support. One type of nanowires, which are interesting nanostructures but will not be discussed here, are horizontal nanowires, i.e. 1D structures growing on the substrate surface at favourable positions (e.g. at step edges) [45, 46]. The footprint[1] of such a structure is proportional to the length of the

[1] The footprint of a structure is the amount of space it occupies on a substrate and is thus important for the number of devices which can be integrated on a chip.

wire, whereas in the case of a vertical wire the footprint scales with the diameter and is thus many times smaller. Hence, a high integration density can be achieved with vertical wires. Size is a very important factor for industrial applications. If the functional structures of a device become smaller, then more of them can be packaged on a single chip. This can increase the speed of the device, increase the memory which can be stored on the chip and the interconnects between structures can be shorter increasing speed and reducing power consumption. In general the size of a device can be reduced without losing functionality, which is important for portable applications. This motivates the endeavour of the semiconductor industry towards continuous reduction of the device size.

There are two ways to pursue this goal. The first is the *top-down* approach, where small features are patterned into bulk materials by means of lithography, etching and deposition steps. By continuously improving these three technologies it has been possible to reduce the resolution limits. However, these improvements in resolution are accompanied by a tremendous increase of the cost with each new level of manufacturing facility. Moreover, the physical principles at the base of the device performance should not change when scaling the device dimensions. At the nanoscale, however, the classical concepts sometimes do not apply anymore, because quantum effects come into play. Therefore alternative approaches have been actively searched after by research institutions and industrial companies alike.

An alternative way is the *bottom-up* approach, in which well-defined chemically and/or physically synthesised nanoscale building blocks are assembled to produce functional nanostructures. Since the building blocks are formed by self-organisation and not by the expensive lithography methods, the production costs are potentially much lower. This method should also allow to combine different materials with a quality not obtainable with a pure top-down method by lithography and etching (cf. Sec. 3.1.1). Also aspect ratios which can be achieved with bottom-up technologies are far beyond the current status of top-down engineering. The large aspect ratio results from enhanced growth in a preferred direction. This can be due to different growth rates for dissimilar crystal facets or the use of a catalyst to enhance the growth in a certain direction (cf. Sec. 3.2).

In the next sections the methods to produce nanowires as well as the corresponding growth mechanisms will be treated. The possible advantages of nanowires will be discussed and the special case of nitride nanowires, which is the subject of this thesis is presented. At the end of the chapter the requirements to implement nanowires in applications are discussed.

3.1.1 Strain engineering

The small lateral dimension of nanowires (typically some tens of nanometers) allows to grow heterostructures of heavily mismatched materials. For compact layers strain can only be accommodated by elastic deformation of the crystal without formation of misfit dislocations up to a critical thickness, which depends on the amount of lattice mismatch. For small enough nanowires and not too large mismatch, however, elastic deformations can be relieved at the surface. Thus, nanowires give more freedom in the choice of materials to combine. The heterointerface can be situated inside of the wire, but the mechanism of strain relief equally holds for the nanowire/substrate junction. This feature is interesting in the context of monolithic integration of III-V semiconductors into silicon technology combining the best

of two worlds: the superior electronic properties of III-V semiconductors with the highly advanced and relatively inexpensive silicon process technology.

A related issue is the problem of thermal expansion mismatch between materials, i.e. either the substrate and the deposited layer or different materials in a heterostructure. Since semiconductors are usually deposited at elevated temperatures, which can be above 1000 °C for III-nitrides grown by MOVPE, upon cooling down to room temperature, at which samples are handled and processed, different thermal expansions can introduce strain. This can lead to defects or even cracks in deposited layers (cf. GaN grown on Si(111)). Also in this case the small diameters of nanowires can more easily relieve strain at the surface elastically leading to higher quality material with less defects.

3.1.2 Fabrication techniques

In the 1950's mercury (Hg) whiskers were grown by bringing a mercury vapour into contact with a glass plate cooled to a temperature below the freezing point of Hg [47]. The whiskers preferentially originated at specific points randomly distributed over the surface area, which were presumed to be step edges in the substrate (cf. Sec. 3.2.1). In 1964 Wagner and Ellis obtained Si whiskers by heating a Si containing source (SiI_2) material which had a small amount of a suitable impurity like Au [48]. The Au catalyzes the reaction in which Si is formed and this dissolves in the Au. When the Au droplet saturates with Si, whiskers grow in preferred crystalline directions (cf. Sec. 3.2.2). In the 1970's Bootsma and Gassen [49] as well as Givargizov [50] used chemical vapour deposition (CVD) to grow Si and Ge whiskers. The Si source was SiH_4 or $SiCl_4$ and this was transported by a carrier gas (H_2 or He) to a heated Si substrate decorated with impurity particles (Au, Ag, Cu, Ni or Pd). The particle size was of the order of $10 - 100\,\mu m$. The wires grow at the position of the particles via the vapour-liquid-solid (VLS) mechanism (cf. Sec. 3.2.2). With advancing technology it became possible to improve the definition of the catalytic particles and also the CVD deposition technique evolved. Metalorganic precursors were used (MOVPE), but the basic principle stayed the same.

Lieber *et al.* employed laser ablation of a source material, which contained the element desired in the nanowire growth as well as the metal catalyst component [51]. The target was placed within a quartz tube in which the temperature and pressure could be varied. In the case of Fe catalysed Si nanowire growth laser ablation with photons of the $Si_{1-x}Fe_x$ target creates a hot vapour of Si and Fe species. Through collisions with the transport gas the hot vapour condenses into small clusters. The furnace temperature is controlled to keep the Si-Fe nanocluster in a liquid state. After the liquid becomes supersaturated with Si, growth starts by the VLS mechanism and continues as long as Si is supplied and the nanocluster remains in a liquid state. When the Si-Fe nanoclusters pass out of the reaction zone onto a cold finger, they solidify and can be collected after the growth run. This method can be applied to other materials for suitable combinations of elements and catalysts and it also allows to incorporate doping elements. Nanowires with diameters as small as 3 nm and lengths up to several microns have been produced.

The above method was improved by replacing the cold finger by a substrate decorated with impurity particles with well-defined diameters instead of embedding the impurity in the

source material [52]. In this way the control of the diameter of the nanowires was improved and the length could also be regulated by the growth time.

Molecular beam epitaxy (MBE) (cf. Sec. 4.1) has also been employed to grow nanowires either with catalyst via the VLS mechanism [53,54] or catalyst-free (cf. Sec. 3.3). The nanowire growth mechanisms of MBE are similar to MOVPE, but the growth conditions can be different (see also discussion at the end of Sec. 3.2.2).

3.2 Origin of anisotropic growth

The high aspect-ratio of whiskers is evidently caused by an enforced anisotropy in growth kinetics [49]. The difference in growth behaviour compared to the growth of bulk crystals can be explained in the following ways. The first possibility is a retarding or suppressing of the growth in directions perpendicular to the length direction of the whiskers (lateral/radial growth). The growth parallel to the length direction (vertical/axial growth) is not affected. The second possibility is an enhanced axial growth, whereas the lateral growth proceeds with a rate similar to bulk crystal growth. A combination of both may also occur: retarded or suppressed lateral growth and stimulated axial growth.

In the 1950's and 1960's two principal models for vapour whisker growth were developed to account for experimental observations. Initial whisker growth studies by Sears [47, 55, 56] explained the anisotropic growth by assuming the presence of a screw dislocation inside such a whisker, which enhances the axial growth (cf. Sec. 3.2.1). The vapour-liquid-solid (VLS) model developed by Wagner and Ellis [57] was employed to explain the whisker formation in the presence of an impurity particle [48–50, 58, 59] (cf. Sec. 3.2.2). The basic ideas and main results of both models will be briefly discussed in the next sections.

3.2.1 Diffusion-dislocation model

The history of the theory of crystal growth divides into two parts [60]. The first theory treats the growth of ideally perfect crystals, which started with Gibbs (1878) and was then developed further by famous names like Volmer, Stranski, Becker, Frenkel and Burton and Cabrera. The latter two were involved in developing the theory of the growth of imperfect crystals together with Frank at the end of the 1940's. The results from these theories were employed by Sears to formulate a model [56] for the whisker growth observed in his experiments [47, 55, 56].

When growing a crystal from the vapour, impinging atoms will condense into lattice positions more readily if neighbours surrounding the site are already in place. Thus an atom is relatively weakly attracted to a perfect crystal surface, more strongly attracted to a step edge between two terraces and most strongly attracted to a corner (cf. [61, p.636]). For a perfect crystal every time a layer is completed the next layer has to be nucleated. Since there are no favourable nucleation sites on such a perfect layer, the attraction of the adatom to the layer is weak and it can easily desorb again before being incorporated in the crystal. Growth proceeding in this manner would be slow. If however screw dislocations emerge in a crystal face then the need for surface nucleation on that face would be eliminated, because it has a step (cf. Fig. 3.1). Growth of the crystal does not eliminate the step, the process of growth consisting of a rotation of the step about the point where it joins the dislocation. The same

is true for any dislocation whose Burgers vector has a component normal to the face in which the dislocation ends [60, 61]. Suitably dislocated crystals are thus able to grow at almost arbitrarily low values of the supersaturation of the vapour.

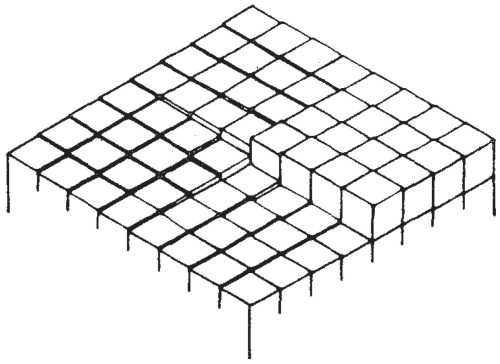

Figure 3.1: The end of a screw dislocation with the accompanying step in a building-block crystal model [60]. Growth can proceed endlessly around the dislocation.

Sears transferred this model to the growth of whiskers by postulating the presence of an axial screw dislocation in the whisker which provides for self-perpetuating growth steps on the tip so that the tip is an *efficient sink for adsorbed atoms*. In addition for sufficiently small vapour supersaturations growth only occurs on the whisker tip by a process involving surface migration to the tip of atoms condensed on the sides of the whisker. Since the side faces do not comprise such a screw dislocation the growth on the side faces rather proceeds in a two-dimensional fashion and is thus much slower. If the supersaturation is below the critical value for two-dimensional nucleation, radial growth cannot occur.

The model proposed by Sears was developed further theoretically by Blakely and Jackson [62], who investigated the influence on the axial growth rate of the ratio between the wire length l and the surface diffusion length λ, which is the mean distance an adatom migrates before it desorbs. They assumed however that there is no net flux between the whisker and the substrate. This assumption which was also used in previous studies had been based on the idea that substrate sites act as a trap for impinging atoms. Ruth and Hirth [63], however, extended the theory further also including whisker growth involving surface diffusion from the substrate onto the whisker.

The proposed theories also account for radial growth if the whiskers reach a certain length. For long enough whiskers for which the diffusion length λ is smaller than the whisker length l, thickening can occur. It is proposed that under these conditions the screw step no longer depletes the concentration of adsorbed atoms at the base of the whisker. The lateral growth is then presumed to occur by intermediation of the substrate-whisker corner in two-dimensional nucleation.

It has to be noted that only in a few cases whiskers with a screw dislocation have been observed. Moreover, for fcc, diamond, sphalerite and wurtzite crystal lattices whiskers grow in preferred directions, $\langle 111 \rangle$ or $\langle 0001 \rangle$, while the side faces are $\langle 211 \rangle$, $\langle 110 \rangle$ or $\langle 11\bar{2}0 \rangle$, $\langle 10\bar{1}0 \rangle$

[50]. These observations are inconsistent with the dislocation model of Sears [55,56]. However, the diffusion models [62,63] do not require the presence of a screw dislocation. They are based on the assumption that there is a sink at the whisker tip for adatoms impinging on the whisker surface and adatoms which do not reach the whisker tip by diffusion along the whisker surface during their stay time re-evaporate. So in other words this is similar to the third condition for anisotropic growth formulated in Sec. 3.2 when the radial growth is suppressed. Hence, the formula for the axial growth rate in the framework of the diffusion model:

$$V = \frac{dl}{dt} = I + \frac{4I\lambda_s}{d} \tanh \frac{l}{\lambda_s} \quad , \tag{3.1}$$

has a more general applicability and is not limited to the case of a screw dislocation. Here V is the axial growth rate, l the whisker length, t is time, I the impingement current at the whisker tip, λ_s the root-mean-square diffusion distance on the whisker surface and d the whisker diameter. The first term 'I' of the equation is the growth rate due to direct impingement of atoms at the tip and the second one is the rate due to the surface diffusion of adatoms on side faces.

3.2.2 Vapour-liquid-solid growth

In 1964 Wagner and Ellis [57] suggested a new concept of whisker-growth from the vapour based on studies of the growth of Si whiskers [48]. The following facts emerged: (a) the Si whiskers do not contain an axial screw dislocation; (b) an impurity is essential for whisker growth; (c) a small globule is present at the tip of the whisker during growth. The absence of a screw dislocation dismissed the mechanism of the diffusion-dislocation model discussed in the previous section. Based on (b) and (c), they proposed a 'vapour-liquid-solid' (VLS) mechanism in which an *impurity particle* acts as a *preferred sink* for arriving Si atoms or perhaps more likely *catalyses* the chemical process involved. The role of the impurity particle is to form a liquid droplet, which is a preferred site for deposition from the vapour. With time the liquid becomes supersaturated and the excess Si is precipitated at the liquid-solid interface. In this way the whiskers grow in a 1D fashion without the need of a structural defect like a screw dislocation to enhance the anisotropic growth. The impurity particle is lifted from the substrate and 'rides' on top of the growing whisker (cf. Fig. 3.2). The size of the liquid particle determines the diameter of the whisker. Only a very small portion of the impurity is incorporated into the whisker, because otherwise the droplet would shrink and thus also the diameter ('tapering effect'). Note, that a reduction of the impurity concentration in the droplet increases the Si supersaturation and thus more Si will precipitate. Hence the Si cannot compensate the size reduction of the droplet caused by the precipitation of the impurity. Wagner and Ellis observed whisker growth for several impurities like Au, Pt, Ag, Pd, Cu and Ni [48, 57]. They also suggested that in the growth of compound crystals, for example GaAs, an excess of one of the components can act as the liquid-forming impurity.

Initial quantitative studies on VLS whisker growth were performed by Bootsma and Gassen [49] and Givargizov [50, 58, 59]. One of the questions they tried to answer was which of the stages in the VLS process (cf. Fig. 3.3) was rate-limiting. Bootsma and Gassen suggested that step 2, the chemical reaction on the vapour-liquid interface determined the growth rate based

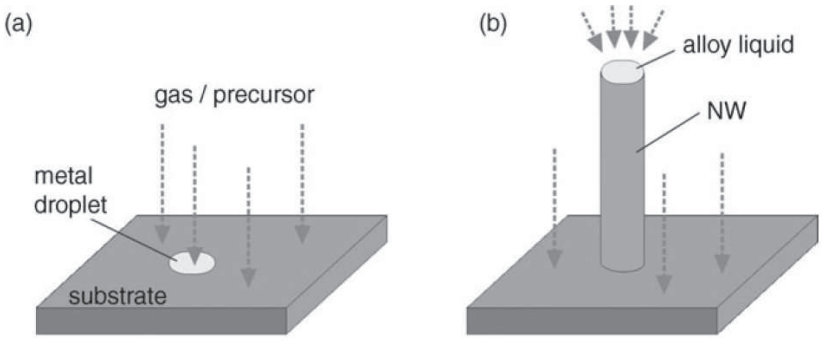

Figure 3.2: Schematic illustration of the VLS mechanism as proposed by Wagner and Ellis [57]. (a) Initial condition with liquid Au droplet on a substrate for the growth of Si whiskers. The vapour impinges on the droplet, which catalyses the decomposition of the precursor molecules; (b) When the droplet is supersaturated with Si, the Si precipitates at the liquid-solid interface and the whisker starts to grow, lifting the impurity particle up from the substrate.

on the dependence on vapour pressure, but Givargizov proposed step 4, the nucleation at the liquid-solid interface, because of the dependence on the growth face of the crystal. Recently Kodambaka *et al.* [64] concluded from in-situ TEM measurements that it is indeed step 2 which has to determine the rate.

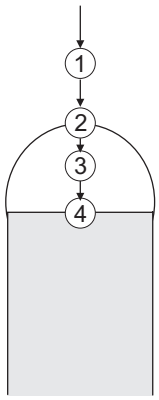

Figure 3.3: Various stages of the VLS process. (1) mass-transport in the gas phase; (2) chemical reaction on the vapour-liquid interface; (3) diffusion in the liquid phase; (4) incorporation of the material in the crystal lattice.

In the early 1990's Hiruma *et al.* studied the growth of GaAs and InAs nanowires by metal organic vapour phase epitaxy (MOVPE) using the VLS mechanism [65]. Thin Au layers were annealed, which results in the formation of small Au droplets. In this way they could produce nanowires with diameters below 100 nm. They also reported the successful incorporation of a p-n junction [66] and an InAs/GaAs heterostructure [67] inside the nanowires. The wires

showed good optical properties. With the help of e-beam lithography positioning of single wires was also achieved [68]. These studies attracted a lot of interest from research groups all over the world, because of the possibility to produce crystals with high crystalline quality which are small enough so that they can potentially show quantum effects.

Due to the enormous scientific interest, great progress has been made in respect to different aspects of VLS whisker growth with important contributions by the groups of Lieber at Harvard [69–71], Samuelson in Lund [72, 73], Gösele in Halle [42], P.D. Yang at Berkeley [44, 74] and Kouwenhoven / Bakkers in Delft and Eindhoven [75, 76]. Also groups in Japan have produced a great deal of interesting publications as well as many other groups. But despite the fact that uniform wires with suitable properties have been grown using the VLS process, optimisation of nanoscale wires for electronic applications requires a more quantitative understanding of the wire growth mechanism, which in many cases is still not fully understood. However, also in this area a lot of progress has been made in recent years expanding the models developed by Sears, Wagner, Bootsma, Givargizov, etc. [54, 64, 77–85].

An issue, which has caused a bit of controversy is the diameter dependence of the growth rate. Givargizov observed [50] that thicker wires grew faster than thinner ones. He attributed this to the Gibbs-Thomson effect, according to which the supersaturation decreases for smaller diameter. Since the growth rate is proportional to the supersaturation $\Delta\mu/kT$ (where $\Delta\mu$ is the difference in chemical potential between the vapour phase and in the whisker), thicker wires should grow faster. In contrast to what Givargizov found, several groups have reported an inverse dependence of the growth rate on the wire diameter for: Si grown by MBE [54], InAs, GaAs, InP and GaP grown by MOVPE [80, 81] and GaAs grown by MBE [77, 83]. Kodambaka, however, investigated the growth of Si nanowires by in-situ TEM [64] and did not observe a dependence on wire diameter. A recent study of Si nanowires grown by CVD showed a similar diameter dependence as Givargizov [86].

An explanation for the different results can be found in the different growth conditions. First, note that one basically can distinguish between two modes of vapour crystal growth: physical condensation and chemical vapour deposition (CVD). In physical condensation (MBE) the elements for the growth are already activated when leaving the source, which results in high sticking coefficients. The vapour pressures are accordingly rather low (typically below 10^{-5} mbar) and the diffusion lengths on the surface can be high. For CVD the vapour pressures are usually a lot higher (typically $1 - 10$ mbar) and the growth species decompose at the surface. The sticking coefficients are thus usually considerably lower. However a catalyst can significantly increase the surface reaction. A combination of both is also used for the growth of III-V semiconductors, where one growth species is presented in elemental form and the other as a precursor, which reacts on the substrate surface (gas-source MBE (GS-MBE), chemical beam epitaxy (CBE)). The vapour pressures are more in the region of physical condensation and therefore the adatom diffusion length is increased. Surface diffusivity and surface reaction are thus important quantities in these deposition techniques.

Comparing the formalism of the diffusion-dislocation model and the VLS model one sees that both postulate an 'active sink' at the whisker tip. In the first case a screw dislocation is the sink and in the second case the droplet. Diffusion on the surface is independent of the screw dislocation, so the VLS model can be extended to a 'diffusion-droplet' model (cf. Fig. 3.4) and Eq. (3.1) should also be valid. Such an equation was formulated and confirmed experimentally

for VLS growth [77, 80, 81]. As noted at the end of Sec. 3.2.1, the equation consists of two parts: one due to direct impingement and the other determined by the surface diffusion. The impingement term does not give a diameter dependence, but the diffusion-term is proportional to 1/d. Thus, the observed behaviour depends on the relative contribution of each term. Johansson *et al.* [81] also showed that for low supersaturations the Gibbs-Thomson effect can become important and an increase of the growth rate with wire diameter is expected like in Givargizov's experiment [50].

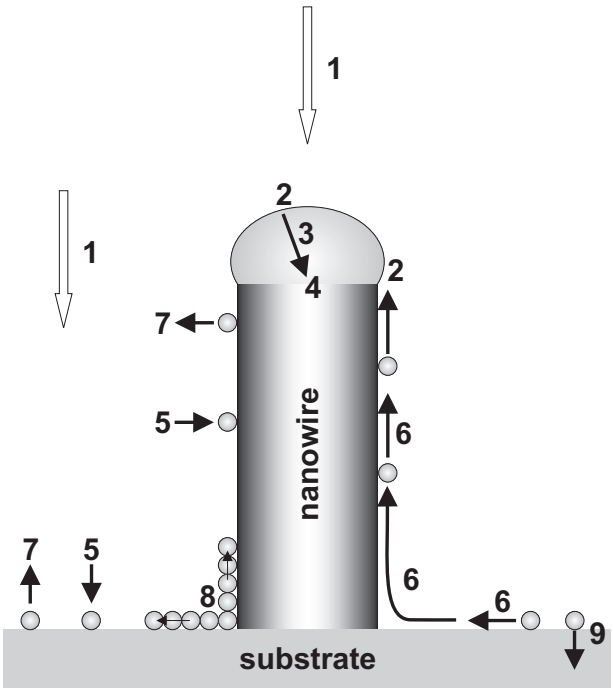

Figure 3.4: Schematic illustration of the diffusion-VLS model. (1) Mass transport through the gas phase; (2) dissociation reaction on the catalyst particle, either directly from the vapour or by diffusion from the side facets of the nanowire to the impurity particle; (3) diffusion of reactants through the metal particle; (4) precipitation of the growth element at the liquid-solid interface forming the semiconductor nanowire; (5) absorption on the substrate or whisker sidewalls; (6) surface diffusion on the substrate or whisker; (7) desorption from the substrate or whisker sidewalls; (8) film growth on the nanowire sidewall or substrate; (9) diffusion into the substrate.

Regarding the impurity droplet: Wagner and Ellis [57] suggested that the impurity particle is in a liquid phase and this was commonly accepted. However, the group of Samuelson has suggested [82, 87] that the particle is solid, because it shows a crystalline diffraction pattern and at temperatures where they expect the droplet to become liquid, growth ceases. They also showed that the activation energy for the growth of GaAs nanowires with a Au particle is similar to the growth of planar GaAs films and concluded that the particle is not catalytically active, but rather just acts as an active sink [81]. At their nanowire growth temperatures

planar growth is kinetically hindered and the growth species diffuse to the metal particle where they are readily incorporated.

3.3 Catalyst-free nitride nanowire growth

Compared to Si/Ge or III-V semiconductors like arsenides and phosphides, the growth of group-III nitrides has proven to be more challenging and only from the 1990's onward considerable progress has been made. Correspondingly, the knowledge about the growth mechanism and physical properties of III-nitrides has not developed to a level comparable with the other semiconductors. Even now fundamental properties of InN are still under debate (cf. Chapter 2). The lack of a suitable homo- or heterosubstrate is one of the main reasons for the underdeveloped knowledge of this material system. The absence of a self-regulating mechanism like in GaAs growth, where the sticking coefficient of As on an As-terminated surface is reduced to 0, also complicates the growth of these compound semiconductors. Accordingly, the interest in the growth of nitride nanowires has lacked behind other III-V nanowires. Dingle *et al.* grew GaN needles in 1971 [88] with diameters of the order of tens of microns, but only at the end of the 1990's significant research activity in nitride nanowires started again. In 1997 Han *et al.* grew GaN nanowires inside carbon nanotubes by reacting Ga_2O with NH_3 [89]. The groups of Kikuchi [90] and Calleja [91, 92] reported the growth of GaN nanocolumns by plasma-assisted MBE (PA-MBE) under N-rich conditions without the use of a foreign catalyst. These nanowires showed excellent structural and optical properties [8]. The only report of GaN MBE nanowire growth by the VLS mechanism using a foreign metal particle was published by Mamutin [53].

Despite the initial low interest, nitride nanowires have big potential in optoelectronic applications. Top-down fabricated nitride light emitting diodes (LEDs) and laser diodes (LDs) showed excellent optical properties [93, 94] and extended the range of the visible electromagnetic spectrum covered by such devices. These are important steps towards full color LED displays and higher optical storage density [95]. The nitride-based devices show high densities of dislocations caused by the lattice mismatch in the heteroepitaxy, however, which can reduce device performance and lifetime by increasing electrical resistivity and heating [95, 96]. Therefore, there is a lot of interest in high-quality nitride substrates.

A promising alternative are nanowires, because several features of nanowires are ideally suited for these optical applications. The small lateral size of the nanowires reduces the problem of lattice mismatch, because strain relief by elastic deformation is easier in nanowires (cf. Sec. 3.1.1). The easier strain accommodation also facilitates the incorporation of heterostructures, thus opening up the full optical range of the nitrides (from 0.7 eV for InN up to 6.2 eV for AlN) despite the lattice mismatch of $\approx 12\%$ between InN and AlN. The superior crystalline quality of these nanostructures and the increased freedom in band gap engineering can drastically improve the device performance. It might also allow the integration into established Si technology despite the large lattice mismatch to this substrate. Due to their one-dimensional geometry, high index of refraction ($n > 2$) and smooth surface morphology the nitride nanowires also act as optical nanocavities making them especially suitable for waveguiding and lasing resonance [97]. Conventional top-down etching processes are not able

to produce such smooth surfaces in these dimensions and often induce additional defects.

A good knowledge of the growth mechanism is essential to control the growth of the nanowires. Calleja *et al.* proposed a mechanism for nanowire growth by PA-MBE [8] based on the VLS model from Wagner and Ellis [57]. As already noted in that paper, an excess of one of the component materials for growth of compound crystals can act as a liquid-forming 'impurity'. Under N-rich conditions the surface mobility of Ga adatoms is reduced [98] which leads to the formation of liquid Ga clusters on the surface ('Ga-balling'). By means of the VLS mechanism anisotropic growth is then promoted. However, in contrast to many reports on Au-mediated VLS NW growth, Calleja nor any other group reported the presence of a residual metal droplet (in this case Ga) on top of the nanowires by post-growth analysis.

An important issue which has to be solved for device applications and did not receive much research attention until recently is the controlled doping of PA-MBE grown nitride nanowires. This comprehends the influence of the doping species on the morphology as well as the determination of the carrier concentration. Due to technical limitations like the resolution of e-beam lithography, conventional Hall measurements are not readily applicable to nanowires with diameters below 100 nm.

The low decomposition temperature of InN has prevented the successful growth of InN nanowires by MOVPE and related methods, although they are particular interesting since the quality of planar InN films has not been optimised. The high crystalline perfection of optimised nanowires could help to determine fundamental physical properties of this material.

3.4 Promising nanowire features for applications

The possibility of 'strain engineering' discussed in Sec. 3.1.1 is an interesting property, which could allow the monolithic integration of III-V semiconductors in Si technology (cf. Sec. 3.5) despite of a lattice mismatch, which normally limits defect-free epitaxial growth to a critical thickness. The principle is also interesting for the formation of heterostructures, which is of considerable importance for optoelectronic applications of nitrides. The insertion of a quantum well greatly enhances the performance of optoelectronic devices [96], but strain can be an issue if alloy compositions with different lattice constants are combined.

Nanowires have been proposed for applications associated with electron field emission [99, 100], such as flat panel displays, because of their small diameter and large curvature at the nanowire tip, which may reduce the threshold voltage for the electron emission [101]. In this respect, the demonstration of very high field emission currents from the sharp tip ($\sim$ 10 nm radius) of a Si cone [99] stimulates additional interest. Recently, field emission from a VLS grown InAs nanowire has also been reported [102] which showed stable emission behaviour and a small energy spread due to Fermi-level pinning in the conduction band. Such nanowires with sharp tips could also be interesting for applications in scanning probe microscopy [103].

For nanowires with a small diameter (smaller than the Bohr radius) quantum effects can come into play, making them interesting systems also for fundamental studies. Ultimately this might lead to devices based on quantum mechanical concepts, which have functionalities not obtainable with conventional devices. An example of quantum behaviour due to confinement

in an InP nanowire is presented by de Franceschi *et al.* [104]. A nanowire with a pn-junction in combination with a source and a drain contact and two gates can possibly be used as a single photon source [105]. The confinement induced by the limited diameter of the nanowires also influences the band gap of the nanowire (for small enough diameters), thus within a certain range the band gap can be tuned during synthesis.

The high surface-to-volume ratio of nanowires make them ideally suited for gas and bio *sensors* [106, 107]. Due to the one-dimensional morphology they overcome sensitivity limitations of previous planar FET sensors. Surface depletion and accumulation regions have a big influence on conductivity of nanowires and absorption of some element can influence this surface region. The effect is much more dramatic for nanowires than for planar devices due to the large surface-to-volume ratio of nanowires. By functionalising the surface of the nanowires with some recognition or receptor groups, selective and highly sensitive detectors can be fabricated. The large surface-to-volume ratio is also interesting for absorption of sun light in solar cells (cf. Sec. 3.5.2).

3.5 From Nanoscience to Nanotechnology

It is without doubt that nanowire systems have been a very interesting playfield for researchers all over the world, which is evidenced by the explosive growth of publications related to nanowires in the last decade (cf. [69, Fig. 1]). However, to be able to make the step from 'nanoscience' to 'nanotechnology' a focus on several key areas is required.

First, the nanoscale 'building blocks' have to have precisely controlled and tunable chemical composition, size and morphology, because these characteristics determine their physical properties. Current technology faces a similar requirement of producing layers with homogeneous composition and properties over the whole wafer (within the tolerable margin of error). A big issue is the deliberate n- and p-type doping of III-V nanowires, which has only been shown by a few groups [66, 108–110]. Efforts should be made toward quantitative control of doping in nanowires. A theoretical work by Erwin [111] addresses the difficulties related with doping of nanostructures. Another problem is the use of a Au catalyst which can be detrimental to device performance because in Si devices Au introduces deep level traps. Therefore there have been attempts to use other elements like Al in NW VLS growth of Si [112] or turning to other methods of selective growth (cf. e.g. [113] and Sec. 3.5.1).

In the top-down approach, the size of the nanostructures is determined by the lithography and etching steps, but for self-assembled nanowires the size is determined during growth. If a catalyst particle is used as in VLS growth then the size of this particle determines the diameter of the nanowire and in addition the growth rate and time determine its length. In a true bottom-up approach the particle is defined by self-assembled steps or self-assembled templates (cf. Sec. 3.5.1), but sometimes they are defined by e-beam lithography thus combining both approaches. For research purposes this is a legitimate formula to gain knowledge about the nanosystem, but to circumvent the economic and physical problems related to the continuous reduction of the feature sizes, a true bottom-up technology needs to free itself from these constraints.

The morphology of nanowires is related to the growth conditions and remarkable control

has already been achieved. The group of Samuelson has for instance shown that it is possible to grow 'nanotrees' with good control of the branches ([72] and references therein). A problem, however, often observed in catalyst-assisted growth is a gradual change in the wire diameter with length, the so-called 'tapering effect' [64, 78, 112, 114].

A second focus point is the investigation of classical device concepts to proof them at the nanoscale where quantum effects can come into play due to the limited size. On the other hand, the quantum effects can open up possibilities for new device concepts not accessible with classical systems and this could improve device performance. This area is ideally suited for research institutions, which can show the industrial partners the way to viable nanoscale (quantum) devices.

The third and most critical point is the issue of designing schemes to implement nanowires in a complex device architecture for high-density integration similar to those currently used in the semiconductor industry for example for thin film transistors (TFTs). Considering that current architectures have multiple layers this is a formidable task. Ordered arrays of nanowires with well-defined position, spacing, diameter and length have been produced for example for InAs [79] and also for other III-Vs [115], although it has to be noted that the patterning of the Au catalysts was done by e-beam lithography.

Compatibility with established technologies and in particular Si would be a great advantage for any new technology. An important issue is therefore the *epitaxial* growth of III-V nanowires on group IV substrates (especially Si) [75, 115–117]. The group at Philips has shown, that only up to a certain lattice mismatch ($\approx 4\%$ for wire diameters of $\sim 20\,\mathrm{nm}$) nanowires grow in well defined directions and with elastic strain relaxation. Relieving strain by the formation of dislocations and other defects deteriorates the electrical properties of the interface and thus ultimately the device performance. Therefore they suggest to use a combination of materials (creating kind of a buffer layer) with gradually increasing lattice mismatch with respect to Si to integrate heavily mismatched materials on Si (or the respective substrate for the envisioned application).

3.5.1 Templates

Self-organisation of catalyst particles removes the necessity to define their size and position with lithography and etching steps and could be a possibility to a full bottom-up approach. A number of patterning and templating methods have been employed to reach this goal (cf. [42]).

Nanosphere lithography (NSL) is one of them. The basis is the self-organisation of submicrometer spheres into a monolayer (ML) with hexagonal close packed structure [118]. Such a ML can act as a highly ordered lithography shadow mask and a template to obtain nanostructures on the substrate surface. Regular patterns of metal particles can be produced in this way. The spheres are removed by etching, leaving only the catalyst particles for the growth of the nanowires. This method is simple, cost-effective and with high throughput and control.

Another method is the use of porous alumina. By electrochemical oxidation of aluminium (anodisation) porous alumina can be fabricated and under the right conditions the pores form ordered hexagonal arrays. The array can then be used as a shadow mask for depositing catalyst particles similar to NSL [119] and then nanowires can be grown by the VLS mechanism inside of the nanopores [120, 121].

An interesting technique to produce small structures at low cost with high throughput (not only as template for nanowire growth) is nanoimprint lithography (NIL). The method basically consists of two steps: imprint and etching. In the imprint step a mold/stamp is first replicated from a relief-structured master and then pressed into a thin resist on a substrate. The mold is then removed, which is a critical step, because the resist could stick to the mold. This step transfers the master pattern into the resist film. By etching the resist film the pattern from the mold is transferred into the underlying substrate. This method was employed to produce a pattern of metal catalyst dots for the growth of position-controlled InP nanowire arrays [122].

Selective growth on prepatterned substrates is an interesting way to get rid of the metal catalyst, which can introduce unwanted contamination. Recently the group of Fukui [123–128] has shown that with such a method they can achieve good control of position and size of the nanowires for several III-V semiconductors. The group of Samuelson and Seifert [113] used a similar approach to grow InAs selectively on patterned SiO_x. The use of SiO_x makes this method compatible with established Si technology and it is also possible to pattern it with one of the methods to produce templates for catalyst particles described above.

3.5.2 Realised devices

Recently several groups [129–132] have shown vertical field effect transistor (FET) devices with promising characteristics. In such a device with a wrap-around gate, the electrostatic coupling of the gate to the channel is enhanced. Nanowires may allow to integrate high-mobility materials like InAs with Si technology despite the lattice-mismatch. Also other devices like a nanoLED [133] could be integrated with a similar device geometry.

Law *et al.* [134] have shown the realisation of solar cells made out of billions of ZnO nanowires with a diameter of $\approx 60\,\mathrm{nm}$ and lengths of $\approx 20\,\mu\mathrm{m}$. The nanowires were coated with a light-absorbing dye and were much more efficient than other nanoparticle-based solar cells currently under development as a result of a much higher conductivity. Nanocrystals, specifically nanowires in this case, have a much larger surface than a planar film and can thus accommodate a much larger amount of the light-absorbing dye. The solar cell's overall light-conversion efficiency was rather low, however, amounting to a poor 1.5 %. By using TiO nanowires and reducing the nanowire size, this efficiency could be improved. The low production cost of these solar cells compared to conventional Si-based solar cells could make them a viable source of energy. The large surface-to-volume ratio of nanowires and their high crystalline quality are important for this application and the device was realised in a complete bottom-up approach.

Some promising results have thus been obtained, but for commercial applications a lot of research and development still has to be done. Apart from improvements of classical concepts, nanowires might allow to use quantum-mechanical effects that are useful and impossible to obtain in standard Si technology. To find, understand and use such effects might be one of the most exciting and challenging tasks of device research today.

Chapter 4

Experimental Details

4.1 Molecular Beam Epitaxy: basics and theoretical background

Molecular Beam Epitaxy (MBE) is a well-established method to produce high-quality layers and a lot of books, papers and reviews have been written about it. A basic description can be found in the review by Arthur [135]. In this section only some basic concepts of MBE will be discussed.

MBE is a very versatile method to grow thin films in a controlled way on a substrate. The word *epitaxy* stems from the Greek words $\epsilon\pi\iota$ (epi = on) and $\tau\alpha\xi\iota\zeta$ (taxis = order), so the layers grow in an ordered way on a substrate or a previously deposited layer. The substrate very much determines the way the layer grows on top of it. The epitaxial films grow from thermal beams of atoms or molecules ("molecular beams") impinging on the substrate, which is usually heated to improve surface diffusion. The growth rate of the order $0.1 - 1\,\mu\mathrm{m/h}$, which corresponds to approximately $0.1 - 1$ monolayer (ML) per second, is low enough that surface migration of the impinging species is ensured and this results in very smooth surfaces, under optimal conditions. This low growth rate also offers the ability to grow abrupt interfaces at the atomic scale and this can be used to grow low-dimensional quantum structures, e.g. quantum wells formed in heterostructures. To switch individual molecular beams on and off, a mechanically operated valve is used, a so-called shutter. The time needed to open and close a shutter must be very short, i.e. a fraction of the time to grow a monolayer. Also doping profiles can be introduced in the growing layer by a dopant cell. Due to the relatively low growth temperatures compared to other growth methods, interdiffusion is significantly reduced thus retaining the grown doping profiles. There are some prerequisites, however, for a successful deposition by MBE. A very low pressure, Ultra High Vacuum (UHV), is needed to produce clean and homogeneous films.

There are several pressure ranges which have to be distinguished, ranging from rough vacuum $1 - 10^{-3}\,\mathrm{mbar}$, via High Vacuum (HV) $10^{-3} - 10^{-9}\,\mathrm{mbar}$, to Ultra High Vacuum (UHV) $< 10^{-9}\,\mathrm{mbar}$. To deposit thin films in a controlled way it is important, that the contamination in the grown layer from the residual gas is low. Also the constituents, that make up the layer, have to reach the surface at a constant rate. This is necessary to get reproducible results, to grow abrupt interfaces and when growing a layer with multiple sources,

to get a homogenous concentration. To make an estimate of the required vacuum, one can use the ideal gas theory. The impingement rate ϕ_i for a certain species i on a surface as a function of its partial pressure p_i in mbar can be calculated. If all quantities are expressed in SI units the following equation can be used [135]:

$$\phi_i = 4.6 \times 10^{22} \frac{p_i}{\sqrt{M_i T}} \, cm^{-2} \cdot s^{-1} \tag{4.1}$$

where M_i is the molecular weight and T the absolute temperature. Now consider for example a residual gas with a partial oxygen pressure of 10^{-6} mbar and a temperature of 300 K; the molecular weight of O_2 is $32 \cdot 10^{-3}$ kg/mol. The impingement rate ϕ_i then amounts to $4.7 \times 10^{14}\,cm^{-2}\,s^{-1}$, which approximately corresponds to one monolayer (ML). So every second 1 ML of oxygen would be deposited at the surface if the sticking coefficient S is one. The necessary vacuum level thus depends on the maximum allowable contamination level and the constituents of the residual gas. Nitrogen for instance is a very inert gas in molecular form and therefore the allowable partial pressure is higher than for oxygen. A convenient exposure (pressure × time) unit can be defined, that gives a direct estimation of the maximum (S=1) adsorbate coverage: 1 Langmuir (1L) is the dosage corresponding to exposure of the surface for 1 s to a gas pressure of 10^{-6} Torr[1]. So for S=1, approximately 1 ML would be deposited every second. The exact coverage depends on the molecular weight of the impinging species, according to Eq. (4.1).

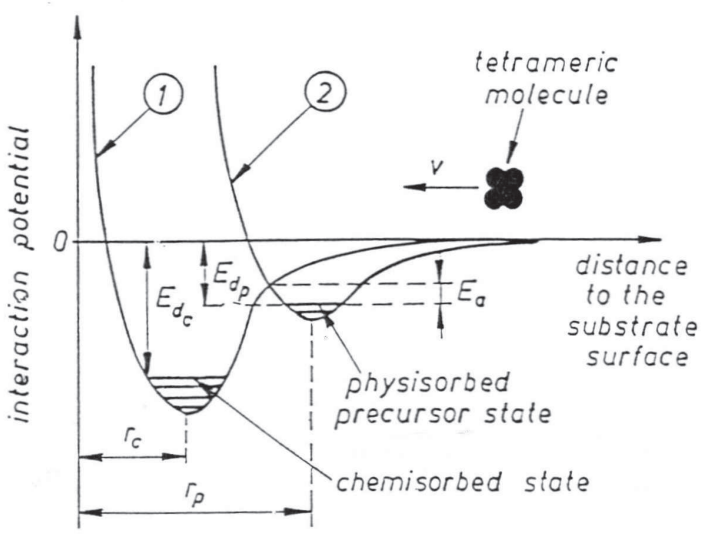

Figure 4.1: Schematic representation of interaction potential for physi- and chemisorption.

Two adsorption types can be distinguished as can be seen from a typical interaction potential due to the surface as seen by an impinging particle: physisorption and chemisorption;

[1] 0.75 Torr ≈ 1 mbar = 10^2 Pa

the potential is shown in Fig. 4.1. When a particle is physisorbed, the attractive force between it and the surface is of the van-der-Waals type and thus relatively weak. It is due to the attraction between mutually induced dipoles. Chemisorption is similar to the formation of covalent or ionic bonds in molecular physics. The electronic structure of the bonding partners is strongly perturbed and new hybrid orbitals are formed. The attractive force is much stronger than for physisorbed atoms or molecules. Usually chemisorption is a two step process: the particle first goes into a physisorbed precursor state and it can then desorb or be chemisorbed. For the interaction potential in Fig. 4.1, the barrier for chemisorption is lower than that for desorption and thus chemisorption is more favourable.

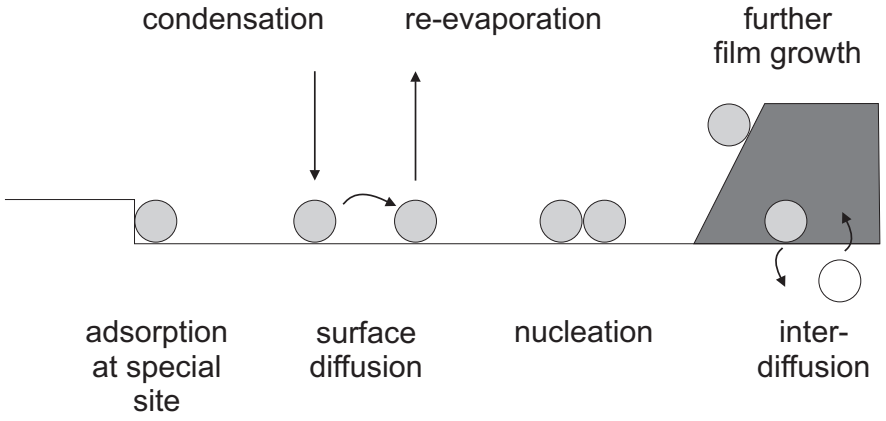

Figure 4.2: Schematic representation of atomic processes involved in film growth on a solid substrate. Film atoms shown as dark circles, substrate atom as open circle (cf. [136]).

In Fig. 4.2 the atomic processes that physisorbed atoms (adatoms) undergo are presented. A physisorbed atom or molecule can desorb or diffuse across the surface. The latter is usually more likely, since there is no net change in energy, if the environment of the atom in the initial and final state is the same. At step edges or corners the situation is a bit different, since these are energetically more favourable. Hence an atom will preferably diffuse along a step edge until it meets a corner, instead of departing from the step. The diffusion probability can be described by the following equation:

$$\mathrm{D} = \nu_0 \cdot \exp\left(-\frac{\mathrm{E_d}}{\mathrm{k_B T}}\right), \tag{4.2}$$

where ν_0 is the attempt frequency (typically $10^{13}\,\mathrm{Hz}$) and $\mathrm{E_d}$ is the activation energy for the respective diffusion type (across surface, along edge, across an edge). Diffusion can also depend on the crystallographic direction. The mean free displacement of an atom as a function of time is given by $< \mathrm{x}^2 >= 2\mathrm{Dt}$ (Einstein relation). If the thermal energy $\mathrm{k_B T}$ is higher than the activation energy, the atom can diffuse freely across the surface. For lower temperatures, however, the atoms are more localized.

Three different growth modes are usually distinguished. They are depicted schematically in Fig. 4.3. Growth takes place either layer by layer (Frank-van der Merwe), in form of

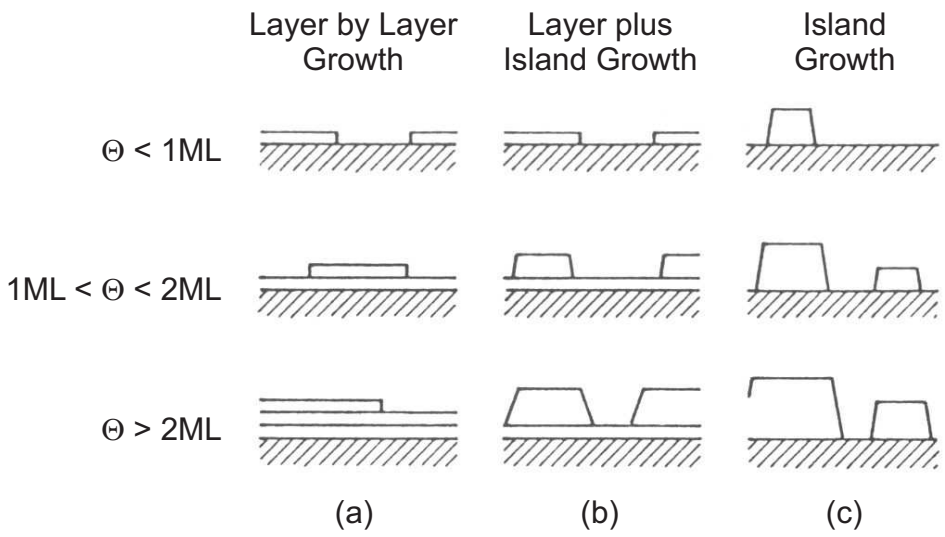

Figure 4.3: Schematic representation of the three important growth modes of a film for different coverage (θ) regimes (ML means monolayer) (cf. [136]). (a) Layer-by-layer growth (Frank-von der Merwe, FM); (b) Layer-plus island growth (Stranski-Krastanov, SK); (c) Island growth (Vollmer-Weber, VW).

islands (Volmer-Weber) or a mixture of both, i.e. at first layer by layer followed by islanding (Stranski-Krastanov). Which mode takes place depends on various parameters like substrate temperature, forces acting between atoms in the growing layer and the substrate, strain in the grown layer and growth rate. Increasing the substrate temperature enhances the probability for an atom to cross the Schwöbel-barrier, but also the interdiffusion increases, so this growth parameter has to be carefully chosen. When the atoms or molecules are more strongly bound to the substrate than to each other, the first atoms form a complete monolayer. The next layers are less tightly bound, but if the decrease in binding is monotonic towards the bulk value, layer by layer growth is obtained. If, however, atoms are more attracted to each other than to the substrate, island growth is preferred from the start. Lattice mismatch between the substrate and the layer(s) grown on top can lead to strain in the thinner layer (usually the epitaxial layer). This can result in islanding. The growth rate also has a major influence on the formation of islands on the surface. For high growth rates the probability for islands to be formed is higher, due to the increased number of atoms diffusing about on the surface. An island diffuses a lot slower than a single atom or molecule and thus layer by layer growth is less likely.

4.2 Molecular Beam Epitaxy system

The MBE growth system (VG V80M) consists of four stainless steel chambers, which are separated from each other by valves. The load-lock introduction chamber is used to load samples into the UHV environment without greatly influencing the pressure in the other

chambers. Due to its small volume, a pressure below 10×10^{-7} mbar is usually reached within half an hour (pumping speed 200 L/s). Samples are mounted on 3-inch molybdenum sample holders and fixed with Mo wires. For growth optimization 3-inch wafers are cut into smaller pieces and the samples are mounted in 3-inch Mo discs with a rectangular cutout of various sizes. The load lock is connected to the analysis chamber via a valve. Up to nine sample holders can be introduced at once and stored in a garage in the analysis chamber. The analysis chamber is used for Auger and LEED measurements, samples can be degassed and it is equipped with an electron beam evaporator to deposit Fe. An oxygen bottle is connected to the load-lock through a leak-valve. It can be used to oxidize samples, for instance Fe grown on GaN. During growth the samples can be rotated and heated up to approximately 800 °C. Temperature is controlled by an Eurotherm. The growth rate can be monitored by the use of a quartz crystal. The base pressure is typically of the order of 3×10^{-10} mbar. This is reached, after a bake-out of the system, with the help of an ion getter pump. Without bake-out a base pressure of about 1×10^{-7} mbar is reached within one day. The system is then heated up to 170 °C for at least one day, mainly to desorb water vapor that has accumulated at the chamber walls.

A chamber with a Scanning Tunneling Microscope (STM) is connected to one side of the analysis chamber and the deposition chamber to the other side. The STM was not used in this work and therefore it is not described here. In the deposition chamber nitrides are grown. Knudsen effusion cells are used to generate Al, Ga, In, Si and Mg fluxes in the range of 5×10^{-10} mbar $- 5 \times 10^{-7}$ mbar. The purity of all materials to charge the cells was 6N or better (i.e. a purity of at least 99.9999%). The cell temperatures are controlled by Eurotherm PID-controllers. The standby temperatures have to be kept well above the melting points of the materials, 660.3 °C for Al, 156.6 °C for In and 29.76 °C for Ga, because frequent solidification of the materials can give rise to cracks in the pyrolitic boron nitride (PBN) crucible due to different thermal expansion coefficients. An ion gauge, which can be moved to a position near the sample by means of an edge-welded bellow, is used to measure the beam equivalent pressures (BEP) of the respective cells.

Molecular nitrogen (N_2) is dissociated into nitrogen radicals and ions by means of a plasma, which is created inside a PBN crucible. The plasma cell consists of a LC circuit matching unit that is operated by a RF generator at 13.56 MHz. The AC voltage accelerates the electrons that oscillate within the plasma and ionize the atoms. Due to their much larger mass, ions in the plasma cannot follow the oscillation. Atoms and molecules within the plasma are excited into excited states and during relaxation to lower energy states, photons are irradiated yielding a characteristic spectrum. Peaks corresponding to certain transitions in molecular or atomic nitrogen can be monitored through an optical view-port with the use of a photodiode in combination with narrow (FWHM[2] = 10 nm) bandpass filters. This allows to monitor the status of the plasma. For the epitaxial growth nitrogen is used with purity 6N, which is further purified by a Mono Torr purifier.

All cells are focussed at one point which coincides with the sample position. Samples can be heated up to approximately 1100 °C by irradiation stemming from a graphite heating coil. Temperature is measured by using an optical pyrometer, which analyzes the light stemming

[2]Full Width Half Maximum

from the sample. Correction factors are necessary for different materials due to differences in reflectivity. A calibration curve was recorded as a function of the current through the graphite coil, but additionally the temperature is always checked before and after an epitaxy. The error of the real temperature is estimated to be less than $\pm\, 30\,^{\circ}\mathrm{C}$, but for a fixed heating current, variations from sample to sample are less than $\pm\, 5\,^{\circ}\mathrm{C}$.

Chapter 5

Nanowire Growth Mechanism

In this chapter the conditions, which lead to columnar structures (nanowires) in III-Nitride growth by plasma-assisted molecular beam epitaxy (PA-MBE) will be discussed. The kinetics of the growth will be determined and a model for the adatom kinetics is proposed. The mechanism, which was proposed in literature by the group of Calleja [8] suggesting a VLS-like growth, will be compared with experimental results.

5.1 Morphology as a function of III-V ratio

Introduction

GaN growth suffers from the lack of high quality homosubstrates (cf. Chapter 2). Therefore other substrates like Si(111) have been employed. Despite the large lattice mismatch between GaN(0001) and Si(111) of -16.9% (the minus-sign refers to tensile strain), this substrate has some advantages over other substrates which are often used (Chapter 2). To reduce the lattice mismatch buffer layers of AlN are often used. Although the lattice mismatch of AlN with Si(111) is even larger (-19.0%), dislocations may be favourably displaced on the Si 7×7 reconstructed surface. The resulting 17 AlN : 14 Si lattice match corresponds to a misfit of only -1.6% [137]. The lattice mismatch between GaN and AlN is only 2.5% and it is compressive, which prevents the formation of cracks if the strain is relieved in the AlN layer [138].

After the growth of the buffer layer the GaN layer is grown, which can proceed under nitrogen-rich, gallium-rich or stoichiometric conditions by controlling the III-V ratio. These lead to different morphologies, which will be presented in the next sections.

Experimental Details

AlN and GaN layers are grown by radio frequency PA-MBE described in Sec. 4.2 on Si(111). After cleaning the substrates with acetone and propanol, the substrates were annealed in ultra high vacuum at 925 °C for 15 min, in order to obtain an oxygen-free surface.

A buffer layer of 100 nm AlN was grown with a predeposition of 8 s Al to prevent the nitridation of the Si substrate. The layer was grown for 25 min at 770 °C with $\Phi_{\mathrm{Al}} = 1.0 \times 10^{-7}$ mbar and nitrogen plasma settings of $P_{\mathrm{RF}} = 450$ W and $\Phi_{\mathrm{N_2}} = 2.5$ sccm. On top

of the AlN buffer layer GaN layers were deposited at fixed substrate temperature and nitrogen settings (T_{sub} = 770 °C and P_{RF} = 500 W, Φ_{N_2} = 4.0 sccm) for 1 h. Φ_{Ga} was varied between 2.0×10^{-8} mbar and 6.0×10^{-7} mbar.

The composition and the crystallinity of the substrate after annealing and the grown layers was determined by Auger spectroscopy and low-energy electron diffraction (LEED). Layer thicknesses were determined by a Dektak profiler or SEM (Leo 1550) cross-sectional images for rough layers. The roughness was also measured by a Nanoscope III AFM.

Experimental Results

After annealing the Si(111) substrate the crystallinity of the surface was checked by LEED, which showed a clear 7×7 reconstruction characteristic of a clean oxygen-free surface. The Auger spectrum was also free of a C, O and SiO_x peak.

The AFM roughness of the AlN buffer layer was 2.51 nm on a $5 \times 5\,\mu m^2$ area. Depending on Φ_{Ga} the roughness of the GaN layers varied between 50 nm for layers with low Φ_{Ga} and 5 nm for high Φ_{Ga}.

The growth rate of the GaN layer as a function of Φ_{Ga} is plotted in Fig. 5.1. For Φ_{Ga} below $\approx 5 \times 10^{-8}$ mbar the rate increases with Φ_{Ga}, which indicates the growth is Ga-limited or N-stable. For Φ_{Ga} above $\approx 5 \times 10^{-8}$ mbar the rate does not depend on the Ga flux and is thus N-limited or Ga stable. the cross section of both lines defines the stoichiometry point where both effective fluxes are constant. The effective flux can be lower than the real flux due to desorption. With increasing Φ_{Ga} in the Ga stable region excess Ga accumulates at the surface and starts to form droplets. The average droplet size increases with Φ_{Ga}.

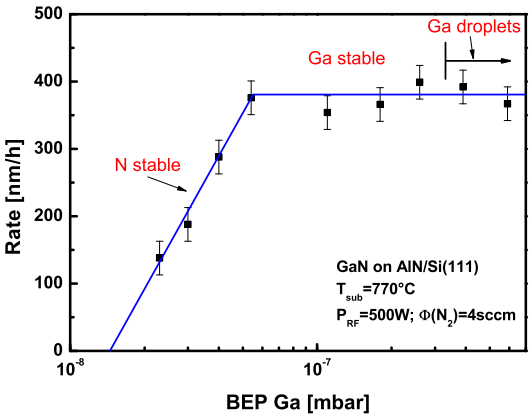

Figure 5.1: Growth rate of GaN layers deposited on AlN buffer layers by PAMBE. The thickness was determined by a Dektak profiler and cross-sectional SEM images. Φ_{Ga} was varied, but T_{sub} and the plasma settings were kept constant. For lower Φ_{Ga}, the rate increases with Φ_{Ga} (N-stable region), but it saturates around 5×10^{-8} mbar. The area for higher Φ_{Ga} is Ga-stable, because growth is limited by Φ_N. If the amount of Ga is too high, excess Ga precipitates at the surface and large Ga droplets form.

The morphology of the samples grown in different growth regions is shown in Fig. 5.2. Different contrasts mark the different layers as well as the substrate. In Fig. 5.2(b) a short dashed line indicates the position of the interface. There is a clear difference between N-rich and Ga-rich sample. The N-rich samples show a rough morphology, whereas in case of Ga-rich conditions the layer is compact although still exhibiting defects due to dislocations, which form at the interface. By a further increase of Φ_{Ga} these pits can be reduced, but if the Ga excess is too large the Ga droplets form.

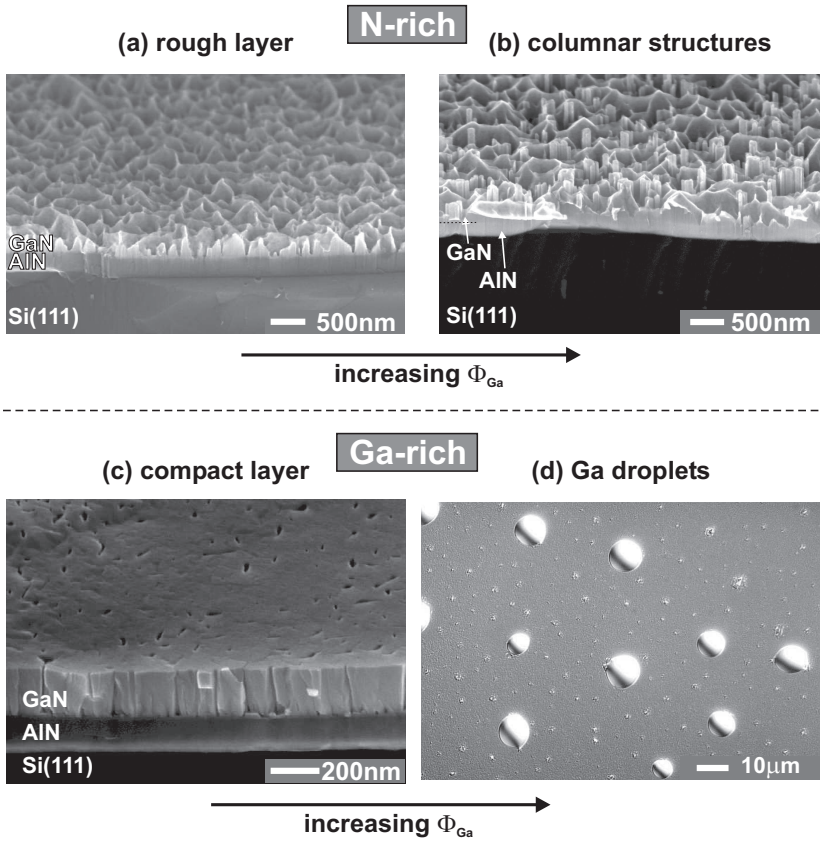

Figure 5.2: Figures (a)-(c) show cross-sectional SEM images of GaN layers grown on AlN buffer layers with increasing Φ_{Ga} from (a)-(c). Figure (d) is a top-view optical microscope image with even higher Φ_{Ga}. The samples in (a) and (b) are grown under N-rich and the ones in (c) and (d) under Ga-rich conditions. N-rich grown samples exhibit a rough morphology (a,b), whereas the layer in (c) is compact and much smoother. It has some defects however originating at the interface. High Φ_{Ga} leads to Ga droplet formation (d).

Fig. 5.3 shows a GaN sample grown with the same parameters as the sample in Fig. 5.2(b), but for 2 h in stead of 1 h and without AlN buffer layer. In contrast to the N-rich samples in Fig. 5.2 there is no clear formation of a compact layer (within the resolution of the SEM). Rather than a rough morphology with some wires at randomly distributed places this sample

has well-defined columns, which are close, but most of them are well separated as can be seen in the top-view image. The wires have clear facets in agreement with the hexagonal structure. The longest wires have lengths between 600 nm and 800 nm, which results in a growth rate of $300 - 400\,\mathrm{nm/h}$ at a Ga flux of 3×10^{-8} mbar, so considerably larger than expected from the growth rate diagram (Fig. 5.1).

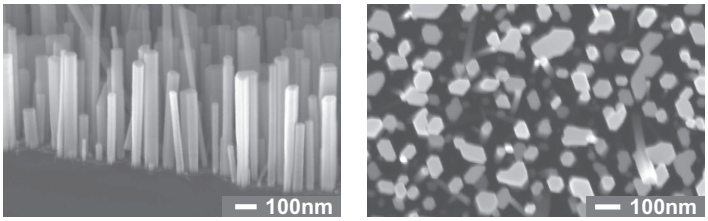

Figure 5.3: Side- and top-view SEM image of a GaN nanowire sample grown directly on Si without AlN buffer layer. There is no obvious compact wetting layer at the base. Well-defined nanowires with high aspect ratios grow and most of them are well separated (cf. top-view image).

Discussion

The dependence of the sample morphology on III-V ratio can be explained in terms of surface diffusivity. Theoretical calculations [139] show that for Ga-polar surfaces, which is commonly observed for GaN grown on Si(111) by MBE, there is a significant difference in surface diffusivity of adatoms depending on the termination of the surface. Ga-terminated surfaces have only one dangling bond per atom, whereas N-termination leads to three dangling bonds per atom. Hence, the mobility of adatoms is much higher on a Ga-terminated surface (for Ga-polar films). Thus, samples grown under N-rich conditions have a rough morphology, whereas the Ga-rich samples are smoother. Moreover, it was shown by the same group [140], that Ga acts as an autosurfactant, i.e. increases the surface mobility promoting two-dimensional growth. Therefore the surface morphology improves with increasing Φ_{Ga}.

If one takes a closer look at the GaN layers grown under highly nitrogen-rich conditions (cf. Fig. 5.2(a,b)), i.e. with a low III/V ratio (Ga/N $\ll$ 1), one can observe the formation of columnar structures with a small diameter in the nanometer range. In Fig. 5.2(a) this is not very pronounced, because Φ_{Ga} was very low and the deposition time too short for the columnar structures to develop. In Fig. 5.2(b) with higher Φ_{Ga} groups of columns can be observed at random places. Due to the very high lattice mismatch between Si(111) and AlN not all the strain can be relieved by the 100 nm AlN buffer. Therefore the GaN layer on top is also strained and this leads to the growth of islands. The reduced surface diffusivity caused by the N-rich growth conditions prevents a quick coalescence of the islands and columns.

For the GaN sample grown directly on Si(111), the lattice mismatch is -16.9% and thus the critical thickness up to which GaN can grow pseudomorph on Si is very low and the formation of islands is favoured. Therefore growth proceeds in a Volmer-Weber growth mode.

Calleja *et al.* suggested [8] that the limited surface diffusivity under N-rich conditions leads to the formation of small Ga clusters (Ga-balling) on the surface. These small Ga droplets then act as catalyst to promote anisotropic axial growth via a self-catalysed VLS mechanism. This proposal will be further explored in Sec. 5.3.

Conclusion

The morphology of GaN thin films depends critically on the III-V ratio. Ga-rich conditions are favoured for smooth compact layers and N-rich growth leads to the formation of columnar structures. Growing GaN directly on Si(111) instead of on an AlN buffer layer improves the separation between the columns. The anisotropic axial growth mode under N-rich conditions is explained by a reduced surface diffusivity for N-terminated surfaces.

5.2 Nucleation and Growth Kinetics

Introduction

Growth of GaN nanowires by PA-MBE has been reported by several groups [8, 141, 142]. The growth mechanism has been suggested to be of the VLS-type and the presence of a liquid Ga droplet on top of the wires has been postulated [8], but it has never been shown (cf. Sec. 5.3). Therefore the growth mechanism is still unclear and reports about detailed experiments concerning the mechanism of GaN nanowire growth by PA-MBE are very rare [53, 143].

In this section the development of the nanowires with time is investigated and the mechanisms driving the growth are deduced with a similar approach as the one used in some papers dealing with Si nanowires [54, 64]. An important difference with nanowire growth performed by many other groups is the fact that in our case no foreign catalyst is used. The catalyst enhances the growth locally and defines the position and diameter of nanowires [79]. However, this catalyst can introduce unwanted contamination in devices. The presence of a Au catalyst for instance can be detrimental to device performance in Si-based circuits. Therefore a catalyst-free approach to grow nanowires is very interesting from technological point of view (see also [113]). In this case however, control of position and diameter does not arise from catalyst position and size and a good knowledge of the nucleation behaviour and mechanisms driving the growth can possibly help to find a way to achieve this control without catalyst.

Experimental Details

A series of GaN nanowire samples was grown with fixed parameters Φ_{Ga}, Φ_N and T_{sub} ($\Phi_{Ga} = 3.0 \times 10^{-8}$ mbar, $P_{RF} = 500$ W & $\Phi_{N_2} = 4.0$ sccm, $T_{sub} = 785\,^{\circ}$C). The only parameter which was varied, was the deposition time in order to investigate how the nanowires nucleate and develop. Another sample (NC16) was grown for 6 h with slightly lower $\Phi_{Ga} = 2.0 \times 10^{-8}$ mbar, but $T_{sub} = 785\,^{\circ}$C, $P_{RF} = 500$ W & $\Phi_{N_2} = 4.0$ sccm. The Ga flux was lowered to reduce the amount of coalescence.

Experimental Results

The SEM images in Fig. 5.4 show top and side-view of 5 different samples grown for 15, 30, 45, 60 and 90 min, respectively. The nuclei form at random places on the terraces of the stepped Si(111) surface and not specifically at the edges as one might expect. Some of the wires do not grow vertically aligned, i.e. parallel to Si⟨111⟩, but tilted. This topic is going to be described in more detail in Sec. 6.4.

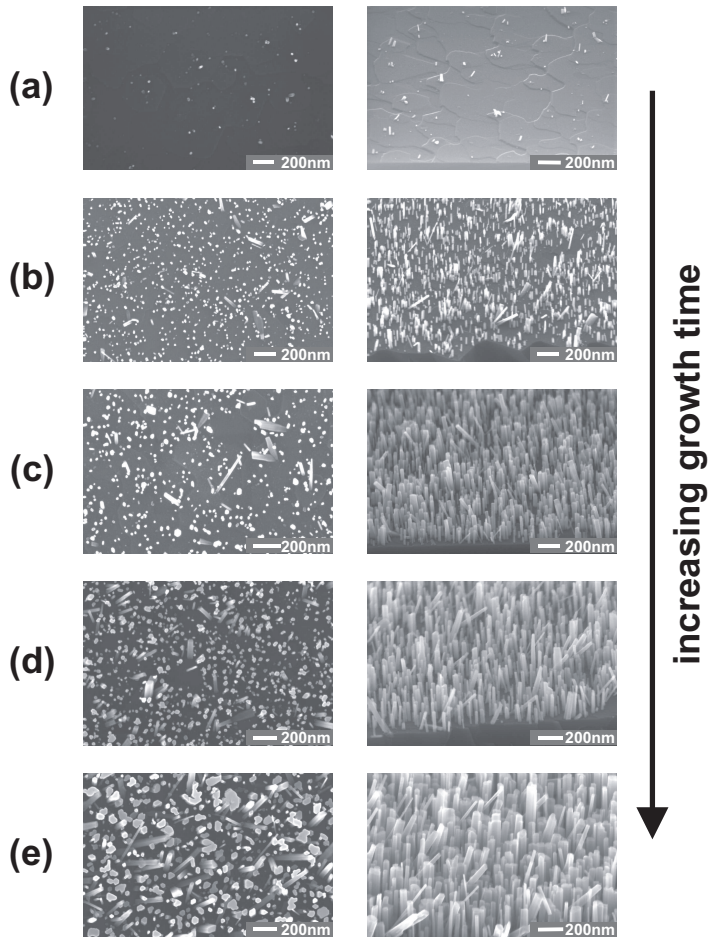

Figure 5.4: SEM images in top- (left) and side-view (right) of GaN nanowires grown at fixed growth parameters varying only the deposition time: (a) 15 min, (b) 30 min, (c) 45 min, (d) 60 min, (e) 90 min. With time, density and length of the nanowires increases.

A first glance at the SEM images shows that the nanowire density increases with time, because new nanowires nucleate. As a result the space between them decreases. Nanowire densities are evaluated as averages from several SEM images of one sample. After 15 min of growth (Fig. 5.4a) the nanowire density is low and of the order of $7 \times 10^8\,\mathrm{cm}^{-2}$ (cf. Fig. 5.5). For a doubled deposition time (30 min) the nanowire density already increases to a value

above $10^{10}\,\mathrm{cm}^{-2}$, which is close to the maximum observed nanowire density (Fig. 5.5). After 60 min of deposition (Fig. 5.4d), the nanowire density has saturated. For longer deposition times the nanowire density decreases to a value of about $3 \times 10^{9}\,\mathrm{cm}^{-2}$ (120 min). For these longer deposition times coalescence of closely spaced nanowires can be observed (cf. Fig. 5.4e, top-view). Nevertheless many wires continue to grow separately.

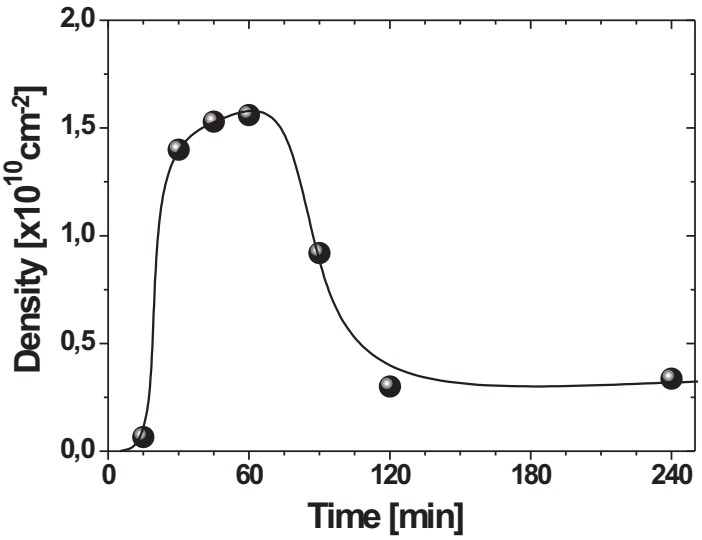

Figure 5.5: Average density of GaN nanowires as a function of deposition time evaluated from SEM images. After an initial steep increase the density saturates between 45 min and 60 min. Coalescence of closely spaced wires leads to a reduction of the density for deposition times longer than 60 min.

Other physical quantities of interest are: (a) nanowire length and (b) nanowire diameter as a function of deposition time. From these values one can then deduce a vertical and lateral growth rate. In Fig. 5.6 the length and diameter of the nanowires, determined as the average of the longest nanowires with similar diameter, is plotted as a function of deposition time. The vertical or axial growth rate can be determined by a linear fit of the data in Fig. 5.6a and amounts to $\approx 3.5\,\mathrm{nm/min}$. The linear fit does not run through the origin, which can be interpreted as a finite time of nucleation. The fit gives a value of approximately 7 min.

The diameter data is also fitted with a linear curve, but the points up to 60 min seem to show a sublinear behaviour. The point at 90 min is confusing, because after 60 min nanowires start to coalesce, which causes an increase of the diameter. The linear fit intersects the y-axis at a positive diameter, which suggests a finite nucleation diameter. It has to be noted that the determination of the diameter is limited by the resolution of the SEM. Lengths are easier to measure due to the larger values. Other methods like TEM are more appropriate to investigate the diameter and lateral growth (cf. Sec. 6.4).

Sample NC16, which was grown for 6 h shows an interesting relation between the length and diameter of the nanowires (cf. Fig. 5.7). There is an increase of the nanowire length for smaller diameters. The experimental points, which stem from several SEM images of the

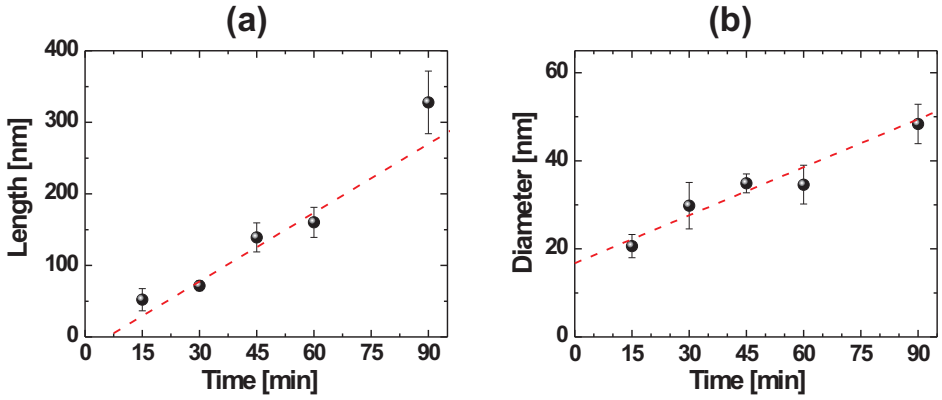

Figure 5.6: Average length and diameter of the longest GaN nanowires vs. deposition time. The dashed lines correspond to linear fits of the experimental data, which suggest a finite nucleation time and diameter.

same sample, can be fitted by the equation $L(d) = C_1 + C_2/d$. The result is:

$$C_1 = (4.7 \pm 0.3) \cdot 10^2 \quad ; \quad C_2 = (3.8 \pm 0.2) \cdot 10^4 \tag{5.1}$$

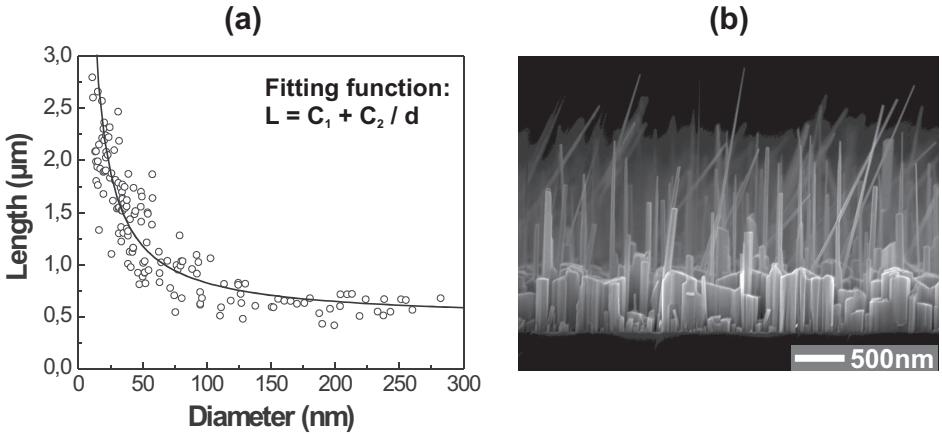

Figure 5.7: (a) Length of GaN nanowires as a function of their diameter for a sample (NC16) deposited for 6 h. The length increases for smaller diameters and the experimental data fits to the relation $L(d) = C_1 + C_2/d$; (b) One of the SEM images of NC16 used to determine the lengths and diameters for the plot in (a).

Discussion

The nuclei in Fig. 5.4a form at random places on the terraces of the stepped Si(111) surface and not specifically at the edges as one might expect. These positions are usually energetically

favoured, because of the additional neighbour to which adatoms can bond. New nuclei will continue to form randomly as long as there is space available. In the beginning the density is low and many new clusters can form, but with time the nanowire density increases and the number of new nuclei will decrease. When the density is high enough as after 60 min, closely spaced nanowires can start to coalesce as a result of the lateral growth. No new nanowires nucleate due to space limitations and therefore the coalescence of nanowires leads to a reduction of the nanowire density.

An important conclusion which can be drawn from the increasing density up to approximately 60 min in Fig. 5.5 is the fact that every nanowire i has a specific time of nucleation t_0^i (one thus has to distinguish between *deposition* and *growth* time), which is smaller than 60 min for the majority of the nanowires. In addition a lower limit to the nucleation time is suggested by the linear fit in Fig. 5.6. It is very difficult to determine every single nucleation time $t_0^{(i)}$ by means of a post-growth analysis. A possibility to determine at least a limited number of nucleation times could be the use of 'time markers' for instance in form of AlN barriers inside of the wire and make a cross-sectional TEM image after the growth. However, real-time in-situ measurements like in the work of Kodambaka *et al.* [64] are of course the best way to treat such a problem. Otherwise one has to resort to statistics, which with a correct interpretation of the statistical data can also give a lot of valuable information.

In general the nanowires with the lowest nucleation time $t_0^{(i)}$ should be longer and therefore the lengths and diameters for Fig. 5.6 are determined from the subset of longest wires, which should have approximately the same $t_0^{(i)}$. Growth rate can depend on diameter as shown in various publications [50, 54, 143], but if the diameter distribution of the longer wires is not too wide, which is the case for deposition times up to approximately 90 min, the effect will be limited. For longer deposition times, however, the distribution will widen and the diameter-dependence of the nanowire length will become more pronounced as observed in Fig. 5.7.

The random position of nuclei, the continuous increase of their number (up to a certain point in time when the space is so dense that no new nuclei can form) as well as a critical nucleation time and diameter fit to a model proposed by Kwon for non-catalytic nanowire growth [144]. Adatoms diffuse across the substrate and when they meet clusters can be formed. Adatoms diffuse to and from the nuclei, which effectively corresponds to cluster migration. When the cluster reaches a certain critical diameter the nanowire starts to grow and for a small reactant dose the free energy is smaller for the anisotropic growth mechanism than for isotropic growth. The small reactant dose corresponds to the N-rich (and thus low Φ_{Ga}) conditions necessary to grow nanowires in our case (cf. Sec. 5.1).

The observed constant growth rate dL/dt as a function of time as evaluated in Fig. 5.6 limits the possible atomistic transport and incorporation mechanisms contributing to the growth. In addition, the following dependence of the length of the nanowires on the diameter for longer growth times (cf. Fig. 5.7) is obtained:

$$L = C_1 + C_2 \cdot \frac{1}{d} \tag{5.2}$$

This is similar to the growth of Si nanowires by MBE in [54] except for the constant C_1. The $1/d$ behaviour is best appreciated for longer deposition times due to the specific nucleation

time of each NW, which leads to different growth times and a statistical distribution of NW lengths for similar diameter. Since the nucleation stops after approximately 1 h, this effect will fade away for longer deposition times and the intrinsic length-diameter correlation will start to dominate as in Fig. 5.7. It has to be noted, that the experimental data was also fitted with an additional constant C_3 in the denominator ($L = C_1 + C_2/(d + C_3)$), where '$d + C_3$' can be interpreted as an effective diameter. The fit, however, gave a value of approximately zero for C_3 and therefore the fit in Fig. 5.7 was performed without this constant.

For the Si NWs [54], the constant growth rate with time and the inverse dependence on the wire diameter leads to the following expression, in which the left hand side is proportional to the total flux incorporated into the wire:

$$\pi R^2 \frac{dL}{dt} = \gamma R \tag{5.3}$$

R is the wire radius, dL/dt the axial or vertical growth rate and γ a time-independent constant. This equation is satisfied for the case of a very fast diffusion of adatoms on the substrate and wire surface, where the flux is limited by the incorporation rate at the boundary of the whisker and the liquid droplet (or in general an active sink at the top of the wire).

If we first neglect the lateral growth, which is considerably smaller than the vertical growth and consider the additional constant C_1, Eq. (5.2) has to be modified. The extra constant C_1 can be obtained if we consider an additional term $\sim R^2$ in Eq. (5.2). This corresponds to the contribution by direct impingement which is time independent and should be proportional to the top area of the whisker, so $\sim R^2$. We then get the following relation:

$$\pi R^2 \frac{dL}{dt} = \gamma_T R^2 + \gamma_S R \tag{5.4}$$

where γ_T and γ_S are time independent constants related to different contributions to the growth. Impinging atoms at the top of the wire (γ_T) and atoms diffusing from the substrate or the lateral sides of the nanowires to the top (γ_S) are both taken into account in the right-hand side of Eq. (5.4). For ease of notation the π will be neglected in the following, which is just a redefinition of the constants γ. If we then suppose a nucleation time t_0 as suggested by the extrapolation of the linear fit in Fig. 5.6 the solution to Eq. (5.4) is:

$$L(t) = \left(\gamma_T + \frac{\gamma_S}{R}\right) \cdot (t - t_0) \tag{5.5}$$

which describes both the linear time dependence of the wire length as well as the dependence of the length on the reciprocal diameter.

If one neglects t_0 in Eq. (5.5) against t for sample NC16 in Fig. 5.7, for which $t = 360\,\mathrm{min}$ and thus much larger than typical nucleation times, then γ_T and γ_S can be determined from the fitted constants C_1 and C_2 (cf. Eq. (5.1)). $\gamma_T \approx 80\,\mathrm{nm/h}$ corresponds to the vertical growth rate for very large diameters, which is equivalent with a planar film. In this case the diffusion channel has no relevance and only direct impingement significantly contributes to the growth. It should therefore agree with the growth rate for compact layers and looking in Fig. 5.1 one finds a value of $\approx 90\,\mathrm{nm/h}$ for $\Phi_{\mathrm{Ga}} = 2.0 \times 10^{-8}\,\mathrm{mbar}$, so there is a good agreement. $\gamma_S \approx 6.3 \times 10^3\,\mathrm{nm^2/h}$, which means that for a wire with a diameter of 100 nm the contribution

from the diffusion channel is $\approx 63\,\mathrm{nm/h}$, thus slightly less than the direct impingement. For a 50 nm wire the contribution is approximately 126 nm/h, which is approximately 1.5 times the contribution by direct impingement.

Conclusion

The nanowire density increases with time until it saturates due to limited space. This means that the nanowires have different nucleation times. For high densities nanowires can coalesce and the effective density is reduced. The nanowire length increases linearly with time and the growth rate is diameter dependent. This growth behaviour is caused by two different contributions to the axial growth. The first is growth by direct impingement, which is diameter independent. The second one is growth by diffusion of adatoms along the wire sidewalls, which enhances the growth rate of wires with a smaller diameter. A finite nucleation time and diameter deduced from linear fits of the time development of the length and diameter of the nanowires is consistent with a theoretical model, which suggests that the formation of clusters with a critical size is required for the anisotropic growth.

Remark concerning lateral growth

Eq. (5.5) is true only if the radius does not change with time, i.e. if there is no lateral growth. If, however, we suppose a simple linear dependence for $R(t)$:

$$R(t) = R_0 + \gamma_R \cdot (t - t_0) \tag{5.6}$$

where γ_R is a time independent constant for the *lateral* growth as opposed to γ_T and γ_S, which are related to the *vertical* growth, then the solution of Eq. (5.4) is:

$$L(t) = \gamma_T \cdot (t - t_0) + \left(\frac{\gamma_S}{\gamma_R}\right) \ln\left(\frac{R(t)}{R_0}\right) \tag{5.7}$$

This should reduce to Eq. (5.5) for small or negligible lateral growth. As one can easily verify this is indeed the case for the following condition:

$$\frac{\gamma_R(t - t_0)}{R_0} \ll 1 \tag{5.8}$$

because with $R(t) = R_0\left(1 + \frac{\gamma_R(t-t_0)}{R_0}\right) \approx R_0$ (cf. Eq. (5.6)) and $\ln(1 + x) \approx x$ for $x \ll 1$ the second term in Eq. (5.7) reduces to the second term in Eq. (5.5):

$$\left(\frac{\gamma_S}{\gamma_R}\right) \ln\left(\frac{R(t)}{R_0}\right) \approx \left(\frac{\gamma_S}{\gamma_R}\right) \frac{\gamma_R(t - t_0)}{R_0} \approx \frac{\gamma_S}{R}(t - t_0) \tag{5.9}$$

It is difficult to determine reliable values for the lateral growth from SEM images, especially for small diameters. TEM investigations are much better suited and therefore the lateral growth will be addressed in Sec. 6.4. A conclusion which can be drawn from the SEM images, however, is that the nanowires can have very different lateral growth rates: in first approximation (i.e. neglecting a possible nucleation time and assuming a linear lateral growth rate) a wire with a diameter of 300 nm after 360 min has a lateral growth rate of $\approx 0.83\,\mathrm{nm/min}$, whereas a 50 nm only grew with $\approx 0.14\,\mathrm{nm/min}$ laterally.

5.3 Growth interruption

Introduction

The group of Calleja [8] suggested a self-catalysed VLS mechanism to be responsible for the observed anisotropic growth leading to nanowires. The reduced surface mobility favours the formation of small Ga droplets on the surface in stead of a smooth layer by layer growth. The Ga droplet then acts as a catalyst or in the case of PA-MBE rather as an active sink, because the growth species are already activated.

The use of a catalyst particle as employed in many VLS-assisted growth studies (cf. Chapter 3) has two important fingerprints. The first one is the so-called memory effect, which means that when switching from one growth species to the other to grow a heterointerface, the catalyst particle is still saturated with the initial growth material. This can reduce the sharpness of the interface, which is very important at nanowire dimensions if one wants to study quantum effects. The second one is the incorporation of the catalyst particle in the growing nanowires. Especially the often used Au catalyst is critical, because it can be detrimental to the electrical performance of the nanowires by introducing deep defect levels as is known for Si planar devices.

For self-catalysed growth the problem of impurity incorporation is absent, but the memory effect can play a role when performing heterostructures. Therefore it is important to determine if our nanowire growth is mediated by a catalyst particle. The group of Calleja has never provided any evidence for the presence of such a particle. The best way to prove it is to study the growth in-situ in real-time like the group at IBM for Au-catalysed Si nanowire growth [64, 78, 84]. Otherwise one has to draw conclusions from post-growth analysis.

The absence of a droplet after growth can be a result of evaporation, especially for small droplets due to the Gibbs-Thomson effect[1]. Ga has a low melting point and therefore high vapour pressure at growth temperatures compared to for instance Au. It has also been reported that the droplet can drop from the nanowire [50]. Thus the absence of a droplet after growth is no good criterium.

An interesting possibility to indirectly proof the presence of a droplet is to change its size during growth, because the droplet determines the nanowire diameter. An example of such a droplet manipulation has been provided by the group at IBM [78]. With the help of in-situ TEM observations of Si nanowires, grown by low-pressure CVD in ultrahigh vacuum on clean substrates, they were able to state an efficient manipulation of the Au catalyst. During the annealing, Au adatoms diffuse over the surface (nanowire sidewalls and substrate surface) and due to Ostwald ripening[2], larger droplets grow and smaller droplets shrink. When continuing the growth the wires grow according to the new droplet size and steps in the nanowire diameter can be observed Fig. 5.8.

In Sec. 5.2 it was shown that diffusion of adatoms on the substrate surface and side faces of the wires plays an important role in the growth of the nitride nanowires. This means that also

[1] Small droplets have a relatively large surface, which increases the vapour pressure. This becomes important for submicrometer droplets [50].

[2] The smaller droplets have higher vapour pressures than the larger ones and therefore they shrink in favour of the larger ones.

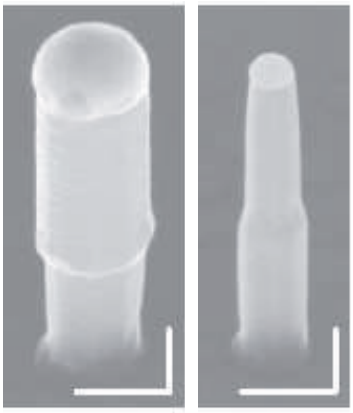

Figure 5.8: SEM images of two Si nanowires grown by a Au-mediated VLS mechanism [78]. Scale bars correspond to 200 nm. An annealing step of 20 min at 650 °C is inserted during which the larger droplet grows and the smaller one shrinks. When growth continues the wire diameter is governed by the new droplet size.

in our experiments if any metal droplet in liquid form serves as catalyst, an annealing step in between the growth should cause a diameter change of the nanowires. Such a behaviour would indirectly evidence the presence of a droplet during growth.

Experimental Details

GaN and InN nanowire samples have been grown directly on Si(111). More details about the growth can be found in Chapter 6 and Chapter 8, respectively. The growth parameters are presented in Tab. 5.1. Three kind of samples have been grown: GaN nanowires and InN nanowires with a growth interruption of 5 min or 15 min and InN nanowires grown on top of GaN nanowires. Because the substrate temperature has to be ramped down for the InN growth, there is an effective growth interruption of 5 min.

Experimental Results

All samples produced in the context of this thesis have been thoroughly investigated with SEM after growth and never has any droplet been observed. This is consistent with observations by the group at NIST[3] [142].

SEM images of the samples grown with a growth interruption of 5 min or 15 min are shown in Fig. 5.9. None of the wires shows a step like in the Si wires in Fig. 5.8. The length of the wires has been compared with samples without growth interruption and no difference can be observed. Since the length of the wires fluctuates, the longest wires have been considered.

In Fig. 5.10 a nanowire sample is shown which consists of InN/GaN heterostructures. Typical growth temperatures of InN are lower than for GaN (475 °C vs. 785 °C) and therefore

[3]National Institute of Standards and Technology, Boulder, Colorado, USA.

Table 5.1: Growth parameters of the samples grown on Si(111) to study the effect of growth interruption. GaN sections are grown at 785 °C and InN sections at 475 °C. The same plasma settings were used for all sections: $P_{RF} = 500\,W$, $\Phi_{N_2} = 4.0\,sccm$. After stage 1 the sample is annealed with all shutters closed. After the annealing time stage 2 is grown.

Sample	**Material**	**Stage 1**			**annealing**		**Stage 2**		
		Φ_{Ga} [$\times 10^{-8}$ mbar]	Φ_{In} [$\times 10^{-8}$ mbar]	time [min]	T_{sub} [°C]	time [min]	Φ_{Ga} [$\times 10^{-8}$ mbar]	Φ_{In} [$\times 10^{-8}$ mbar]	time [min]
NC108	GaN	3.0	-	60	785	15	3.0	-	60
NC110	InN	-	7.0	60	475	15	-	7.0	60
NC111	GaN	3.0	-	60	785	5	3.0	-	60
NC115	InN	-	7.0	60	475	5	-	7.0	60
NC117	InN on GaN	3.0	-	180	785 ↘ 475	5	-	7.0	120

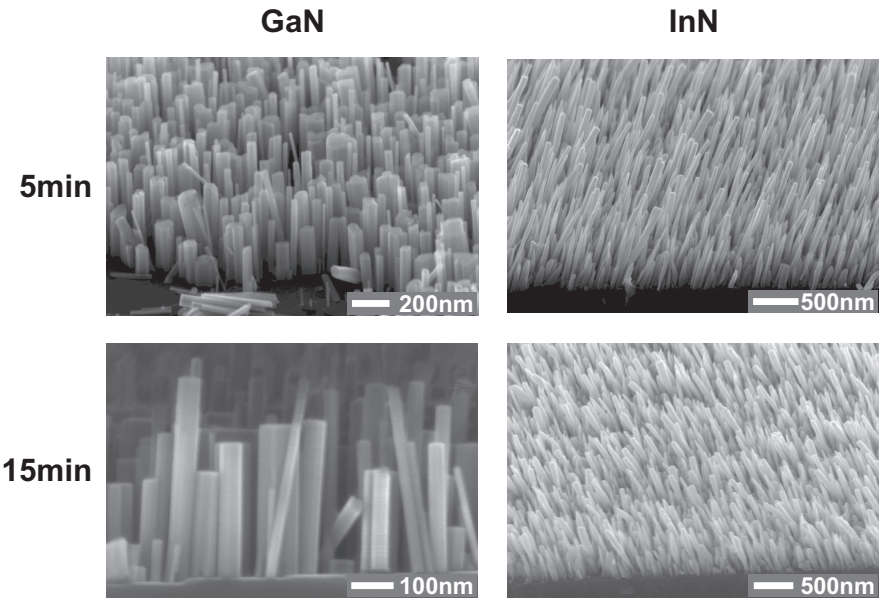

Figure 5.9: Side-view SEM images of the GaN and InN nanowire samples with a growth interruption of 5 min and 15 min. No apparent step like in Fig. 5.8 can be observed in either image.

the temperature had to be ramped down before the InN growth started. This effectively leads to a growth interruption of 5 min, but InN grows on the GaN after the interruption. There is no nucleation of new InN nanowires which can be distinguished by their less uniform shape.

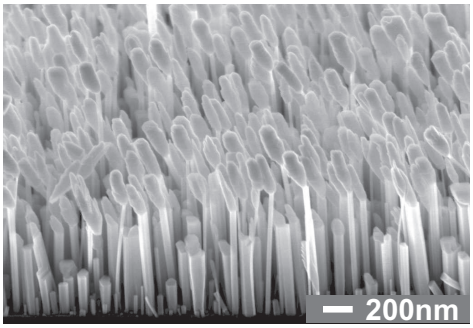

Figure 5.10: Side-view SEM image of InN/GaN heterostructure nanowires. Despite the growth interruption InN nanowires grow afterwards. The InN nanowires grow on top of the GaN nanowires and no new InN wires are nucleated.

Discussion

If a catalytic particle is present on top of the wires, the growth interruption could lead to an altered diameter. Evaporation of catalyst material, diffusion on the surface away from the particle or into the wire are mechanisms, which reduce the droplet size. If, however, the droplets collect the adatoms still present on the surface after stopping the growth, then the droplet increases. In case of a VLS-mediated growth, the diameter of wires with larger or smaller droplet size should be different when growth commences after the interruption. There is no evidence of this in the SEM images, however.

If the wires do not grow anymore after the interruption, because the droplet evaporates or is removed in some other way, then also no step will be observed. However, since the length of interrupted wires is comparable to wires without interruption and the growth rate is approximately linear (cf. Sec. 5.2), the wires must have grown after the interruption. The wires in Fig. 5.10 also evidence this, because there is a clear distinction between the InN and GaN nanowires. The tilt of the InN section, which can also be observed to a lesser extend in the InN samples in Fig. 5.9 is related to the asymmetric position of the In effusion cell relative to the sample normal.

The absence of nucleation of InN nanowires on the substrate is a result of the very high density of GaN nanowires. There is no more space for newly nucleated wires and probably the GaN wires effectively collect the In adatoms.

Conclusion

To conclude, no evidence has been found to support the model of a VLS-like growth mechanism mediated by a droplet on top of the wires. Moreover, sharp interfaces in TEM images in Sec. 6.4 show the absence of a memory effect. An interruption of the growth does not have an influence on the morphology of the nanowires.

Chapter 6

Characterisation of GaN nanowires

In the beginning of this chapter, the influence of the III-V ratio and the substrate temperature on the wire morphology will be discussed. Then the crystal structure of the nanowires and their epitaxial relation to the substrate is presented, followed by an investigation of the optical properties of the wires. In the last part of the chapter transmission electron microscopy is employed to gain valuable information about the nanowires as well as their growth behaviour.

6.1 GaN nanowire morphology

Abstract

In Sec. 5.1 it was shown that nitrogen-rich conditions are necessary to grow GaN nanowires. Nitrogen-rich means that the effective III-V ratio is smaller than one. The effective ratio, however, does not only depend on Φ_{Ga} and Φ_{N}, because desorption plays an important role. The amount of desorption is influenced by the substrate temperature. Therefore the combination of Φ_{Ga}, Φ_{N} and $\mathrm{T_{sub}}$ determines the actual morphology and is studied in this section.

Experimental Details

GaN nanowires are grown directly on Si(111). The same cleaning procedure for the Si as described in Sec. 5.1 is used. The substrate temperature is varied between 620 °C and 840 °C. Plasma cell forward power is $\mathrm{P_{RF}} = 500\,\mathrm{W}$ for all samples and the molecular nitrogen flow is chosen between $\Phi_{\mathrm{N_2}} = 2.7\,\mathrm{sccm}$ and $\Phi_{\mathrm{N_2}} = 4.0\,\mathrm{sccm}$. Φ_{Ga} ranges between $2.0 \times 10^{-8}\,\mathrm{mbar}$ and $2.0 \times 10^{-7}\,\mathrm{mbar}$ and deposition times between 1 h and 4 h were used. The growth parameters of the samples presented in this section are summarised in Tab. 6.1.

Experimental Results

A series of samples was grown with substrate temperature between 620 °C and 815 °C and fixed $\Phi_{\mathrm{Ga}} = 3.0 \times 10^{-8}\,\mathrm{mbar}$, $\mathrm{P_{RF}} = 500\,\mathrm{W}$, $\Phi_{\mathrm{N_2}} = 4.0\,\mathrm{sccm}$ and 2 h deposition, except for the sample grown at 815 °C, which was deposited for 4 h. SEM images of cross-sections of the samples are presented in Fig. 6.1.

Table 6.1: Growth parameters of the samples used to study the influence on the wire morphology of the parameters Φ_{Ga}, Φ_N and T_{sub}.

Sample	T_{sub} [°C]	Φ_{Ga} [$\times 10^{-8}$ mbar]	P_{RF} [W]	Φ_{N_2} [sccm]	time [min]
NC082	620	3.0	500	4.0	120
NC081	700	3.0	500	4.0	120
NC132	785	3.0	500	4.0	120
NC130	805	3.0	500	4.0	120
NC060	815	3.0	500	4.0	120
NC107	785	3.0	500	2.7	240
NC106	785	3.0	500	4.0	240
NC197	820	15	500	4.0	240
NC190	840	15	500	4.0	240
NC123	820	20	500	4.0	60
NC124	820	20	500	4.0	240

The sample grown at 620 °C is compact and has a rough morphology. The layer thickness is approximately 200 nm. A very low number of columnar structures can be observed at random places on the surface. At a higher T_{sub} of 700 °C, the morphology is rougher, but some nanowires can be observed in between the rough compact layer. The thickness of the compact layer is also ≈ 200 nm, but some wires have lengths around 400 nm. A further increase of T_{sub} to 785 °C leads to vertical free-standing nanowires without a compact layer in between. The length of the longer wires is between 400 nm and 600 nm. At 805 °C the nanowire density is drastically reduced and many very thin and short wires can be observed. A few longer wires have lengths up to $600 - 700$ nm. Finally at 815 °C almost no growth occurs anymore. Small islands form on the surface and the steps originating from the Si substrate are visible. Only one or two short nanowires on an area of $3 \times 3\,\mu m^2$ are present.

A SEM image of a sample grown at 820 °C and a higher $\Phi_{Ga} = 1.5 \times 10^{-7}$ mbar for 4 h is shown in Fig. 6.2. Despite the high substrate temperature many wires have grown into an array of nanowires. Further increasing T_{sub} to 840 °C again results in almost no growth despite the high Φ_{Ga}.

Another difference compared to growth at lower T_{sub} is shown in Fig. 6.3. In Fig. 5.5 it has been shown that the maximum density of the order of 10^{10} cm^{-2} is achieved after approximately 1 h, but at $T_{sub} = 820$ °C the density after 1 h is still very low ($\sim 10^7 - 10^8$ cm^{-2}). For 4 h of growth, however, the density is similar to densities obtained at lower substrate temperatures. The homogeneity of the length of the nanowires is also better than in the sample grown at 785 °C in Fig. 6.1. The average length of the longer nanowires is $\approx 1.4\,\mu m$.

The influence of the nitrogen flux on the nanowire growth is shown in Fig. 6.4. The diameters of the wires grown with $\Phi_{N_2} = 2.7$ sccm are a bit larger than the ones of wires

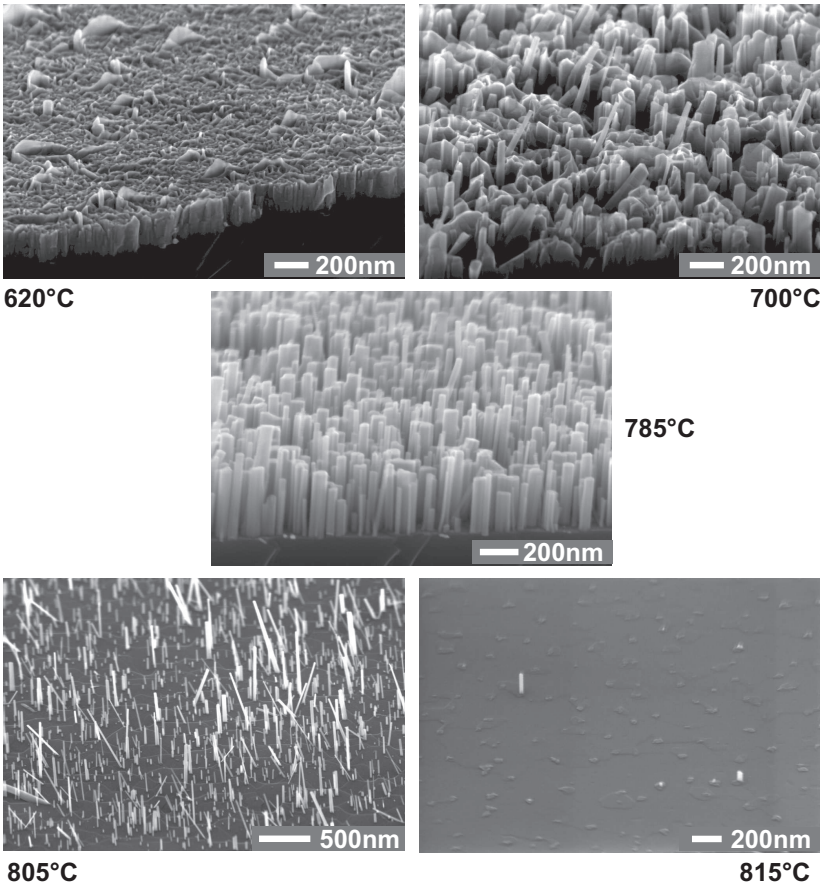

Figure 6.1: Side-view SEM images of GaN nanowire samples grown at different substrate temperature, but fixed Φ_{Ga} and Φ_N. The sample grown at 815 °C was grown for 4 h; the other samples for 2 h. With increasing substrate temperature the morphology first changes from a rough compact layer to columnar growth and then the nanowire density is gradually reduced. At high temperature there is almost no growth.

grown with $\Phi_{N_2} = 4.0\,\text{sccm}$ and there is more coalescence. At lower Φ_{N_2} there are also no very thin and long wires.

Discussion

By increasing T_{sub} the Ga desorption increases, thus effectively reducing the III-V ratio. This shifts the balance to more nitrogen-rich conditions and the surface diffusivity on the polar surfaces decreases (cf. Sec. 5.1). This promotes the formation of islands rather than a more compact layer and the morphology changes to a columnar one. Nonpolar surfaces are not affected by the reduced diffusivity under nitrogen-rich conditions and on them the diffusivity increases as a result of the higher substrate temperature. The diffusion channel

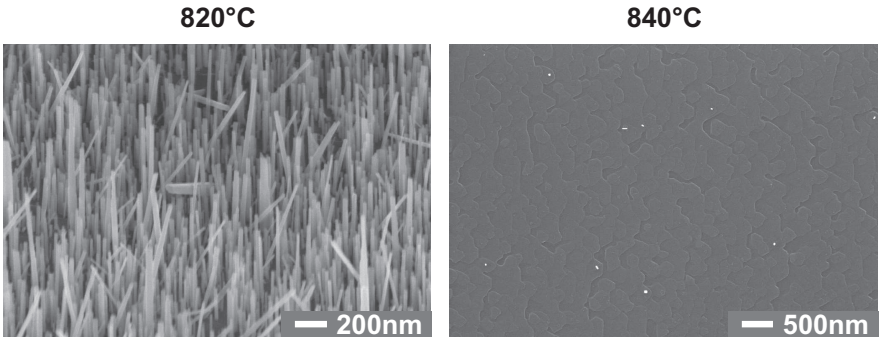

Figure 6.2: Side-view SEM images of two samples grown at 820 °C and 840 °C. A higher Φ_{Ga} than for the samples in Fig. 6.1 allows growing nanowires at higher substrate temperature, but it is still too low for $T_{sub} = 840\,°C$.

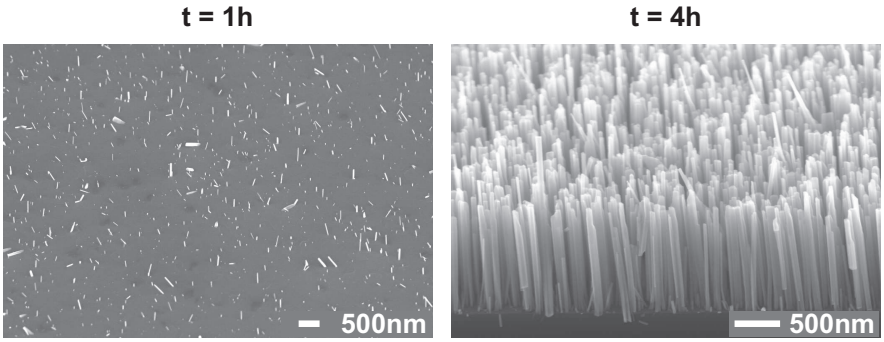

Figure 6.3: Side-view SEM images of samples grown at a high T_{sub} of 820 °C with different deposition times. The density after 1 h is much lower than for the samples in Sec. 5.2 grown at lower T_{sub}, but after 4 h it is at least comparable.

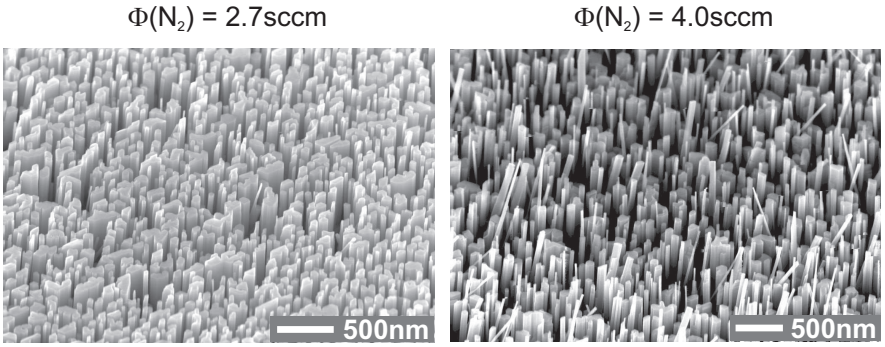

Figure 6.4: Side-view SEM images of two GaN nanowire samples grown with different plasma settings. The one deposited with lower Φ_{N_2} shows a bit more coalescence and thus a slightly higher average diameter.

discussed in Sec. 5.2 increases and the nanowire growth becomes more pronounced. At a certain temperature, however, the Ga desorption becomes so large, that Ga adatoms desorb before they form islands or incorporate in the growing structures. As a result the nanowire density decreases until almost no wires form at all.

The sample in Fig. 6.2 grown at 820 °C has many well-defined nanowires despite the high substrate temperature at which no growth occurred anymore at lower Φ_{Ga} (cf. Fig. 6.1). This shows the growth was limited by desorption and the high temperature is not a fundamental limit. By increasing Φ_{Ga} the desorption can be compensated and growth occurs again.

With increasing substrate temperature desorption increases and the stay time of adatoms on the surface is reduced. Therefore the adatoms have less time to form stable Ga or GaN clusters and the nucleation is slower or does not happen at all. This can be compensated by increasing Φ_{Ga}, but the sample grown for 1 h in Fig. 6.3 shows that the nucleation stage is longer in respect to the results presented in Sec. 5.2 for $T_{sub} = 785\,°C$. However the high density of the 4 h sample, which is comparable to densities of samples grown with lower Φ_{Ga} at lower T_{sub} indicates that when preferential nucleation sites are present in form of wires, the incorporation ratio drastically increases. The growth rate calculated by dividing the length after 4 h by the total deposition time ($\approx 350\,nm/h$) is at least comparable to compact layer growth rates at 770 °C and $\Phi_{Ga} = 2.0 \times 10^{-7}$ mbar. However, as indicated by the 1 h sample in Fig. 6.3, the actual growth time of many wires is considerably less. Moreover, as shown by Calleja *et al.* [92, Fig. 7], due to desorption the growth rate of compact layers decreases with higher T_{sub}. Therefore we can conclude that the incorporation of Ga adatoms is more efficient in the nanowire growth, which is consistent with the model proposed in Chapter 5 of efficient incorporation at the top of the nanowire. Comparing the growth rates of the nanowires in Fig. 6.1 and Fig. 6.3 grown at different T_{sub} a trend can be observed: the rate increases at higher T_{sub}. This can be explained in terms of a higher contribution of the diffusion channel to the growth (cf. Sec. 5.2) and thus also supports the proposed diffusion-induced model.

The efficiency of the production of atomic nitrogen by the SVTA plasma cell was studied in [145]. With increasing P_{RF} and Φ_{N_2} the amount of atomic nitrogen (Φ_N) also increased. The maximum Φ_N that can be achieved is therefore given by the limits of the plasma parameters, which allow stable operation ($\approx P_{RF} = 500\,W and \Phi_{N_2} = 4.0\,sccm$). The two images in Fig. 6.4 show that a reduction of Φ_N by reducing Φ_{N_2} leads to thicker wires and more coalescence, which is a result of the increased III-V ratio.

Results of this section and Sec. 5.1 are summarised in a qualitative phase diagram for growth of GaN at fixed plasma cell settings (Fig. 6.5). A cross section through the diagram at 770 °C corresponds to the growth regions in Fig. 5.1. At fixed Φ_{Ga} of 3.0×10^{-8} mbar a cross section relates to the images in Fig. 6.1. At higher substrate temperatures, desorption is higher and the Φ_{Ga} window for GaN nanowire growth narrows, because due to the higher mobility coalescence can more easily occur. Above $\approx 850\,°C$ GaN starts to dissociate under vacuum conditions and limits the MBE growth [146]. By changing the nitrogen flux, the effective III-V ratio is changed and the phase diagram shifts accordingly. For lower Φ_N the regions in the diagram thus shift to the left. The 'no growth' region, however, which is determined by the amount of Ga desorption, shifts downwards at lower Φ_N as a result of a lower Ga incorporation probability. Hence the nanowire growth region shrinks if Φ_N is reduced.

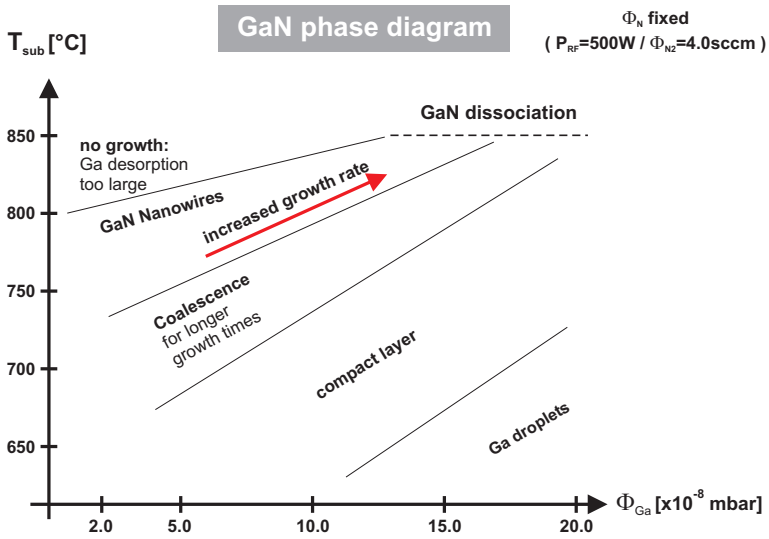

Figure 6.5: Qualitative phase diagram for GaN growth by PA-MBE as a function of Φ_{Ga} and T_{sub} at fixed plasma settings. Depending on the combination of growth parameters there is either compact layer growth, columnar growth or no growth at all. Above approximately 850 °C, GaN starts to dissociate under MBE growth conditions.

Conclusion

The GaN nanowire morphology depends critically on the combination of three growth parameters: Φ_{Ga}, Φ_N and T_{sub}. Lower III-V ratios are favoured for nanowire growth, whereas an increase of the III-V ratio leads to coalescence of nanowires or a compact morphology. Increasing the substrate temperature leads to higher Ga desorption and a lower effective III-V ratio. A higher T_{sub} also increases the growth rate by enhancing the diffusion along the wire sidewalls. However, for too high T_{sub} no growth occurs due to Ga desorption.

6.1.1 Tapering effect

Abstract

Some GaN nanowires show a pronounced reduction of their diameter at a certain height, which varies from wire to wire (cf. Fig. 6.6). The reduction can be quite fast and different from the slow tapering effect observed in several VLS grown nanowires [78, 112]. A changing net flux of Ga or N could explain this behaviour. Since growth occurs nominally under N-rich conditions, Φ_{Ga} should be a more sensitive parameter. Moreover, it is easier to control Φ_{Ga} than Φ_N and therefore we have varied Φ_{Ga} with the goal of obtaining wires with homogeneous diameter. The resulting nanowire morphology is studied in this chapter.

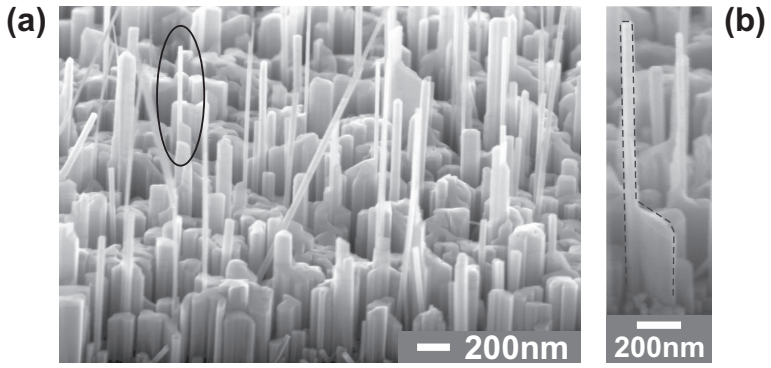

Figure 6.6: SEM images of GaN nanowire sample (NC16) grown with constant Φ_{Ga}. (a) The sample shows a distribution of diameters of the GaN nanowires. A few of them, like the one, which is encircled and enlarged in (b), feature a reduction of their diameter at a certain height; (b) Example of a reduction of the diameter of a GaN nanowire by the formation of a facet. After the diameter reduction the thin wire grows with a uniform diameter.

Experimental Details

As shown in Sec. 5.1 the formation of GaN nanowires is closely related to the III-V ratio. If Φ_{Ga} is too high for fixed Φ_{N}, the growth mode will change to a more compact one and the number of well-developed wires will go down. Especially in the nucleation stage the III-V ratio is important and therefore the nanowires are grown in different stages:

1. Growth is initiated with a set of parameters that lead to well-separated nice columns. The deposition time for this growth step is $30 - 60\,\mathrm{min}$;

2. Gradually ramp Φ_{Ga} to a higher value. The ramp can either be fast and only limited by the time necessary to change Φ_{Ga} or gradual with a constant rate of change of Φ_{Ga};

3. In the final stage growth commences at a fixed Φ_{Ga} higher than the initial Φ_{Ga}.

The growth parameters of the investigated samples are summarised in Tab. 6.2.

Experimental Results

A large and fast change of Φ_{Ga} ($\Delta\Phi_{\mathrm{Ga}} \equiv \Phi_{\mathrm{Ga,2}} - \Phi_{\mathrm{Ga,1}}$) leads to a broadening and strong coalescence of the GaN nanowires in sample NC20 (Fig. 6.7). The nanowires display a homogeneous height ($\sim 1.7\,\mu\mathrm{m}$). The top view SEM image (Fig. 6.7b) allows to identify new facets but a pronounced tapering is not present anymore (Fig. 6.7a), which means that the Ga graded flux was sufficient to ensure a suppression of tapering, but too high to prevent coalescence between nanowires. This coalescence mechanism can be used to form a compact layer useful for different applications in which one takes advantage of the strain release in nanowires and simultaneously have the advantage of a closed layer structure [141].

Table 6.2: Growth conditions for GaN nanowires. The last three samples were grown using three different growth stages: in stage 1 growth is started with an initial Ga-flux $\Phi_{Ga,1}$; then the flux is raised gradually (ramp stage) to the final flux $\Phi_{Ga,2}$, where it is kept constant till the end (stage 2).

Sample	Substrate temp. [°C]	Stage 1 $\Phi_{Ga,1}$ [$\times 10^{-8}$ mbar]	Stage 2 $\Phi_{Ga,2}$ [$\times 10^{-8}$ mbar]	Stage 1 time [min]	Ramp time [min]	Stage 2 time [min]
NC16	780	2.7	-	360	-	-
NC20	800	3.0	7.8	60	2	240
NC23	800	3.0	5.5	30	30	180
NC29	805	3.0	4.3	30	15	255
NC93	790	3.0	40	30	240	-

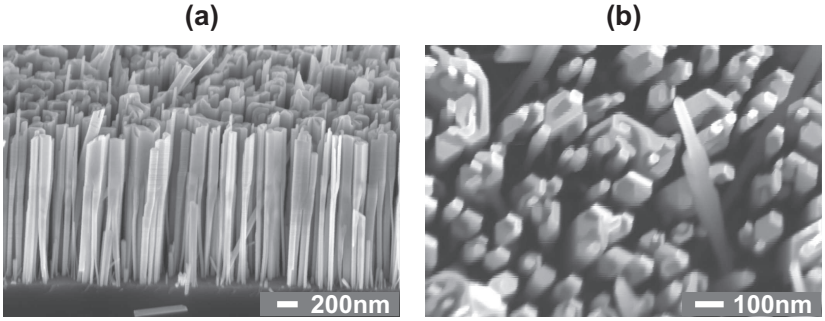

Figure 6.7: SEM images of sample NC20, which was grown with a fast increase of Φ_{Ga} to a value double the initial one. (a) The wires have coalesced, but show a homogeneous height and no apparent tapering; (b) The top-view SEM image shows the coalescence of thinner wires into thicker ones.

For sample NC23 shown in Fig. 6.8 $\Delta\Phi_{Ga}$ was reduced to prevent coalescence without reintroducing the tapering effect. The amount of coalescence is very low, but the structures show an enlargement of their diameter starting at approximately the middle to two-thirds of the nanowire length as is evidenced in the corresponding SEM image (Fig. 6.8a). The nanowire height is quite homogeneous at about 800 nm. Facets on top of the nanowires can still be identified (Fig. 6.8b), but they are more rounded than the usual GaN nanowires (cf. Chapter 5). In addition some new items looking like crowns can be recognised on top of the nanowires (Fig. 6.8a).

Sample NC29 shown in Fig. 6.9 has been obtained with an even lower $\Delta\Phi_{Ga}$ than in sample NC23. To obtain free-standing nanowires, which are well separated from each other the substrate temperature was slightly increased for this sample from 800 °C to 805 °C, but Fig. 6.9a shows it was not enough. The morphology of the nanowires, however, is very homogeneous

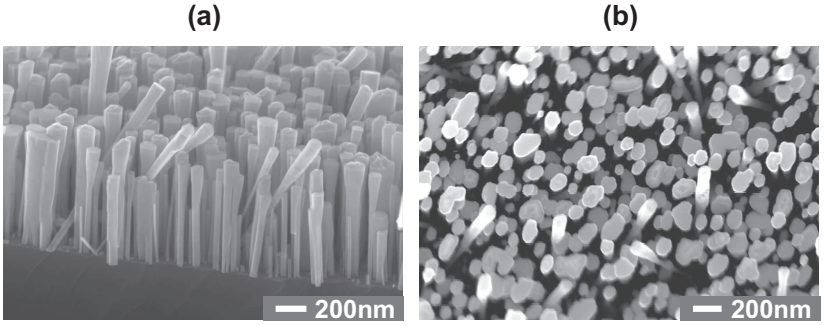

Figure 6.8: SEM images of Sample NC23, which was grown with a slower and smaller increase of Φ_{Ga} than the sample in Fig. 6.7; (a) Side-view SEM image evidencing a gradual increase of the nanowire diameter (inverse tapering effect); (b) Top-view SEM image shows that many wires are still separated from each other. The shape of the wires is more rounded and less faceted than typical GaN nanowires (cf. Chapter 5).

with respect to their diameter: no tapering and no enlargement is visible. The height is approximately 600 nm and facet-formation or crowns on top of the nanowires are not visible. Near the edge of the sample, the temperature is approximately $5 - 10\,^{\circ}\mathrm{C}$ higher, which leads to the desired separation between the wires (Fig. 6.9b,c) and also in this case the nanowires have a uniform diameter and flat top surfaces.

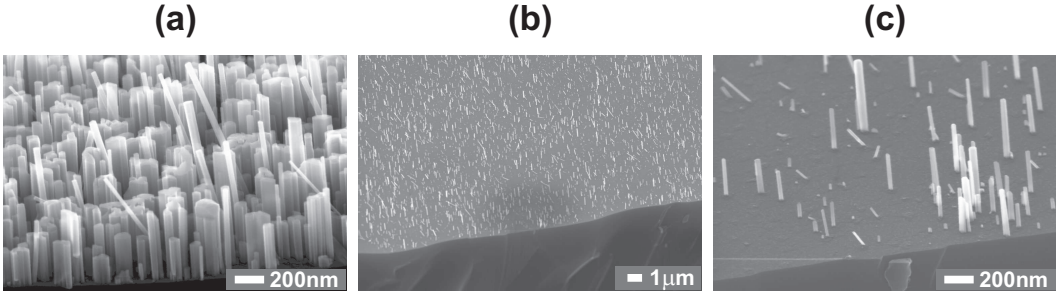

Figure 6.9: SEM images of sample NC29, for which the Ga ramping was optimised to produce wires with uniform diameter. (a) Image from the centre of the sample, which does not display any wires with a tapering effect. The higher Φ_{Ga} leads to a bit of coalescence; (b,c) SEM images at different magnifications from an area near the edge of the sample, where the temperature is slightly higher. This results in a lower nanowire density without coalescence and the diameters of the wires remain constant along their length.

A very slow, but large $\Delta\Phi_{\mathrm{Ga}}$ in sample NC93 results in coalescence of nanowires, but it is considerably lower than in Fig. 6.7 and the hexagonal facets of the wires are well-developed. The height is homogeneous around 1.9 μm and the top facets are flat. There is no apparent evidence for a sudden broadening like in Fig. 6.8a.

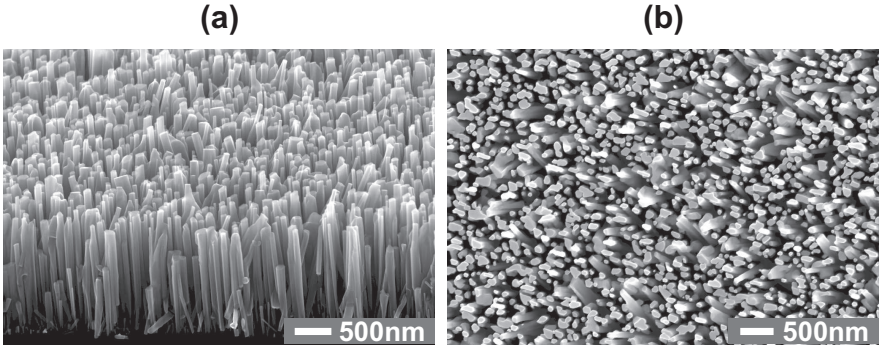

Figure 6.10: Side- and top-view SEM images of sample NC93, which was grown with a large, but very gradual increase of Φ_{Ga}. Despite the higher change of the Ga flux the amount of coalescence is lower than in Fig. 6.7. The wires have a homogeneous height and a hexagonal shape. The top facet is very smooth in contrast to the wires in Fig. 6.7 and Fig. 6.8.

Discussion

The images Fig. 6.7, Fig. 6.8, Fig. 6.9 and Fig. 6.10 show that the tapering effect can be suppressed by an increase of Φ_{Ga} during growth. However, the balance between Φ_{Ga} and Φ_N is very delicate, because if the increase of Φ_{Ga} is too high then a broadening of the wires is observed, although more gradual than in Fig. 6.7. The fact that the wires in sample NC23 broaden above the middle of the wire (cf. Fig. 6.8), although Φ_{Ga} was already increased after one-eight of the total deposition time suggests that there is a delicate equilibrium between the different fluxes, not only the impinging one, but also the diffusion channel. Comparing NC20 and NC93 (Fig. 6.7 and Fig. 6.10, respectively) shows, that the abruptness rather than the amount of the flux change determine whether wires of a sample will broaden at higher flux.

In general, at higher temperatures (cf. corresponding SEM images in Sec. 6.1) nanowires have a more uniform diameter, i.e. tapering is almost never observed. This can be explained by the fact that higher temperatures enhance the influence of the diffusion channel and changes to the delicate equilibrium can more easily be compensated.

Conclusion

In conclusion, the tapering and coalescence effect can be controlled by ramping Φ_{Ga} and optimising the growth temperature. The best results are obtained for sample NC29 grown at a temperature of 810 °C (near the edge) with the help of a gradual change of Φ_{Ga}. For this sample neither coalescence of nanowires nor a tapering effect has been observed. Where a gradual change of Φ_{Ga} is appropriate for wires with uniform diameter, an abrupt change helps to form a continuous layer on top of the wire by coalescence of the nanowires.

6.2 Crystal structure and epitaxial orientation

Abstract

The crystalline structure and orientation of the crystal relative to the substrate are important aspects, which have to be investigated. They can influence all kinds of optical and electronic properties; the radiative behaviour in a certain direction for instance as well as the spontaneous and piezoelectric polarisation depend significantly on the orientation of the crystal. A first question is whether the GaN nanowires consist only of the thermodynamically stable wurtzitic phase or if also other phases like the metastable cubic phase are present. These cubic phases have been observed in compact GaN layers and they can be distinguished from their wurtzitic counterparts by the XRD peak positions. A second question is whether there is an epitaxial relation between the wires and the substrate. These subjects will be addressed in this section.

Experimental Details

A $\Theta/2\Theta$-scan is measured with a STOE powder diffraction system of a GaN nanowire sample (NC03, $\Phi_{\mathrm{Ga}} = 2.7 \times 10^{-8}\,\mathrm{mbar}$, $\mathrm{T_{sub}} = 770\,^{\circ}\mathrm{C}$, $\mathrm{P_{RF}} = 500\,\mathrm{W}$, $\Phi_{\mathrm{N_2}} = 4.0\,\mathrm{sccm}$, $\mathrm{t_{depo}} = 2\,\mathrm{h}$) to determine the phase and the crystallinity of the sample. The sample was grown directly on a Si(111) substrate. Cu $K_{\alpha 1}$ radiation was used with a wavelength of 1.54056 Å.

Pole figures have been measured by a Philips MPD1880/HR with the same kind of x-ray source as the STOE system and hence the same wavelength, to study the epitaxial relation between a GaN nanowire sample similar to NC03 also grown directly on Si(111).

Experimental Results

The $\Theta/2\Theta$ - spectrum of sample NC03 displays only three peaks at 28.4°, 34.58° and 73.04° (Fig. 6.11a). Simulations of powder diffraction patterns for Si (Fig. 6.11b) and wurtzitic GaN (Fig. 6.11c) with bulk lattice parameters (Si: $a = 5.4286\,$Å and GaN : $a = 3.189\,$Å $c = 5.185\,$Å) allow to identify the experimental diffraction peaks. Simulated peaks that match the experimental values (within the margin of error of the measurement) are: 28.45° for Si(111), 34.57° for GaN(002) and 72.92° for the second order peak GaN(004). The theoretical value for the ratio between the intensities of both GaN peaks is $35.7/2.2 \approx 16.2$ and the experimental value is ≈ 20.9. The latter is a bit larger, which could be due to the accuracy of the measurement and different sensitivities of the detector in the respective ranges.

For comparison, the diffraction pattern of cubic GaN (Fig. 6.11d) for a bulk lattice value of $a = 4.5036\,$Å [147] has peaks at 34.46° for c-GaN(111) and 72.67° for the second order peak c-GaN(222). The ratio is similar to the wurtzitic phase: $100/6.4 \approx 15.6$. The first order peak of the cubic GaN phase is very close to the wurtzitic and experimental one, i.e. its centre lies within the FWHM of the experimental peak, but for the second order the distance is large enough to exclude a cubic phase. The measured intensity of a phase depends on its volume and a small amount of cubic grains inside of the nanowires is not measurable within the resolution of this method. This has to be determined with more sophisticated methods like TEM.

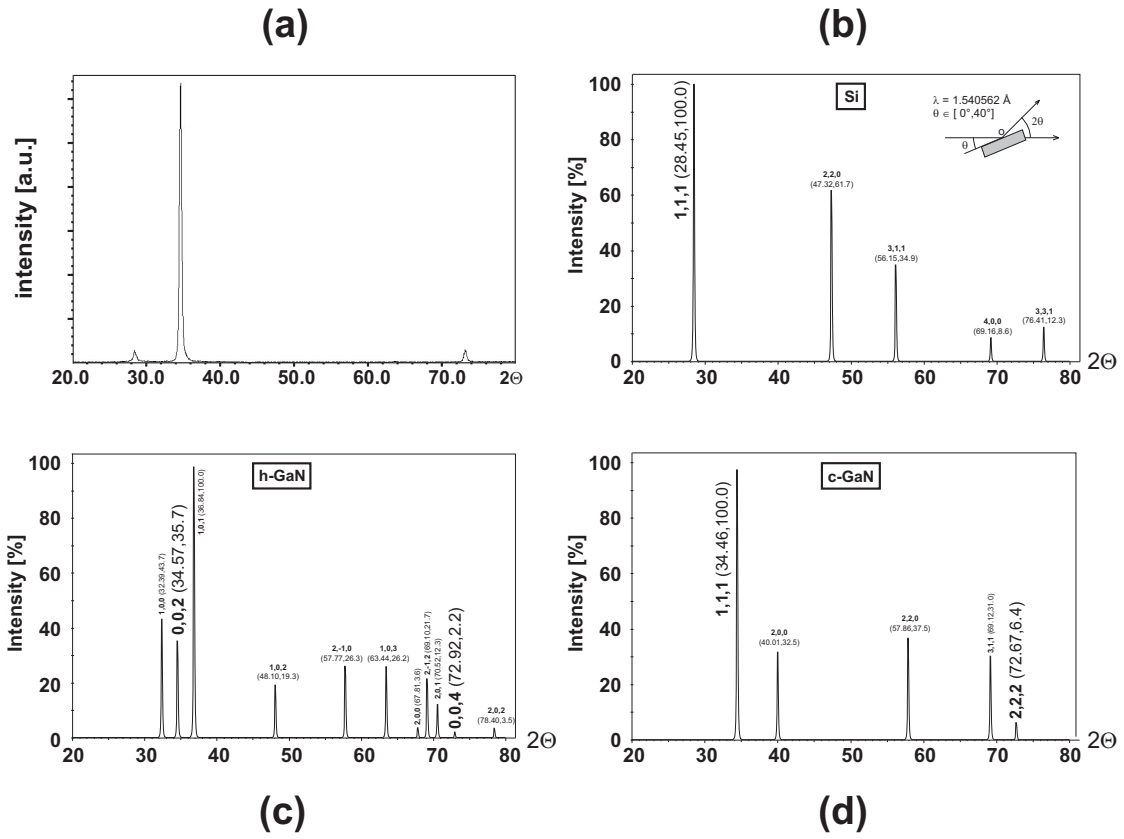

Figure 6.11: (a) Experimental $\theta - 2\theta$-scan of sample NC03; (b,c,d) Calculated powder diffraction patterns of Si, wurtzite (h-GaN) and zinc-blende GaN (c-GaN) respectively. The inset of (b) shows the measurement geometry. For clarity only the text of the peaks of interest in the calculated spectra are enlarged.

The presence of both the Si(111) and GaN(002) peak for the symmetric measurement setup shows that the wires grow in the c direction with GaN$\langle 001 \rangle$ // Si$\langle 111 \rangle$.

The $\Theta/2\Theta$-spectrum discussed above does not allow to determine the relative orientation between the Si(111) surface (lattice A) and the deposited GaN(001) layer or nanowires in our case (lattice B). A so-called pole figure, however, can be used to measure the epitaxial relation. In some cases it is even possible to determine it in one measurement without having to readjust the experimental conditions to satisfy the Bragg condition for the other lattice (A $\rightarrow$ B or B $\rightarrow$ A). This is possible when there is a family of lattice planes in Si and another one in GaN which have approximately the same lattice spacing (i.e. within the energy resolution of the probing X-Ray). For the Si/GaN heterostructure, this is the case for the Si(044), GaN(105) and GaN(122) lattice planes ($d = 0.960\,\text{Å}, 0.971\,\text{Å}$ and $0.968\,\text{Å}$ respectively). The corresponding Bragg angle is 52.45°.

Fig. 6.12a presents the results of a pole figure measurement for $\Theta = 52.45°$ of a GaN

nanowire sample grown on Si(111) (NC61). In this graph the intensity of the refracted beam is plotted against the polar angle θ and the azimuthal angle ϕ. θ corresponds to the radial distance and ranges from 0° to 90° in steps of 10° at each concentric circle. The measurement was performed between $\theta = 10°$ and $\theta = 70°$. The Si(044) peaks correspond to the dots centred around $\theta = 35.4 \pm 0.2°$. The other peaks at $\theta = 21 \pm 1°$ and $\theta = 69 \pm 1°$ belong to the GaN(105) and GaN(122) diffraction spots, respectively. The symmetry of the Si as well as the GaN pattern is hexagonal as expected.

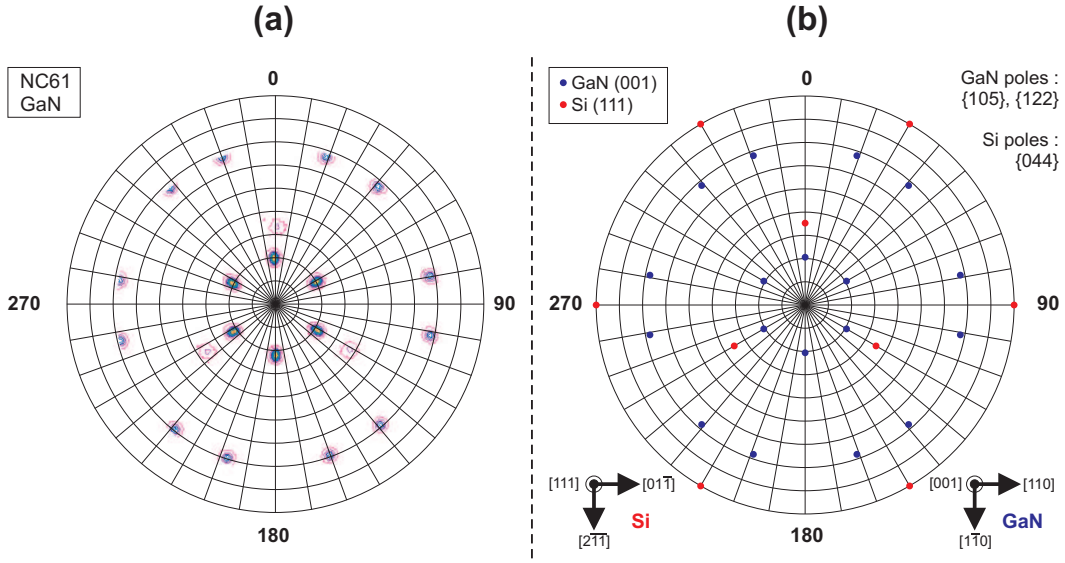

Figure 6.12: Experimental and calculated pole figure of sample NC61. (a) The poles at $\theta = 21 \pm 1°$ and $\theta = 69 \pm 1°$ correspond to GaN(105) and GaN(122), respectively. The other points at $\theta = 35.4 \pm 0.2°$ belong to Si(044); (b) Calculated pole figure for the epitaxial relation in Fig. 6.13a (cf. discussion below). There is a good correspondence between the experimental and theoretical pole figures.

Discussion

The result of the $\Theta/2\Theta$ - scan that GaN grows in the wurtzitic phase and GaN$\langle 001 \rangle$ // Si$\langle 111 \rangle$ can be expected for GaN grown on Si(111). GaN(001) is grown on the (111) surface of Si, because both surfaces have a hexagonal symmetry. The epitaxial orientation, i.e. the relative direction of lattice B to lattice A, is determined by the minimum free energy F_{hetero} of the heterostructure, which depends on the surface energies γ_A, γ_B of both lattices and the interfacial energy γ_{Int} [148]. Lattice mismatch, which we define as:

$$\frac{a_{layer} - a_{substrate}}{a_{substrate}} \times 100\% \tag{6.1}$$

and a resulting strain (compressive or tensile) increases the surface and interfacial energies and is thus not favourable for the condition of minimum free energy. So even though both

lattices have hexagonal symmetries, another orientation where lattice B is rotated relative to lattice A might have a lower free energy if the relative position of the atoms in A and B give rise to a lower free energy.

Since lattice A and B are semiconductors the surface can reconstruct when dangling bonds interact to lower the free energy. Such reconstructions can alter $\gamma_A, \gamma_B, \gamma_{Int}$. A clean Si(111) surface for instance can form a 7×7 reconstruction, which we have observed with LEED and STM (images not shown). Moreover, the initial growth stage can alter the Si surface, because Ga can alloy with Si and in the presence of N, Si_xN_y can form. It also determines the polarity of the growing GaN crystal and hence the number of bonds at the interface. For a full theoretical calculation all these arguments have to be taken into account, but we will use a simple model to compare simulated pole figures with experimental ones: in the simplest approximation where both lattices A and B are assumed to be rigid (rigid lattice approximation) the relative orientation of the two components A and B has to be such that the total system is in a state of minimum free energy. For rigid lattices the orientation relationship is essentially independent of the relative thickness of the layers and the interactions within and between the layers. Therefore only the geometries of the two lattices determine the configuration. In general, preferred orientations are those in which most densely packed rows in both lattices are parallel to each other, e.g. epitaxial relation I: Si$\langle 0\bar{1}1\rangle$ ∥ GaN$\langle 110\rangle$ (cf. Fig. 6.13a). The lattice mismatch in this case, however, is -16.9% in the directions Si$\langle 0\bar{1}1\rangle$ as well as Si$\langle 2\bar{1}\bar{1}\rangle$. Rotating the GaN crystal relative to Si over 30° results in epitaxial relation II: Si$\langle 0\bar{1}1\rangle$ ∥ GaN$\langle 1\bar{1}0\rangle$ (cf. Fig. 6.13b). For a 1:2 lattice match between Si and GaN in direction Si$\langle 2\bar{1}\bar{1}\rangle$ and a 3:2 lattice match in direction Si$\langle 0\bar{1}1\rangle$ the mismatch is only -4.1%. The Si atoms occupy two positions relative to the Ga (or N) layer: either a direct 1 to 1 relation or they form a tetrahedron with 3 neighbouring Ga (or N) atoms, which is typical for zinc-blende and wurtzite structures. A detailed knowledge of the interface is necessary to calculate the free energy and compare it with the other epitaxial relation, but as mentioned above surface reconstructions can completely alter the picture. STM measurements of very thin GaN layers (or very short GaN nanowires in our case) could give some more insight. However, the easiest way is to compare the simulated stereographic projections for the epitaxial relations with a measured pole figure.

To interpret the measured pole figure (Fig. 6.12a) the stereographic projections of the Si(111) and GaN(001) planes have been determined for the family of poles Si(044), GaN(105) and GaN(122). By rotating the projections around $\langle 111\rangle$ or $\langle 001\rangle$ respectively it is possible to superimpose the calculated graph to the experimental data. A combination of the simulated Si and GaN stereographic projections in one pole figure is shown in Fig. 6.12b. This graph corresponds to the following epitaxial relation I: (111)$\langle 0\bar{1}1\rangle$ Si ∥ (001)$\langle 110\rangle$ GaN. There is a good agreement between the experimental and theoretical data (compare Fig. 6.12a vs. Fig. 6.12b). The calculated poles at $\Theta = 90°$ are not visible in the experimental graph, because the measurement was only performed up to 70°. The intensity for measurements near to 90° is low and it is therefore difficult to measure. But the other points already unequivocally determine the epitaxial relation. The epitaxial orientation determined in the pole figure measurement is the same as was found by Krost *et al.* for compact GaN layers grown on Si(111) by MOCVD [149].

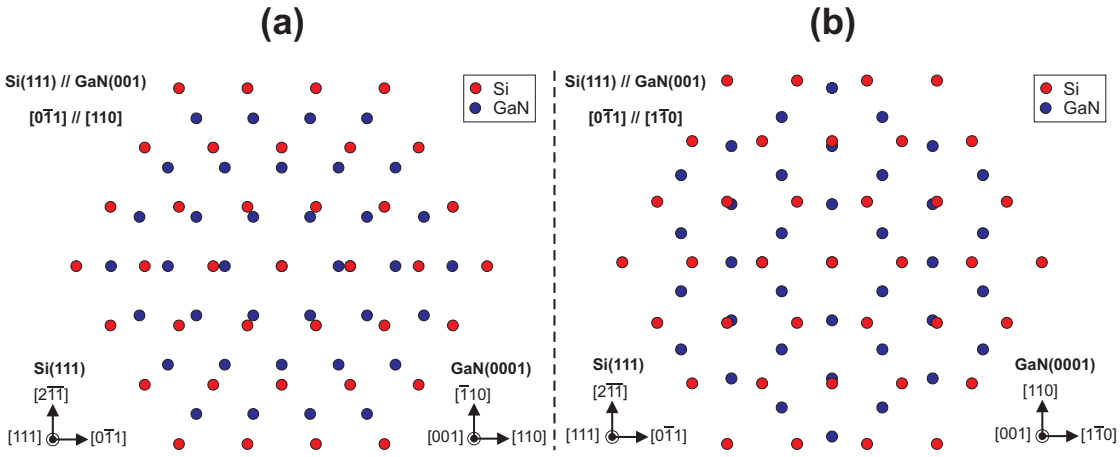

Figure 6.13: Possible epitaxial relations between Si(111) and GaN(001). (a) One-to-one relation where similar directions in the hexagonal lattices of Si(111) and GaN(001) are parallel; (b) The GaN lattice is rotated by 30° around Si⟨111⟩ relative to the relation in (a).

Conclusion

To conclude, GaN nanowires grow epitaxially on Si(111) in the wurtzitic phase in the following epitaxial relation, which is pictured in Fig. 6.13a: $(111)\langle 0\bar{1}1\rangle$ Si ∥ $(001)\langle 110\rangle$ GaN. No evidence for cubic phases has been found.

6.3 Optical characterisation of GaN nanowires

GaN is a semiconductor with a large *direct* band gap, making it an interesting material for optoelectronic applications. Therefore it is very important to study the optical properties of the grown material. Nanowires are especially interesting, because of the large surface-to-volume ratio and thus surface effects can strongly influence the spectra. Also the limited lateral size should allow for strain relaxation and thus less defects than in compact layers grown on a mismatched substrate are expected [150].

Several optical methods have been employed to characterise the nanowire samples. Cathodoluminescence (CL) as well as photoluminescence (PL) are very powerful non-destructive methods, i.e. the samples can be used for other measurements after the CL or PL measurement is done in contrast to for instance SIMS. In principle the measurements can also be done very quickly, giving fast feedback about the quality and specific features of the samples. In combination with an appropriate cooling stage it is possible to measure at low temperatures, which reduces the thermal broadening of peaks and therefore it is easier to resolve weaker features. At lower temperatures the scattering at phonons is lower and due to a lower diffusion length of the photo-carriers the trapping of carriers at nonradiative centres (in the bulk or at the surface) is lower. This increases the PL intensity. Several optical features depend very much on temperature or used power (sometimes called "pumping power"), which can also be

investigated with cooling and heating stages.

The main advantage of CL over PL is the possibility to study the spatial origin of the optical emission, i.e. a CL system in combination with a SEM gives information about the place on the sample or even inside the crystal where the measured light is coming from. By using the monochromator at a fixed wavelength or energy this can be done for all features in the optical spectrum.

PL on the other hand normally has a higher resolution because the energy resolution of the laser light typically used in PL setups is much higher than for a SEM/CL filament. In addition power control is easier for a PL laser than for the CL filament. The penetration depth of the laser light used in our PL measurements ($\approx 100 - 200\,\mathrm{nm}$) is smaller than for electrons typically used in the CL measurements [8, inset in Fig.8]. This reduces the investigated area giving the spectra a more local character than the CL spectra. For instance in our case the PL focuses on the top of the nanowires, whereas the CL measurements average over the whole wire. The electron beam in CL systems can also cause some carbon contamination on the surface, reducing the optical efficiency of the nanowires.

6.3.1 GaN cathodoluminescence results

Abstract

Although the typical resolution of a CL system is lower than for instance for a PL system, the combination of CL and SEM allows to obtain spatially resolved information from the sample. This can help assign parts of the spectrum to specific features of the sample.

The growth parameters, which lead to nanowire growth and the corresponding morphology are investigated in Sec. 5.1 and Sec. 6.1. For fixed Ga and N fluxes the substrate temperature to obtain well-separated nanowires is limited to a tight window. In this section the influence of the growth temperature on the optical spectrum of the nanowires is studied for a fixed Ga and N flux. In addition the spatial origin of the different contributions to the CL spectrum is determined.

Experimental Details

Cathodoluminescence was performed in a Leo 1550 SEM equipped with a Zeiss VIS grating monochromator, a photomultiplier tube connected to a preamplifier and a He-cooling cryostat ($6 - 475\,\mathrm{K}$ range). The electron beam energy is variable between 2.5 keV and 25 keV and currents range from 4 pA to 10 nA. The CL setup was calibrated by using a Cd-Hg spectral lamp, which emits at the following specific wavelengths: Cd 361.1 nm, 480.0 nm and 643.8 nm; Hg 365.2 nm and 404.7 nm. They cover the range in which one expects to find transitions in GaN.

A set of GaN nanowire samples has been grown with fixed nominal Φ_{Ga} and Φ_{N} just varying the substrate temperature (cf. Tab. 6.3). The deposition time ranges between 4 h and 6 h for all samples.

Table 6.3: Growth parameters as well as data about typical lengths and diameters of GaN nanowires characterised by CL with a focus on the influence of the substrate temperature. All samples were grown with $\Phi_{Ga} = 2.7 \times 10^{-8}$ mbar, $P_{RF} = 500$ W and $\Phi_{N_2} = 4.0$ sccm.

Sample		$\mathbf{T_{sub}}$ [°C]	**time** [min]	**height** [μm]	**diameter** [nm]
NC13		770	285	0.6 - 1.0	50 - 200
NC16	base	780	360	0.4 - 0.6	50 - 200
	long wires			1.0 - 2.5	20 - 70
NC10		790	240	0.35 - 0.65	20 - 90
NC11		800	240	0.1 - 0.65	20 - 95

Experimental Results

The CL spectra of four GaN nanowire samples NC13, NC16, NC10 and NC11 grown at a substrate temperature of 770 °C, 780 °C, 790 °C and 800 °C respectively (cf. Tab. 6.3) are presented in Fig. 6.14. Top- and side-view SEM images of the samples are shown in Fig. 6.15. The measurements have been performed at a nominal temperature of 10 K. It has to be noted that it is not possible to use the same settings for the aperture and amplification factor of the preamplifier for all samples due to the different sample-specific intensity of the CL signal and the limited dynamic range of the detector (i.e. the maximum measurable intensity divided by the minimal measurable change in intensity), which is of the order of $2^8 = 256$. This means that it is not possible to compare the absolute intensity of the samples and the spectra have therefore been normalised to the maximum intensity in the spectrum. However, there is a clear trend that for higher T_{sub} the CL intensity increases and the amplification has to be reduced to prevent "clipping" of the measurement signal (i.e. the signal runs out of the detection limit). For each sample the amplification is chosen such that the most intense peak is at $90 - 95$ % of the detection limit to maximise the signal to noise ratio. The samples are measured at an electron beam energy of 20 keV, for which a penetration depth into GaN of 2 μm is expected [8, inset in Fig.8]. This means that in our case with typical nanowire lengths of 1 μm the signal is an average over the whole wire.

There are two dominating features in the spectra of the samples shown in Fig. 6.14, but they differ considerably from sample to sample. The broad band centred at approximately 2.2 eV can be attributed to the yellow luminescence (YL). With increasing T_{sub} the relative contribution of this band with respect to the band edge peak decreases and for sample NC11 the YL signal is very weak if at all measurable. The other feature, which dominates in all CL spectra, lies between approximately 3.0 eV and 3.6 eV. The spectra of sample NC13 clearly shows two local maxima, whereas for NC16 this seems to become one broad peak. For NC10 there is only one clear peak and a small hump around 3.3 eV. The spectrum of NC11 consists of a single peak, which has a faint shoulder on the lower energy side. The peak seems to be shifted relative to the other samples, because the high energy tail does not match with the

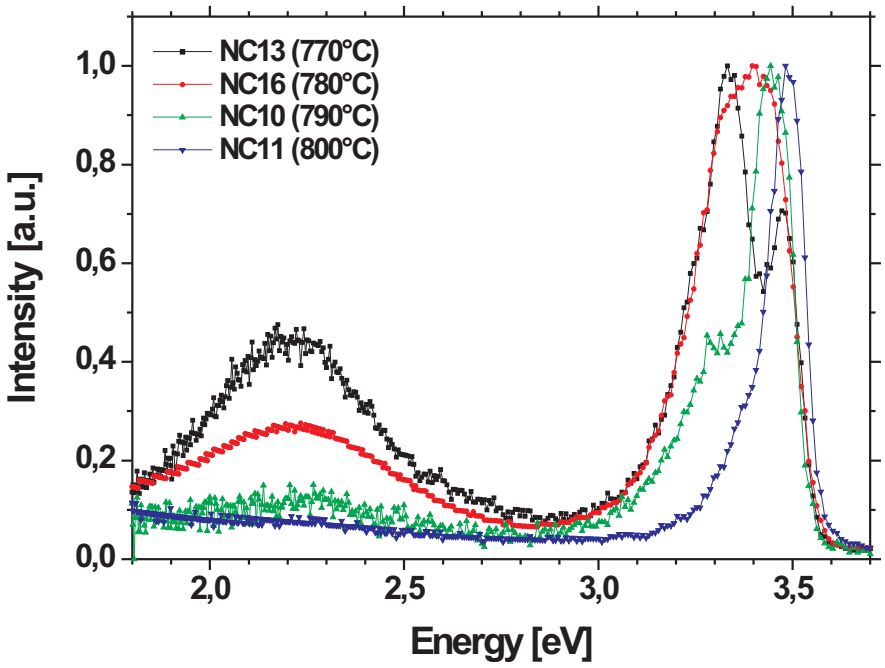

Figure 6.14: CL spectra obtained from samples grown at different substrate temperature. The spectra correspond to samples NC13 (770 °C), NC16 (780 °C), NC10 (790 °C) and NC11 (800 °C). The YL decreases with increasing T_{sub} and the shape of the spectra between approximately 3.0 eV and 3.6 eV is also altered with increasing T_{sub}.

other spectra. On the other hand it is interesting to note that the high energy tails of samples NC13, NC16 and NC10 are quite similar. There also seems to be a correlation between the relative intensity of the YL and the feature around 3.3 eV, because they both decrease relative to the peak around 3.45 eV with increasing T_{sub}.

Furthermore, it is possible to measure a CL spectrum in parallel with a SEM image. This allows to locate the origin of the CL emission. There are two possible modes: panchromatic and monochromatic. In the first case, the detector integrates over the entire spectral range for each scanned point (the monochromator is not used in this mode). This means there is a mapping $\vec{r} \rightarrow I_{tot}$, where $\vec{r}$ is a two-dimensional vector corresponding to the position in the SEM image and I_{tot} is the integrated intensity, resulting in a two-dimensional image. Bright colours correspond to a high signal at that point and dark colours to low intensities. In monochromatic mode, the detector only measures a signal at the current wavelength of the monochromator (I_λ) and thus it is possible to locate the origin of the selected spectral feature. Due to the finite resolution of the monochromator it is rather a wavelength range then a single wavelength, which is measured and this range is about 1 nm. The corresponding mapping is $\vec{r} \rightarrow I_\lambda$.

Fig. 6.16a is a top-view panchromatic CL image of a typical distribution of nanowires. A comparison of CL and SEM image (Fig. 6.16(a) and (b), respectively) shows that the nitride

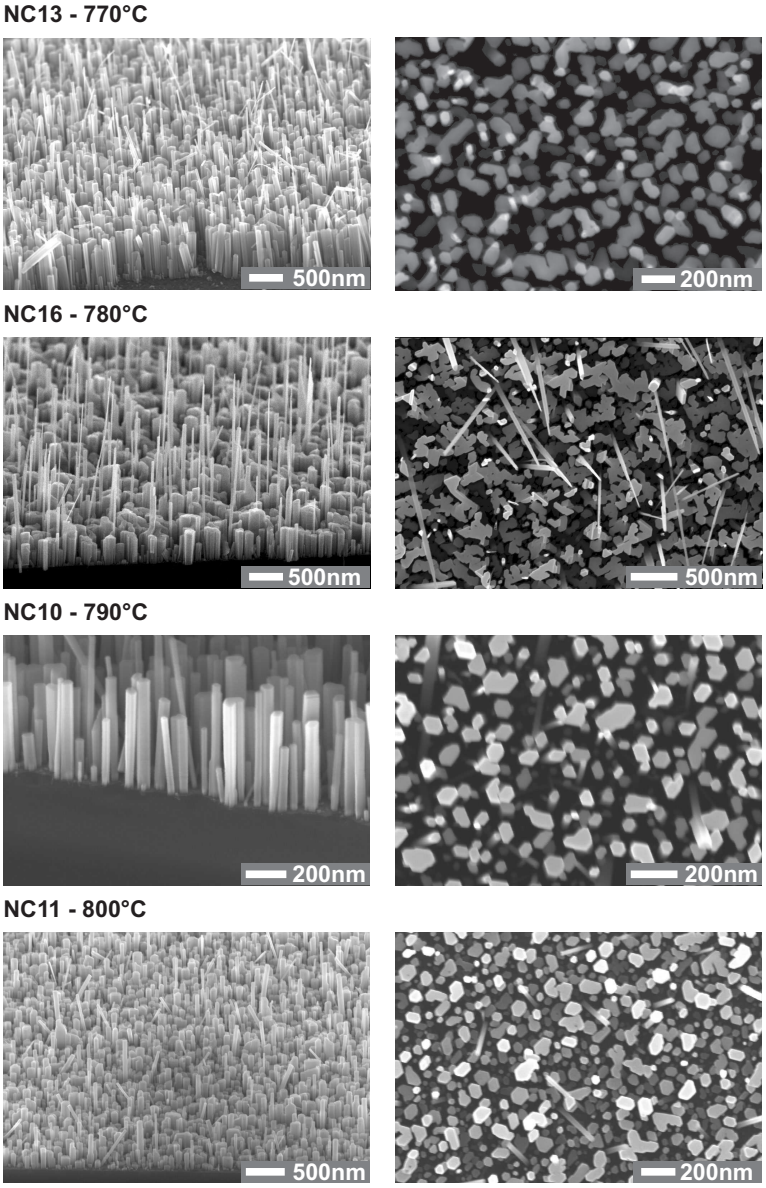

Figure 6.15: Side- and top-view SEM images of GaN nanowire samples grown at different substrate temperatures: NC13 (770 °C), NC16 (780 °C), NC10 (790 °C) and NC11 (800 °C). With increasing T_{sub} the density and amount of coalescence as well as the average length decreases.

structures are highly luminescent. The lateral dimensions of the spots in the CL image are well comparable to the structures observed in the secondary electron image revealing a high resolution of the CL image. In general, the spatial resolution of the CL image is limited by the volume excited by the electron beam. This volume depends on the electron beam

energy (cf. [8]) and at 20 keV the penetration depth of the electrons into GaN is $\approx 2\,\mu m$ as mentioned above. Laterally the resolution is limited by the diameter of the nanowires because it is smaller than the typical diffusion length of the electrical carriers [151, 152].

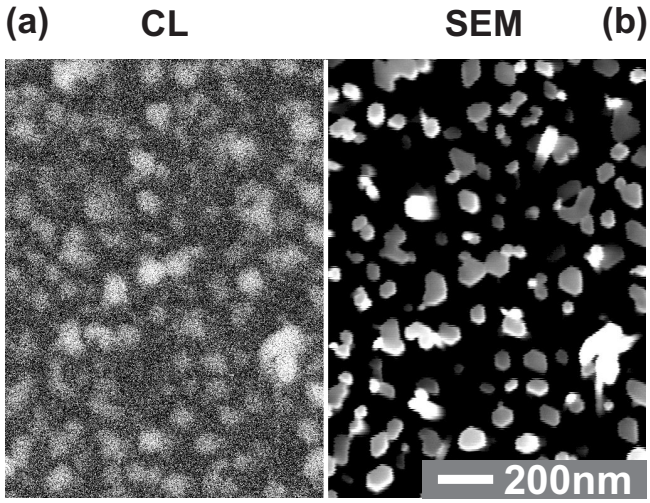

Figure 6.16: Sample NC10: (a) top-view panchromatic CL image and (b) corresponding top-view SEM micrograph. A comparison of both images shows that the bright luminescence spots correspond to the nanowire positions.

Monochromatic CL images have been recorded on a high quality sample NC11, obtained at high deposition temperature (Fig. 6.17a,c): the first one was taken at 520 nm (yellow luminescence) and the other one at 360 nm (donor-bound-exciton transition). At 520 nm there is no appreciable luminescence from this defect band at any position of the sample (gray colours dominate Fig. 6.17a). At 360 nm however, a strong near-band luminescence is detected (white areas in Fig. 6.17c). In some areas nanowires have been accidentally removed (see the corresponding SEM image Fig. 6.17d) and these areas are reproduced in the CL image Fig. 6.17c as dark areas, again indicating that the intense near-band luminescence originates in the nanowires and not in some other part of the sample.

Discussion

The CL spectra of GaN nanowires grown at different T_{sub} in Fig. 6.14 differ considerably, but it is clear that all spectra are a superposition of several peaks. Directly drawing conclusions from such a total spectrum can be quite misleading and result in wrong interpretations. It is also difficult to extract information about the width and relative intensity of the peaks. To make things even more difficult phonon replicas of transitions can occur, which are less probable with increasing phonon number and as a consequence have lower intensity. Thus it is difficult to distinguish them in the vicinity of a strong transition. A deconvolution of the spectrum with the help of a fitting programme can help find 'hidden' peaks and determine important values like the peak centre, intensity and width. The fitting is not straightforward

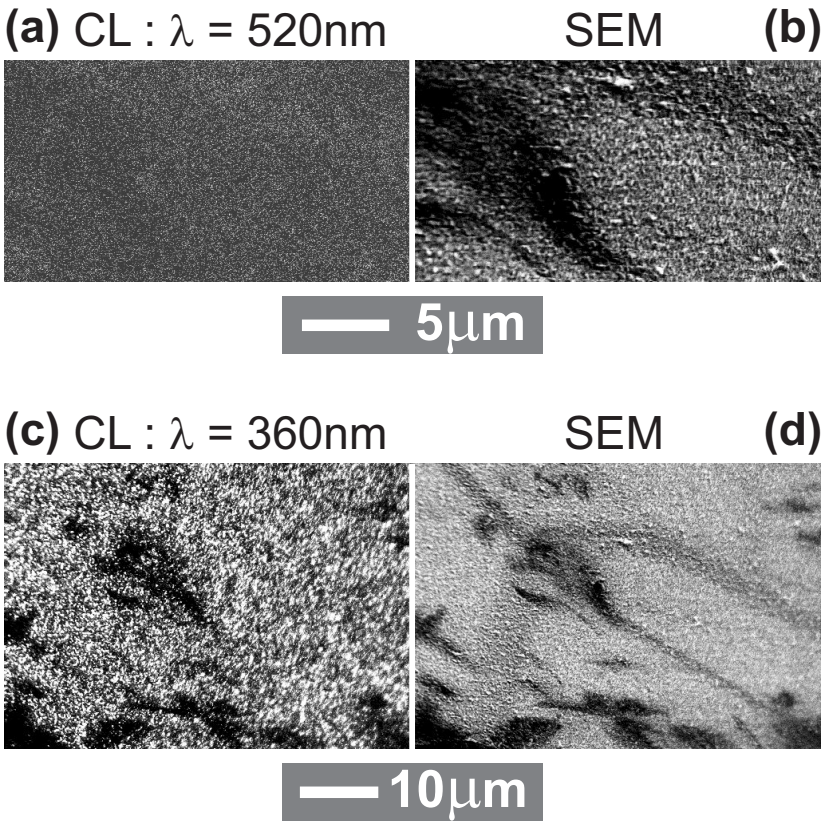

Figure 6.17: Sample NC11: top-view monochromatic CL images acquired at 520 nm (a) and 360 nm (c); (b) and (d) are the corresponding top-view SEM images. In the CL images, black/gray regions correspond to low luminescence and white areas to high luminescence. Comparing the images (a) and (c) one can observe that luminescence is much more efficient at 360 nm (c). Also the relation to the SEM image is more evident at 360 nm.

however and depends very much on the initial fitting parameters. Therefore one has to look in literature for the position of possible peaks and decide which can occur. An extensive review of observed transitions in GaN is given by Reshchikov and Morkoç [153] and this work has been used to estimate starting spectra for the fitting programme. Transitions, which have a higher probability in nanowires than in compact layers are surface related transitions due to the large free surface area and can thus be present in the spectra. In addition due to the use of a Si substrate an unintentional Si-doping, especially at the interface, can occur and related transitions should be taken into account.

To determine the composition of the CL spectra a Gaussian deconvolution of the CL spectra has been performed for all samples. The YL is reported to have a Gaussian shape [153] and the other peaks fit best to a Gaussian. This can be related to small statistical fluctuations in the properties of the wires with different length and diameter. Strain and Si diffusion into GaN can be higher at the substrate interface and since the CL beam probes the whole wire,

there is an average over areas with different physical properties.

The result of the 'fit' for sample NC13, NC16, NC10 and NC11 is shown in Tab. 6.4: peak centre, width and intensity relative to the highest peak are given for all peaks which have been found. It has to be noted that some transitions in [153, Table I] are very close to each other and can only be resolved with high resolution PL systems. The step size of the monochromator in our CL system is 1 nm, which corresponds to ≈ 9.6 meV at 360 nm and therefore it is impossible to resolve all peaks. In addition some spectra are a bit noisy, which is almost unavoidable with the low dynamic range of the CL setup. As a result one has to use a noise reduction filter to be able to use the fitting programme. Otherwise a large amount of peaks will be found and in general for weak features it is not possible then to distinguish real peaks and peaks caused by noise. This means that despite the deconvolution it cannot be excluded that a group of closely spaced peaks will be fitted as a single peak with a correspondingly large FWHM.

Tab. 6.4 shows that there are six peaks in all the spectra and additionally some phonon replicas. The optical phonon in GaN has an energy of 92.3 meV [154] and within the error of the fitting procedure the spacing between peaks is consistent with this value. Sometimes the replicas are too weak to be resolved like in NC11 where for instance the zero-phonon-line (ZPL) of the DAP is already quite weak and correspondingly its replicas even weaker.

The peak with the highest energy has approximately the same value of 3.48 eV in all the samples except for NC11, where it is a bit higher. According to [153] this peak corresponds to a donor-bound-exciton (DBX) or some free excitons (FX). In our case it is probably a superposition of several peaks in this energy range, although free excitons only occur in very high quality material. The excitonic peak in GaN is very sensitive to strain and shifts accordingly: the peak redshifts for tensile strain and blueshifts for compressive strain (cf. [155] and references therein). Since the lattice mismatch between GaN and Si(111) for the epitaxial relation determined in Sec. 6.2 is -16.9% a redshift can be expected. Although nanowires should be able to relax very quickly due to their limited lateral size, the amount of the lattice mismatch is very high. However, the value determined for samples NC13, NC16 and NC10 is in good agreement with reference values for strain-free GaN in [8, 153, 154]. This shows that there is not much strain if any in the GaN nanowires of these samples. The higher value for NC11 would correspond to a compressive strain, which is not expected for a Si(111) substrate and more likely it is due to an additional contribution of one or more free excitons. The absolute intensity for NC11 is the highest of all the samples and this suggests that it has the best quality and the biggest probability of observing free excitons.

The second peak at $\approx 3.41 - 3.42$ eV is labeled Y_2 in [153] and its origin is not clear at present. It is presumed that it is related to some structural defect at the surface and hence one can expect to find it in nanowire samples, which have a large surface-to-volume ratio. Fig. 6.18 shows that except for NC13 there is a reduction of the relative peak intensity with increasing T_{sub}, so the results suggest that the quality of the surface increases with T_{sub} and again NC11 has the highest quality. Concerning NC13 it is possible that the peak is underestimated in the fitting procedure of this sample due to the strong peak at ≈ 3.34 eV. The peak was also observed in other MBE-grown GaN nanowire samples of high quality [8, 154] and there it was suggested that it is due to a highly disordered region near the interface with the substrate. However, Tab. 6.3 and Fig. 6.15 show that NC10 and NC11 have the shortest wires and thus

Table 6.4: Fitting data of the CL spectra of Fig. 6.14. The peak centre, FWHM as well as absolute and normalised intensity relative to the DBE peak as determined from the fitting procedure are presented. Within the error margins of the fitting, the peak centres are quite similar for all samples except for NC11, where the peaks appear at a bit higher energies. The FWHM of the peaks are also similar for all samples. The intensity of the different peaks varies considerably, however, which is best appreciated for the normalised intensity relative to the DBE peak. The normalised intensities are plotted in Fig. 6.18.

	peak center				**FWHM**			
	NC13	**NC16**	**NC10**	**NC11**	**NC13**	**NC16**	**NC10**	**NC11**
DBE	3,482	3,476	3,475	3,494	99,5	107,4	87,8	90,3
Y_2	3,413	3,412	3,420	3,422	79,5	104,6	86,3	100
$Y_4 - Y_6$	3,344	3,333	3,336	3,353	93,8	118,3	109,6	74,2
UVL	3,274	3,261	3,271	3,293	93,3	117,8	88,7	69,3
Y_7	3,209		3,215	3,228	78,3		71,9	155
$UVL - 1 \cdot LO$		3,184	3,168			131,8	73,1	
$Y_7 - 1 \cdot LO$	3,145		3,125		86,2		131	
$UVL - 2 \cdot LO$	3,091	3,087			193	207,4		
$Y_7 - 2 \cdot LO$			3,038				218	
YL	2,210	2,229	2,252	2,236	460	521	387	??
	intensity				**normalised intensity**			
	NC13	**NC16**	**NC10**	**NC11**	**NC13**	**NC16**	**NC10**	**NC11**
DBE	18,5	15,2	22,9	26,4	1,000	1,000	1,000	1,000
Y_2	7,65	16,4	19,7	7,96	0,414	1,079	0,860	0,302
$Y_4 - Y_6$	24,8	19,2	10,3	4,13	1,341	1,263	0,450	0,156
UVL	14,7	8,31	7,67	1,79	0,795	0,547	0,335	0,068
Y_7	7,14		3,8	1,29	0,386		0,166	0,049
$UVL - 1 \cdot LO$		4,78	2,26			0,314	0,099	
$Y_7 - 1 \cdot LO$	3,02		2,34		0,163		0,102	
$UVL - 2 \cdot LO$	2,17	1,76			0,117	0,116		
$Y_7 - 2 \cdot LO$			1				0,044	
YL	10,6	4,93	1,61		0,573	0,324	0,070	

the biggest relative contribution from the base of the wire. Therefore the peak should be more prominent for samples with short wires like NC10 and NC11, but the opposite is true.

The next peak at $\approx 3.33 - 3.35\,\mathrm{eV}$ could be one of the peaks Y_4, Y_5 or Y_6 [153] and also for these peaks the origin is still under debate. The presumed origins are an exciton bound to a structural defect at the surface or the bulk, Y_4 and Y_5 respectively, or a surface donor-acceptor pair (Y_6). A phonon replica of the DBE or Y_2 peak can be excluded, because in NC13 and NC16 the intensity of this peak is higher than for the first two peaks. The peak shows a similar trend as Y_2: it decreases monotonically with increasing T_{sub}. The intensity relative to the DBE peak is significantly lower in NC10 and NC11 compared to NC13 and NC16. Looking at Fig. 6.15 one could give a possible explanation: the top-view images of

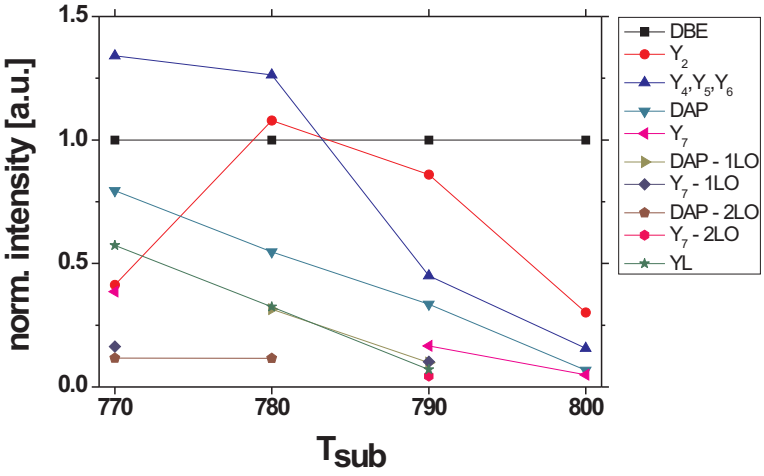

Figure 6.18: Graphical overview of the normalised intensity of the different peaks relative to the donor-bound-exciton (DBE) peak. All defect-related peaks show a downward trend with increasing T_{sub}. The Y_2 peak in NC13 (770 °C) might be underestimated by the fitting procedure due to a strong neighbouring peak.

NC10 and NC11 show that the major part of the wires is well-separated, whereas in NC13 and NC16 there is significant coalescence. The interface of the grains which form could be a source of this defect peak.

There is a number of possible transitions in the region around $3.26 - 3.29\,\text{eV}$. Theoretically one could find some second order phonon replicas of near band edge (NBE) excitons, but for NC13, NC16 and NC10 the relative intensity is too high and we can exclude them. Keeping Sec. 6.2 in mind and the fact that wurtzite GaN is favoured thermodynamically under these growth conditions we can also rule out a DBE in cubic GaN as the origin of this peak. The other possibilities in [153] are usually denoted by a DAP band. However, as explained in [153] it is better to call it the ultra-violet luminescence (UVL) band, which can have its origin in a shallow DAP- or an e-A-type transition. It is not always possible to distinguish them and often it is a combination of both. The DAP transitions involving shallow donors usually give way to the e-A transitions at elevated temperatures as free electrons thermally released from the shallow donor to the conduction band recombine with holes bound to the same acceptor. Possible candidates for the shallow donor are Si_{Ga} or O_N, but the assignment of the shallow acceptor is still controversial. Concerning the shallow donor, Si_{Ga} has the highest probability in our case, because we grow under N-rich conditions and the presence of O_N is thus less probable. Mg-doping can enhance the UVL band, but we can also rule out this possibility, because the nanowires were not intentionally doped. The UVL band decreases in our samples with increasing T_{sub}. This means that the concentration of the shallow donor or of the shallow acceptor or both decrease. A lower incorporation of Si due to a higher segregation to the surface at higher T_{sub} could explain the observed results.

Also the peak around $3.21 - 3.23\,\text{eV}$ labeled Y_7 in [153] decreases with increasing T_{sub}. It

was not found in NC16 by the fitting programme, but this could be due to an overestimation of the other peaks close to this one (UVL & UVL - $1 \cdot$LO). It is attributed to an exciton bound to a structural defect [153] and this means the quality improves for increased T_{sub} as observed with the other defect-related peaks.

The final peak around 2.2 eV which is the YL, as already mentioned above, follows the same trend as the other intra band gap peaks: its intensity decreases with increasing T_{sub}. Since the YL is attributed to defects [153] the ratio between the excitonic emission and the YL is often used as a figure of merit for the quality of the GaN. We can thus conclude that the quality of the wires improves with increasing T_{sub}. This is consistent with the trend observed for the other defect-peaks (cf. Fig. 6.18).

It is interesting to note, that the GaN nanowires have a strong luminescence, comparable to for instance high quality compact layers (at similar settings of the measurement setup). This was also observed by Kikuchi *et al.* [156] and Bertness *et al.* [157]. It is difficult to compare both intensities due to the different volumes: naturally nanowire samples have a lower density and thus smaller bulk volume and also the compact layers were much thicker (although it has to be noted that the penetration depth is limited). A larger volume (of material with similar quality of course) means that there is more material to excite which can emit luminescence and thus in principal the signal is higher.

Another important quantity determining luminescence intensity is the surface area (or maybe better: the surface-to-volume ratio), which is very large for nanowires compared to compact layers. The influence of the surface on the luminescence intensity is a bit more complicated than for the volume. On the one hand, intrinsic as well as extrinsic defects (e.g. impurities) can more easily segregate at the surface of the nanowires than for compact layers (see for instance [111]), leaving the bulk of the nanowires with a relatively small concentration of defects. The bulk part of the nanowires should therefore have a higher quality, which is associated with a higher CL efficiency. On the other hand if surface states and impurities at the surface, which can also accumulate after the growth, are present, they can cause non-radiative or defect-related transitions quenching the near-band emission, because minority carrier diffusion lengths in GaN are larger than the lateral dimensions of the nanowires [151,152]. Thus almost all generated carriers can reach the surface and recombine there. In view of the high band edge CL intensity revealed in the GaN nanowire samples it can be suggested that there is a low density of defects at the free surfaces. Another possible explanation of this strong luminescence could be that carrier diffusion towards the surface is hampered by a potential barrier induced by surface states, which will be discussed in Sec. 9.4.

Conclusion

The cathodoluminescence spectra of GaN nanowires exhibit different defect-related peaks and their intensity decrease with increased substrate temperature indicating a higher quality of the nanowires. The nanowires strongly luminesce despite the large surface-to-volume ratio, indicating either a high quality of the surface or a barrier for diffusion to the surface.

6.3.2 GaN photoluminescence results

Abstract

Photoluminescence (PL) measurements with higher resolution than the CL spectra have been performed on similar samples to confirm the results of the CL measurements. Due to the higher resolution it should also be possible to get more information on the origin of the peaks and maybe some additional features can be observed. The penetration depth of the PL laser light is lower than the one of the electron beam in the CL setup and therefore the material, which gives rise to the spectra, is closer to the top of the wires and is expected to have a higher crystalline quality.

Experimental Details

The photoluminescence was excited by a continuous wave (cw) UV laser line centred at 244 nm. Starting from the 488 nm wavelength of an Ar+ laser, the UV line was obtained by doubling and admixing the second harmonic with the fundamental frequency and by using an intracavity non-linear BBO (β-BaBO4) crystal. The 244 nm output beam was then focussed on the samples kept at regulated temperature in an optical helium bath cryostat ($1.2 - 300\,\mathrm{K}$). The laser power varied between 0.24 mW and 0.50 mW. The luminescence signal was dispersed by a 0.75 m focal length Czerny-Turner type monochromator (SPEX 1702) and detected by a water-cooled silicon photodiode array detector. From absorption measurements in GaN at 1.2 K the penetration depth of the UV light in GaN was estimated to be approximately 100 nm. This limits the information depth of the PL signal.

By using gratings with a higher number of lines per mm it is possible to improve the resolution, but this also reduces the acquired PL intensity. Therefore different gratings were used to measure a full spectrum ($\approx 1.6 - 5.5\,\mathrm{eV}$) and to focus on the region near the band edge ($\approx 2.9 - 3.7\,\mathrm{eV}$). Gratings with respectively 50 and 300 lines per mm were employed. Since the total number of measurement points for a spectra is fixed at $2^{10} = 1024$, the step size is reduced for a smaller range, which suits the increased resolving power.

A set of samples similar to the ones in Sec. 6.3.1 has been measured by PL. In addition a sample with lower nitrogen flux is examined (NC12). The growth parameters of the samples are summarised in Tab. 6.5.

Experimental Results

Fig. 6.19 shows the spectra of all samples for the full range. Since it is difficult to compare the absolute intensity of the spectra due to a different volume of the investigated area, the spectra have been normalised to the DBE peak, which dominates in most spectra. The nanowire density and (average) length of the wires vary from sample to sample which means a slightly different investigated volume, although the limited penetration depth of the laser beam reduces the effect of the length on the volume.

There is a huge difference between the different PL spectra. With increasing substrate temperature the YL is reduced. Only NC16 has a lower YL than NC10. The UVL band and its replicas show a similar trend. Both YL and UVL are very low in NC11, which confirms

Table 6.5: Growth parameters of GaN nanowires characterised by PL with a focus on the influence of the substrate temperature. All samples were grown with $\Phi_{Ga} = 2.7 \times 10^{-8}$ mbar and $P_{RF} = 500$ W.

Sample	$\mathbf{T_{sub}}$ [°C]	Φ_N [sccm]	**time** [min]
NC12	770	3.0	240
NC04	770	4.0	240
NC16	780	4.0	360
NC10	790	4.0	240
NC11	800	4.0	240

the conclusion from the CL measurements that this is the sample with the highest crystalline quality. The centre of the DBE peak has a similar position for all samples, which can be expected for strain-free nanowires. NC12 has a very large YL: the ratio between the YL and the DBE peak is 5. Also the UVL band has a higher intensity than the DBE.

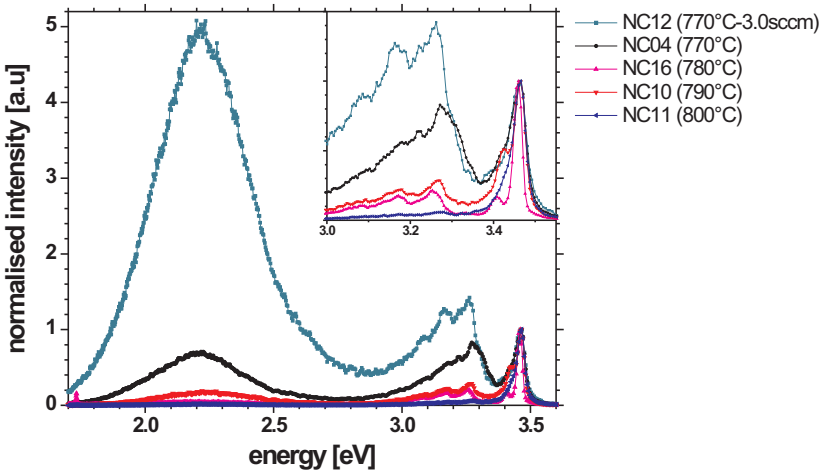

Figure 6.19: Overview of all full range PL spectra. The spectra are normalised relative to the DBE peak to compare the relative contributions of the various defect peaks. The inset zooms in on the region near the band edge. With increasing T_{sub}, the YL and the other defect peaks decrease relative to the DBE peak.

The PL spectrum of NC16 grown at 780 °C is comparable to NC10 although the substrate temperature of the latter was 10 °C higher. It has to be noted however, that NC16 was grown for 6 h. The longer growth time can improve the quality of the upper part of the nanowires, which we probe in the PL measurements, because in general the lattice mismatch with the substrate can introduce strain, disorder or defects at the base of the wires. For longer wires,

however, the substrate influence should be reduced. Since the investigated depth in our PL is estimated to be $\approx 100\,\mathrm{nm}$, the measurement is focused on the top of the wires, whereas in CL one probes a much larger volume for typical beam energies. These facts can explain the similar PL spectra of NC16 and NC10.

Zooming into the near band edge region and measuring with higher resolution Fig. 6.20 allows to better distinguish the defect peaks and study their development with substrate temperature. The width of the DBE peak is reduced for NC10 and NC11 compared to NC04. Also the UVL band and its replicas decrease with higher T_{sub}. In NC11 they are not even distinguishable anymore. The Y_4, Y_6 and Y_7 peaks are visible in NC04, but absent in the spectra of NC10 and NC11.

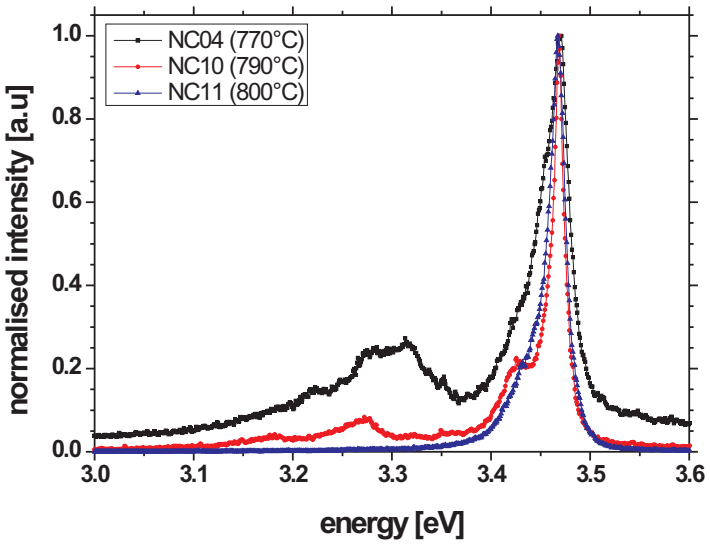

Figure 6.20: Near band edge PL spectra of NC04, NC10, NC11 confirming the reduction of the defect bands with increasing T_{sub}.

Discussion

The SEM images of the samples corresponding to the PL spectra in Fig. 6.19 presented in Fig. 6.15 and Fig. 6.21 can help to explain the different spectra depending on T_{sub} or Φ_N. The GaN nanowires in NC12 grown with a lower nitrogen flux and hence a higher effective III/V-ratio have a tendency to coalesce. Although neither SEM-image in Fig. 6.21 gives a clear indication of structural defects in the regions where wires have grown together, an investigation at the atomic scale could of course give a quite different picture. Well-defined facets are clearly visible, however, and their orientation is predominantly in one of six hexagonal directions confirming that there is an epitaxial relation between the nanowires and the substrate. NC16 was grown for a longer time than the others and therefore the amount of coalescence is even higher than in NC12 (cf. Fig. 6.15). However the wire agglomerates show different morphologies. In NC12 they consist of a few larger coalesced thicker wires, whereas in NC16

a lot of thinner wires have grouped to irregular shapes. Of course this can be expected for longer growth times, since due to a small lateral growth the space between wires continuously decreases. NC16, however has a very low YL and also the UVL is considerably lower than the DBE, which suggests that the III-V ratio rather than the grain boundaries caused by coalescence of wires could be the origin of the YL and the UVL. This points to a bulk character of these defects and since both decrease by lowering the III-V ratio (i.e. for increased Φ_{N} or higher $\mathrm{T_{sub}}$), N-vacancies are a possible candidate for the defect. Although we are growing under N-rich conditions on a macroscopic scale, there can be Ga-rich conditions locally. N-vacancies act as a donor and substitutionals like Si_N and C_N are shallow acceptors [153]. Increasing the N-content can thus reduce the donor and acceptor concentration and lead to a lower DAP transition (UVL band) as well as a lower YL.

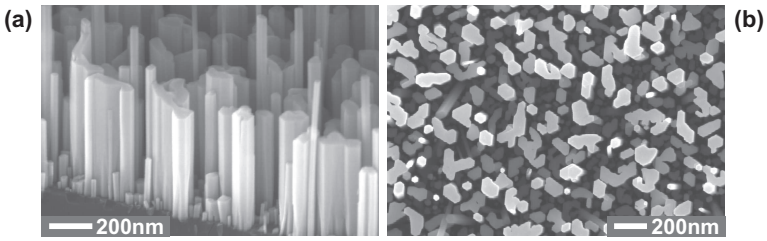

Figure 6.21: (a) Side- and (b) top-view SEM images of NC12. Both images show that the wires tend to coalescence. The resulting structures can have a wire-like or broadened irregular shape depending on the relative position of the coalescing wires. Well-defined facets are clearly visible, however, and their orientation is predominantly in one of six hexagonal directions confirming that there is an epitaxial relation between the nanowires and the substrate.

The PL spectra are deconvoluted with a peak fitting programme, Peakfit, in a similar fashion as performed for the CL spectra. The spectra of the full measurement range shows that the peak position of the near band edge peak of all samples is approximately the same ($3.463 \pm 0.002\,\mathrm{eV}$). The measurements at higher resolution (with a grating of 300 lines per mm) show that the peak is actually a superposition of a DBE peak at $3.469 \pm 0.001\,\mathrm{eV}$ and another peak at $3.456 \pm 0.002\,\mathrm{eV}$, which was assigned to an acceptor bound exciton (ABE) in [154] and to Ga-interstitials in [8]. So despite different growth temperatures and different column lengths, the position of the DBE peak is the same in all samples. The transition is very sensitive to strain and therefore it is expected to shift if any strain is present. As mentioned the wires grown at different $\mathrm{T_{sub}}$ have different lengths and if there is any strain one would expect that longer wires show a larger amount of strain relaxation, but the peak position is the same (within the experimental error). This suggests that all wires investigated by PL are strain-free, or at least the upper part of them.

A fit of the higher resolution spectra of NC04, NC10 and NC11 confirms the presence of $\mathrm{Y_4}$, $\mathrm{Y_6}$ and $\mathrm{Y_7}$ in NC04, but in NC10 there is only a faint $\mathrm{Y_4}$ signal. In NC11 they are absent. Also the $\mathrm{Y_2}$ peak area reduces with increasing $\mathrm{T_{sub}}$ and this suggests a better surface quality, because $\mathrm{Y_2}, \mathrm{Y_4}$ and $\mathrm{Y_6}$ are attributed to excitons bound to surface defects and a surface DAP, respectively.

Conclusion

In summary, the PL results confirm the conclusions from the CL measurements that the quality of the wires grown at higher substrate temperature increases. The higher resolution of the PL measurements allows an easier determination of the positions of peaks which are hidden in the CL spectra and had to be determined by a deconvolution. A decrease of the III-V ratio by increasing T_{sub} or increasing Φ_N leads to a higher PL signal, which can be explained by a lower number of N vacancies or less substitutionals like Si_N and C_N.

6.4 Transmission electron microscopy

Abstract

Transmission electron microscopes (TEM) typically operate at $200 - 300\,\mathrm{keV}$ allowing a resolution of 1-2 Å. This is much better than typical scanning electron microscopes (SEM) and ideally suited to study very small dimensions. Since a TEM measures in transmission geometry the samples have to be very thin (typically below 100 nm), so only thinner nanowires can be measured without thinning of the sample.

In this section the crystalline structure and quality of the GaN nanowires is studied as well as interfaces with the substrate, other materials and the surrounding environment. The study of heterostructures also allows to quantify the lateral growth mentioned in Sec. 5.2.

Experimental Details

TEM measurements have been performed at the Brookhaven National Laboratory[1] in a JEOL JEM 3000F field-emission TEM equipped with a Gatan 652 high-temperature sample holder. They covered the temperature range between room temperature and 500 °C at pressures of $2 \times 10^{-7}\,\mathrm{mbar}$. Low electron-irradiation intensities have been used to prevent any uncontrolled electron-beam-induced structural changes. The accelerating voltage was set to 300 keV.

Different kinds of samples were analysed. To study the crystal structure, the wire/substrate interface, the sidewall as well as the top morphology plain GaN wires deposited on Si(111) were used (NC113: $\Phi_{Ga} = 3 \times 10^{-8}\,\mathrm{mbar}$, $P_{RF} = 500\,\mathrm{W}$, $\Phi_{N_2} = 4.0\,\mathrm{sccm}$, $T_{sub} = 785\,^\circ\mathrm{C}$ and deposition time = 45 min). One sample was capped with a 5 nm Fe layer in-situ by electron beam evaporation at room temperature to protect the surface from ambient atmosphere during transport. GaN nanowires with AlN barriers have been employed to study interface sharpness and lateral growth of the wires (the layer structure of the wires is described in more detail in Fig. 6.25).

Samples have been prepared in two ways. The first one is to remove the nanowires from their native substrate and transfer them on a lacey carbon TEM grid. The amorphous carbon film has small holes, smaller than the pitch of the grid to allow smaller nanowires to be investigated. The nanowires should not be too thick in this case. The second method is the conventional way of thinning the as-grown sample by chemical etching and ion-milling to a

[1] E. Sutter, Center for Functional Nanomaterials, Brookhaven National Laboratory, Upton, New York 11973

thickness appropriate for transmission measurements ($10 - 100\,\mathrm{nm}$). This allows to investigate the interface between the wires and the substrate. The nanowires have to be protected against the thinning process and for this purpose they are covered with a PECVD[2] grown SiO_2 layer (cf. Sec. 9.2).

Experimental Results

The crystal structure of GaN nanowires is studied in Fig. 6.22. (a),(c) show cross-sections of sample NC113 covered with PECVD grown SiO_2, after thinning to a thickness appropriate for TEM. The wire in (c) has no horizontal stripes originating from different diffraction contrast, which would point to stacking faults or other defects. Also the higher resolution image in (a) is free of defects and the surface is very smooth on both sides. The wire diameter is constant over its length in (a) and (c). The diffraction pattern in (b) is a FFT[3] of a part of a high-resolution image like in (a) and has sharp spots with a pattern that corresponds to wurtzitic GaN. The images and the diffraction pattern thus evidence the high quality of the wires.

In Fig. 6.22 (d) a GaN wire is shown, which is still attached to the substrate and has grown under an angle of $\approx 55°$ relative to the substrate surface. Thus it is tilted at an angle of $\approx 35°$ relative to the substrate normal (Si$\langle 111\rangle$) to which most wires grow parallel. The tilted direction corresponds to the direction $\langle 110\rangle$ (and equivalent directions) in the Si crystal, which has a calculated value of 35.26° relative to Si$\langle 111\rangle$. The tilted wire also has the wurtzite structure and grows in the $\langle 0001\rangle$ direction of GaN.

The TEM images in Fig. 6.23 illustrate the interface between GaN nanowires and the Si substrate. A thin layer of approximately 3 nm can be observed in all images covering the whole interface and is also present underneath the nanowires with the same thickness. This suggests that it is formed before the wires grow and is not related to the deposition of the SiO_2 layer. In most images this layer is amorphous like in (a) and (b). It has been suggested in literature [92, 158] that this is an amorphous Si_xN_y layer. However, in some images it is crystalline like in (c) and (d). In either case the GaN wires on top of the wetting layer are single-crystalline. The crystal structure of the wetting layer in (c) and (d) resembles the substrate structure and has the same lattice spacing of approximately 3.1 ± 0.1 Å perpendicular to the surface, but does not look like the GaN wires, so a GaN wetting layer can be ruled out. The lattice spacing agrees with the theoretical lattice spacing for Si(111) of 3.134 Å. In addition there is no appreciable GaN-related luminescence coming from the regions between the wires (cf. Sec. 6.3.1).

Fig. 6.24 shows a GaN nanowire with a diameter of 80 nm capped in-situ with an Fe layer for protection of the top of the wire against contamination from the ambient. There is a sharp interface between the GaN nanowire and the Fe layer, which is almost atomically smooth. Also the sidewalls of the wires are very smooth. The wire is faceted at the cross section of the wire top and its sidewalls on both sides. The inner part of the wire is free of defects and the lattice planes are clearly resolved. Fe oxidises quickly in ambient atmosphere, but only a

[2]Plasma Enhanced Chemical Vapour Deposition

[3]Fast Fourier Transform

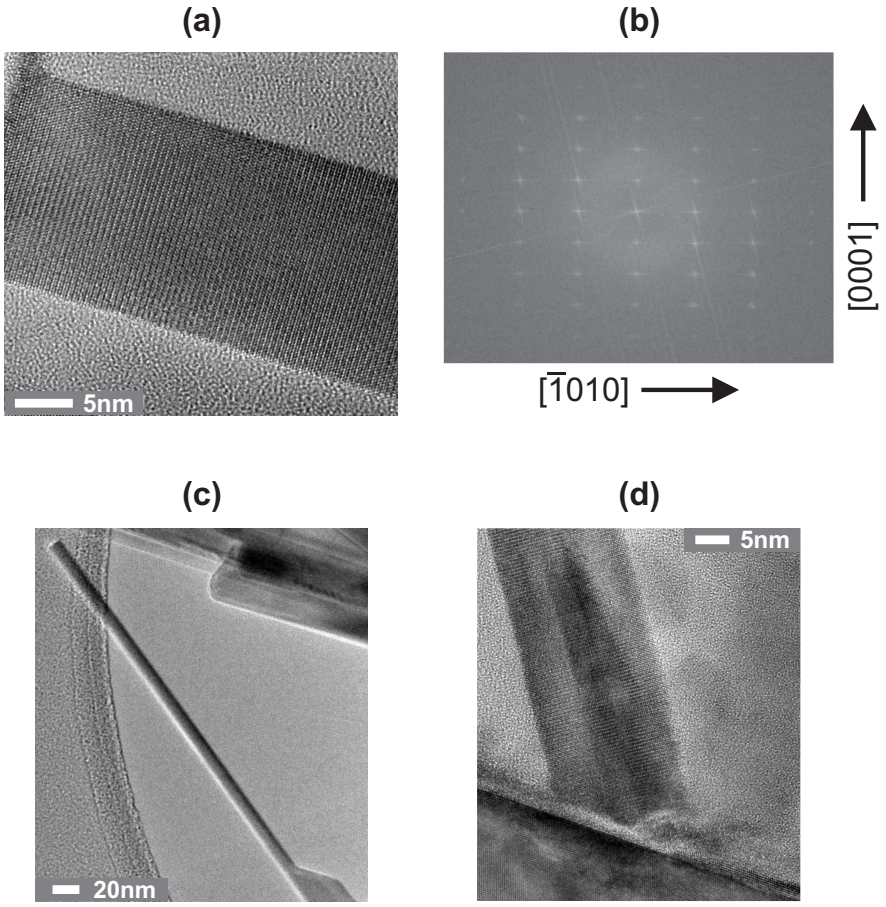

Figure 6.22: (a) High resolution TEM image of a GaN nanowire with a diameter of 18 nm. There are no visible defects or stacking faults and the atomic planes are nicely resolved. The surfaces are very smooth. (b) Diffraction pattern along the $\langle 1\bar{2}10 \rangle$ direction with sharp bright spots and a pattern in agreement with the wurtzite GaN structure. (c) A long thin GaN wire after suffering a diameter reduction by the formation of a facet. The diameter is approximately 12 nm and the length after the tapering process $\approx$ 300 nm. Also for this longer wire no stacking faults are visible. (d) TEM image of a tilted wire relative to the Si substrate (bottom part of the image). The angle amounts to $\approx 55^\circ$ relative to the substrate.

few nm (cf. [159] and references therein).

The growth scheme for a sample with GaN nanowires interrupted by AlN barriers is shown in Fig. 6.25a. Such wires allow to study lateral and vertical growth kinetics as well as interface sharpness. TEM images of the top part of such wires are shown in Fig. 6.25b,c and Fig. 6.26. The image contrast between the AlN and GaN layers is due to the different mass of Ga and Al (mass contrast). Heavy atoms (Ga) interact more with the electrons than light ones (Al) and therefore the contrast is darker for the GaN layers in this bright-field TEM image. The alternation of AlN and GaN layers is not only visible in the axial direction but also laterally,

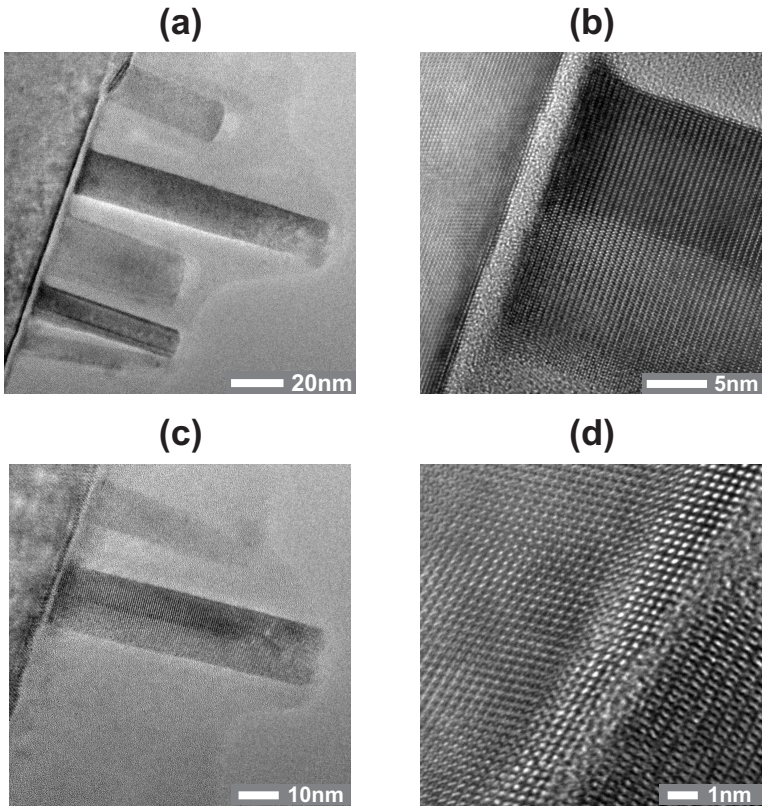

Figure 6.23: The TEM images represent cross sections of GaN nanowires on a Si(111) substrate. The wires were covered with oxide for protection against the thinning process. A thin layer of approximately 3 nm covers the whole substrate and is also present beneath the nanowires. At many places the layer is amorphous like in (a) and (b), but sometimes it has a partial crystalline structure, which resembles the Si substrate, rather then the wurtzite structure of GaN. Some wires also have a pedestal at their base like in the upper part of (b). On the other side of the wire and in (c) it is not apparent. The substrate area underneath the nanowires has no defects.

indicating lateral growth. Energy dispersive spectroscopy (EDS) also gave an Al signal along the whole length of the wire. The thicker AlN barrier in Fig. 6.26 has a faceted side like the GaN wire in Fig. 6.24.

Length and diameter have been determined for some 60 wires from TEM images of the oxide covered sample NC113 (Fig. 6.27). The data scatters a lot with lengths up to 150 nm and diameters between approximately 7 nm and 35 nm. Interestingly no nanowire with a diameter below 7 nm has been found, which suggests there is a lower limit of the nucleation diameter.

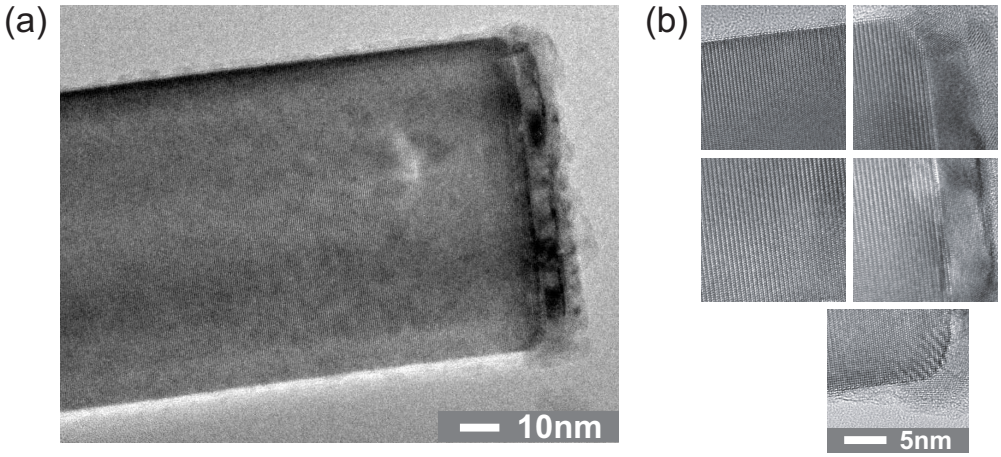

Figure 6.24: GaN nanowire with a 5 nm Fe capping layer. (a) Lower magnification image of the upper part of the wire. On the right hand side the Fe cap can be seen, which is partly oxidised; (b) High resolution images of parts of the wire in (a). The side walls are very smooth as well as the interface. The GaN wire is faceted at the corners.The inner part is free of defects. Note that these images due to the high resolution only cover part of the wire in (a), but they are exemplary for the whole wire.

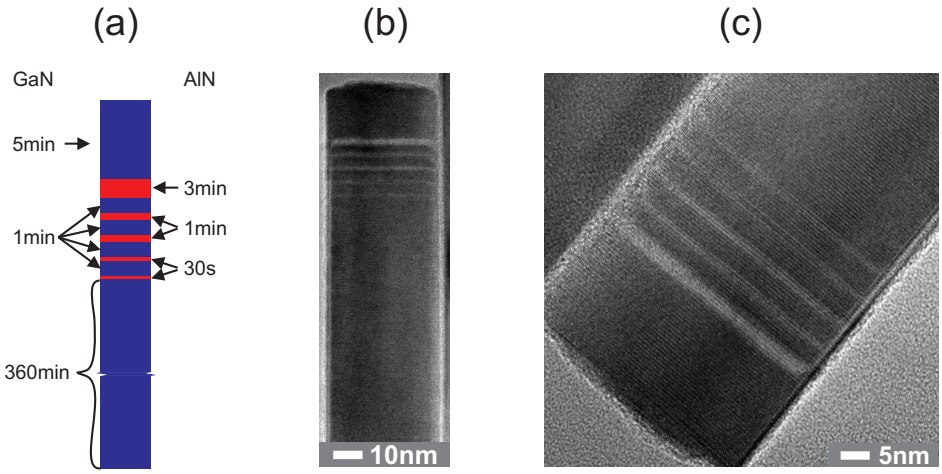

Figure 6.25: (a) Scheme of sample NC168: a GaN nanowire is grown with several AlN barriers of different nominal thickness (30 s, 1 min and 3 min). They are separated by GaN layers; (b) in the upper part of the nanowire the AlN barriers can be distinguished by the brighter contrast; (c) a close-up of the regions with the barriers. At the right side of the wire one can also observe an alternating contrast laterally. A close examination of (b) also shows this.

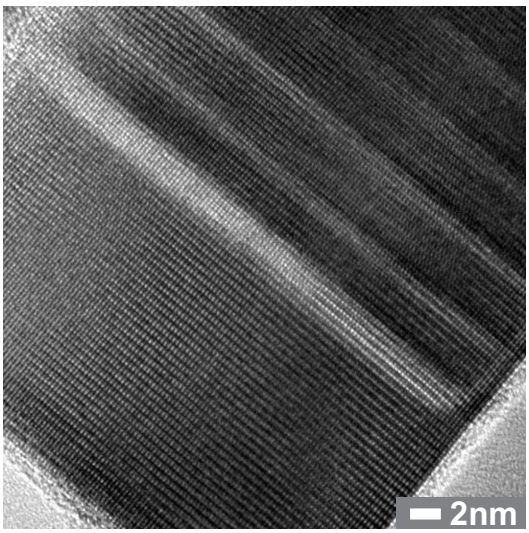

Figure 6.26: High resolution image of the area in Fig. 6.25. The interfaces are sharp and the edge of the thicker AlN barrier is faceted. On the right side of the image one can observe the lateral alternating sequence of AlN and GaN layers. The sidewall surface is atomically smooth.

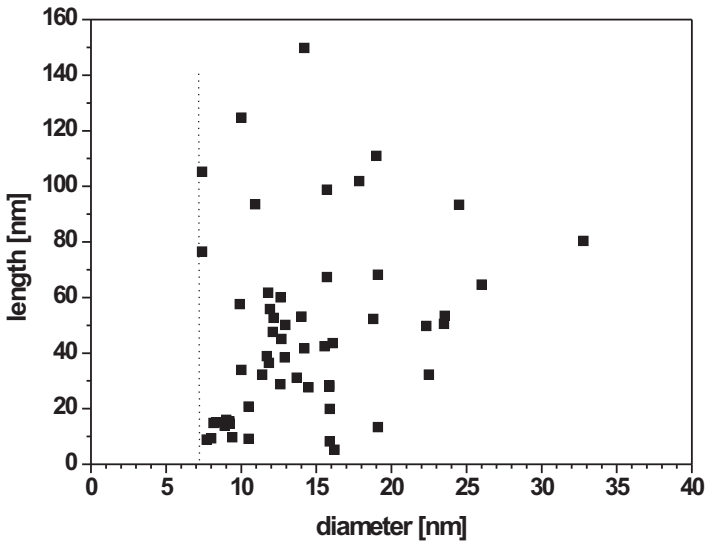

Figure 6.27: Length vs. diameter of GaN nanowires from sample NC113. The data scatters a lot. No wires are observed with a diameter below 7 nm.

Discussion

Fig. 6.22a,b and Fig. 6.24b allow to determine the lattice constants 'a' and 'c' of GaN. The vertical lattice constant 'c' can be determined from the spacing of the lattice planes along the

growth direction. Averaging over many planes gives a value of 5.18 ± 0.01 Å, which agrees well with the literature value of $c = 5.185$ Å (cf. Chapter 2). The lattice constant 'a' can be determined from the ratio of the lattice spacings in the reciprocal lattice (Fig. 6.22b). Note that distances in the reciprocal lattice are inversely proportional to the distances in real space. Hence if g_a and g_c denote the lattice spacings in reciprocal space, then $g_a : g_c = \frac{1}{a} : \frac{1}{c}$. For $c = 5.18$ Å the horizontal spacing is determined as 2.77 Å. The actual lattice spacing in the direction $\langle \bar{1}010 \rangle$ is $\frac{1}{2}\sqrt{3}a$, which then gives a value of 3.198 ± 0.01 Å for a, which also agrees with the literature value of $a = 3.189$ Å.

Concerning the lattice constant it has to be noted that it depends on strain and since there are no homosubstrates available very thick layers grown by HVPE[4] are usually employed to determine reliable values. Nanowires represent an interesting alternative, because due to the limited lateral size they can relax more easily. The good agreement between the experimental value for the nanowires and the literature value for strain-free GaN is thus expected.

Most wires grow perpendicular to the substrate and all have the wurtzitic phase, which is the thermodynamically stable phase of GaN. For growth of GaN on Si(111) this is expected. The thin amorphous layer does not seem to destroy the epitaxial relation. This is also evidenced by the specific directions in which tilted wires grow (and not just a random one): the wire in Fig. 6.22d grows parallel to Si$\langle 110 \rangle$. The corresponding lattice plane Si(110) is, apart from Si(111), one of the most densely packed planes. Most nanowires favour growth in this direction [75]. The dense packing leads to lower surface-to-volume ratios and thus minimisation of surface energy, which can be the reason for the anisotropic growth suggested by Kwon (cf. Sec. 5.2).

The observations regarding the thin interface layer are consistent with nitridation of the Si substrate. Surface nitridation is a process similar to thermal oxidation of Si, which starts quickly and then the speed reduces because the oxygen atoms (in our case nitrogen) have to diffuse through the oxidised (nitridated) layer. The thickness is limited by the diffusion length and this explains the homogeneous thickness of the layer over the sample. Wires which form early can prevent a further nitridation and therefore the amorphous layer is thinner. The tilted wires usually form at the beginning of the growth and wires which nucleate later on are mostly perpendicular to the substrate. The nitridation can mask steps or facets in the substrate, which can lead to other growth directions and thus the tilting is usually observed for low nucleation times.

The Si substrate in Fig. 6.23 has no visible defects whether underneath nanowires nor in the area in between them. This indicates that the wires do not induce strain in the substrate in contrast to what has been observed for MBE grown Si nanowires [54]. The amorphous wetting layer probably helps to reduce much of the strain of the GaN/Si system.

The smooth sidewall surfaces and the faceted top of the wires fits to the model of preferential nucleation at the top of the wire. As predicted by Frank (cf. Sec. 3.2.1) nucleation and thus growth is slow on perfect two-dimensional surfaces whereas the nucleation at steps is expected to be high. The slow surface diffusion on the polar top surface under nitrogen-rich conditions effectively traps the adatoms, such that it is more probable to get incorporated and also the density of this surface is high. The pedestal at the base of some wires could

[4] Hydride Vapour Phase Epitaxy

promote lateral growth, because it also offers a stepped surface. The presence or absence of such a pedestal then leads to different lateral growth rates.

The sharp interfaces observed in Fig. 6.24, Fig. 6.25 and Fig. 6.26 support the conclusion of Sec. 5.3, that the nanowire growth is not related to a VLS-like mechanism with a Ga droplet at the top of the wire. A droplet would result in a memory effect of the growth species and broaden the interfaces. This is not in agreement with the abrupt contrast change in the TEM images.

The images in Fig. 6.25 and Fig. 6.26 allow to determine the axial and lateral growth rates of the AlN and GaN sections. For the AlN barriers they amount to approximately 0.8 nm/min and 0.2 nm/min respectively, whereas for GaN values of 3.8 nm/min and 0.15 nm/min are obtained. It has to be noted, that the images would have to be compared to extensive theoretical calculations and even higher resolution images are necessary to determine the exact positions of the atoms. However, the current calculations allow to obtain estimations and to compare AlN and GaN. Note that Φ_{Ga} was six times higher than Φ_{Al} (3×10^{-8} mbar vs. 5×10^{-9} mbar) for the grown layers and therefore a lower growth rate of AlN could be expected. Since the desorption of Ga is higher than for Al, the effective ratio between the two fluxes is a bit lower. The lateral growth of AlN on the other hand is higher than for GaN despite the much lower Φ_{Al}. The ratios between axial and lateral growth are approximately 4 : 1 for AlN and 25 : 1 for GaN indicating the enhanced tendency of AlN for lateral growth. This explains why it is difficult to grow AlN nanowires by our catalyst-free approach and why there are no reports of AlN nanowires in literature.

The data in Fig. 6.27 suggests that there is a critical diameter of 7 nm for the formation of nanowires, because no wires are observed which have a smaller diameter. Such a critical diameter was also suggested by the investigations in Sec. 5.2 (although it was difficult to determine a value), but since the resolution in TEM is significantly better than in SEM, the current results are much more reliable. Two wires have diameters close to the critical one, but lengths of 75 nm and 105 nm, which means that the lateral growth in these wires is negligible. The longest wires seem to show a $1/d$ behaviour like observed in Sec. 5.2 for long deposition times, but the number of points is too low and the uncertainty in the nucleation time too large, to draw any conclusion. Up to approximately 16 nm nanowires with very short lengths are observed, which suggests, that there are different nucleation diameters between approximately 7 nm and 16 nm.

Conclusion

In general the TEM images confirm the high quality of the GaN nanowires and no extended defects are present. The measurements agree with the results of Sec. 5.2 which suggests a nucleation diameter. The upper limit is determined to be approximately 7 nm. Radial growth is quantified for GaN and AlN and is significantly larger for GaN. For AlN the ratio between axial and lateral growth is only 4 : 1, which explains why it is difficult to grow AlN nanowires. Sharp heterointerfaces are consistent with the absence of a droplet, which was already suggested in Sec. 5.3. Despite a thin wetting layer of approximately 3 nm, which we suggest is an amorphous $\mathrm{Si_xN_y}$ layer, the wires grow in well-defined directions governed by the substrate.

Chapter 7

Characterisation of doped GaN nanowires

7.1 Introduction

The major advantage of semiconductors in comparison to for instance metals lies in the possibility to dope the semiconductor with a certain amount of impurity elements. This allows to tune the electrical properties of the material to obtain the behaviour which is required by the envisaged application. A good control of the amount of doping species is essential and consists of two tasks. The first task is to build the required amount of doping elements into the layer of interest, typically during growth. The nominal quantity of dopants can however differ considerably from the real number of atoms actually present in the layer, depending on the growth process and parameters. Therefore the second task, which is to determine the amount of dopants actually build into the layer, is very important. Moreover, the dopants inside the layer do not all behave in the same way, i.e. they can occupy different positions in the crystal and therefore differently contribute to the electrical behaviour of the material. Typically an activation step is necessary to activate the dopants for electrical conduction.

There are several investigation techniques to study the composition of a material and its electrical behaviour. For compact layers, Hall measurements are well-established to determine the type and level of doping. For nanowires, however, it is very difficult to produce a contact configuration suitable for Hall measurements with the current status of e-beam lithography. Especially for wires with sub-100 nm diameters there is not enough space to fabricate good contacts to the sides of the wires. The large influence of the surface and the resulting depletion/accumulation layer can also complicate the interpretation of the measurements.

Optical measurements like cathodoluminescence (CL) can also give information about the incorporation of impurity elements. The spectra can show additional bands related to the impurity and other defects like vacancies can be compensated by the impurity, which reduces the luminescence related to the vacancy. A major advantage of optical methods is the non-destructive nature of the optical techniques.

In the next section the influence of Si and Mg on the morphology of GaN nanowires is studied. Then, CL is employed to investigate the optical properties of the doped samples.

7.2 Morphology of doped GaN nanowires

Abstract

In this section the influence of adding Si or Mg to the growing GaN nanowires is investigated with respect to their morphology. Mg is reported to be a surfactant for GaN growth [160], which means that it enhances the surface mobility and promotes two-dimensional growth. For Si an anti-surfactant behaviour has been predicted under N-rich conditions [161].

Experimental Details

The growth parameters of the Si- and Mg-doped samples studied in this section are summarised in Tab. 7.1 and Tab. 7.2. The other parameters: $\Phi_{Ga} = 3.0 \times 10^{-8}$ mbar, $P_{RF} = 500$ W, $\Phi_{N_2} = 4.0$ sccm and $T_{sub} = 785\,^{\circ}$C are the same for all samples.

Experimental Results

A series of GaN nanowire samples doped with Si is presented in Fig. 7.1. A nominally undoped sample is shown as a reference (Fig. 7.1a). The morphology as well as the density of the wires changes with Φ_{Si}. A higher Si flux reduces the density of the wires as can be seen in the images in Fig. 7.1d,e,f. The amount of wires which are slightly tilted also increases. In addition the wires broaden from bottom to top. The ratio between the diameter at the top of the wires and the base is approximately 6 for the highest Φ_{Si} in sample NC62 (cf. Tab. 7.1), whereas it is close to one for low Si doping in NC158 (Fig. 7.1b). Its density is also comparable to

Table 7.1: Growth parameters of Si-doped GaN nanowire samples used to study the influence of Φ_{Si} on the wire morphology. The parameters $\Phi_{Ga} = 3.0 \times 10^{-8}$ mbar, $P_{RF} = 500$ W, $P_{RF} = 4.0$ W and $T_{sub} = 785\,^{\circ}$C are fixed. Typical lengths and diameters at the base as well as the top of the wires are also given. The last column presents a typical ratio between the diameter at the top and at the base of the wires. Sample NC69 is grown in two stages. The first stage of 60 min is grown without Si doping and the second one of 180 min with the same Φ_{Si} as NC62.

Sample	Φ_{Si} [$\times 10^{-9}$ mbar]	time [min]	length [µm]	d_{bottom} [nm]	d_{top} [nm]	ratio top/bottom
NC061	-	240	0.75-0.90	30-70	30-70	1
NC158	0.6	240	0.80-0.85	35-90	35-90	1
NC133	1.0	120	0.35-0.45	40-50	70-90	1.8
NC067	2.0	240	0.55-0.80	40-60	180-210	4
NC068	4.0	240	1.0-1.3	40-90	300-375	6
NC062	6.0	240	0.95-1.3	40-100	325-375	6
NC069	-/6.0	60/180	0.60-0.75	25-55	140-200	4

Table 7.2: Growth parameters of Mg-doped GaN nanowire samples used to study the influence of Φ_{Mg} on the wire morphology. The parameters $\Phi_{Ga} = 3.0 \times 10^{-8}$ mbar, $P_{RF} = 500$ W, $P_{RF} = 4.0$ W and $T_{sub} = 785\,^{\circ}$C are fixed.

Sample	Φ_{Mg} [$\times 10^{-9}$ mbar]	time [min]	length [µm]
NC160	0.5	240	0.55-0.85
NC131	1.5	120	0.25-0.30

the undoped sample in Fig. 7.1a. Electrical measurements show however, that the amount of Si is enough to change the conductance of the wire despite no apparent change to the wire morphology.

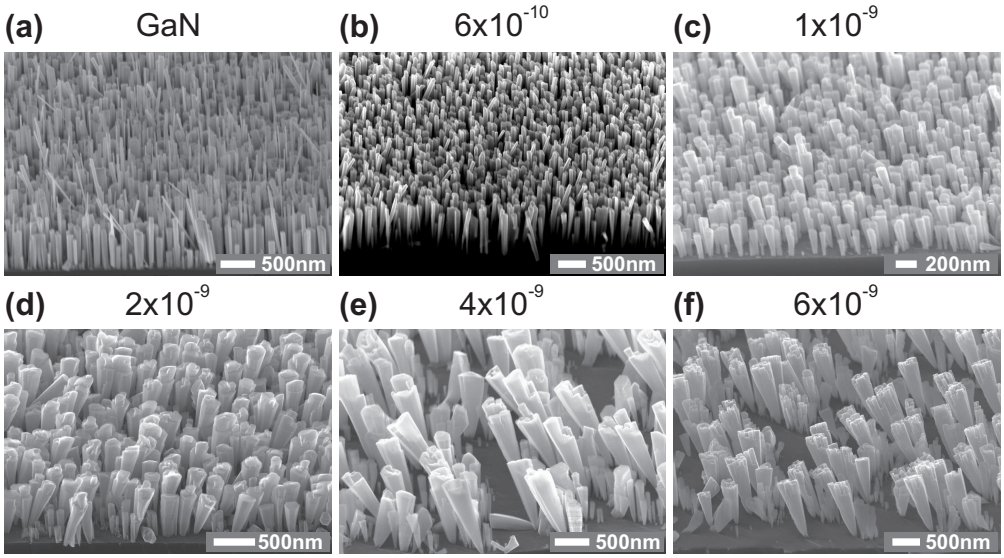

Figure 7.1: SEM images of GaN nanowire samples doped with different Si fluxes (b-f). A nominally undoped sample is shown in (a) as a reference. By increasing Φ_{Si} the density of the nanowires is reduced. In addition the wires broaden towards the top and this effect is enhanced by increasing Φ_{Si}. The number of tilted wires also increases with Φ_{Si}. For larger Si fluxes (d-f) new nanowires start to grow at the top of the wires.

A close look at the interface with the substrate in Fig. 7.1(c-f) shows another effect of the Si doping. With increasing Φ_{Si} a thin wetting layer forms between the wires. This is easier observed in Fig. 7.2a, which is a zoom of the interface in sample NC62 (Fig. 7.1f). In this image the wetting layer is approximately 40 nm. For lower Φ_{Si} (Fig. 7.1d,e), the wetting layer is thinner and it is difficult to determine the thickness with the limited resolution of the SEM. In Fig. 7.1c, the atomic steps of the Si(111) substrate is still visible indicating that the

wetting layer is very thin if at all present. More sophisticated methods like TEM are required to investigate this further.

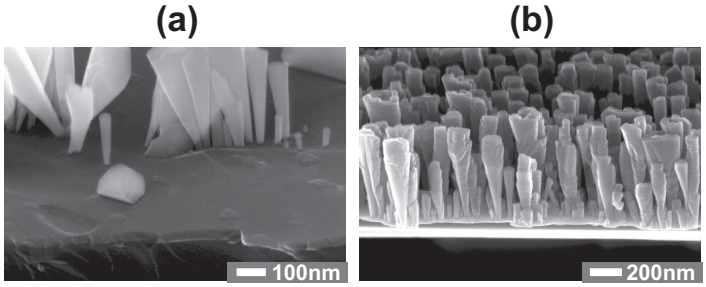

Figure 7.2: (a) High magnification SEM image of the interface with the substrate for sample NC62 (cf. Fig. 7.1f), which shows the presence of a thin wetting layer of approximately 40 nm. (b) A Si doped GaN nanowire sample grown with the same Si flux as NC62, but the first hour of growth was performed without Si-doping. The wires are aligned perpendicular to the substrate and the density is similar to the undoped sample in Fig. 7.1a. The broadening, however, is similar to the samples with a high Φ_{Si}.

Apart from the broadening, the top of the higher doped GaN nanowires also often displays the formation of several new wire like structures, which also evidence a hexagonal symmetry. In general the Si-doped wires exhibit clear hexagonal facets, although the surface of the wires with lower Φ_{Si} is smoother.

The samples with high Si-doping have a lower density and more tilted wires. For nominally undoped GaN nanowires like in sample NC61 (Fig. 7.1a) the nanowire density increases up to approximately 1 h (cf. Sec. 5.2) and the major part of the wires also grows perpendicular to the substrate. Therefore a sample has been grown in which GaN nanowires are nucleated without Si-doping and after 1 h, when the nucleation stage is presumed to be finished, the Si doping is started with the same Φ_{Si} as in NC62. The sample morphology is presented in Fig. 7.2b. The density of the wires is considerably higher than in NC62 and comparable to the nominally undoped sample NC61. Also almost all the wires are perpendicular to the substrate. Otherwise the morphology has not changed. The wetting layer is also present in this sample. The ratio between the top and bottom part is lower, but this is related to the shorter deposition time of the Si doped part of the wire. The number of new wire structures at the top of the wires is also reduced. This is due to the smaller diameter of the wires, because the images in Fig. 7.1 show, that the probability to observe these structures is higher in thicker wires.

In conclusion, a separate nucleation stage can thus help to control the density and the alignment to the substrate of the nanowires for higher Si fluxes.

Compared to Si-doping, the influence of Mg-doping on the morphology of GaN nanowires is different as is evidenced in Fig. 7.3. A small Φ_{Mg} (NC160) increases the tendency of the wires to coalesce (Fig. 7.3a,b). Otherwise the morphology does not change. The wire diameter is constant over its length and does not broaden or taper. A further increase of Φ_{Mg} (NC131) leads to more coalescence already after 2 h of growth. The density is very high, but hexagonal

facets can still be distinguished, which is also the case for the first sample with lower Mg doping. However, the thin long wires usually present in undoped GaN nanowires (cf. Sec. 5.2 or Sec. 6.1) and also visible in NC160 (Fig. 7.3a) are absent in NC131 (Fig. 7.3c). The length distribution of the nanowires is also smaller. These facts can be understood with the help of Fig. 5.7a in Sec. 5.2 p. 37. The coalescence leads to thicker wires for which the diffusion channel plays a minor role and therefore growth by direct impingement is the main contribution. In Sec. 5.2 it is shown that growth by impingement is diameter-independent and therefore the lengths of the nanowires are similar in Fig. 7.3c despite a distribution of diameters.

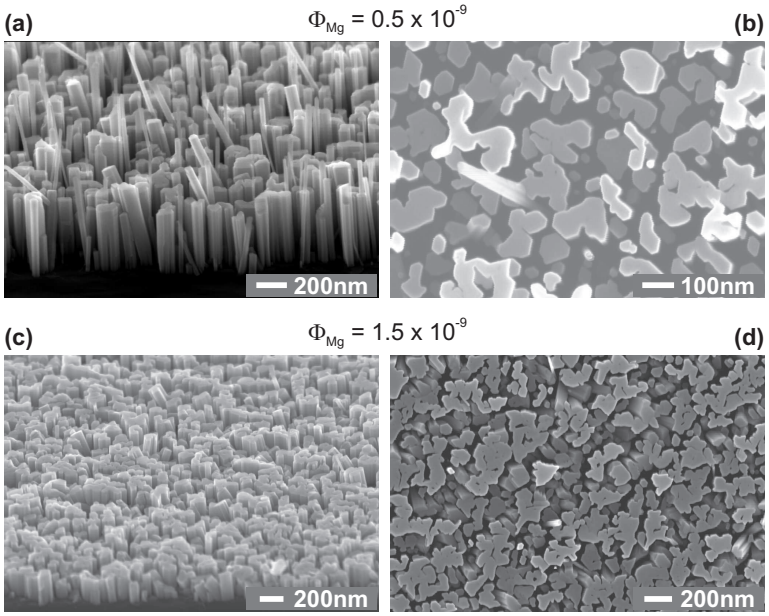

Figure 7.3: The SEM images in (a) and (b) of GaN nanowires doped with a small amount of Mg show that there is more coalescence than in nominally undoped GaN nanowires (cf. Fig. 7.1a). Clear hexagonal facets are visible, however. An increase of the Mg flux (c,d) enhances the amount of coalescence. The wires still have hexagonal facets, but they group into larger irregular shaped clusters.

Discussion

The influence of Si and Mg on the morphology of GaN nanowires are in agreement with the expected anti-surfactant and surfactant behaviour reported in literature [160, 161]. Mg as a surfactant enhances lateral growth, which in our case leads to quicker coalescence of the nanowires. The reduced surface mobility of adatoms due to the N-rich conditions is (partially) compensated by the enhancement caused by Mg. The mobility on top of the wires is also enhanced, which effectively reduces the behaviour of an active sink of the top of the wire since adatoms can more easily diffuse away. Si, on the other hand as an antisurfactant, reduces the surface mobility and this leads to the nucleation of new clusters on top of thicker wires

rather than the formation of a smooth growth front. Excess Si on the substrate surface forms a wetting layer of probably Si_xN_y, which covers new GaN nuclei and therefore the density of the GaN nanowires is reduced.

The reduced surface diffusivity also disturbs the adatom equilibrium between the substrate, the nanowire sidewalls and the top of the wires: The bottom part of some Si-doped wires has a uniform thickness whereas others broaden right from the base. Especially the shorter ones which are masked by the tall and thick wires have a more uniform diameter. Growth as a result of direct impingement seems to be the main mechanism driving the growth when the Si-flux is added and diffusion along the sides of the wires can be hampered by the antisurfactant Si. This can also result in an increased lateral growth, because the adatoms do not preferentially diffuse to the top of the wire anymore.

Conclusion

GaN nanowire samples have been grown with Si- and Mg-doping to study the influence on the morphology. Mg acts as a surfactant and enhances lateral growth leading to coalescence of the wires. Si, on the other hand, acts as an antisurfactant and reduces the surface mobility. For higher Si fluxes, this leads to broadening of the wires towards the top and nucleation of new small wires at the growth front. In addition a wetting layer forms, which can cover new GaN nuclei and therefore the density of the GaN nanowires is reduced. Φ_{Si} has to be chosen carefully to obtain wires with a uniform diameter and high density.

7.3 Cathodoluminescence of doped GaN nanowires

Introduction

Doping species which are supplied during growth can, instead of being incorporated in the growing layer, for instance also segregate at the surface. This is predicted for Si under N-rich conditions [161] and also surface-segregation of Mg has been reported [162]. Lower substrate temperatures (typically $650 - 700\,^{\circ}C$ for MBE growth [162]) favour Mg incorporation. However, growth of GaN nanowires is typically performed at higher T_{sub} (cf. Sec. 6.1) and the quality improves with T_{sub} (cf. Sec. 6.3.1 and Sec. 6.3.2). On the other hand Mg incorporation increases under N-rich conditions [163], which is favourable for GaN nanowire growth.

In addition theoretical calculations predict difficulties in doping nanowires due to a 'self-purification' effect [111, 164]. The formation energy of defects in nanocrystals increases as the size of the nanocrystals decreases and impurities tend to segregate at the surface. However, an anion-rich environment can increase the doping probability [164] and thus N-rich growth conditions like in GaN nanowire growth are favourable.

In the previous section it is shown that the morphology of the GaN nanowires is influenced by the doping species. In this section CL is employed to study if the dopants change the luminescence of the nanowires, which would indicate an incorporation of the dopants in the nanowire crystal.

Experimental Details

The same CL setup as employed in Sec. 6.3.1 is used to characterise doped GaN nanowire samples. Growth parameters of the samples presented in this section (NC11, NC131 and NC133) are given in Tab. 6.3, Tab. 7.1 and Tab. 7.2. Sample NC133 is moderately doped and shows a slight increase of its diameter from bottom to top (cf. Sec. 7.2).

Experimental Results

The CL spectra of three GaN nanowire samples in Fig. 7.4 show the influence of dopant species on the optical behaviour of the nanowires. The undoped (NC11) and Si-doped (NC133) spectra are quite similar, but the Mg-doped sample (NC131) has a very different spectrum. The position of the donor-bound-exciton (DBE) (cf. Sec. 6.3.1) is the same for the undoped and Si-doped sample at $\approx 3.48\,\mathrm{eV}$. Only the peak width is increased by the Si-doping. Despite a slightly lower T_{sub} (785 °C vs. 800 °C) the YL in NC133 is the same or even lower than for the undoped sample. Anyhow, the peak intensity is very low in both samples.

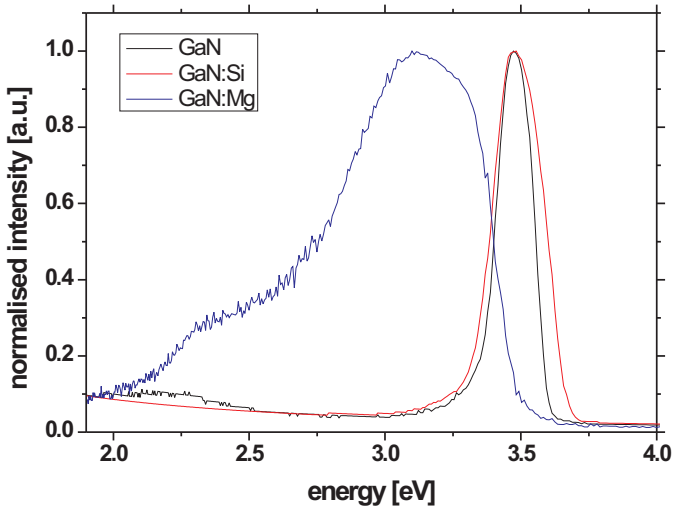

Figure 7.4: CL spectra of an undoped (NC11), Si-doped (NC133) and Mg-doped (NC131) GaN nanowire sample recorded at 10 K. The spectra of the undoped and Si-doped sample are quite similar. The peak position of the DBE peak is the same at $\approx 3.48\,\mathrm{eV}$. The high-energy tail of the Si-doped sample drops of more slowly resulting in a broader peak. The YL in the Si-doped sample is negligible just as for the undoped sample. The spectrum of the Mg-doped sample is very different and the near band edge peak is only a faint shoulder in the broad peak centred at $\approx 3.1 - 3.2\,\mathrm{eV}$. The broad peak is a superposition of several Mg related defect bands [153].

Studies of the optical behaviour of Mg-doped GaN show that Mg leads to the formation of several bands in the optical spectrum of GaN ([153,165,166]). A similar spectrum is observed in Fig. 7.4 for the Mg-doped sample. The near band edge peak is quenched and only visible as

a faint shoulder in the high energy tail of the broad peak. The broad peak is a superposition of the ultra violet luminescence (UVL) band centred around $3.1 - 3.26\,\mathrm{eV}$, the blue band (BL) centred at $\approx 2.7 - 2.8\,\mathrm{eV}$ and probably also some phonon replicas. The resolution of our CL, however, is not high enough to clearly distinguish the different contributions and higher resolution measurements are necessary to reliably deconvolute the spectrum.

Discussion

Si-doping leads to a broader peak. The high energy tail is less steep, which indicates a larger fluctuation of the properties in the nanowires. A Si dopant can slightly change the band structure locally, due to a different doping concentration and this causes a fluctuation of the optical transition energy. The peak position is the same, however, which shows that the Si doping does not introduce strain. The similarity of the Si-doped GaN spectrum with the high-quality undoped GaN sample NC11 despite a slightly lower T_{sub} shows that the Si-doping reduces the defect density of the wires. The reason can be an occupation of a vacancy by a Si atom. The results of Sec. 6.3.1 suggest that these would be N-vacancies.

With the limited resolution of the CL it is difficult to study the optical spectrum of the Mg-doped sample in detail, but the similarity with optical spectra for Mg-doped samples in literature [153, 165, 166] shows that Mg is incorporated in the nanowires and thus has not completely segregated at the surface.

Conclusion

A comparison of CL spectra of a nominally undoped GaN nanowire sample with a Si- and Mg-doped GaN nanowire sample shows that Mg is incorporated in the GaN nanowires despite the relatively high substrate temperature for Mg-doping. The Si-doping does not change the position of the DBE peak and the quality of the GaN is improved. The spectrum is similar to a GaN nanowire sample grown at slightly higher T_{sub}, which should have a better CL spectrum according to Sec. 6.3.1. The Si-doping does however broaden the near band edge peak slightly, which indicates an enhanced fluctuation of the doping concentration compared to an undoped sample.

7.4 Remark concerning electrical measurements of Si-doped nanowires

Even though the results of the previous section shows that Si and Mg are incorporated in the GaN nanowires, it is important to study the electrical behaviour of the nanowires. Wires with uniform diameter are preferred for these studies to facilitate the interpretation. Therefore moderately doped nanowires have been chosen (NC158). Electrical measurements on the Si-doped nanowires performed by Thomas Richter evidence the efficient incorporation of the Si-dopant. The conductivity of the doped nanowires has increased compared to undoped GaN. Electrical measurements on Mg-doped GaN nanowires show that the conductivity changes, but more measurements are necessary to fully investigate their behaviour. The results will be presented in detail in the PhD thesis of Thomas Richter.

Chapter 8

Characterisation of InN nanowires

In Chapter 5 it was shown that nitrogen-rich conditions are required to grow GaN nanowires, which corresponds to a low III-V ratio. In Sec. 8.1 we will see that also for InN nitrogen-rich growth leads to the formation of nanowires. The substrate temperature is a key parameter for InN growth due its low dissociation temperature. The first section of this chapter will therefore focus on the influence of the III-V ratio and T_{sub} on the wire morphology. Then the crystal structure of the nanowires and their epitaxial relation to the substrate is studied by x-ray diffraction. The optical properties of the InN nanowires are investigated with photoluminescence and finally transmission electron microscopy is employed to get more insight into the crystalline quality of the InN nanowires.

8.1 InN nanowire morphology

Abstract

The growth of InN is studied under N-rich conditions to obtain nanowires. This section will focus on the morphology of the wires as a function of the III-V ratio and the substrate temperature T_{sub}. The goal is to obtain wires with a uniform diameter and smooth surfaces, which reduce potential surface scattering. The III-V ratio depends on the substrate temperature as already seen for GaN nanowires (cf. Sec. 6.1), but for InN a higher T_{sub} increases the III-V ratio due to dissociation of InN and desorption of nitrogen. For GaN on the other hand, the III-V ratio decreases with higher T_{sub} due to an increased Ga desorption. Hence the combination of Φ_{In}, Φ_N and T_{sub} determines the actual morphology of the wires and has to be optimised.

Experimental Details

InN nanowires are grown on Si(111) substrates under N-rich conditions. The substrate temperature is chosen between 400 °C and 550 °C and Φ_{In} is set in the range between 2.0×10^{-8} mbar and 1.5×10^{-7} mbar. The plasma cell settings, which determine Φ_N, are kept constant: $P_{RF} = 500$ W and $\Phi_{N_2} = 4.0$ sccm. Deposition times vary between 15 min and 8 h. The growth parameters of the samples presented in this section are summarised in Tab. 8.1.

Table 8.1: Growth parameters and average length of InN nanowires presented in this section. Some samples have wires with two typical lengths and then two values for the average of both kind of wires is given. All samples were grown with the same plasma settings: $P_{RF} = 500\,W$ & $\Phi_{N_2} = 4.0\,sccm$.

Sample	T_{sub} [°C]	Φ_{In} [$\times 10^{-8}$ mbar]	time [min]	length [µm]
NC059	440	3.9	240	0.70
NC032	475	3.9	240	1.20
NC033	525	3.9	240	2.00
NC058	475	2.3	120	0.28
NC056	475	2.8	120	0.37 / 0.60
NC057	475	3.9	120	0.35 / 0.65
NC044	475	7.0	120	0.65 / 1.10
NC045	475	10.0	120	0.90
NC046	475	15.0	120	1.20
NC154	475	2.3	15	0.07
NC058	475	2.3	120	0.28
NC031	475	2.3	240	0.80
NC129	475	4.6	120	0.60 / 0.85
NC141	475	4.6	240	1.60
NC136	475	4.6	480	2.20

Experimental Results

The substrate temperature is an important growth parameter for InN. It necessarily has to be grown at considerably lower substrate temperatures than GaN, because the dissociation temperature of InN, is much lower than the one of GaN. This is due to a weaker chemical bond in InN; the bond energy E_B between the group-III atoms and nitrogen atoms is 2.2 eV for GaN and 1.93 eV for InN [17, 18]. Where GaN is stable up to $\approx 850\,°C$ [146] InN already starts to dissociate around 450 °C [167]. This is the result of a rapidly increasing equilibrium nitrogen vapour pressure. When InN dissociates, the nitrogen evaporates, leaving In atoms behind on the wire surface. This limits the temperature range which can be used for the growth of InN.

A series of samples has been grown to investigate the influence of T_{sub} and to find a suitable temperature range to grow InN and in particular nanowires. Φ_{In} and Φ_N were kept constant and the substrate temperature was chosen within the range of 400 °C to 550 °C. Initial values for Φ_{In} and Φ_N for this series were chosen in the same range as the optimised parameters for GaN nanowire growth, in particular $\Phi_{In} = 3.9 \times 10^{-8}$ mbar, $P_{RF} = 500\,W$ and $\Phi_{N_2} = 4.0\,sccm$. The deposition time was 4 h for all samples.

SEM images of three samples representing a different substrate temperature are shown in Fig. 8.1. The samples were grown at 440 °C (NC59), 475 °C (NC32) and 525 °C (NC33), respectively. At the lowest growth temperature of 440 °C, columnar growth is obtained, but the wire density is high and many wires have coalesced (Fig. 8.1(a)). The tendency goes towards a compact layer. The smoothness of the side and top surface varies from wire to wire. Some wires broaden towards the top and especially thicker wires often have a small dip in the top surface. For other wires the top surface is flat. Part of the wires also show clear hexagonal facets as expected for wurtzite InN.

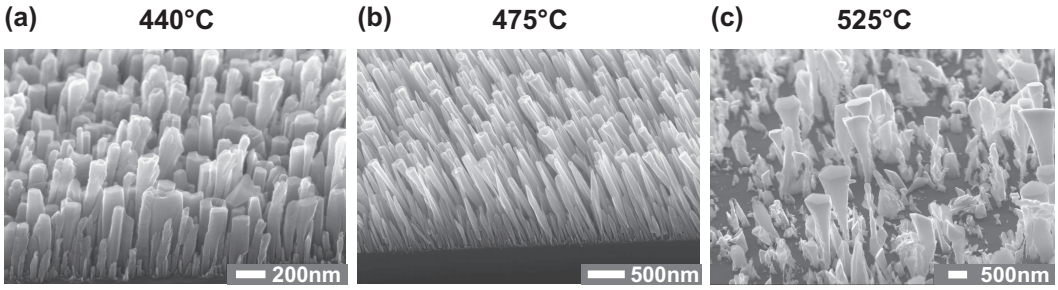

Figure 8.1: The SEM images show the influence of the substrate temperature on the InN nanowire morphology. The wires are grown with the same Φ_{In} and Φ_N for 4 h, but at different T_{sub}. (a) Wires grown at 440 °C (NC59) have a very high density and some have coalesced to thicker wires. (b) At 475 °C (NC32) the density is slightly reduced and the wires are longer. Some wires end in sharp tips, but others broaden toward the top. (c) A substrate temperature of 525 °C (NC33) results in a considerably reduced density and irregular-shaped wires, which broaden with increasing length.

The wires of sample NC32, deposited at an intermediate temperature of 475 °C, which are shown in Fig. 8.1(b) are longer than those of NC59 and the density is lower. In contrast to sample NC59 the amount of coalescence is low. Part of the wires show a broadening towards the top, which is accompanied by a rough top surface. There sometimes is a dip in the centre, especially for the thicker wires and the top looks like a crown. Other wires display an opposite diameter behaviour, a so-called tapering effect, i.e. the wire diameter gradually reduces towards the top, ending in a tip.

Increasing the substrate temperature up to a high value of 525 °C results in a low density of nanowires (Fig. 8.1(c)). The wires are well separated and thus there is no coalescence. A small part of the wires is much longer than the others and has a very nonuniform diameter increasing considerably towards the top. The diameter of the long wires increases from approximately $50 - 70$ nm at the base to well over 500 nm at the top. The top surface looks very flat and it displays the hexagonal shape of the wurtzite InN. There are also a lot of very short structures with a large variety of diameters and shapes and only some of them look like wires. The relatively high substrate temperature and the correspondingly high nitrogen vapour pressure cause a decomposition of the InN.

The images in Fig. 8.1 show that initially a higher T_{sub} improves the formation of InN nanowires, but that the increase is limited by a dissociation of InN. To further optimise the

wires, Φ_{In} has been varied for $T_{sub} = 475\,°C$, which displayed the nicest wires at fixed Φ_{In} and Φ_N. Therefore a series of samples has been grown at this substrate temperature to investigate the influence of Φ_{In} on the wire morphology. Φ_N is kept constant at $P_{RF} = 500\,W$ and $\Phi_{N_2} = 4.0\,sccm$, so changing Φ_{In} directly corresponds to a change of the III-V ratio. The control of the group-III flux is much easier, because the BEP-gauge cannot distinguish between the different atoms, ions and molecules coming from the plasma cell; therefore it is difficult to estimate the effective Φ_N. The deposition time for this series was chosen to be 2 h for each sample.

In Fig. 8.2 SEM images of six samples are shown with Φ_{In} ranging from 2.3×10^{-8} mbar to 1.5×10^{-7} mbar. In all cases a columnar morphology results indicating we are still in the N-rich regime and the increase of the wire length with Φ_{In} (cf. Tab. 8.1) confirms the growth is limited by the available In. In addition the morphology of the wires changes with Φ_{In}.

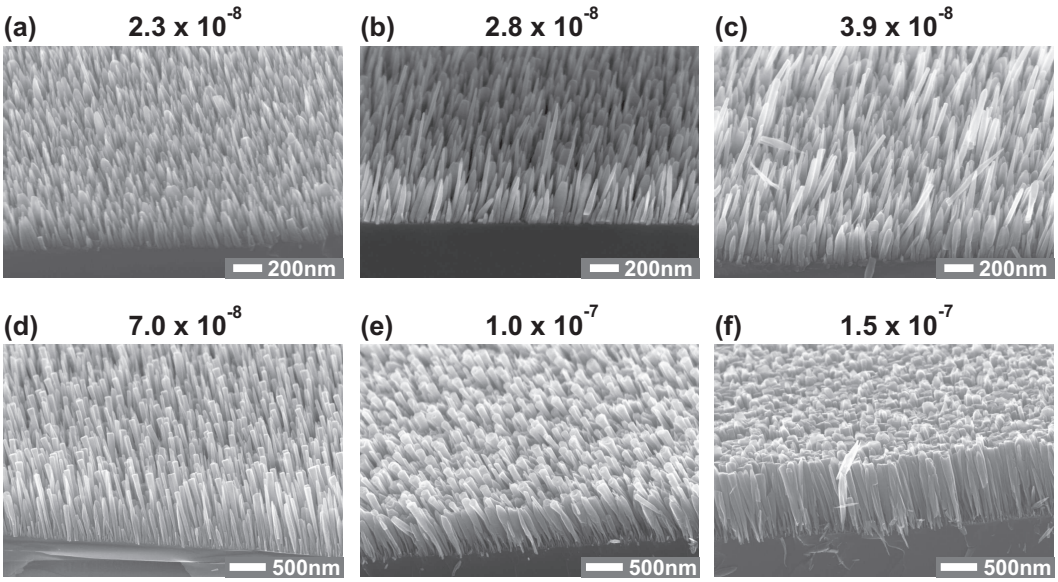

Figure 8.2: SEM images of InN nanowire samples showing the influence of Φ_{In} on the growth of InN nanowires. With increasing Φ_{In} the density and the length of the wires increases and for $\Phi_{In} = 1.5 \times 10^{-7}$ mbar the morphology is a quasi-compact layer of coalesced wires. The top of the wires also changes; for low fluxes the tip tapers, i.e. the diameter reduces into a sharp tip. By increasing Φ_{In} the diameter stays more uniform up to the end and a further increase eventually leads to broadening of the wires at the top. All samples were grown for 2 h at 475 °C with fixed plasma cell settings. The images correspond to the following samples in Tab. 8.1: (a) NC58, (b) NC56, (c) NC57, (d) NC44, (e) NC45 and (f) NC46.

The first sample (NC58, Fig. 8.2(a)) with $\Phi_{In} = 2.3 \times 10^{-8}$ mbar has wires which end in tips due to a tapering effect. Both thicker and thinner wires show this effect, although for thicker wires the tips are more rounded. There is a distribution of lengths, which can be related to different nucleation times as in the case of GaN, but the longer wires have a similar

length of approximately $270 - 290\,\text{nm}$ regardless of their thickness. Despite the high density, the number of wires which have coalesced is low.

Increasing Φ_{In} up to $2.8 \times 10^{-8}\,\text{mbar}$ (sample NC56, Fig. 8.2(b)) increases the diversity in wire lengths. There are many wires with similar length of approximately 370 nm, but there is also a small number of considerably longer wires with a length of $500 - 750\,\text{nm}$. These longer wires are thinner than the average ones and their diameter is uniform almost up to the top. Many wires still have pointed tips, but the tapering occurs mainly in the upper part of the wire, whereas the lower part has a uniform diameter.

A further increase of Φ_{In} to $3.9 \times 10^{-8}\,\text{mbar}$ (sample NC57, Fig. 8.2(c)) increases the ratio between long and short wires. Their lengths are similar to sample NC56, i.e. $\approx 600 - 700\,\text{nm}$ and $\approx 350\,\text{nm}$ respectively. A significant difference however is the fact, that the tapering effect is further reduced, especially in the longer wires: the diameter is uniform up to the top of the wire.

For $\Phi_{\text{In}} = 7.0 \times 10^{-8}\,\text{mbar}$ in sample NC44 (Fig. 8.2(d)) the tapering behaviour has changed to a broadening of the wire at the top. The number of long wires compared to the shorter ones further increases and the ratio is now at least of the order of 1. The top of the long wires is flat in most cases and their average length is $\approx 1.0 - 1.2\,\mu\text{m}$, where the shorter ones are $\approx 600 - 700\,\text{nm}$ high. Still some wires have a pointed tip, but they are a minority and their length is shorter than the long wires.

Sample NC45 (Fig. 8.2(e)) with $\Phi_{\text{In}} = 1.0 \times 10^{-7}\,\text{mbar}$ continues the trend set by sample NC44. The wires broaden and are considerably thicker than in the other samples. Some wires have coalesced due to the very high density. There is no real distinction between short and long wires anymore. The major part of the wires has a length of $\approx 850 - 1000\,\text{nm}$.

Fig. 8.2(f) shows that an increase of Φ_{In} to $1.5 \times 10^{-7}\,\text{mbar}$ leads to a quasi-compact layer of coalesced nanowires with similar height of $\approx 1.2\,\mu\text{m}$. Many thin wires are visible at the base, which widen gradually and then coalesce if they meet another wire. In the previous samples the wires are well separated, but in sample NC46 there is almost no space left between the wires.

So the SEM images in Fig. 8.2 show that in order to get long InN nanowires with uniform diameter at $T_{\text{sub}} = 475\,^{\circ}\text{C}$, Φ_{In} has to be chosen close to the value of NC44 ($\Phi_{\text{In}} = 7.0 \times 10^{-8}\,\text{mbar}$) . Higher fluxes lead to coalescence and lower ones can result in tapering.

The images Fig. 8.2d,e,f show that the roughening of the top surface increases with increased Φ_{In}. It is interesting to note, that the top part of sample NC32 in Fig. 8.1b has a similar morphology as NC45 in Fig. 8.2e although it is grown with a lower Φ_{In}. The growth time for NC32 is longer however than for NC45 (4 h vs. 2 h). For comparison the top part of NC44, NC45 and NC32 is shown (cf. Fig. 8.3). It is thus interesting to see the development of the nanowires with deposition time. Since we cannot monitor the wire growth in-situ, different samples with the same growth parameters but different deposition time have been grown. In addition the time development has been investigated for different Φ_{In}, but T_{sub} and Φ_{N} are the same for all the samples ($T_{\text{sub}} = 475\,^{\circ}\text{C}$, $P_{\text{RF}} = 500\,\text{W}$ and $\Phi_{\text{N}_2} = 4.0\,\text{sccm}$).

At $\Phi_{\text{In}} = 2.3 \times 10^{-8}\,\text{mbar}$ the length of the wires increases with deposition time (Fig. 8.4: (a) NC154, 15 min; (b) NC58, 120 min; (c) NC31, 240 min), but the diameter does not change much. In all images almost all the wires show a tapering effect with a rounded or sharp tip

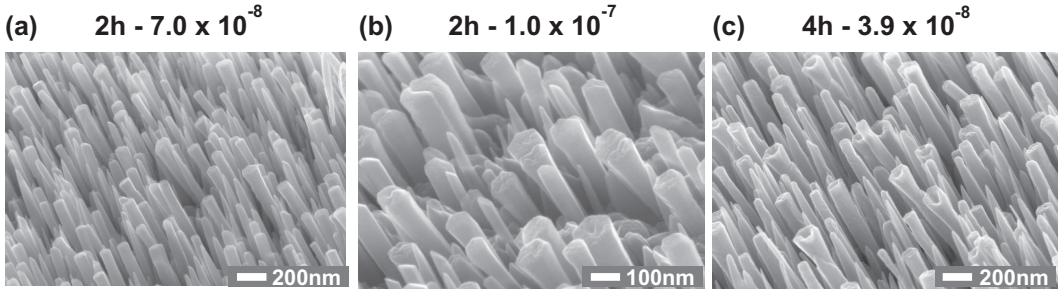

Figure 8.3: SEM images of the upper part of InN nanowires grown with different parameters. (a) The sample NC44 grown for 2 h with $\Phi_{\mathrm{In}} = 7.0 \times 10^{-8}$ mbar has wires with a faceted top and some wires show a small roughness of this top. (b) For a higher Φ_{In} of 1.0×10^{-7} mbar (sample NC45) the number of wires with a rough surface increases and also the roughness itself is a bit higher. (c) A longer growth time of 4 h, but lower $\Phi_{\mathrm{In}} = 3.9 \times 10^{-8}$ mbar shows an even more pronounced roughening of the wire top and sometimes even the formation of a tube-like structure.

and there is no broadening.

By increasing Φ_{In} up to 3.9×10^{-8} mbar at the same T_{sub} of 475 °C (Fig. 8.4d,e), the longer wires have a uniform diameter after 120 min deposition (NC57). After 4 h of growth (NC32) however, the longer wires show a pronounced broadening and the top looks like a crown. Some of the shorter wires have sharp tips. As mentioned earlier the morphology is similar to sample NC45 (Fig. 8.2(e)) grown with higher Φ_{In} but shorter deposition time (2 h).

A further increase of Φ_{In} up to 4.6×10^{-8} mbar does not significantly change the morphology after 120 min (Fig. 8.4f). Only the number of long wires increases. After 4 h however, a significant part of the wires has a broadened tip and is hollow at the top (Fig. 8.4g). The tube has a hexagonal shape and thin walls. Still some wires have a sharp tip, but they are shorter in general. Increasing the deposition time to 8 h leads to the formation of conically broadening hexagonal tubes with diameters up to 1 µm (Fig. 8.4h). The other wires have very rough top surfaces and also tend to form a tube.

The probability to form a crown at the top of the wires is thus enhanced with increasing Φ_{In} and with longer deposition time and eventually leads to nanotubes.

Discussion

GaN and InN nanowires show a pronounced dependence on substrate temperature, but the physical origin is different. For typical InN growth temperatures the vapour pressure of In is two orders of magnitude smaller than for Ga (Tab. 8.2). This means that desorption plays a more significant role for GaN growth than for InN. For GaN Ga desorption is a limiting factor, whereas for InN the nitrogen effusion is more critical. Despite these facts the typical Φ_{In} is the same or a bit higher than Φ_{Ga} for the same Φ_{N}. It has to be noted that although InN and GaN are grown at different temperatures this should not affect the effective nitrogen flux very much. The plasma cell produces active nitrogen in the form of atomic nitrogen, which

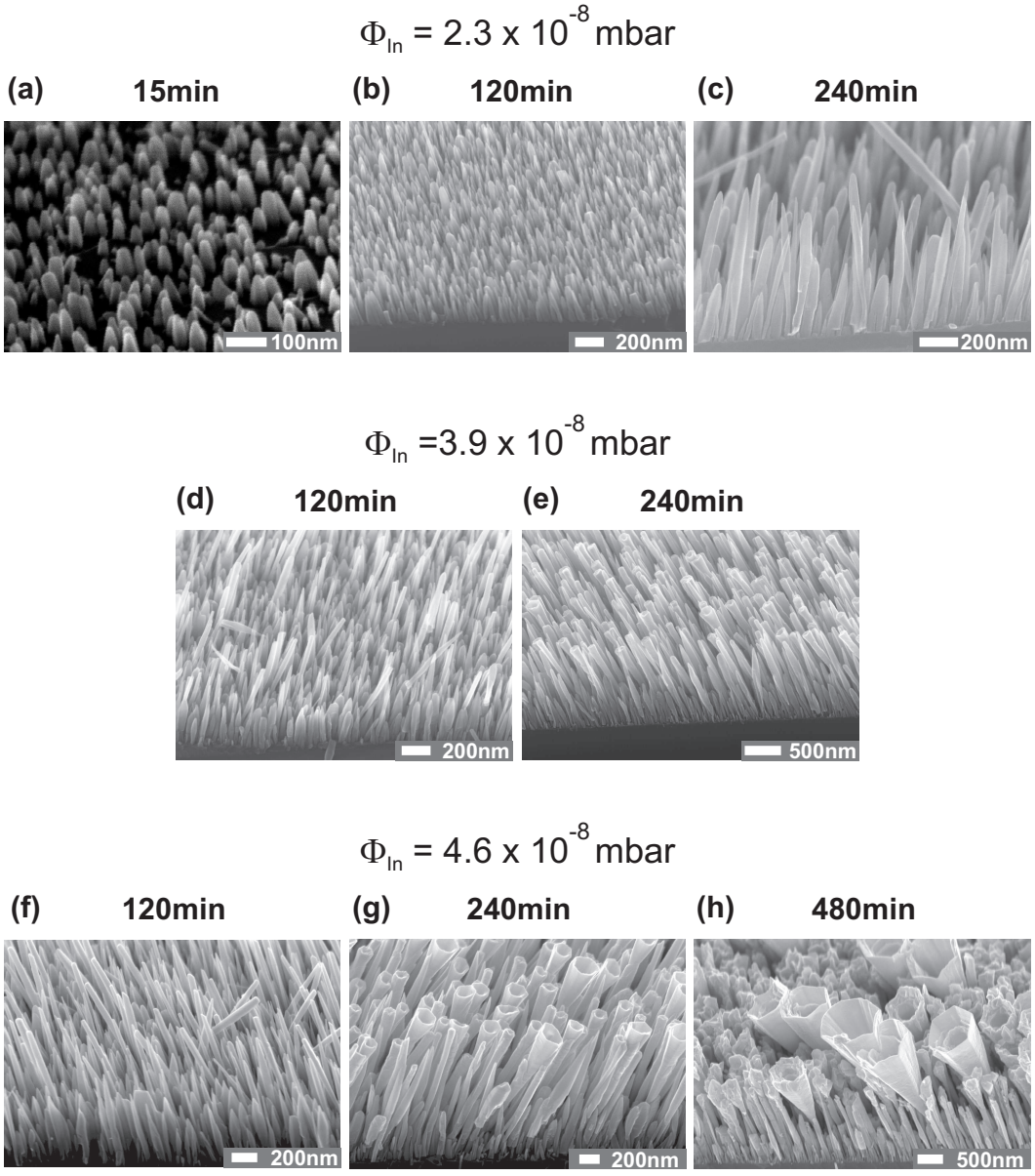

Figure 8.4: For the images grown at low Φ_{In} (a,b,c) the length of the wires increases with deposition time, but there is no broadening of the wires at the top. There rather is a small tapering effect. At slightly higher In flux (d,e) the wires still have a uniform diameter after 2 h, but the roughening and the start of the formation of tubes is visible in some wires. A further increase of Φ_{In} still shows uniform wires after 2 h (f), but the amount of tube-like wires has significantly increased after 4 h (g). (h) After 8 h of growth tubes with large diameters have formed in addition to wires with rough upper parts.

Table 8.2: Vapour pressures [Torr] for Ga and In for specific temperatures [°C], which correspond to the substrate temperature range for nanowire growth. Note: 1 Torr ≈ 1.333 mbar.

Element symbol	Element name	10^{-8}	10^{-7}	10^{-6}	10^{-5}
Ga	Gallium	619	677	742	817
In	Indium	488	539	597	664

is a very reactive radical and thus has a low activation energy for absorption. Hence, the substrate temperature is expected to play a subordinate role in the incorporation of nitrogen at the surface in contrast to for instance MBE or MOCVD growth which use NH_3. In this case the NH_3 has to react/dissociate at the surface and the substrate temperature has a significant influence on the reaction constant.

The InN nanowires in Fig. 8.1 are grown with the same nominal Φ_{In} and Φ_N; only T_{sub} is changed. Tab. 8.1 shows that by increasing T_{sub} the length of the wires and thus the growth rate increases. Growth by direct impingement only has a low temperature dependence in our case, because in Sec. 5.3 it was shown that there is no evidence for a droplet-mediated growth just as for GaN nanowires. Hence, since the growth species are already activated they can thus readily absorb on the nanowire surface and the temperature dependence of this process is low. Growth enhancement by a contribution of adatom diffusion along the wire sidewalls to the top of the wire, on the other hand, depends very much on temperature. This shows that just as for GaN nanowires the diffusion channel is important in the InN nanowire growth. It explains the enhanced growth rate for higher T_{sub}. These observations suggest a similar growth mechanism for InN as determined for GaN nanowires in Sec. 5.2. A higher T_{sub} thus improves the columnar morphology of the wires, but the dissociation of InN limits the range, which can be used.

The tapering and broadening behaviour of the wires in the SEM images in Fig. 8.1 can also be explained with the help of the diffusion channel. For a limited diffusion length the adatoms coming from the substrate surface and diffusing along the sidewalls to the top of the wires can only reach this top up to a certain length. Therefore, the wires start to taper if the contribution from the diffusion decreases. With increasing Φ_{In} more adatoms are available and the tapering probability is reduced due to a higher supply of adatoms from the substrate to the wire. At a certain point the behaviour changes to a broadening. Note that excess In can also enhance the diffusion length as reported in [140] for GaN. A thin metallic layer reduces the diffusion barrier for diffusion inside of this adlayer rather than on top of it. This explains why the broadening is not observed right from the start, but only after some time, because the metallic In layer first has to form as a result of an excess of In. With increasing deposition time, the In excess increases and thus the broadening becomes more likely. With increasing Φ_{In} the accumulation occurs faster and the broadening starts earlier. Since a wire with an adlayer enhanced lateral diffusion (AELD) channel will attract adatoms on the substrate surface with a higher probability than wires without such a layer, it will thus effectively reduce the number of adatoms diffusing along the wires without an AELD channel and therefore the

'AELD wires' broaden and the 'no-AELD wires' taper. The collection area of such wires causes a finite distance between them and therefore the longer wires are randomly distributed rather than grouped together at a certain position on the substrate.

The time development of the nanowires also indicates that broadening of the wires is related to accumulation of In. For lower Φ_{In} like in Fig. 8.4 the broadening only occurs for longer deposition times. By increasing Φ_{In} the amount of broadening increases. More In leads to more In accumulation. The combination of these two facts leads to the conclusion that the broadening and thus also the formation of the tubes is a result of In accumulation at the top of the wire. It can be explained by a so-called Schwöbel barrier at the top of the wire, which means that adatoms diffusing to the top of the wire cannot cross the barrier to the top of the wire and then lateral growth occurs. At higher temperatures like in GaN nanowire growth there is more energy to cross the barrier and also for InN an increase of 25 °C leads to a reduction of the broadening at otherwise fixed growth parameters.

Conclusion

The influence of T_{sub}, Φ_{In} and the deposition time on the growth of InN nanowires has been investigated. Within the chosen range of Φ_{In} and Φ_N an optimum T_{sub} of 475 °C is determined. At a lower temperature the growth is more compact like and higher temperatures result in dissociation of InN. At low In fluxes the wires tend to taper, which is reduced with increased Φ_{In}. If Φ_{In} is too high, however, it leads to coalescence. Wires grown for different times show that with time In accumulates and this can lead to broadening of the wires and the formation of tubes. Increasing T_{sub} reduces this effect.

8.2 Crystal structure and epitaxial orientation

Abstract

There is a considerable number of reports in literature on InN growth and the grown material displays quite different physical properties. For instance two distinct band gaps have been found. The quality of the grown material seems to be the key to explain the different results. In clusters have been suggested to be a source of the variations. Due to the small size of the In clusters it is difficult to observe them in XRD and therefore TEM is better suited for this task.

As for the GaN nanowires it is important to determine the epitaxial orientation of the InN nanowires to the substrate. This also allows to calculate the lattice mismatch, which can lead to defects.

Experimental Details

The same experimental setup as in Sec. 6.2 is used to measure a pole figure for an InN nanowire sample (NC59, $\Phi_{In} = 3.9 \times 10^{-8}$ mbar, $T_{sub} = 440$ °C, $P_{RF} = 500$ W, $\Phi_{N_2} = 4.0$ sccm, $t_{depo} = 4$ h).

Experimental Results

As explained in Sec. 6.2 one can determine the epitaxial relation with a single pole figure measurement if there is a family of lattice planes in InN and in Si, which have approximately the same lattice spacing, i.e. within the resolution of the equipment. The following lattice families satisfy this condition: InN(204), Si$(11\bar{5})$ and Si$(\bar{3}33)$ (d = 1.042 Å for InN and 1.045 Å for Si). The corresponding Bragg angle is 47.6°.

Fig. 8.5a shows the result of a pole figure measurement of an InN nanowire sample grown on Si(111) with $\Theta_{\mathrm{Bragg}} = 47.6°$. In this graph the intensity of the refracted beam is plotted against the polar angle θ and the azimuthal angle ϕ. θ corresponds to the radial distance and ranges from 0° to 90° in steps of 10° at each concentric circle. The InN(204) peaks correspond to the extended dots at $\theta \approx 43 \pm 2°$. It has to be noted, that the intensity of the (204) poles is rather low and since the volume of a nanowire sample is also considerably lower than for a compact layer, the peaks are rather weak and broadened. The other peaks at $\theta \approx 39°$, $\theta \approx 57°$ and $\theta \approx 71°$ belong to the Si(115) and Si$(\bar{3}33)$ diffraction spots. The InN peaks have a hexagonal symmetry, but for Si it is only 3-fold. The reason is that despite the hexagonal symmetry of the Si(111) surface, Si$\langle 111 \rangle$ is only a 3-fold symmetry axis.

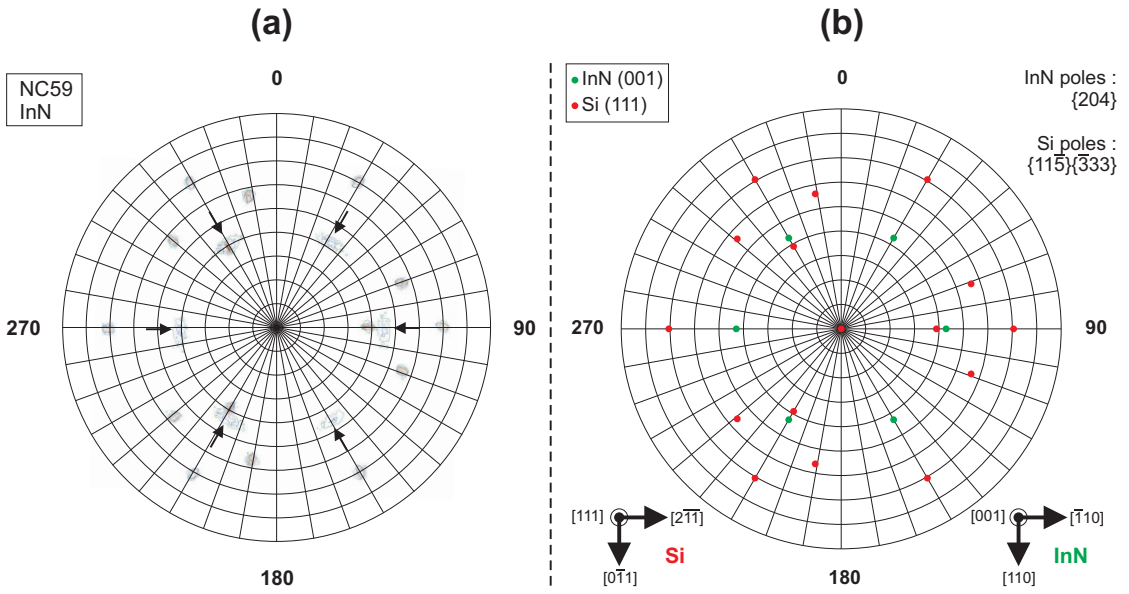

Figure 8.5: Experimental and calculated pole figure of sample NC59. (a) The poles at $\theta = 43 \pm 2°$ correspond to InN(204) (marked by arrows). The other points at $\theta \approx 39°$, $\theta \approx 57°$ and $\theta \approx 71°$ belong to the Si(115) and Si$(\bar{3}33)$ diffraction spots.; (b) Calculated pole figure for the epitaxial relation in Fig. 8.6a (cf. discussion in text). There is a good correspondence between the experimental and theoretical pole figures.

Discussion

Since the wurtzitic phase of InN, which has a hexagonal symmetry around $\langle 001 \rangle$, is thermodynamically stable it is deposited on Si(111). The expected relation between InN and Si is InN(001) ∥ Si(111), similar to GaN deposited on Si(111). The in-plane lattice constants, however, differ considerably ($a_{\mathrm{Si}} = 3,839$Åand $a_{\mathrm{InN}} = 3,533$Å) resulting in a lattice mismatch of -8.0%, i.e. tensile strain, which is approximately half the value for GaN, but still large. It has to be noted, that this holds for the 'one-to-one' epitaxial relation, where similar rows in Si and InN are aligned to each other. The corresponding epitaxial relation (I) is: $\mathrm{Si}\langle 0\bar{1}1 \rangle$ ∥ $\mathrm{InN}\langle 110 \rangle$ (cf. Fig. 8.6a). Because both lattices have similar symmetry, the lattice mismatch for the perpendicular directions is the same.

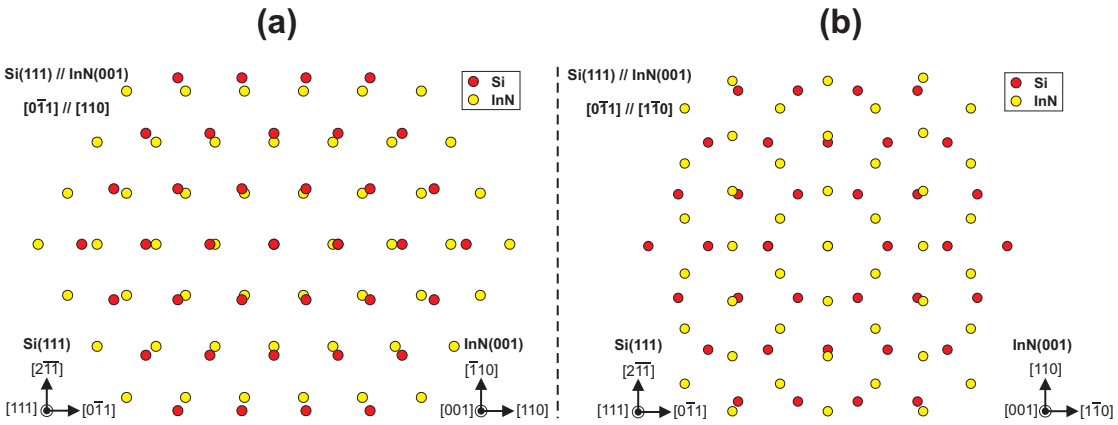

Figure 8.6: Possible epitaxial relations between Si(111) and InN(001). (a) One-to-one relation where similar directions in the hexagonal lattices of Si(111) and InN(001) are parallel; (b) The InN lattice is rotated by 30° around $\mathrm{Si}\langle 111 \rangle$ relative to the relation in (a).

Another possibility, which was also explored for GaN on Si(111), is the following epitaxial relation (II) obtained by rotating the InN crystal around 30° relative to Si: $\mathrm{Si}\langle 0\bar{1}1 \rangle$ ∥ $\mathrm{InN}\langle 1\bar{1}0 \rangle$ (cf. Fig. 8.6b). For a 1:2 lattice match between Si and InN in direction $\mathrm{Si}\langle 2\bar{1}\bar{1} \rangle$ and a 3:2 lattice match in direction $\mathrm{Si}\langle 0\bar{1}1 \rangle$ the mismatch is $+6.3\%$, i.e. compressive strain. This means the mismatch is slightly lower than for the direct epitaxial relation, however, as for GaN the Si atoms occupy two positions relative to the In (or N) layer: either a direct 1 to 1 relation or they form a tetrahedron with 3 neighbouring In (or N) atoms, which is typical for zinc-blende and wurtzite structures. Theoretical calculations are necessary to fully investigate the effect of such an interface on the free energy, but the gain in strain energy for the rotated epitaxial relation is lower than for GaN cf. Sec. 6.2 and there we already found that the direct coordination of the interface atoms seems to be favored. Therefore we also expect to find relation I for InN.

The measured pole figure (Fig. 8.5a) has been compared with the stereographic projections of the InN(001) and Si(111) planes for the families of poles InN(204), $\mathrm{Si}(11\bar{5})$ and $\mathrm{Si}(\bar{3}33)$. To determine the epitaxial relation, the projections have to be rotated against each

other such that the calculated image fits with the experimental one. A combination of the simulated Si and InN stereographic projections in one pole figure, which agrees with the experimental data, is shown in Fig. 8.5b. This graph corresponds to the epitaxial relation I: (111) $\langle 0\bar{1}1\rangle$ Si ∥ (001) ⟨110⟩ InN, so the same relation as for GaN. Thus, the lattice mismatch for InN is significantly lower and one can expect less strain-induced defects. However, it has to be noted that the InN nanowires have to be grown at considerably lower T_{sub}, which can reduce the crystal quality.

Conclusion

To conclude, InN nanowires grow epitaxially on Si(111) in the wurtzitic phase in the following epitaxial relation, which is pictured in Fig. 8.6a: (111) $\langle 0\bar{1}1\rangle$ Si ∥ (001) ⟨110⟩ InN. It is the same epitaxial relation as found for GaN and also for InN no cubic phase has been found.

8.3 InN photoluminescence results

Abstract

In Sec. 8.1 the formation of InN nanowires was studied with the aim of growth optimisation, in particular to obtain wires with uniform diameter. In this section the optical quality of the wires will be investigated by photoluminescence (PL) measurements, which is also an indication of the general quality of the nanowires, because imperfections in the crystal can reduce the optical efficiency by enhancing irradiative recombination. An important issue is also the value of the band gap for which different values have been reported (cf. Sec. 2.2).

The PL of InN nanowire samples is studied as a function of Φ_{In}, T_{sub} and deposition time. In addition as-grown samples are compared to free-standing nanowires (FSNWs).

Experimental Details

Photoluminescence spectra are measured using a Fourier transform spectrometer (BIORAD FTS40) equipped with a cooled Ge detector and an argon ion laser emitting 50 mW at 488 nm wavelength. The laser-beam power can be varied between 0.1 mW and 50 mW by changing the laser current or using neutral density filters. The measurements are performed in a He cryostat, which allows a temperature range of $4 - 300$ K. The measurement range, which can be investigated lies between approximately 0.7 eV and 1.5 eV.

Another PL setup using a He-Cd laser and a grating monochromator with a Si detector is employed to measure the visible range, which is not accessible to the setup with the Ge detector. These measurements are performed at 2 K.

The measurements were performed on as-grown samples as well as FSNW samples. FSNWs have been obtained by putting droplets of silicon grease on the original silicon substrate and transferring it with included nanowires to sapphire substrates. A control measurement shows that no PL signal is obtained from a sapphire substrate covered with grease without InN nanowires in the range under investigation.

SEM images of samples, which represent the growth parameters of samples investigated in this section are presented in Sec. 8.1. The growth parameters are listed in Tab. 8.3

Table 8.3: Growth parameters and average length of as-grown as well as free-standing nanowires characterised by PL. All samples are grown with the same plasma settings: $P_{RF} = 500\,W$ & $\Phi_{N_2} = 4.0\,sccm$.

Sample	T_{sub} [°C]	Φ_{In} [$\times 10^{-8}$ mbar]	time [min]	length [µm]
NC59	440	3.9	240	0.70
NC58	475	2.3	120	0.28
NC56	475	2.8	120	0.37 / 0.60
NC57	475	3.9	120	0.35 / 0.65
NC44	475	7.0	120	0.65 / 1.10
NC45	475	10.0	120	0.90
NC46	475	15.0	120	1.2
NC31	475	2.3	240	0.80
FSNW31	475	2.3	240	0.80
NC32	475	3.9	240	1.20
NC33	525	3.9	240	2.00
FSNW33	525	3.9	240	2.00

Experimental Results

Different band gaps have been reported for InN: one group of publications suggest a band gap below 1 eV [30, 167–174] and the other group suggests a value of approximately 1.9 eV [38,175–179]. Therefore the visible range as well as the IR range has been investigated for the InN nanowires, but only in the IR a PL signal could be obtained for all investigated growth parameters. The influence of these parameters is investigated in the following.

In Fig. 8.7 the influence of the Indium flux Φ_{In} on the shape (a), intensity (b) and position (c) of the PL peak is presented. To compare the shape of the spectra, they have been normalised to the maximum intensity of the peak. For low Φ_{In} the spectrum is noisy and for clarity the low end part of the spectra of samples with an In flux below $\Phi_{In} = 3 \times 10^{-8}$ mbar are not shown in Fig. 8.7a. With increasing Φ_{In} the noise is reduced and the peak width decreases. There is also a redshift of the peak maximum, which is also evident from (c). In (a) only samples grown for 2 h are shown, but in (c) samples grown for 4 h show an additional redshift with deposition time. The peak intensity (Fig. 8.7b) initially increases with Φ_{In} and reaches a maximum around 1×10^{-7} mbar. For longer deposition time the intensity goes up.

Increasing the substrate temperature has a similar effect on the PL intensity, peak position and peak width as an increased Φ_{In} has (cf. Fig. 8.8a,b,c). The intensity increases (b), the peak redshifts (a,c) and narrows (a) with increased T_{sub}.

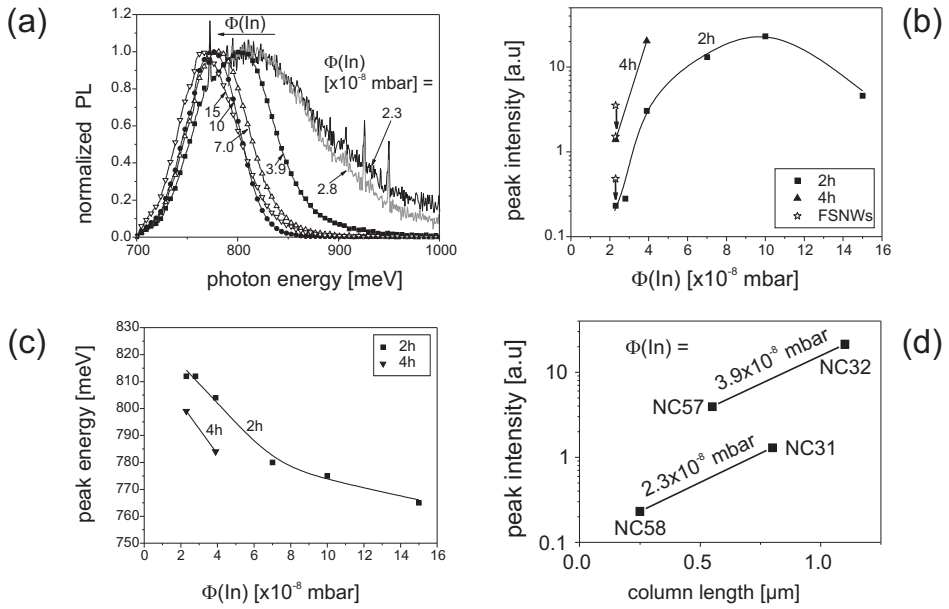

Figure 8.7: Influence of Φ_{In} on the PL spectra of InN nanowires deposited at 475 °C for 2 h and 4 h. All spectra are measured at 20 K with a laser power of 50 mW. (a) The spectra are normalised to the maximum intensity to compare the peak shape. With increasing Φ_{In} the peak width decreases and redshifts. For clarity the low end tail of the samples grown with low Φ_{In} is not shown. (b) The peak intensity increases with Φ_{In} up to approximately 1×10^{-7} mbar and then decreases. Samples grown with the same parameters but longer deposition time have a higher PL intensity. FSNWs display higher PL intensities than their as-grown counterparts. (c) A plot of the peak position vs. Φ_{In} showing a redshift also observed in (a). Longer deposition times also cause a redshift of the peak energy. (d) Peak intensity vs. column length for two In fluxes showing that the intensity increases with column length, but also with Φ_{In} for similar diameter.

Measurement parameters like temperature and excitation power can give further information about the quality of the wires and the origin of the PL peaks and have also been investigated. The temperature dependence of the PL spectrum of NC44 measured using a laser power of 50 mW is shown in Fig. 8.9a,b. With increasing T_{sub} the PL is quenched and the peak broadens on the high energy side. A semi-logarithmic plot evidences an exponential dependence of the high-energy tail and a specific energy E_0 can be determined (Fig. 8.9c). The specific energy E_0 is plotted as a function of measurement temperature in Fig. 8.9d for different samples grown at 475 °C. It shows a nearly constant value for lower temperatures and an increase at higher temperatures. Higher intensities in Fig. 8.7b correlate with a lower value of E_0.

The dependence of the PL spectra on excitation power for sample FSNW33 is presented in Fig. 8.10. There is only a small broadening and blueshift of the peak when the laser power is changed over two orders of magnitude (Fig. 8.10a). The PL intensity varies almost linearly

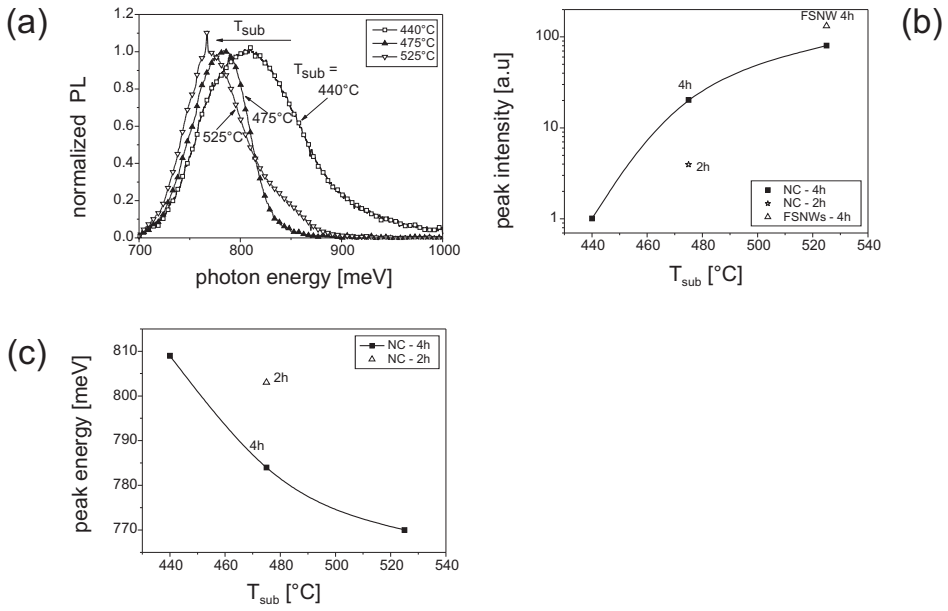

Figure 8.8: Influence of T_{sub} on the PL spectra of InN nanowires. All samples are grown with an In flux of $\Phi_{In} = 3.9 \times 10^{-8}$ mbar. (a) Comparison of samples grown for 4 h at different T_{sub}. The peak redshifts and narrows with increased substrate temperature. (b) By increasing T_{sub} from 440 °C up to 525 °C, the intensity increases by two orders of magnitude. (c) Redshift of the peak energy with increased T_{sub} determined from (a).

with excitation power: the peak area depends on excitation power Φ approximately as Φ^m with m between 0.9 and 1 for different samples and temperatures (Fig. 8.10b). The position of the peak shows a small blueshift with laser power for all measurement temperatures.

It is also interesting to compare as-grown and freestanding nanowires. It is difficult to control the InN nanowire density of the FSNW samples, but it is in general lower than the as-grown sample. The different density leads to different absolute intensity of the FSNW samples prepared from the same as-grown sample, but in all measurements it was higher than the intensity of the as-grown sample (cf. Fig. 8.7b and Fig. 8.8b). To compare the shape normalised spectra of as-grown as well as the corresponding FSNW samples are presented in Fig. 8.11. NC33 is grown at 525 °C and has a high PL intensity. The FSNW spectrum is very similar and only shows a very small blueshift and slightly lower high energy tail compared to the as-grown sample. Sample NC31, grown at 475 °C and lower Φ_{In} than NC33, has a lower PL intensity. The corresponding FSNW sample is blueshifted by approximately 16 meV. The result was confirmed by another individually prepared FSNW sample, which showed the same blueshift.

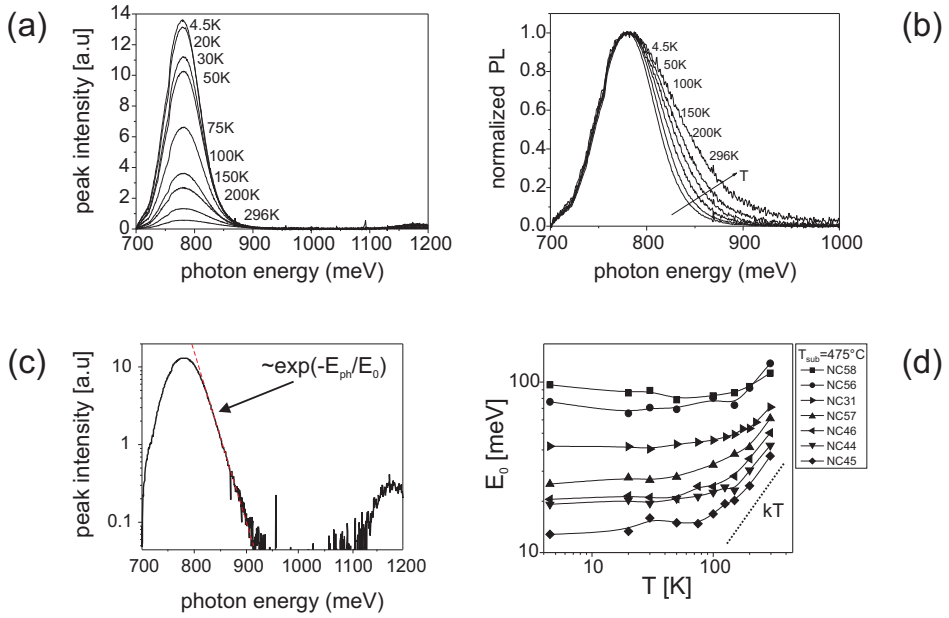

Figure 8.9: Dependence of the PL spectrum of InN nanowires (sample NC44) on the measurement temperature using a laser power of 50 mW. (a) With increasing temperature the PL is quenched. (b) Normalised PL spectra of (a) to compare the shape of the spectra. With increasing temperature the peak broadens on the high energy side. (c) Semi-logarithmic plot, which shows the exponential dependence of the high-energy tail of the PL spectrum with the specific energy E_0. (d) Temperature dependence of the specific energy E_0 for different samples deposited at 475 °C. For comparison the thermal energy k_BT of the Boltzmann factor is shown. At lower temperatures E_0 is approximately constant, but at higher temperatures thermal broadening becomes important.

Discussion

The PL intensity depends on the excitation volume and therefore the density of the investigated material plays an important role. The length of the wires plays a lesser role for InN with the used laser wavelength, because InN is highly absorbing for this wavelength. For nanowire samples, however, the density can vary considerably from sample to sample and therefore it is difficult to directly compare the absolute intensity. The PL intensity increases with Φ_{In} (up to a certain point) and also with deposition time, but the density and volume of the material also increase. However, the intensity increase for 4 h over 2 h samples is of the order of 8 in Fig. 8.7b, whereas the volume only doubles approximately for doubled deposition time (due to the high absorption of InN the actual excited volume less than doubles). Fig. 8.7d confirms that the increase of the PL intensity is not only due to an increased volume; a linear interpolation of the points with the same Φ_{In} shows that the intensity shifts upwards at increased Φ_{In}, but similar wire length. So although the PL intensity increases with Φ_{In} and deposition time due to an increased excitation volume, there is also an increase of the intrinsic quality

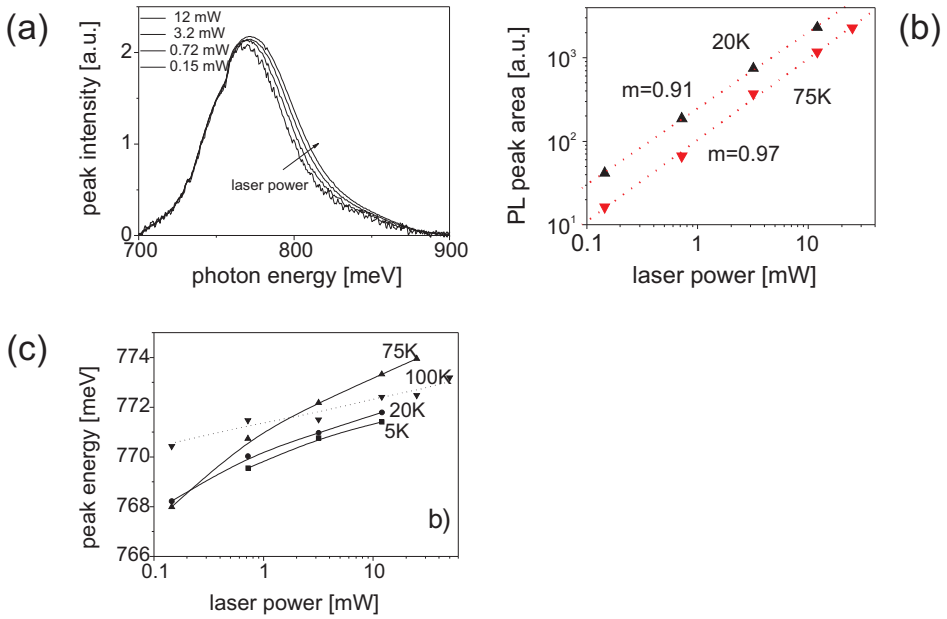

Figure 8.10: Dependence of PL spectrum of FSNW33 on laser power. (a) Increasing the laser power from 0.15 mW to 12 mW results in a small blueshift and broadening of the peak. The measurements are performed at 20 K. (b) The PL intensity increases almost linearly with excitation power as evidenced by a slope close to 1 for two measurement temperatures. (c) For all measurement temperatures a small blueshift of the peak energy with excitation power is observed.

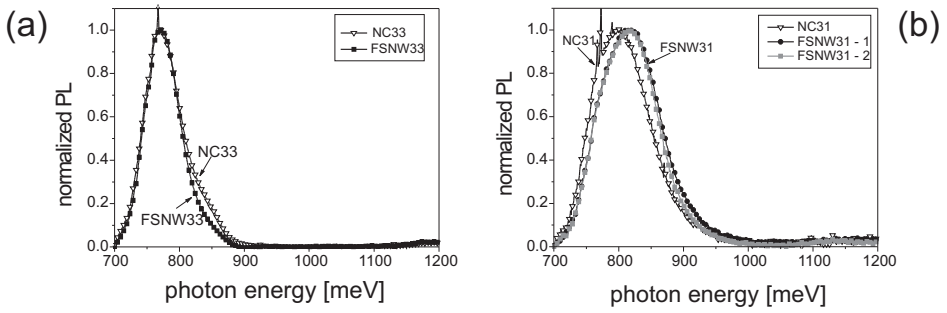

Figure 8.11: Comparison of normalised PL spectra of as-grown and free-standing InN nanowires. (a) The as-grown and FSNW spectra of sample NC33 are very similar. There is only a very small blueshift and a slightly lower high-energy tail for the FSNW spectrum. (b) Two separately prepared FSNW samples of NC31 as well as the as-grown sample are compared. Both FSNW samples show the same blueshift relative to the as-grown sample.

of the nanowires.

The increase of the quality with wire length can be explained in the following way: the Si substrate can induce defects at the base of the wires due to strain or unintentional doping by Si diffusion into the wire. The lower quality of the nanowire base is evidenced by TEM images in Sec. 8.4, which show a considerable number of stacking faults in the lower part of the wires. With increasing length (e.g. due to a longer growth time), the relative (and due to the high absorption also the absolute) contribution of the wire base is reduced and the quality improves. The upper part of the wires shown in Sec. 8.4 are free of stacking faults, evidencing higher quality. The higher PL intensity of FSNWs is also related to the influence of the substrate. By freeing wires from the substrate any residual strain induced by the substrate can be relieved and the quality improves leading to a higher PL efficiency. Also nonradiative recombination at the Si/InN interface is avoided. A difference between as-grown and FSNW spectra are small sharp peaks, which can be observed in some spectra of as-grown samples, but are not present in any FSNW spectrum. They are also not observed on a bare Si(111) substrate before InN deposition. From the absence of the features in the FSNW spectra we conclude that these peaks originate in the Si substrate or at the Si/InN interface.

The blueshift of FSNWs can be explained by a larger contribution of the lower part of the wires in FSNWs. For as-grown samples the laser is focused on the top part of the wires, whereas in FSNW samples the random orientation of the wires leads to equal probability to illuminate the top and bottom part. Since the lower part of the wires have a lower quality, i.e. more defects, the doping concentration in the lower part is higher, which effectively leads to a blueshift of the average over all wires in NC31. NC33 grown at higher substrate temperature has a small base compared to the upper part of the wires and therefore the contribution of the lower part is small, whereas for sample NC31, with a more uniform diameter, the base has a more significant contribution. Due to the higher T_{sub} the quality of the interface for sample NC33 is also expected to be better than in NC31. Hence, the blueshift for sample NC33 should be smaller than in NC31, which is observed.

The PL intensity in Fig. 8.10 scales linearly with excitation power and does not saturate, which suggests a band-to-band behaviour rather than a defect band proposed by the group of publications who suggest the band gap to be around 1.9 eV. The linear dependence is also easily explained assuming a high background n-type doping. In general InN layers exhibit a high background electron concentration (cf. Sec. 2.2 and [180]). The common view is that the nitrogen vacancy (V_N) is the most probable reason for n-type conductivity in InN, but also an antisite defect (N_{In}) has been proposed. Impurities like O, Si and H are other possible candidates. There are conflicting views, however, based on theoretical calculations and experimental results. The low photocarrier concentration for the weak excitation conditions relative to the high background doping in our experiments explains the linear dependence of PL intensity on excitation power. There is only a weak band filling effect, which results in the small broadening and blueshift observed in Fig. 8.10c.

The different peak widths and positions in the spectra in Fig. 8.7 and Fig. 8.8 can be interpreted in terms of different carrier concentrations induced by background doping [181]. Lower doping leads to narrower PL lines and a lower peak position, which are observed for increased Φ_{In} and T_{sub} in Fig. 8.7 and Fig. 8.8 (both within a certain parameter range). In addition the PL intensity increases. These facts thus suggest a reduction of the background

carrier concentration by increasing Φ_{In} and T_{sub}. It also allows to speculate on the origin of the n-type background doping. Note, that by increasing T_{sub} the effective III-V ratio increases due to an enhanced outdiffusion of nitrogen at higher temperatures. Thus, nitrogen vacancies are not a probable candidate for the n-type doping in our nanowires since increasing the III-V ratio should enhance the number of V_N and lead to higher doping. Also V_N are not very probable under N-rich conditions. A reduction of the doping concentration in InN planar films determined by Hall measurements for increased III-V ratio has also been reported in [23].

A nitrogen antisite N_{In} would be consistent with the observed dependence on III-V ratio, but according to theoretical calculations by Stampfl *et al.* [182] the antisite cannot explain the n-type conductivity in InN. An oxygen impurity on a nitrogen site (O_N) can also be ruled out to be replaced by In, due to the large ionic radius of In, which makes it reluctant to occupy a nitrogen site. Then, the most probable candidate for the n-type doping in our InN nanowires is Si on an In site (Si_{In}), which is readily available in the substrate. By increasing the III-V ratio the number of Si_{In} will go down and the background doping decreases.

The temperature dependence of the PL spectra of NC44 presented in Fig. 8.9a shows a quenching of the intensity with increased measurement temperature. This can be explained by a larger diffusion of the photo-carriers to nonradiative recombination centres in the nanowires or at the substrate at higher temperatures. This results in an increase of nonradiative recombination and thus a reduction of radiative recombination processes.

With measurement temperature also the high-energy tail of the PL peak changes. In general, the high-energy tail reflects the thermal distribution of carriers above the Fermi-level, because the PL intensity as a function of energy is proportional to the distribution of carriers in the band. This distribution is governed by the Fermi-function

$$f(E,T) = \frac{1}{\exp\left(\frac{E-E_F}{k_B T}\right)+1} \tag{8.1}$$

which at energies more than $2k_BT$ above E_F can be approximated by $f(E,T) \sim \exp\left(\frac{E_F-E}{k_B T}\right)$. The high-energy tail of the PL spectrum should thus have a dependence on photon energy $\sim \exp\left(\frac{-E}{k_B T}\right)$, which gives a specific energy of k_BT. Only for higher energies the k_BT dependence is found approximately. Up to 100 K the specific energy E_0 is approximately constant within the range of $10-100$ meV. This value E_0 reflects the fluctuations in the nanowire properties and a smaller value corresponds to a higher quality. Lower values for E_0 are obtained for the samples with the highest PL intensity in Fig. 8.7b, which again confirms the high quality of these samples.

Conclusion

The PL spectra show that there is a significant influence of the growth parameters. With increasing Φ_{In} and T_{sub} the PL intensity increases, which is a sign for a higher crystalline quality of these samples since defects quench the PL intensity. In addition to the increased PL intensity the peak width and position are reduced by increasing Φ_{In} and T_{sub}, which is related to a lower doping concentration. A reduction of the number of Si_{In} is proposed as the origin.

The power dependence of the PL spectra show a linear dependence, which suggests a band-to-band behaviour and a band gap between approximately 0.75 eV and 0.80 eV is obtained. The high energy tail of the PL is reduced for higher Φ_{In} and T_{sub}. It is approximately constant at lower measurement temperatures indicating that fluctuations in the nanowire properties dominate and behaves like the thermal distribution of the carriers for higher temperatures. Within the parameter range to obtain well separated nanowires, higher Φ_{In} and T_{sub} are thus favourable for high crystalline quality InN nanowires.

8.4 Transmission electron microscopy

Abstract

In this section the crystallinity of InN nanowires is studied by TEM. In the section about the PL of InN (Sec. 8.3) it was concluded that the base of the nanowires has a lower quality than the upper part, which is thus a topic investigated in this section. There have also been reports in literature that InN clusters cause the low band gap of InN [32] and the presence or absence of such clusters can be determined by TEM.

Experimental Details

TEM measurements on InN nanowires have been performed with the same setup as in Sec. 6.4 at the Brookhaven National Laboratory[1]. The covered temperature range is between room temperature and 500 °C at pressures of 2×10^{-7} mbar. Low electron-irradiation intensities have been used to prevent any uncontrolled electron-beam-induced structural changes. The accelerating voltage was set to 300 keV. These parameters are the same as for the GaN nanowires.

Just as for GaN nanowires, InN nanowire samples have been prepared in two ways: by dispersing single wires on a lacey carbon TEM grid (NC44) and by conventional TEM thinning of as-grown samples covered with PECVD-grown SiO_2 (NC182). The growth parameters are summarised in Tab. 8.4.

Table 8.4: InN nanowire samples investigated by TEM.

Sample	T_{sub} [°C]	Φ_{In} [$\times 10^{-8}$ mbar]	P_RF [W]	Φ_{N_2} [sccm]	time [min]
NC044	475	7.0	500	4.0	120
NC182	490	2.0	500	4.0	30

[1] E. Sutter, Center for Functional Nanomaterials, Brookhaven National Laboratory, Upton, New York 11973

Experimental Results

TEM images of InN nanowire samples dispersed on a lacey carbon TEM grid are shown in Fig. 8.12. Several differences with GaN nanowires presented in Sec. 6.4 can be observed. At one end of the nanowires in Fig. 8.12a,b a number of horizontal stripes, i.e. perpendicular to the growth direction, can be seen. They are due to different diffraction contrast and the result of stacking faults (SFs) or other defects. The wire diameter increases in this area as long as the stripes are visible and then the diameter stays approximately constant (a,b). In Sec. 8.1 it was shown by SEM images that the bottom part of the wires is typically thinner than the upper part, except for the wires, which taper into sharp tips. Therefore the part with the thinner diameter (and the defects) is linked to the base of the wires. The top of the wires (Fig. 8.12c,d,e) is almost free of defects and has a more homogeneous diameter, except for the wire which evidences the sharp tapering effect. The wire in Fig. 8.12(d) has a sudden diameter reduction near the top, which is accompanied by some stacking faults. The surface smoothness varies from wire to wire (compare Fig. 8.12e vs. f) and in general the surface is not atomically smooth as for GaN nanowires.

InN nanowires still attached to the Si substrate (NC182) confirm that the wires broaden at the base and continue to grow with a uniform diameter when reaching a certain length (cf. Fig. 8.13). The diameter of the upper wire in Fig. 8.13b increases from approximately 37 nm up to $\approx$ 55 nm. The horizontal stripes observed in Fig. 8.14a,b are not visible in Fig. 8.13.

There is a thin amorphous (presumably Si_xN_y) wetting layer of approximately $1.5 - 2.5$ nm on which the InN nanowires grow. In contrast to the case of GaN a very thin upper layer of the Si substrate seems to be affected, especially near the InN nanowires.

A high-resolution TEM (HRTEM) image of the inner part of a high quality wire (sample NC44), which does not display any defects in the investigated area is shown in Fig. 8.14a. The c-axis of the nanowire is slightly tilted against the vertical direction (3.1°) and therefore the corresponding diffraction pattern obtained by a FFT of the HRTEM image is tilted by the same angle. The diffraction pattern corresponds to the pattern along the direction $\langle 1\bar{2}10 \rangle$ for wurtzite InN and the sharp spots confirm the high-quality of this area of the wire. The wurtzite structure can also be deduced by the ABAB... stacking order in the real space image.

Discussion

The TEM images in Fig. 8.14 and Fig. 8.13 suggest that strain is present in the InN nanowires and there is also a slight influence on the Si substrate. With increasing length of the wire the strain slowly relaxes and the diameter widens. When the wires are removed from their substrate as for the ones in Fig. 8.14, the substrate-induced strain relaxes partially by the formation of defects in the wire base. The upper part of the wire is strain-free or only slightly strained from the beginning, i.e. during growth of the wire. Since the lattice mismatch between InN(001) and Si(111) is approximately half the value for GaN (8% vs. 16.9%, cf. Chapter 2) the critical thickness is larger and the first InN layers can grow pseudomorphically on the substrate, whereas for GaN the strain energy is so high that direct relaxation is preferred.

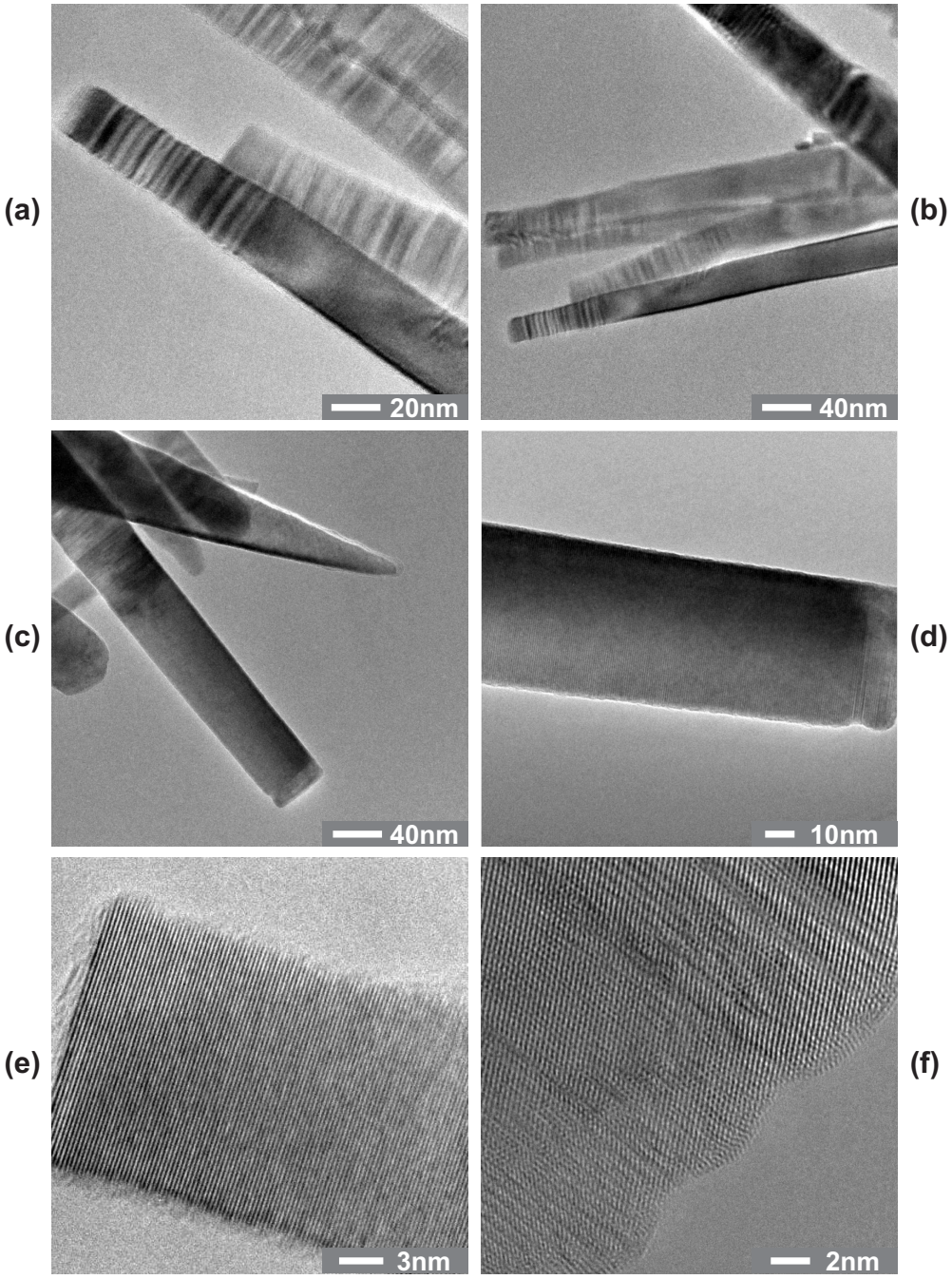

Figure 8.12: TEM images of different wires from an InN nanowire sample (NC44). The ends of the wires in (a,b) contain a lot of stacking faults (SFs) and the diameter increases up to a certain height and then continues with a constant diameter. The wire with the sharp tip in (c) has no apparent SFs and the other wire with a homogeneous diameter is also free of SFs almost up to the end. Near the top there is a small diameter reduction, which is accompanied by some SFs (cf. d). The rest of the wire has a high quality and the lattice planes can be observed. The surface however is less smooth than for GaN nanowires and the smoothness also varies from wire to wire. The wires in (d,e) have a quite smooth surface, although not atomically flat, but the wire in (f) has a pronounced roughness.

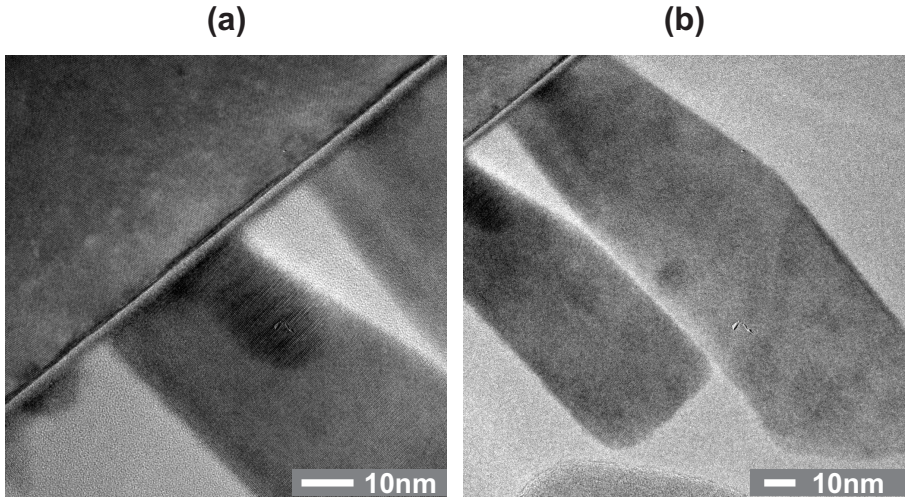

Figure 8.13: TEM images of InN nanowires grown on Si(111) (sample NC182). As in the case of GaN nanowires a thin wetting layer of approximately $1.5 - 2.5\,\text{nm}$ covers the entire substrate surface. Some small disorder seems to be induced in the Si substrate directly underneath the wetting layer. The images also show that the wires broaden from their base (diameter $\approx 37\,\text{nm}$ for the upper wire in (b)) up to a certain height and then continue to grow with a uniform diameter ($\approx 55\,\text{nm}$). There are no apparent stacking faults, which is also confirmed by higher resolution images.

The increased surface roughness compared to GaN can be a result of the lower substrate temperature, which reduces the surface mobility of adatoms. These adatoms thus have more difficulty reaching the top of the wire and therefore the relative lateral growth is higher. The roughness also promotes lateral growth due to a more effective nucleation (cf. Sec. 3.2.1).

Determination of the lattice constants from Fig. 8.14 allow to compare the InN nanowires with literature values for InN. The vertical lattice constant 'c' can be determined from the spacing of the lattice planes along the growth direction in Fig. 8.14a. Averaging over 37 planes gives a value of 5.69 ± 0.03 Å, which agrees well with the literature value of $c = 5.704$ Å (cf. Chapter 2). The horizontal lattice constant 'a' can be determined in a similar way, but note that the observed horizontal lattice spacing in Fig. 8.14a in the direction $\langle \bar{1}010 \rangle$ is only $\frac{1}{2}\sqrt{3}a$. Averaging over 68 planes gives a value of 3.52 ± 0.02 Å, which also agrees well with the literature value of $a = 3.537$ Å (cf. Chapter 2). The ratio 'c/a' between both constants is also very similar for literature and experiment: 1.617 (experiment) vs. 1.613 (literature).

The diffraction pattern also allows to determine the ratio between the constants 'a' and 'c'. It has to be noted that the distances in the reciprocal lattice are inversely proportional to the distances in real space, so the ratio between the vertical and horizontal spacing in the diffraction pattern has to be inverted to obtain the ratio 'c/a'. By averaging over multiple rows and columns of spots the measurement error can be reduced and the obtained ratio is: 1.628 ± 0.035, which agrees, within the margin of error, with the value obtained in real space and the literature value.

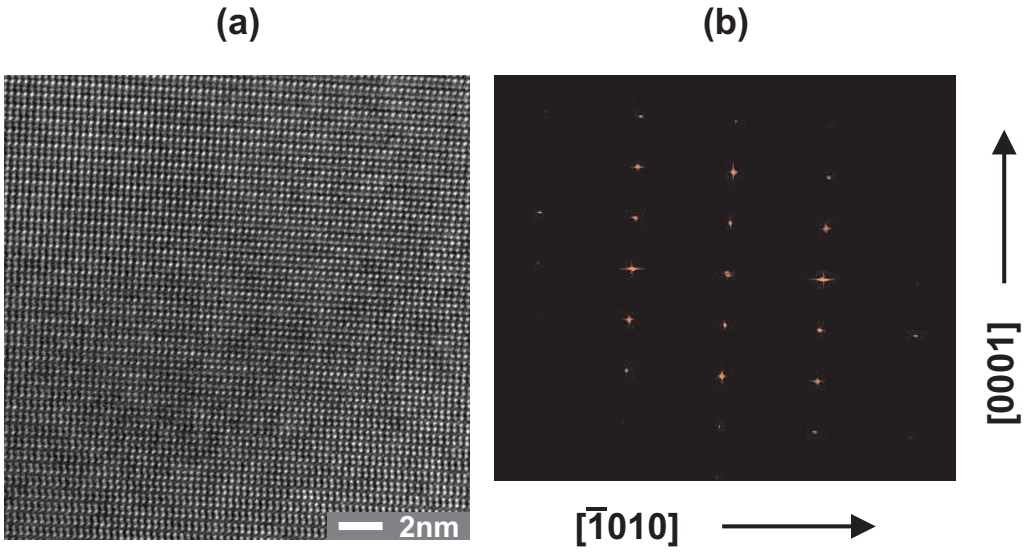

Figure 8.14: (a) High resolution TEM image of a part of an InN nanowire. There are no visible defects or stacking faults and the lattice planes are nicely resolved. (b) Diffraction pattern along the $\langle 1\bar{2}10 \rangle$ direction with sharp bright spots and a pattern in agreement with the wurtzite InN structure. Since the real space image is slightly rotated (3.1° clockwise) also the diffraction pattern is rotated. The directions below and to the right of the diffraction pattern should therefore also be rotated around this angle, but this has not been done for clarity.

As already noted in Sec. 6.4, the lattice constants are sensitive to strain and thus depend very much on the quality of the material. Since it is difficult to obtain high quality InN, the literature values scatter. The literature values mentioned above and in Tab. 2.1 are reported in [16] and correspond to planar InN films grown on sapphire. The lattice mismatch to sapphire is 25% [180] and thus strain can be present, although the authors have shown the high-quality of their materials. In nanowires strain relaxation is easier due to the limited lateral dimensions (cf. [150]) and therefore they are better suited to determine lattice constants for strain-free material.

Conclusion

In general the quality of the InN nanowires is less than the quality of GaN nanowires reported in Sec. 6.4. There is also more scattering of the quality between wires from the same sample. However, in none of the TEM images any evidence for In clusters has been found. The substrate induces strain in the wire, which relaxes at a certain length and is accompanied by a slight diameter increase. Just as for GaN the wires grow on a thin amorphous wetting layer, which is suggested to be Si_xN_y. The lattice constants agree well with the values for the highest quality compact InN layers.

Chapter 9

Technological processing and electrical characterisation of nanowires

9.1 Introduction

Growing nanowire functional elements is just one step in creating a nanowire device. The elements also have to be contacted to each other and to the 'outer world' to be able to apply power to the device. It is probably very difficult and maybe even impossible to achieve this with a completely bottom-up approach, but if the resolution of the lithography and etching steps can be lower than the resolution obtained during assembly of the elements, this still is an improvement. Interesting results in connecting nanowires in a self-assembled fashion have been reported by Dick in the group of Samuelson (cf. Fig. 9.1) [72, 183–186]. However, in any case when conventional top-down technology is used, it has to be certain, that the nanowire material is resistent to the different post-growth steps that have to be performed. Etching for instance can degrade the surface quality and since the surface-to-volume ratio of nanowires is very high, changes to the surface may have a great impact on the nanowire device performance.

As described in Chapter 3 the monolithic integration of III-V nanowires into Si technology would offer many exciting possibilities. Since the growth of semiconductors is usually performed at higher temperatures than the temperatures used during processing of Si, it is advisable to first grow the nanowires on the Si substrate and then process the Si. Depending on the device layout this might be mandatory and in many cases it will be required to produce contacts after the epitaxy. Also high temperatures like in GaN nanowire growth (around 800 °C) are often not compatible with processed Si devices, because these temperatures could change doping profiles and broaden interfaces. Hence, the nanowires will most likely be exposed to the technological steps for Si processing, which implies the necessity to be resistant to technological processes.

It is thus important to investigate the influence of processing steps on the properties of the nanowires. Now, group-III nitrides are known for their thermal and chemical stability (InN to a lesser extend). It is well known (cf. [22] and also Chapter 2) that acids have almost no influence on them in wet-etching steps, but as mentioned, due to the much higher surface-

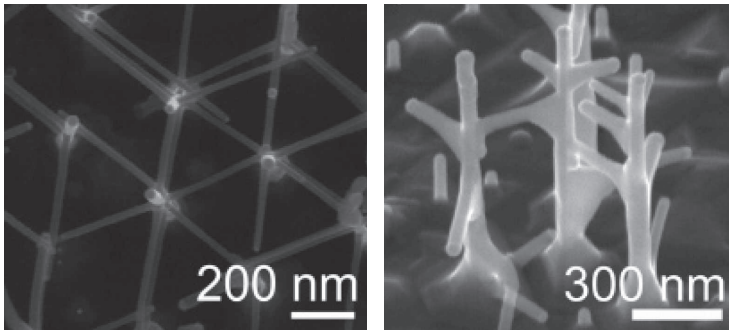

Figure 9.1: Top- and side-view SEM image of interconnected nanowires [185]. The position of the seed particles was determined by e-beam lithography, but the growth of the nanowires and the interconnection was performed by a bottom-up approach [185]. Recently the group has reported control over the height of the nanobranches [186].

to-volume ratio than for planar films the sensitivity of the properties to surface damage is significantly increased. Passivation/capping layers can protect the surface against subsequent etching steps and also provide a better defined surface than in the case of ambient air. However, the passivation step can also change the physical properties of the wires.

Another issue is the mechanical stability of the nanowires against processing steps like spinning on a photoresist. Such photoresists could be used to planarise the nanowire sample which would facilitate subsequent processing steps like contacting the nanowires with a top-contact. However, the high aspect-ratio of nanowires makes them prone to tumbling.

The first part of this chapter deals with the investigation of the influence of processing steps on the nanowires. For fundamental studies of the properties of single wires the transfer of nanowires to a host substrate is also of interest, so this will also be investigated. After the transfer process single wires can then be contacted by lithography.

The contact preparation in a cleanroom environment (class 100[1]) and electrical characterisation of the grown nanowires was not the goal of this thesis. This work has been performed by Thomas Richter and will be presented in detail in his PhD thesis. The results of these measurements, however, are important to understand the physical properties of the nanowires and to give feedback to the crystal growth, for instance about the doping concentration. A summary of important results from Thomas' work will therefore be presented in the final sections. The growth of GaN and InN nanowires has been optimised for the electrical measurements, because long wires with uniform diameter facilitate the contacting and interpretation of the results.

[1]Cleanrooms are classified according to the number and size of particles permitted per volume of air [187].

9.2 Stability of as-grown nanowires during technological processing

Abstract

In this section first the mechanical stability of nanowires against ultrasonics and spinning is studied followed by a comparison of the influence of different chemicals on the nanowires. Selective etching of a SiO_2/Si substrate allows to pattern the nanowires. Finally the coverage of nanowires with PECVD-grown SiO_2 is shown.

The intention of this section is to show the fundamental influence of the different steps. Depending on the application the steps will then have to be optimised keeping the results of this section in mind.

Experimental Details

To study the mechanical stability an as-grown GaN nanowire sample NC167 was cut into several small pieces. NC167 was grown on a 3 inch p-Si(111) wafer at 790 °C for 4 h with $\Phi_{Ga} = 3 \times 10^{-8}$ mbar, $P_{RF} = 500$ W and $\Phi_{N_2} = 4.0$ sccm. Two samples were subjected to spinning for s30 at 4000 rpm (programme 4) and one of them was covered with a photoresist (AZ5206) before the spinning process. Two other pieces were subjected to ultrasonics at maximum power, where one of them was submerged in propanol.

Another GaN sample (NC74) grown with the same parameters as NC167, but on a $19 \times 19\,mm^2$ p-Si(111) substrate was also cut into smaller pieces and then treated with different chemicals for 5 min. Typical acids, HF (1%), HCl (10%), and a basic solution of KOH (AZ400K 1/3) were investigated as well as solvents like acetone and propanol.

Optical lithography was employed to etch windows in a SiO_2 layer on Si(100). GaN nanowires were then grown on the substrate with the same parameters as NC74 and NC167 for 2 h. Part of the as-grown sample was etched in HF (10%) and a buffered HF solution (AF-91) for at least 10 min. To speed up the removal of the oxide mild ultrasonics was used.

Several GaN and InN nanowire samples were covered with PECVD-grown SiO_2. 300 nm and 600 nm SiO_2 was deposited at 300 °C. The deposition temperature was kept low to minimise the influence on the nanowires. For an InN sample (NC219, $T_{sub} = 475\,°C, \Phi_{In} = 7 \times 10^{-8}$ mbar, $P_{RF} = 500\,W, \Phi_{N_2} = 4.0$ sccm, $t_{depo} = 2$ h) the PL was measured before and after the coverage with SiO_2 as well as after removing it in AF-91 for 15 min. The influence of HF on the PL of InN was also measured.

Experimental Results

The mechanical stability of a GaN nanowire sample under different treatments is shown in Fig. 9.2. Subjecting the sample to ultrasonics or spinning at 4000 rpm does not have any effect on it and the SEM images are similar to the images of the as-grown sample in (a,b) and are therefore not shown separately. When the sample is submerged in a solution like propanol, however, a strong ultrasonic treatment removes a big part of the wires (c,d). By collecting the solution with the nanowires and spreading it on a host substrate, it is possible to transfer wires onto the host, where they can be contacted. Fig. 9.2e,f shows the sample after spinning

on a photoresist. The nanowires are still standing like in (a,b) and they are covered with the photoresist down to the substrate. A slightly thicker resist, multiple layers or a lower spinning speed are required to improve the coverage and fully embed the nanowires in the photoresist.

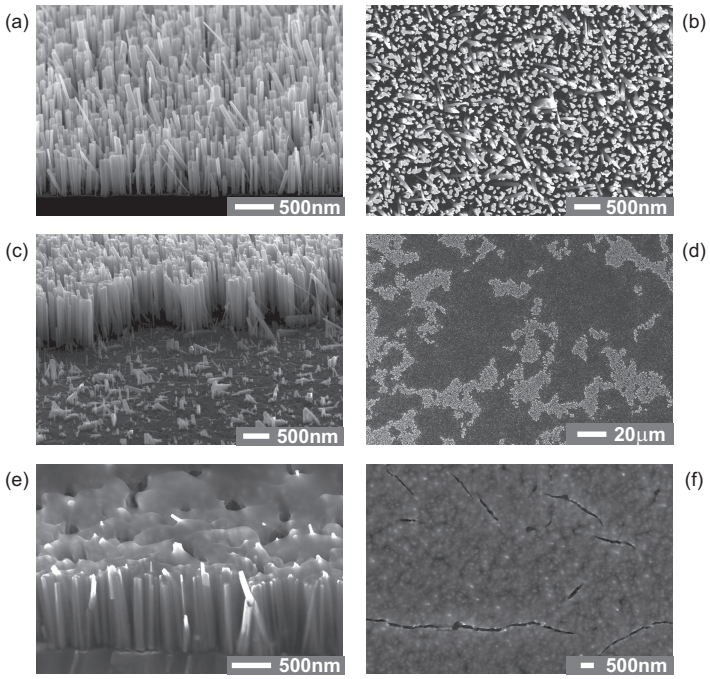

Figure 9.2: Side and top-view SEM images after different preparation steps. In the images (a,b) the as-grown sample NC167 is shown. Ultrasonics and spinning at 4000 rpm do not change the sample and the SEM images are similar (not shown). The images (c,d) show the sample after subjecting it to ultrasonics submerged in propanol at maximum power. Only when the sample is submerged in a solution and it is subjected to a strong ultrasonic treatment are the wires removed from their substrate. The images in (e,f) show the sample after spinning on a photoresist at 4000 rpm.

There is no evidence of a change of GaN nanowires after etching in HCl or HF (cf. Fig. 9.3) and also etching InN in HF did not produce a difference. Solvents like acetone and propanol have no effect either. KOH however, seems to etch the top surface of the GaN wires, although only slowly, so this has to be considered when using alkaline solutions.

The inertness of the nanowires against etching in HF can be exploited to produce arrays of nanowires by selective etching of SiO_2 on Si. Patterns have been transferred into SiO_2 on Si(100) by optical lithography (Fig. 9.4a,b). GaN nanowires grow on the Si as well as on the oxide (Fig. 9.4c,d). The Si(100) causes a tilt of many wires, but on the oxide all wires are perpendicular (Fig. 9.4e). By etching away the SiO_2 in AF-91 only the patterns of nanowires grown on the Si remain (Fig. 9.4f,g,h).

In Fig. 9.5 and Fig. 9.6 nanowires are compared before and after depositing different thick-

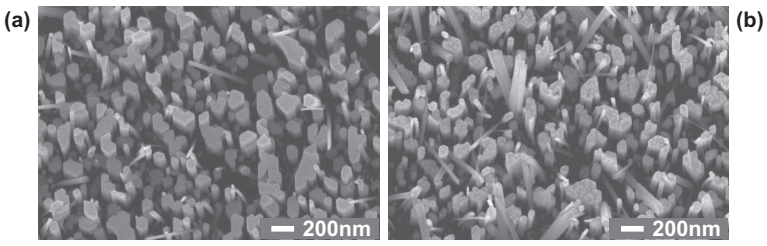

Figure 9.3: (a) GaN nanowire sample after etching 5 min in HF. There is no visible change to the wires. (b) GaN nanowires after etching in KOH for 5 min. Although the shape and side surfaces of the wires do not seem to be affected, the top has roughened a bit.

nesses of SiO_2 by PECVD. With increasing thickness the wires get completely covered and the surface smoothes. The images with low coverage Fig. 9.6b,c show that the oxide forms a shell around the wires. The method works equally well for GaN as for InN.

Etching an InN nanowire sample in HF (AF-91) for 10 min does not change its morphology nor does it change the PL spectrum: both the shape and the intensity of the PL signal are exactly the same. The influence of covering a similar InN sample with SiO_2 is shown in Fig. 9.7. Although the absolute PL intensity of the InN sample is quenched after covering it with SiO_2 (Fig. 9.7a) the shape of the spectrum is exactly the same as evidenced by the normalized spectra (Fig. 9.7b). Removing the oxide again with AF-91 also has no influence on the shape of the spectrum, but the intensity is fully recovered; it is even a bit higher.

Discussion

The mechanical and chemical stability of the nanowires shown in Fig. 9.2, Fig. 9.3 shows that the nanowires are quite rigid. Only severe mechanical vibrations when submerged in a solution (an ultrasonic bath) and alkaline solutions influence the wires. PECVD grown SiO_2 can be used as protection and stabilizing medium.

The size of the patterned structures can be further reduced by using better lithography techniques like e-beam lithography. The etching can probably also be optimised to reduce the number of wires in between the patterns. The arrays can be interesting for applications, where many wires are grouped as one element.

Apart from the morphology the physical properties are of course even more important and PL is a good measure of the quality. Etching InN nanowires in HF does not only have no influence on the morphology, but also does not change the PL. Similarly, the shape of the PL spectra of the InN sample in Fig. 9.7 does not change by covering the InN with oxide and removing it, which shows that the InN itself is not changed. The reduction in intensity with oxide can be a result of enhanced nonradiative surface recombination or an increase of scattering of the PL by the oxide layer. Removing it again recovers the PL, which shows the InN is not degraded by the oxide coverage. The increase of the PL after removing the oxide can be a result of a better defined surface than before oxide deposition, because the formation of the surface layer happens in a more controlled environment than in ambient air.

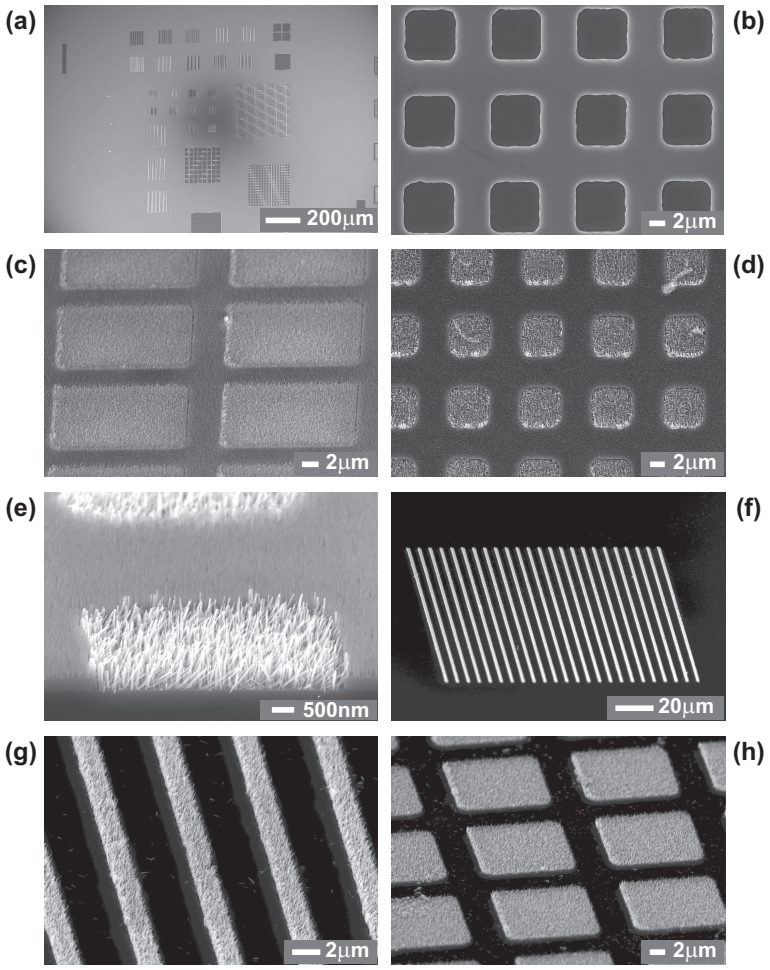

Figure 9.4: (a) Patterns in SiO_2 on Si(100) obtained by optical lithography. (b) Zoom of a part of the patterns in (a). (c,d) GaN nanowires grown on the patterned substrate. Wires grow both on the Si(100) and on the oxide. Where the wires on oxide are all perpendicular to the substrate, many wires on Si(100) are tilted. (e) Cross-section of one of the patterns in (c). (f,g,h) Patterns of nanowires obtained by selectively etching away the SiO_2 together with the nanowires on top of it. All wires grown on the Si(100) are still standing. A few wires from the oxide are scattered between the patterns.

Conclusion

Despite the large aspect ratio the nanowires are very stable against vibrations and spinning. Only severe ultrasonics in a solution removes them efficiently from the substrate. Nitride nanowires show the same chemical stability as planar nitride films against etching in acids. KOH etches the wires slightly. The mechanical and chemical resistance of the nanowires allows to process them with photoresists or passivate them with a PECVD-grown SiO_2 without

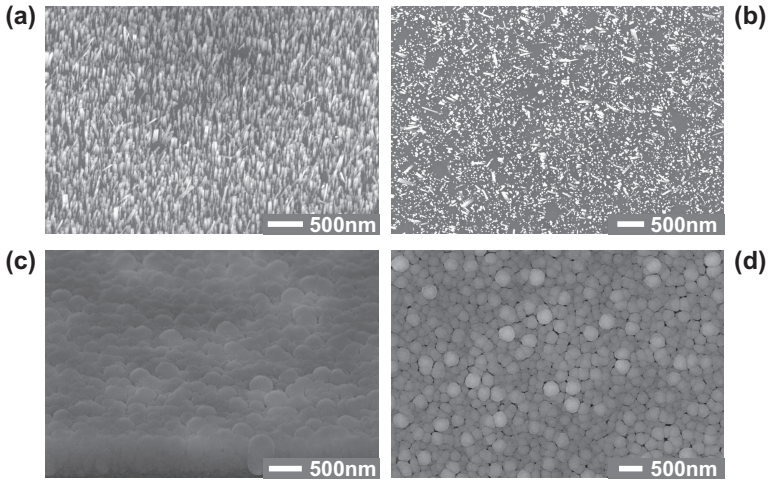

Figure 9.5: Side- and top-view SEM images of NC113 before (a,c) and after (b,d) depositing 300 nm SiO_2 by PECVD. The oxide completely covers the nanowires and the oxide seems to have grown around the wires.

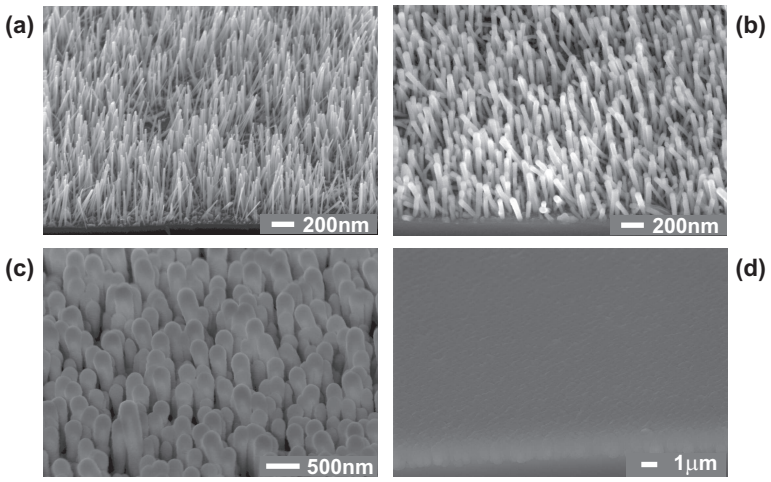

Figure 9.6: Side-view SEM images of GaN nanowires covered with nominally: (b) 50 nm; (c) 150 nm and (b) 600 nm SiO_2. For comparison an as-grown sample is shown in (a). The images (b,c) show that the SiO_2 covers the wires and with increasing thickness they grow together. For 600 nm SiO_2 the wires are covered and the surface smoothes.

changing the properties of the wires. This is useful for TEM sample preparation. Growing nanowires on patterned SiO_2 and a subsequent etching step also allows to produce dense arrays of nanowires on a μm-scale.

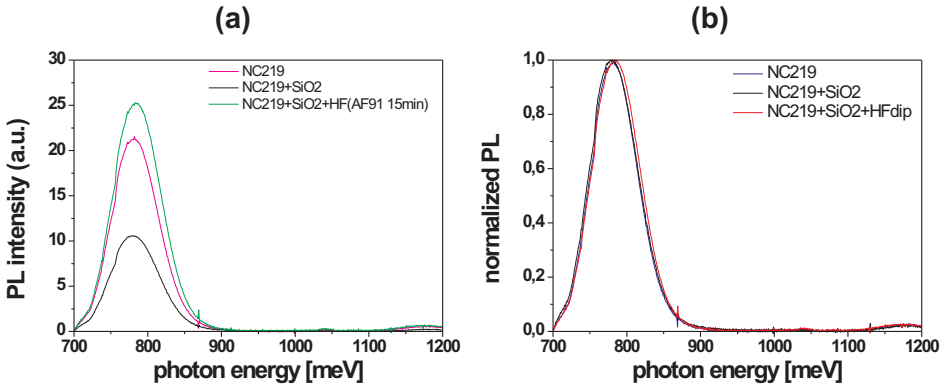

Figure 9.7: PL spectra of an InN sample (NC219) at 20 K and $P = 50$ mW. The as-grown sample is compared with the sample after covering it with PECVD-grown SiO_2 and after removing the oxide again with HF. The spectra in (a) show the PL intensity of the samples. The SiO_2 reduces the intensity by approximately a factor of two, but after removing it again the PL is completely recovered and even a bit higher. The spectra in (b) are normalised spectra of (a) and they show that the shape of all three samples is very similar.

9.3 Contacting single nanowires

After epitaxial growth, the nanowires are released from the native Si(111) substrate by exposure to an ultrasonic bath submerged in a solvent (acetone, propanol or methanol) and deposited on a Si(100) host substrate covered with an insulation layer of 100 nm SiO_2 and patterned contact pads on top. SEM images are taken to determine the position of the dispersed wires. Then contacts have to be defined with e-beam lithography to individual wires, which connect the wires with the bigger pads. These can be contacted by needles positioned with micromanipulators. The composition of the contacts depends on the nanowire material and the device requirements.

Different contact patterns and schemes have been tested towards the goal of contacting *single* wires. The optimised pattern is shown in Fig. 9.8a,b. Firstly, the contacting pads are written including markers in the centre area between the pads. These markers (a cross and many small dots with a size of nominally 100 nm and a real size of ≈ 140 nm) are used to position masks for subsequent lithography steps. After definition of the pads nanowires are scattered on the substrate with the procedure described in Sec. 9.2. SEM images are used to select individual wires, which are single, i.e. not clumped together in a cluster, and preferably with uniform diameter, smooth surfaces and large lengths (which facilitate the contacting). If wires with different diameters can be found, diameter-dependent measurements are possible. An individually defined e-beam mask is then prepared to contact the selected nanowires. The position of the nanowires is determined relative to the markers defined in the first e-beam step. An e-beam step with subsequent development of the e-beam resist, deposition of the contact material and a lift-off define the nanocontacts (cf. Fig. 9.8c). It has to be noted, that the position of the wires on the substrate does not change during these processing steps due to

van-der-Waals forces between the nanowires and the substrate. A close-up of single contacted wires in top-view and under an angle of 60° relative to the substrate normal are shown in Fig. 9.8(d) and (e), respectively. The wire in Fig. 9.8d is contacted at three positions, which allows to compare the electrical behaviour of the upper and lower part of the wire. A marker is visible in the left side of the image. In Fig. 9.8e one can recognise a marker in the lower right corner and the different contrasts of the upper and lower part of the contacts are due to different materials (top: 100 nm Au, bottom: 20 nm Ti). More details about the contacting procedure can be found in [188].

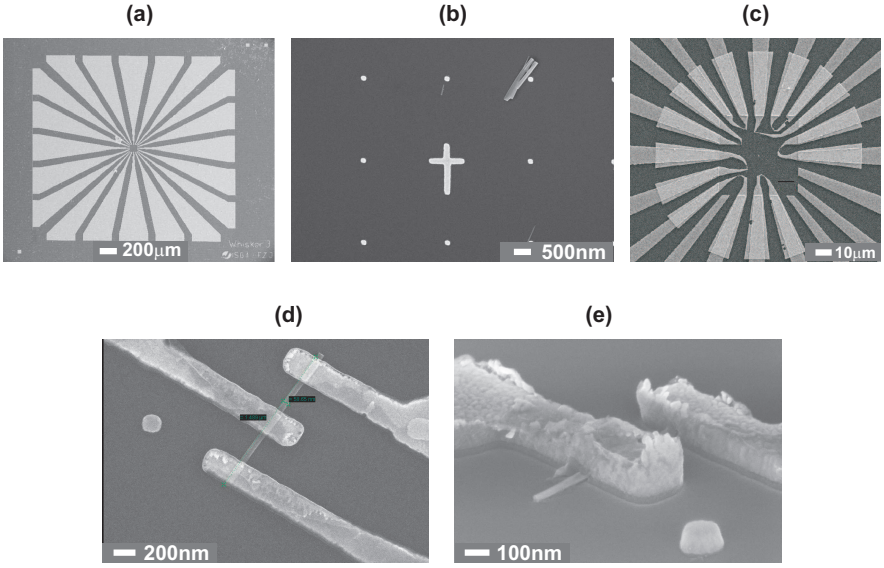

Figure 9.8: Top-view SEM images (except for image (e) which was taken under an angle of 60°) of the different steps in contacting single nanowires [188]: (a) Overview of the Au contacting pads; these can be used to contact the single nanowires with measurement needles attached to micromanipulators or through bonding with a Au wire, for use in a chip carrier; (b) markers (a cross and dots) in the centre area between the Au pads; (c) sample after definition of pairs of contacts to eight selected nanowires; (d) a GaN nanowire, approximately 1.5 µm long and 60 nm wide with three contacts; (e) a GaN nanowire with two Ti/Au contacts, where the different contrast clearly indicates the upper (Au) and lower (Ti) part of the contact.

9.4 Electrical characterisation of GaN nanowires

This section and Sec. 9.5 describe some basic electrical properties of GaN and InN nanowires as determined from the electrical measurements by Thomas Richter. There is a strong influence of the surface. Two-terminal devices have been used to measure the electrical as well as optoelectronic behaviour of single GaN nanowires.

9.4.1 IV-measurements

Abstract

To determine the intrinsic electrical properties of the GaN wires it has to be assured that the influence of the measurement setup is minimised. One requirement is that the contacts to the wires have no significant effect on the electrical performance of the device. Ohmic contacts are thus required, which are defined as metal-semiconductor contacts that have a negligible contact resistance relative to the resistance of the semiconductor. In addition the environment in which the measurements are performed, in terms of the material surrounding the wire, could play a role, because of the large surface-to-volume ratio of the nanowires. The influence of pulsed and steady-state illumination of the wire with above band gap UV light has also been investigated. Measurements have been performed on wires with different diameters to study its influence on the electrical performance.

Experimental Details

Single GaN nanowires were transferred to a Si(100) host substrate and contacted by e-beam lithography as described in the preceding sections. Ti/Au contacts were employed.

Current-voltage (IV) measurements were performed with a HP 4145 B semiconductor parameter analyser. The current measurement range runs from pA to mA and voltages from mV to 100 V can be measured. The contact pads on the sample were connected to the analyser by fine Au needles fixed to micromanipulators, which can be positioned with the help of an optical microscope. For measurements under illumination the light of a Hg-Xe UV lamp ($\approx 15\,\mathrm{W/cm^{-2}}$) was focussed onto the sample by a waveguide.

To investigate the influence of the environment transport measurements were performed under a vacuum of 10^{-5} mbar as well as in atmosphere.

Experimental Results

No difference between measurements under a vacuum of 10^{-5} mbar and in atmosphere were found, so the following results were obtained under atmospheric pressure. The leakage current, measured without a sample connected to the needles, was determined to be of the order of 5 pA at 2.5 V, which corresponds to the measurement limit of the device.

Ti/Au contacts have been shown to form ohmic contacts on n-type GaN for planar films [189,190], but this does not necessarily mean, that the contacts are also ohmic at the nanoscale when contacting nanowires. To study the nature of the contact two-probe measurements have been used and voltages between -2.5 V and $+2.5$ V have been applied. Ohmic behaviour corresponds to a linear dependence between the measured current and applied voltage. The results of such measurements for wires with different diameters is shown in Fig. 9.9. The lower curves correspond to measurements in the dark and the upper ones were performed under UV illumination with fixed intensity. For small voltages the dark current of the 190 nm wire shows ohmic behaviour (slope ~ 1), but between 0.1 V and 0.2 V the slope increases to approximately 3. The dark current of the 90 nm wire is below the measurement limit for smaller voltages, but above ≈ 1 V also in this wire a nonohmic current-voltage behaviour can

be observed with $I \sim V^{2.5}$. Under UV illumination the conductivity of the wires increases and the device shows an ohmic behaviour for both diameters.

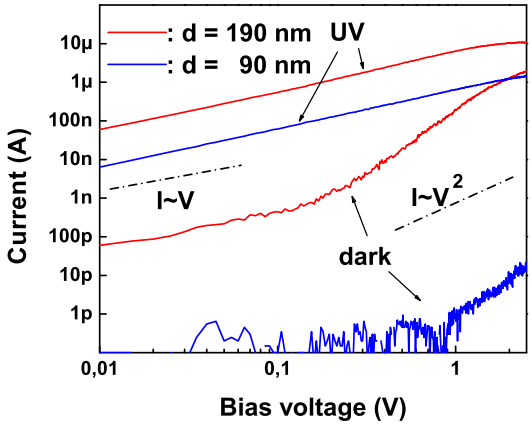

Figure 9.9: Current-voltage measurements on single GaN nanowires contacted by Ti/Au contacts [188]. Double logarithmic plot of the IV-curves for a 90 nm and 190 nm wire; under UV illumination both wires show an ohmic behaviour. The dark current for the 190 nm shows an ohmic behaviour up to approximately 0.2 V and then changes to a space-charge limited current. The dark current for the 90 nm wire is below the measurement limit for voltages below 1 V and shows space-charge limited transport above 1 V.

In Fig. 9.10 IV curves in a semilogarithmic scale are presented for different diameters ranging from 500 nm down to 70 nm. For all three wires the current increases under UV illumination, but the effect is most significant for the 70 nm wire where it increases by three orders of magnitude at 2.5 V. In addition, with decreasing diameter both UV and dark current values decrease too.

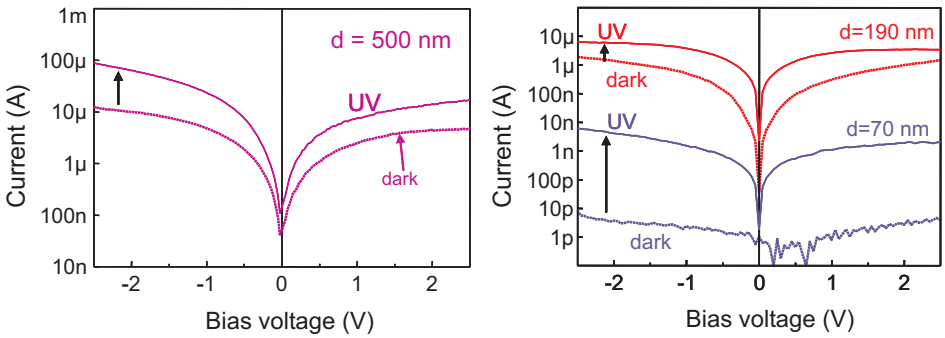

Figure 9.10: IV curves of GaN nanowires with diameters of 500 nm, 190 nm and 70 nm with and without UV illumination [188]. The dark and UV current decrease with diameter, but especially for the 70 nm wire there is a significant increase of three orders of magnitude under UV illumination.

The photocurrent as a function of diameter is presented in Fig. 9.11. The graph shows two distinct regions: in the upper part for diameters above $\approx 80\,\mathrm{nm}$, there is a linear dependence of the photocurrent on the wire diameter; below 80 nm the photocurrent rapidly drops off to immeasurable values.

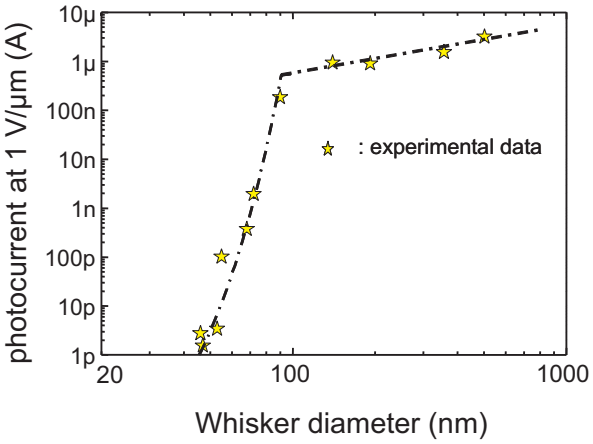

Figure 9.11: Diameter dependence of the photocurrent where two regions can be distinguished [191]. For larger diameters the photocurrent scales linearly with the diameter. Below $\approx 80\,\mathrm{nm}$, however, the photocurrent drops of rapidly. Note that the photocurrent was determined at a fixed electric field of $1\,\mathrm{V/\mu m}$.

The time-dependence of the IV curves after UV illumination was investigated for continuous and pulsed illumination. The results are shown in Fig. 9.12. In Fig. 9.12 (a) the dark current, photocurrent and dark current 120 s after UV illumination are shown for a 500 nm wire. The latter is significantly above the initial dark current value. In Fig. 9.12 (b) a similar measurement was performed for 190 nm and 70 nm wires, but with pulsed illumination, i.e. during the voltage sweep the light was turned on and off. In the case of the 190 nm wire there is a persistent photocurrent after switching off the light, but for the 70 nm wire the recovery of the initial dark current value is quasi-instantaneous. Fig. 9.12 (c) and (d) illustrate the same behaviour at a fixed bias voltage of 2 V. For the 500 nm wire there is an initial rapid drop, but then the current decays slowly and is still significantly above the dark current value after 400 s. No persistence is observable for the 70 nm wire.

Discussion

The dark current behaviour of the 90 nm and 190 nm wires in Fig. 9.9 is characteristic for space-charge-limited currents in insulators [192]. For an ideal crystal the slope is 2, but due to traps this can change to a much higher power dependence on voltage. The occurrence of the space-charge-limited current indicates that the wires are almost completely depleted of charge carriers. This is due to the surface depletion region induced by Fermi-level-pinning at the wire surface. Surface states pin the Fermi level at the surface at a position of $\approx 0.5 - 0.6\,\mathrm{eV}$ below the conduction band. The slopes of 3 and 2.5 for 190 nm and 90 nm respectively indicate that

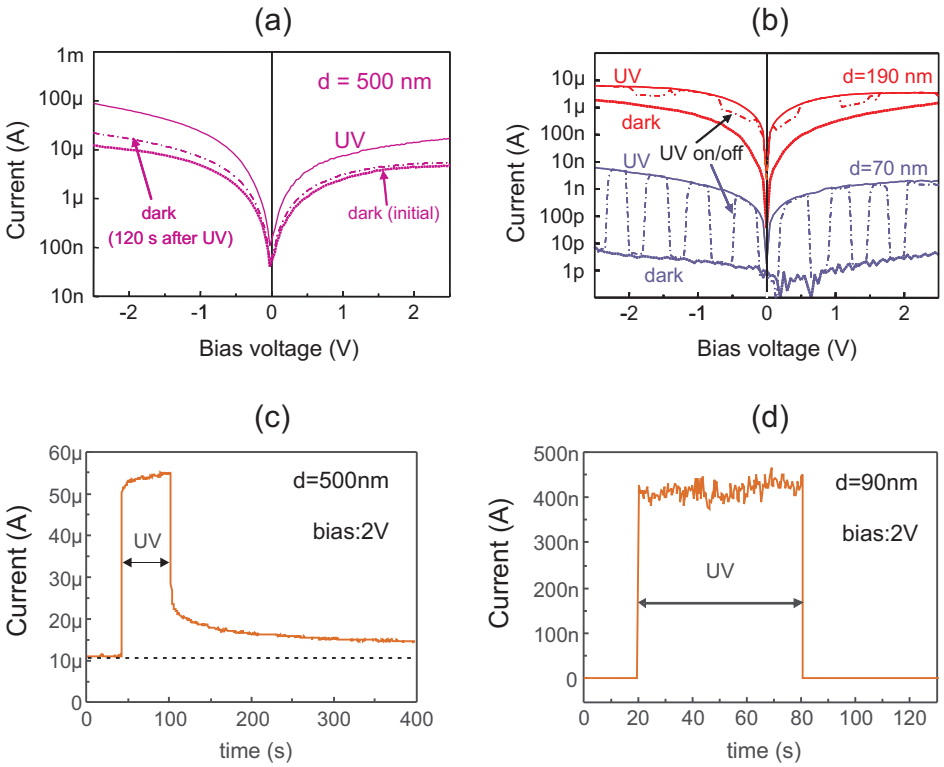

Figure 9.12: The images show the time-dependence of the IV-current after UV illumination [191]. (a) For the 500 nm wire the dash-dotted IV curve was measured 120 s after switching off the UV light and is still above the dark current; (b) The dash-dotted IV curve was measured by intermittently switching the UV light on and off. For the 190 nm there is a persistent photocurrent, whereas the 70 nm switches immediately between 'on' and 'off' current value; (c) Current vs. time for a 500 nm wire. At $t = 40$ s UV light is switched on and at $t = 100$ s it is switched off. The current decays slowly and at $t = 400$ s it is still above the value before illumination; (d) Current vs. time for a 90 nm wire. At $t = 20$ s UV light is switched on and at $t = 80$ s it is switched off. The current immediately returns to the initial value.

traps are present and that the 90 nm wire has a lower amount of them. Thinner wires can more easily relax strain induced by the substrate and thus less defects are expected (cf. [150]).

Under UV illumination photons can generate electron-hole pairs, which increases the free carrier concentration and the conductivity of the wire; for both diameters in Fig. 9.9 the device then shows an ohmic behaviour. This indicates that the contacts are ohmic, because only if the resistance of both contacts and the wire itself are ohmic, then and only then can the total resistance be ohmic. For the dark current the resistance of the depleted wire dominates the total resistance. A four-probe measurement is required to determine the relative contribution of the wire and the contacts, but the lengths of the wires that were investigated (typically 1 µm) were too short to be able to design four contacts. The limitation is due to the resolution

of the e-beam writer and the positioning accuracy relative to previously written layers.

The observed diameter-dependence presented in Fig. 9.10 can be explained by the semi-classical model shown in Fig. 9.13 [193]. The critical diameter d_{crit} in this model is determined by twice the width of the surface depletion region, which for an n-type semiconductor can be calculated by the following equation [136, chapter 7]:

$$W = \sqrt{\frac{4\epsilon\epsilon_0|U_D|}{en_e}}, \tag{9.1}$$

where W is the width of the depletion region, ϵ is the relative dielectric constant, U_D the diffusion voltage and n_e the donor concentration. The factor '4' in stead of '2' in [136] is due to the cylindrical symmetry of the wire compared to the case of a planar interface. In fact nitride nanowires typically have a hexagonal symmetry in stead of a cylindrical one, but for an estimation of the dimension of the depletion zone the simpler cylindrical model suffices. When $d \geq d_{crit}$ then $e \cdot U_D = \Phi$. Due to the band-bending electrons prefer the inner part of the wires, whereas holes tend to move to the surface. This means that photogenerated nonequilibrium carriers are spatially separated and recombination via surface traps is reduced, because of the barrier Φ. For GaN with $\epsilon = 8.9$, $U_D \sim 0.5\,\mathrm{V}$ [194] and typical n-type doping concentrations of the order of $10^{17}\,\mathrm{cm}^{-3}$, the depletion space charge layers should have extensions of $\approx 50\,\mathrm{nm}$. That means that wires with diameters of $\approx 100\,\mathrm{nm}$ or less should be fully depleted, because the depletion region extends on both sides ($d_{crit} = 2 \cdot W$), whereas for $d > d_{crit}$ there is still a tight conducting channel, which increases with d. Therefore the photocurrent increases with diameter in the region above d_{crit}.

The linear dependence of photocurrent versus d can be explained by considering generation and recombination of photogenerated carriers [193]. The generation rate G_{BE} at band edge (BE) illumination is proportional to the volume of the wire, so scales with d^2. If we assume that surface recombination is the prevailing recombination path then photogenerated electrons must move to the surface to recombine with photogenerated holes. Hence, the recombination rate R_{BE} is proportional to the surface, which means it scales with d. R_{BE} is also proportional to the total amount of N of photogenerated electrons. Since for steady-state conditions generation and recombination have to be in equilibrium, the following relationship holds: $G_{BE} = R_{BE}$ and thus also $d^2 \sim d \cdot N$. This means that the total amount N of photogenerated carriers is proportional to the wire diameter d and since the photocurrent is proportional to N, there is a linear relationship between the photocurrent and the diameter.

In the other region below the critical diameter, the surface band bending does not fully 'develop' and the surface barrier height Φ for surface electron-hole pair recombination is reduced (cf. Fig. 9.13). This means that the recombination process is strongly enhanced and the photocurrent decays rapidly with decreasing barrier height, i.e. column width.

The critical diameter d_{crit} can be used to calculate the doping concentration n_e from Eq. (9.1). It can be evaluated as the diameter at which the transition between the linear and exponential decaying of the photocurrent in Fig. 9.11 occurs. For $U_D \sim 0.5\,\mathrm{V}$, $d_{crit} = 80\,\mathrm{nm}$ and thus $W = 40\,\mathrm{nm}$ one obtains: $n_e = 6.2 \times 10^{17}\,\mathrm{cm}^{-3}$.

The diameter dependent behaviour of the current after switching of the UV light can also be explained in terms of the model in Fig. 9.13. For diameters above d_{crit} the surface barrier

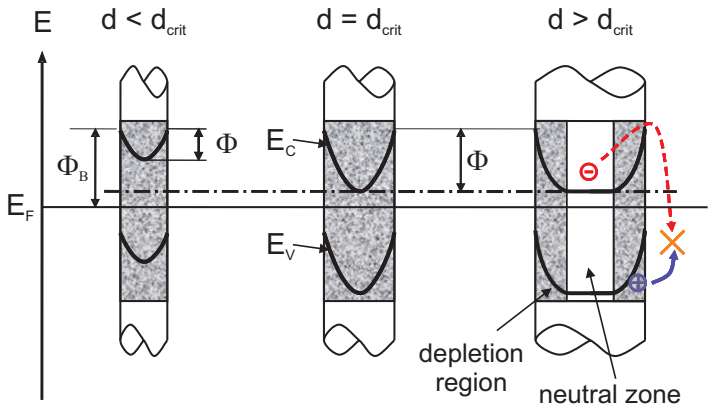

Figure 9.13: Three wires are depicted schematically which represent three characteristic diameters: smaller, equal or larger than a critical diameter d_{crit} (from left to right). The band diagrams correspond to cross-sections of the wires. The critical diameter is defined by the diameter at which the wire is just fully depleted. The gray areas in the wires correspond to the depletion region induced by the surface states. It is clear that for $d < d_{crit}$ the wire is fully depleted, whereas for larger diameters there is still a small conducting channel. The surface band bending induced by Fermi-level pinning forms a barrier for surface recombination and below d_{crit} the barrier is reduced. Note that the relative position of E_F, E_C and E_V are not to scale.

Φ hampers the recombination at the surface of photogenerated electrons and holes. However, below d_{crit} the surface barrier is reduced and this recombination path becomes more active, quickly reducing the concentration of carriers generated by the UV light. The observed behaviour is thus in agreement with our assumption above that surface recombination is the prevailing recombination path for photogenerated carriers. The fast reaction of the photocurrent in fully depleted ($d < d_{crit}$) wires makes them interesting for applications as fast photodetectors.

Conclusions

The intrinsic electrical conductance of GaN nanowires depends on their diameter. Fermi-level pinning due to surface states induces a depletion region and as a result thin nanowires are almost completely depleted. Photogenerated carriers by illumination with above band gap UV light enhances the conduction by several orders of magnitude depending on the diameter. Below a critical diameter of the nanowires, which is defined as twice the extension of the depletion layer width, the photocurrent drops off quickly as a result of a lowering of the barrier for surface recombination. The response to pulsed illumination for wires below the critical diameter is instantaneous within the time resolution of the experiment, but above the critical diameter there is a persistent photocurrent after switching off the illumination. The doping concentration can be determined form the critical diameter and amounts to approximately $n_e = 6 \times 10^{17}\,\mathrm{cm}^{-3}$.

9.5 Electrical characterisation of InN nanowires

In this section, the electrical properties of InN nanowires are presented. Since InN is a narrow-gap semiconductor with Fermi-level pinning in the conduction band [195,196], the behaviour is expected to be very different from GaN nanowires. Two-terminal devices have been processed by Thomas Richter and used to measure the electrical properties of single InN nanowires with and without UV illumination.

9.5.1 IV-measurements

Abstract

Also for InN nanowires *ohmic* contacts have to be used to minimise the influence of the measurement setup, which should be easier to produce than for GaN due to the low band gap and the Fermi-level pinning in the conduction band. This gives rise to a surface accumulation layer, which is expected to be highly conductive. The influence of UV illumination has also been investigated as in the case of GaN. Measurements have been performed on wires with different diameters to study its influence on the electrical performance.

Experimental Details

The contacting of single InN nanowires with different diameters was performed by e-beam lithography in the same way as for GaN nanowires.

For the current-voltage measurements with and without illumination the same experimental setup was used as in Sec. 9.4.1 for GaN nanowires.

Experimental Results

Ti/Au contacts which were used to contact the GaN nanowires were also employed for InN. The IV-measurements were performed in the dark and under UV illumination, but there was no difference. Therefore also no time dependence could be studied as was done for GaN in Sec. 9.4.1. The results of IV measurements without illumination are shown in Fig. 9.14 for three different diameters [197]. All three wires show ohmic behaviour. The voltage was limited to $\pm 0.25\,\mathrm{V}$, because of the very high currents running through the wires, which could destroy the device. Higher voltages have been employed also showing ohmic behaviour, but at a certain point the wire melted. SEM investigations afterwards showed that there still is connection between the contacts and the wire, but the wire itself has been divided into two separate pieces by melting of the middle part or electromigration. Note, that even at $0.25\,\mathrm{V}$ the current in these wires is of the same order as in the $500\,\mathrm{nm}$ GaN wire at $2.5\,\mathrm{V}$ (cf. Fig. 9.10). This means that the current densities are much higher in these InN nanowires.

Discussion

InN has proven to be a narrow-gap semiconductor (cf. Sec. 8.3) and just like other narrow-gap semiconductors such as InAs and InSb it exhibits Fermi-level pinning in the conduction

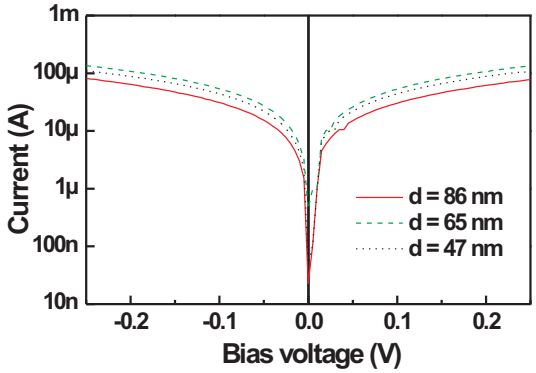

Figure 9.14: Current-voltage measurements on single InN nanowires with a diameter of 65 nm (upper curve), 47 nm (middle curve) and 86 nm (lower curve) contacted by Ti/Au contacts without illumination in a logarithmic-linear plot [197]. There is no influence of UV illumination. The voltage has been limited to 0.25 V.

band [195, 196]. This facilitates the formation of ohmic contacts, because it leads to a metal-like inversion layer at the surface. Simulations[2] have shown that it has an extension of only a few nm. As expected the InN nanowires thus show ohmic behaviour with the Ti/Au contacts.

InN is known to have a high background n-type doping of which the origin is still controversial. It has often been attributed to N-vacancies, but experiments are not in agreement with such an intrinsic defect (cf. Sec. 8.3, [23]). This high n-type doping, the absence of a depletion layer and significantly lower band gap lead to much higher currents than in GaN nanowires. Since the carrier concentration is already high without illumination and there is no depletion region, there is no influence from UV illumination. Photogenerated carriers can also easily recombine at the surface, because there is no surface barrier for electrons as in the case of GaN and the barrier in the valence band is thin due to the narrow extension of the band bending (see below). This could be another reason for the negligible effect of illumination on the electrical conductivity.

Due to the Fermi-level pinning in the conduction band the band scheme of a cross-section through the centre of the wire is very different from the one for GaN nanowires (Fig. 9.15). There is a surface accumulation layer, which is narrow due to the high doping concentration. The position of the Fermi-level depends on the doping concentration so can vary from sample to sample. Therefore it has been depicted as a shaded area. Qualitatively there is no significant difference for thinner and thicker wires (unless the wires are below ≈ 15 nm, but our wires are usually thicker). Depending on the position of the Fermi-level the current will either be confined mainly to the surface accumulation layer (in case the Fermi level is significantly below the conduction band edge in the centre of the wire) or will flow through the whole cross-section of the wire (if E_F is above E_C in the centre of the wire). In the first case the current scales

[2] thanks to Jakob Wensorra

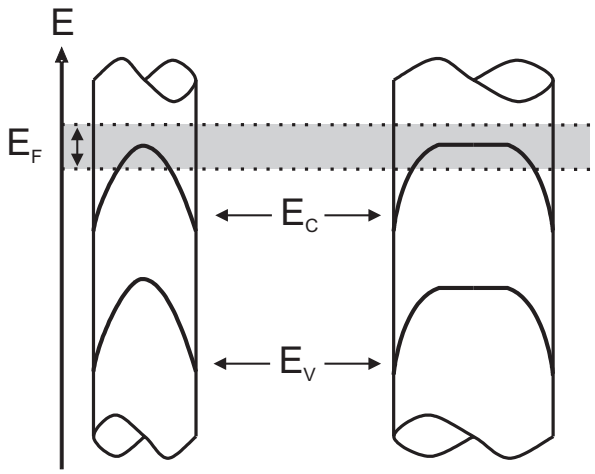

Figure 9.15: Schematic representation of the band diagram for InN nanowires with different diameter. The extend of the surface accumulation layer is only a few nm so for wires with diameters above $\approx 20\,\mathrm{nm}$ there is no real qualitative difference. The Fermi-level depends very much on the doping concentration and can be above and below the conduction band edge in the centre of the wire. This has been depicted by the gray shaded area. Note that the relative position of E_F, E_C and E_V are not to scale.

with the surface area, so should be proportional to d. In the latter case it is proportional to the wire cross-sectional area, so should scale with d^2 (in both cases a constant doping concentration as a function of diameter is assumed). However, no dependence of the current on the wire diameter was observed (Fig. 9.14). A possible explanation is the influence of the contacts. Even though they are ohmic they could influence the result if their resistances are of the same order or larger than the resistance of the wire.The contact resistance can depend on the fabrication process. More measurements are required to investigate this further.

Conclusions

The electrical behaviour of InN nanowires is significantly different compared to GaN nanowires. There is no pronounced diameter dependence and no influence of UV illumination due to an already very high intrinsic conduction several orders of magnitude higher than GaN nanowires and also higher than Si-doped wires. Even very thin wires still exhibit a high conduction. This is caused by Fermi-level pinning in the conduction band, which results in a highly conductive surface accumulation layer. Even though the contacts are ohmic there is a bit of scatter in the conduction values, which can be related to a fluctuation of the contact resistances.

Chapter 10

Summary and Outlook

One of the main goals of this thesis was to get more insight into the mechanisms driving the growth of nitride nanowires by plasma-assisted molecular beam epitaxy (PA-MBE). The influence of the group-III and group-V flux as well as the substrate temperature T_{sub} has been studied leading to the conclusion that the III-V ratio determines the growth mode. N-rich conditions lead to nanowire growth and T_{sub} has an important influence. For GaN an increase of T_{sub} enhances the Ga desorption, thus lowering the III-V ratio, whereas for InN higher temperatures lead to a higher N evaporation and increases the III-V ratio. Ga desorption limits the temperature range to grow GaN nanowires and dissociation of InN is the limiting factor for InN nanowire growth. A reduction of the surface diffusivity on polar surfaces under N-rich conditions explains the anisotropic growth.

Growth kinetics of the nanowires show that there are two important contributions to the growth. The first is growth by direct impingement and its contribution is independent of the nanowire diameter. The second contribution comes from atoms, which absorb on the substrate or wire sidewalls and diffuse along the sidewalls to the top of the wire, which acts as an effective sink for the adatoms due to a reduced surface mobility on the polar top of the wires. This diffusion channel, which is enhanced at higher T_{sub}, becomes more significant for smaller wire diameters, because its contribution scales like 1/d. Experiments with an interruption of the growth and sharp interfaces in TEM images of heterostructures show that the suggestion in literature of a droplet-mediated PA-MBE nitride growth has to be discarded.

An accumulation or depletion of group-III adatoms during growth can lead to an increase or a reduction of the wire diameter. This can be compensated by changing one of the fluxes or the substrate temperature to produce wires with a uniform diameter.

Despite a thin amorphous silicon nitride wetting layer on the substrate surface, both GaN and InN nanowires grow in the wurtzite structure and epitaxially in a one-to-one relation to the Si(111) substrate surface. There is no evidence for cubic phases.

TEM images and optical studies display a high crystalline and optical quality of GaN and InN nanowires. Lattice constants determined from TEM images agree well with literature values for strain-free GaN and high-quality InN. The substrate induces some strain in the bottom part of the nanowires, especially in InN due to the lower T_{sub} than for GaN, which is released without the formation of dislocations. Only some stacking faults sometimes form at

the base of the wires. Optical spectra also exhibit a band gap consistent with strain-free GaN in the upper part of the wires. For InN a band gap value of $0.7 - 0.8\,\mathrm{eV}$ has been determined at low temperatures in agreement with recent literature reports for InN of high crystalline quality. The doping concentration and the position of the Fermi-level in InN depend very much on the crystalline quality. In general the luminescence of GaN and InN improves with increased T_{sub}. For GaN the defect-related peaks decrease and in InN the carrier concentration is reduced, which changes the shape of the PL spectrum.

Si- and Mg-doping can change the morphology of GaN nanowires, but the growth parameters can be chosen to produce wires with uniform diameter. Optical spectra confirm the effective incorporation of the dopant species in the nanowires despite a large nanowire surface and unfavourable growth conditions for doping, which are required for nitride nanowire growth.

GaN and InN nanowires display a high mechanical and chemical resistance against common processing steps in spite of a high aspect ratio and large free surface. Producing contacts to the wires by e-beam lithography allows to determine the electrical behaviour of GaN, InN and Si-doped GaN nanowires. Fermi-level pinning due to surface states has a major influence on all nanowires especially for diameters below 100 nm. For GaN the pinning induces a depletion region, which depends on the doping concentration. The conductivity for small diameters is low for undoped GaN, but can be significantly enhanced by UV illumination or Si-doping. The diameter dependence of the photocurrent displays a rapid drop below a critical radius equal to the extension of the depletion layer and the wires show a fast photoresponse in this region caused by a lowering of the barrier for surface recombination. The carrier concentration of GaN nanowires can be determined from the critical radius and is enhanced by Si-doping. In InN nanowires the Fermi-level pinning in the conduction band induces a highly conductive surface accumulation layer and as a result the nanowires display very high currents several orders of magnitude higher than the GaN nanowires, independent of illumination. There is no pronounced diameter dependence.

10.1 Outlook

The TEM investigations with AlN barriers have provided interesting information on the axial and lateral growth behaviour of GaN nanowires. Studying the lateral growth as a function of substrate temperature and III-V ratio could give valuable information on how to control lateral growth, which is important for growing core-shell structures. The influence of Si- and Mg-doping on the morphology of the nanowires could also be determined in more detail. In addition, samples with AlN barriers would allow to study the initial stages of the nanowire nucleation.

A deeper understanding of the lateral growth might help to find growth parameters for GaN nanowires at lower T_{sub}, which is favourable for Mg incorporation and a combination with In containing alloys (InN or InGaN).

By growing sequential Si- and Mg-doped sections in GaN nanowires a p-n junction can be created for applications as light emitting diode.

The surface has a major influence on the physical properties of the wires and changing the

surface by a passivation layer could show interesting effects. Initial experiments with capped InN nanowires show promising results. Lateral growth control is also important for in-situ passivation.

The cooperation with the group of Anna Cavallini at the University of Bologna has produced some interesting results on the electro-optical properties of the GaN nanowires as a function of their diameter. There is still a lot to learn, however. Also regarding the luminescence behaviour of nanowires a lot of questions remain open and hopefully the exciting experiments from Jaime Gomez Rivas and Gabriele Vecchi from the Center for Nanophotonics at the High Tech Campus in Eindhoven will produce a lot of interesting results.

Chapter 11

Zusammenfassung

Einer der Hauptziele dieser Arbeit war die Untersuchung der Wachstumsmechanismen von Nitrid Nanodrähten unter Benutzung der plasma-unsterstützten Molekularstrahlepitaxie. Der Einfluss des Gruppe-III und Gruppe-V Flusses sowie der Substrat-Temperatur wurde untersucht und führte zu der Schlussfolgerung, dass das III-V Verhältnis den Wachstumsmodus bestimmt. Stickstoffreiche Bedingungen führen zum Wachstum von Nanodrähten, wobei die Substrat-Temperatur einen wichtigen Einfluss hat. Ein Erhöhen der Substrat-Temperatur erhöht für GaN die Ga Desorption und letzteres erniedrigt das III-V Verhältnis. Für InN führen höhere Temperaturen zu einer höheren N-Verdampfung und diese erhöhen somit das III-V Verhältnis. Die Ga-Desorption begrenzt den Temperaturbereich, der für das Wachstum von GaN Nanodrähten genutzt werden kann. Dissoziation ist der einschränkende Faktor beim Wachstum der InN Nanodrähte. Eine Reduktion der Oberflächendiffusion auf polaren Oberflächen unter stickstoffreichen Bedingungen erklärt das anisotrope Wachstumsverhalten.

Die Wachstumskinetik der Nanodrähte zeigt, dass es zwei wichtige Beiträge zum Wachstum gibt. Der Erste ist das Wachstum durch direktes Auftreffen der Atome an der Oberseite der Nanodrähte. Der zweite Beitrag rührt her von Atomen, die auf dem Substrat oder den Seiten der Drähte adsorbieren und anschließend zur Oberseite hin diffundieren. Diese wirkt als eine effektive Senke für die Adatome infolge einer reduzierten Oberflächendiffusion an der polaren Oberseite der Nanodrähte. Der Diffusionskanal, der bei höherer Substrat-Temperatur an Bedeutung gewinnt, hat den größten Einfluss auf Nanodrähte mit kleinerem Durchmesser, da sein Beitrag wie 1/d skaliert. Experimente mit einer Wachstumsunterbrechung und die in TEM Bildern beobachteten scharfen Übergänge von Heterostrukturen zeigen, dass das in der Literatur vorgeschlagene Modell eines durch Tröpfchen unterstütztes Nitrid-Wachstums verworfen werden muss.

Eine Anreicherung oder Verarmung von Gruppe-III-Adatomen während des Wachstums kann zu einer Vergrößerung oder Reduktion des Nanodrahtdurchmessers führen. Durch Veränderung einer der Flüsse oder der Substrat-Temperatur kann man diesen Effekt kompensieren und somit Drähte mit gleichmäßigem Durchmesser herstellen.

Trotz einer dünnen amorphen Siliziumnitrid-Benetzungsschicht an der Substratoberfläche, wachsen GaN sowie InN Nanodrähte in der Wurzit-Struktur und in einem epitaktischem eins-zu-eins Verhältnis zur Si(111) Oberfläche. Kubische Phasen wurden nicht festgestellt.

TEM Bilder und optische Untersuchungen zeigen die hohe kristalline und optische Qualität der GaN und InN Nanodrähte. Die Gitterkonstanten, die mittels TEM bestimmt wurden, stimmen gut mit Literaturwerten für verspannungsfreies GaN und hochwertiges InN überein. Das Substrat kann im unteren Teil der Nanodrähte eine Verspannung induzieren, die relaxiert ohne dabei Versetzungen hervorzurufen. Dies gilt insbesondere für InN infolge der niedrigeren Substrat-Temperatur im Vergleich zu GaN. Nur Stapelfehler bilden sich gelegentlich im unteren Bereich der Drähte aus. Optische Spektren im oberen Bereich der Drähte zeigen eine Bandlücke, die mit verspannungsfreiem GaN übereinstimmt. Für InN wurde eine Bandlücke von $0.7 - 0.8\,\mathrm{eV}$ bei tiefen Temperaturen bestimmt. Dies ist in Übereinstimmung mit aktuellen Berichten in der Literatur für InN hoher kristalliner Qualität. Die Dotierungskonzentration und die Position des Fermi-Niveaus in InN hängen sehr stark von der kristallinen Qualität ab. Im allgemeinen verbessert sich die Lumineszenz des GaN und InN bei Erhöhung der Substrat-Temperatur. Die Intensität der durch Defekte hervorgerufenen Übergänge nimmt ab für GaN und in InN wird die Ladungsträgerkonzentration reduziert, die die Form des PL Spektrums verändert.

Si- und Mg-Dotierung können die Morphologie der GaN Nanodrähte verändern. Allerdings können die Wachstumsparameter so gewählt werden, dass Drähte mit gleichmäßigem Durchmesser resultieren. Optische Spektren bestätigen den effektiven Einbau von Dotierstoffen in den Nanodrähten trotz der großen Nanodrahtoberfläche und der ungünstigen Wachstumsbedingungen für Dotierung. Diese Bedingungen sind auf der anderen Seite jedoch notwendig für das Wachstum von Nitrid Nanodrähten.

GaN und InN Nanodrähte zeigen einen hohen mechanischen und chemischen Widerstand gegen herkömmliche Prozessschritte trotz eines hohen Aspektverhältnisses und einer großen freien Oberfläche. Die Herstellung von Kontakten zu den Drähten mittels Elektronenstrahllithographie erlaubt es, das elektrische Verhalten von GaN, InN und Si-dotierten GaN Nanodrähten zu bestimmen. Fermi-Niveau Pinning infolge von Oberflächenzuständen hat einen großen Einfluss auf das elektrische Verhalten aller Nanodrähte, insbesondere für Durchmesser unterhalb 100 nm. Für GaN induziert das Pinning eine Verarmungszone, die von der Dotierungskonzentration abhängt. Für undotiertes GaN ist die Leitfähigkeit für kleine Durchmesser niedrig, kann jedoch erheblich erhöht werden durch UV Beleuchtung oder Si-Dotierung. Die Durchmesserabhängigkeit des Photostroms zeigt einen starken Abfall unterhalb eines kritischen Radius, der mit der Ausdehnung der Verarmungszone korreliert. Außerdem zeigen die Nanodrähte in diesem Bereich einen instantanen Photoresponse, der von einer Reduktion der Barriere für Oberflächenrekombination herrührt. Die Ladungsträgerkonzentration von GaN Nanodrähten kann aus dem kritischen Radius bestimmt werden und wird durch eine Si-Dotierung erhöht. In InN Nanodrähten induziert das Fermi-Niveau-Pinning im Leitungsband einen sehr stark leitenden Oberflächenanreicherungskanal, und demzufolge zeigen diese Nanodrähte sehr hohe Ströme, und zwar um einige Größenordnungen höher als für GaN Nanodrähte und dies unabhängig von der Beleuchtung. Es gibt keine prägnante Durchmesserabhängigkeit.

List of Figures

List of Tables

Bibliography

[1] M. T. Bjork, B. J. Ohlsson, T. Sass, A. I. Persson, C. Thelander, M. H. Magnusson, K. Deppert, L. R. Wallenberg, and L. Samuelson, 'One-dimensional heterostructures in semiconductor nanowhiskers', *Appl. Phys. Lett.*, **vol. 80 (2002)(6)**, pp. 1058–1060, doi:10.1063/1.1447312.

[2] M. T. Bjork, B. J. Ohlsson, C. Thelander, A. I. Persson, K. Deppert, L. R. Wallenberg, and L. Samuelson, 'Nanowire resonant tunneling diodes', *Appl. Phys. Lett.*, **vol. 81 (2002)(23)**, pp. 4458–4460, doi:10.1063/1.1527995.

[3] X. Duan, Y. Huang, R. Agarwal, and C. Lieber, 'Single-nanowire electrically driven lasers', *Nature*, **vol. 421 (2003)**, pp. 241–245, doi:10.1038/nature01353.

[4] A. Greytak, L. Lauhon, M. Gudiksen, and C. Lieber, 'Growth and transport properties of complementary germanium nanowire field-effect transistors', *Appl. Phys. Lett.*, **vol. 84 (2004)(21)**, p. 4176, doi:10.1063/1.1755846.

[5] C. Thelander, T. Martensson, M. T. Bjork, B. J. Ohlsson, M. W. Larsson, L. R. Wallenberg, and L. Samuelson, 'Single-electron transistors in heterostructure nanowires', *Appl. Phys. Lett.*, **vol. 83 (2003)(10)**, pp. 2052–2054, doi:10.1063/1.1606889.

[6] Z. Zhong, D. Wang, Y. Cui, M. Bockrath, and C. Lieber, 'Nanowire crossbar arrays as address decoders for integrated nanosystems', *Science*, **vol. 302 (2003)(5649)**, pp. 1377–1379, doi:10.1126/science.1090899.

[7] Y. Taniyasu, M. Kasu, and T. Makimoto, 'An aluminium nitride light-emitting diode with a wavelength of 210 nanometres', *Nature*, **vol. 441 (2006)**, pp. 325–328, doi:10.1038/nature04760.

[8] E. Calleja, M. Sanchez-Garcia, F. Sanchez, F. Calle, F. Naranjo, E. Munoz, U. Jahn, and K. Ploog, 'Luminescence properties and defects in GaN nanocolumns grown by molecular beam epitaxy', *Phys. Rev. B*, **vol. 62 (2000)(24)**, p. 16826, doi:10.1103/PhysRevB.62.16826.

[9] H. Morkoç, *Nitride Semiconductors and Devices*, Springer (1999).

[10] Ioffe Physico-Technical Institute, 'New Semiconductor Materials. Characteristics and Properties', `www.ioffe.ru/SVA/NSM/`.

[11] V. Y. Davydov, A. A. Klochikhin, V. V. Emtsev, S. V. Ivanov, V. V. Vekshin, F. Bechstedt, J. Furthmuller, H. Harima, A. V. Mudryi, A. Hashimoto, A. Yamamoto, J. Aderhold, J. Graul, and E. E. Haller, 'Band gap of InN and In-rich $In_xGa_{1-x}N$ alloys (0.36 $< x < 1$)', *Phys. Status Solidi B*, **vol. 230 (2002)**, pp. R4–R6, doi:10.1002/1521-3951(200204)230:2<R4::AID-PSSB99994>3.0.CO;2-Z.

[12] C. Stampfl and C. G. Van de Walle, 'Energetics and electronic structure of stacking faults in AlN, GaN, and InN', *Phys. Rev. B*, **vol. 57 (1998)(24)**, pp. R15052–R15055, doi:10.1103/PhysRevB.57.R15052.

[13] E. S. Hellman, 'The Polarity of GaN: a Critical Review', *MRS Internet Journal of Nitride Semiconductor Research*, **vol. 3 (1998)(11)**, pp. 1–11.

[14] Office of Naval Research, 'National Compound Semiconductor Roadmap', `www.onr.navy.mil/sci_tech/31/312/ncsr/properties.asp`.

[15] M. Levinshtein, S. Rumyantsev, and M. Shur, *Properties of advanced semiconductor Materials: GaN, AlN, InN, BN, SiC, SiGe*, Wiley, New York (2001).

[16] V. Y. Davydov, A. A. Klochikhin, R. P. Seisyan, V. V. Emtsev, S. V. Ivanov, F. Bechstedt, J. Furthmuller, H. Harima, V. Mudryi, J. Aderhold, O. Semchinova, and J. Graul, 'Absorption and emission of hexagonal InN. Evidence of narrow fundamental band gap', *Phys. Status Solidi B*, **vol. 229 (2002)**, pp. R1–R3, doi:10.1002/1521-3951(200202)229:3<R1::AID-PSSB99991>3.0.CO;2-O.

[17] S. Keller and S. P. DenBaars, 'Metalorganic chemical vapor deposition of group III nitrides–a discussion of critical issues', *J. Cryst. Growth*, **vol. 248 (2003)**, pp. 479–486, doi:10.1016/S0022-0248(02)01867-5.

[18] S. Pearton, R. J. Shul, and F. Ren, 'A Review of Dry Etching of GaN and Related Materials', *MRS Internet Journal of Nitride Semiconductor Research*, **vol. 5 (2000)(11)**, pp. 1–38.

[19] L. Pauling, *The Nature of the Chemical Bond (and the Structure of Molecules and Crystals: An Introduction to Modern Structural Chemistry)*, Cornell University Press, 3 ed. (1960).

[20] D. Koleske, A. Wickenden, R. Henry, W. DeSisto, and R. Gorman, 'Growth model for GaN with comparison to structural, optical, and electrical properties', *J. Appl. Phys.*, **vol. 84 (1998)(4)**, pp. 1998–2010, doi:10.1063/1.368353.

[21] Y. Seki, H. Watanabe, and J. Matsui, 'Impurity effect on grown-in dislocation density of InP and GaAs crystals', *J. Appl. Phys.*, **vol. 49 (1978)(2)**, pp. 822–828.

[22] S. Pearton, Z. C. Zopler, R. J. Shul, and F. Ren, 'GaN: Processing, defects, and devices', *J. Appl. Phys.*, **vol. 86 (1999)(1)**, pp. 1–78.

[23] H. Lu, W. J. Schaff, J. Hwang, H. Wu, W. Yeo, A. Pharkya, and L. F. Eastman, 'Improvement on epitaxial grown of InN by migration enhanced epitaxy', *Appl. Phys. Lett.*, **vol. 77 (2000)(16)**, pp. 2548–2550, doi:10.1063/1.1318235.

[24] T. Inushima, V. V. Mamutin, V. A. Vekshin, S. V. Ivanov, T. Sakon, M. Motokawa, and S. Ohoya, 'Physical properties of InN with the band gap energy of 1.1 eV', *J. Cryst. Growth*, **vol. 227-228 (2001)**, pp. 481–485, doi:10.1016/S0022-0248(01)00747-3.

[25] V. Y. Davydov, A. A. Klochikhin, V. V. Emtsev, D. A. Kurdyukov, S. V. Ivanov, V. A. Vekshin, F. Bechstedt, J. Furthmüller, J. Aderhold, J. Graul, A. V. Mudryi, H. Harima, A. Hashimoto, A. Yamamoto, and E. E. Haller, 'Band Gap of Hexagonal InN and InGaN Alloys', *Phys. Status Solidi B*, **vol. 234 (2002)**, pp. 787–795, doi:10.1002/1521-3951(200212)234:3<787::AID-PSSB787>3.0.CO;2-H.

[26] J. Wu, W. Walukiewicz, K. M. Yu, J. W. A. III, E. E. Haller, H. Lu, W. J. Schaff, Y. Saito, and Y. Nanishi, 'Unusual properties of the fundamental band gap of InN', *Appl. Phys. Lett.*, **vol. 80 (2002)(21)**, pp. 3967–3969, doi:10.1063/1.1482786.

[27] F. Bechstedt, J. Furthmüller, M. Ferhat, L. K. Teles, L. M. R. Scolfaro, J. R. Leite, V. Y. Davydov, O. Ambacher, and R. Goldhahn, 'Energy gap and optical properties of InxGa1-xN', *Phys. Status Solidi A*, **vol. 195 (2003)(3)**, pp. 628–633, doi:10.1002/pssa.200306164.

[28] E. Burstein, 'Anomalous Optical Absorption Limit in InSb', *Physical Review*, **vol. 93 (1954)(3)**, pp. 632–633, doi:10.1103/PhysRev.93.632.

[29] T. S. Moss, 'The Interpretation of the Properties of Indium Antimonide', *Proceedings of the Physical Society. Section B*, **vol. 67 (1954)(10)**, pp. 775–782, doi:10.1088/0370-1301/67/10/306.

[30] J. Wu, W. Walukiewicz, W. Shan, K. M. Yu, J. W. A. III, E. E. Haller, H. Lu, and W. J. Schaff, 'Effects of the narrow band gap on the properties of InN', *Phys. Rev. B*, **vol. 66 (2002)(20)**, 201403, doi:10.1103/PhysRevB.66.201403.

[31] J. Wu, W. Walukiewicz, S. X. Li, R. Armitage, J. C. Ho, E. R. Weber, E. E. Haller, H. Lu, W. J. Schaff, A. Barcz, and R. Jakiela, 'Effects of electron concentration on the optical absorption edge of InN', *Appl. Phys. Lett.*, **vol. 84 (2004)(15)**, pp. 2805–2807, doi:10.1063/1.1704853.

[32] T. Shubina, S. Ivanov, V. N. Jmerik, D. D. Solnyshkov, V. A. Vekshin, P. S. Kop?ev, A. Vasson, J. Leymarie, A. Kavokin, H. Amano, K. Shimono, A. Kasic, and B. Monemar, 'Mie Resonances, Infrared Emission, and the Band Gap of InN', *Phys. Rev. Lett.*, **vol. 92 (2004)(11)**, 117407, doi:10.1103/PhysRevLett.92.117407.

[33] G. Mie, 'Beiträge zur Optik trüber Medien, speziell kolloidaler Metallösungen', *Ann. Phys. (Leipzig)*, **vol. 25 (1908)**, pp. 377–445.

[34] F. Bechstedt, J. Furthmuller, O. Ambacher, and R. Goldhahn, 'Comment on "Mie Resonances, Infrared Emission, and the Band Gap of InN"', *Phys. Rev. Lett.*, **vol. 93 (2004)(26)**, 269701, doi:10.1103/PhysRevLett.93.269701.

[35] T. V. Shubina, S. V. Ivanov, V. N. Jmerik, P. S. Kop'ev, A. Vasson, J. Leymarie, A. Kavokin, H. Amano, B. Gil, O. Briot, and B. Monemar, 'Shubina et al. Reply:', *Phys. Rev. Lett.*, **vol. 93 (2004)(26)**, 269702, doi:10.1103/PhysRevLett.93.269702.

[36] T. V. Shubina, S. V. Ivanov, V. N. Jmerik, D. D. Solnyshkov, V. A. Vekshin, P. S. Kop'ev, A. Vasson, J. Leymarie, A. Kavokin, H. Amano, K. Shimono, A. Kasic, and B. Monemar, 'Erratum: Mie Resonances, Infrared Emission, and the Band Gap of InN [Phys. Rev. Lett. **92**, 117407 (2004)]', *Phys. Rev. Lett.*, **vol. 95 (2005)(20)**, 209901, doi:10.1103/PhysRevLett.95.209901.

[37] B. Monemar, P. Paskov, and A. Kasic, 'Optical properties of InN–the bandgap question', *Superlattices Microstruct.*, **vol. 38 (2005)(1)**, pp. 38–56, doi:10.1016/j.spmi.2005.04.006.

[38] P. Specht, J. Ho, X. Xu, R. Armitage, E. Weber, R. Erni, and C. Kisielowski, 'Band transitions in wurtzite GaN and InN determined by valence electron energy loss spectroscopy', *Solid State Commun.*, **vol. 135 (2005)**, pp. 340–344, doi:10.1016/j.ssc.2005.04.041.

[39] B. Arnaudov, T. Paskova, P. P. Paskov, B. Magnusson, E. Valcheva, B. Monemar, H. Lu, W. J. Schaff, H. Amano, and I. Akasaki, 'Energy position of near-band-edge emission spectra of InN epitaxial layers with different doping levels', *Phys. Rev. B*, **vol. 69 (2004)(11)**, 115216, doi:10.1103/PhysRevB.69.115216.

[40] A. Klochikhin, V. Davydov, V. Emtsev, A. Sakharov, V. Kapitonov, B. Andreev, H. Lu, and W. J. Schaff, 'Photoluminescence of n-InN with low electron concentrations', *Phys. Status Solidi A*, **vol. 203 (2006)(1)**, pp. 50–58, doi:10.1002/pssa.200563512.

[41] P. Preuss, 'On the horizon: a virtually perfect solar cell', Science beat (2002), `www.lbl.gov/Science-Articles/Archive/MSD-perfect-solar-cell.html`.

[42] H. J. Fan, P. Werner, and M. Zacharias, 'Semiconductor nanowires: From self-organization to patterned growth', *Small*, **vol. 2 (2006)(6)**, pp. 700–717, doi:10.1002/smll.200500495.

[43] L. Samuelson, 'Self-forming nanoscale devices', *Materials Today*, **vol. 6 (2003)(10)**, pp. 22–31, doi:10.1016/S1369-7021(03)01026-5.

[44] Y. Xia, P, Yang, Y. Sun, Y. Wu, B. Mayers, B. Gates, Y. Yin, F. Kim, and H. Yan, 'One-Dimensional Nanostructures: Synthesis, Characterization, and Applications', *Adv. Mater.*, **vol. 15 (2003)(5)**, pp. 353–389, doi:10.1002/adma.200390087.

[45] M. Zach, K. Ng, and R. Penner, 'Molybdenum Nanowires by Electrodeposition', *Science*, **vol. 290 (2000)**, p. 2120, doi:10.1126/science.290.5499.2120.

[46] M. Kawamura, N. Paul, V. Cherepanov, and B. Voigtländer, 'Nanowires and Nanorings at the Atomic Level', *Phys. Rev. Lett.*, **vol. 91 (2003)(9)**, p. 096102, doi: 10.1103/PhysRevLett.91.096102.

[47] G. W. Sears, 'Mercury Whiskers', *Acta Metallurgica*, **vol. 1 (1953)(4)**, pp. 457–459, doi:10.1016/0001-6160(53)90131-X.

[48] R. S. Wagner, W. C. Ellis, K. A. Jackson, and S. M. Arnold, 'Study of the Filamentary Growth of Silicon Crystals from the Vapor', *J. Appl. Phys.*, **vol. 35 (1964)(10)**, pp. 2993–3000, doi:10.1063/1.1713143.

[49] G. A. Bootsma and H. J. Gassen, 'A quantitative study on the growth of silicon whiskers from silane and germanium whiskers from germane', *J. Cryst. Growth*, **vol. 10 (1971)(3)**, pp. 223–234, doi:10.1016/0022-0248(71)90188-6.

[50] E. I. Givargizov, 'Fundamental aspects of VLS growth', *J. Cryst. Growth*, **vol. 31 (1975)**, pp. 20–30, doi:10.1016/0022-0248(75)90105-0.

[51] A. M. Morales and C. M. Lieber, 'A Laser Ablation Method for the Synthesis of Crystalline Semiconductor Nanowires', *Science*, **vol. 279 (1998)(5348)**, pp. 208–211, doi: 10.1126/science.279.5348.208.

[52] M. Gudiksen, J. Wang, and C. Lieber, 'Synthetic Control of the Diameter and Length of Single Crystal Semiconductor Nanowires', *J. Phys. Chem. B*, **vol. 105 (2001)(19)**, pp. 4062–4064, doi:10.1021/jp010540y.

[53] V. V. Mamutin, 'Growth of A^3N whiskers and plate-shaped crystals by molecular-beam epitaxy with the participation of the liquid phase', *Tech. Phys. Lett.*, **vol. 25 (1999)(9)**, pp. 741–744.

[54] L. Schubert, P. Werner, N. D. Zakharov, G. Gerth, F. M. Kolb, L. Long, U. Gosele, and T. Y. Tan, 'Silicon nanowhiskers grown on <111>Si substrates by molecular-beam epitaxy', *Appl. Phys. Lett.*, **vol. 84 (2004)(24)**, pp. 4968–4970, doi:10.1063/1.1762701.

[55] G. W. Sears, 'A mechanism of whisker growth', *Acta Metallurgica*, **vol. 3 (1955)(4)**, pp. 367–369.

[56] G. W. Sears, 'A growth mechanism for mercury whiskers', *Acta Metallurgica*, **vol. 3 (1955)(4)**, pp. 361–366, doi:10.1016/0001-6160(55)90041-9.

[57] R. S. Wagner and W. C. Ellis, 'Vapor-Liquid-Solid mechanism of single crystal growth', *Appl. Phys. Lett.*, **vol. 4 (1964)(5)**, pp. 89–90, doi:10.1063/1.1753975.

[58] E. I. Givargizov and N. N. Sheftal', 'Morphology of silicon whiskers grown by the VLS-technique', *J. Cryst. Growth*, **vol. 9 (1971)**, pp. 326–329, doi:10.1016/0022-0248(71)90250-8.

[59] E. I. Givargizov, 'Periodic instability in whisker growth', *J. Cryst. Growth*, **vol. 20 (1973)(3)**, pp. 217–226, doi:10.1016/0022-0248(73)90008-0.

[60] F. Frank, 'Crystal growth and dislocations', *Advances in Physics*, **vol. 1 (1952)(1)**, pp. 91–109, doi:10.1080/00018735200101171.

[61] N. Ashcroft and N. Mermin, *Solid state physics*, Harcourt College Publishers (1976).

[62] J. M. Blakely and K. A. Jackson, 'Growth of crystal whiskers', *J. Chem. Phys.*, **vol. 37 (1962)(2)**, p. 428.

[63] V. Ruth and J. Hirth, 'Kinetics of Diffusion-Controlled Whisker Growth', *J. Chem. Phys.*, **vol. 41 (1964)(10)**, pp. 3139–3149.

[64] S. Kodambaka, J. Tersoff, M. C. Reuter, and F. M. Ross, 'Diameter-Independent Kinetics in the Vapor-Liquid-Solid Growth of Si Nanowires', *Phys. Rev. Lett.*, **vol. 96 (2006)(9)**, 096105, doi:10.1103/PhysRevLett.96.096105.

[65] K. Hiruma, M. Yazawa, T. Katsuyama, K. Ogawa, K. Haraguchi, M. Koguchi, and H. Kakibayashi, 'Growth and optical properties of nanometer-scale GaAs and InAs whiskers', *J. Appl. Phys.*, **vol. 77 (1995)(2)**, pp. 447–462, doi:10.1063/1.359026.

[66] K. Haraguchi, T. Katsuyama, K. Hiruma, and K. Ogawa, 'GaAs p-n junction formed in quantum wire crystals', *Appl. Phys. Lett.*, **vol. 60 (1992)(6)**, pp. 745–747, doi:10.1063/1.106556.

[67] M. Yazawa, K. Haraguchi, M. Koguchi, T. Katsuyama, K. Hiruma, and H. Ohta, 'Nanocolumns composed of GaAs-InAs jointed whiskers and SiO[sub 2] covers', *Appl. Phys. Lett.*, **vol. 65 (1994)(9)**, pp. 1157–1158, doi:10.1063/1.113010.

[68] T. Sato, K. Hiruma, M. Shirai, K. Tominaga, K. Haraguchi, T. Katsuyama, and T. Shimada, 'Site-controlled growth of nanowhiskers', *Appl. Phys. Lett.*, **vol. 66 (1995)(2)**, pp. 159–161, doi:10.1063/1.113549.

[69] C. M. Lieber and Z. L. Wang, 'Functional nanowires', *Mrs Bulletin*, **vol. 32 (2007)(2)**, pp. 99–108.

[70] Y. Huang, X. Duan, and C. M. Lieber, 'Nanowires for Integrated Multicolor Nanophotonics', *Small*, **vol. 1 (2005)(1)**, pp. 142–147, doi:10.1002/smll.200400030.

[71] D. Whang, S. Jin, and C. M. Lieber, 'Large-Scale Hierarchical Organization of Nanowires for Functional Nanosystems', *Jpn. J. Appl. Phys.*, **vol. 43 (2004)(7B)**, pp. 4465–4470, doi:10.1143/JJAP.43.4465.

[72] K. A. Dick, K. Deppert, L. S. Karlsson, M. W. Larsson, W. Seifert, L. R. Wallenberg, and L. Samuelson, 'Directed growth of branched nanowire structures', *Mrs Bulletin*, **vol. 32 (2007)(2)**, pp. 127–133.

[73] L. Samuelson, C. Thelander, M. Bjork, M. Borgstrom, K. Deppert, K. Dick, A. Hansen, T. Martensson, N. Panev, A. Persson, W. Seifert, N. Skold, M. Larsson, and L. Wallenberg, 'Semiconductor nanowires for 0D and 1D physics and applications', *Physica E*, **vol. 25 (2004)**, pp. 313–318, doi:10.1016/j.physe.2004.06.030.

[74] M. Law, J. Goldberger, and P. Yang, 'Semiconductor nanowires and nanotubes', *Annu. Rev. Mater. Res.*, **vol. 34 (2004)**, pp. 83–122, doi: 10.1146/annurev.matsci.34.040203.112300.

[75] E. P. A. M. Bakkers, M. T. Borgstrom, and M. A. Verheijen, 'Epitaxial growth of III-V nanowires on group IV substrates', *Mrs Bulletin*, **vol. 32 (2007)(2)**, pp. 117–122.

[76] Y.-J. Doh, J. A. van Dam, A. L. Roest, E. P. A. M. Bakkers, L. P. Kouwenhoven, and S. D. Franceschi, 'Tunable Supercurrent Through Semiconductor Nanowires', *Science*, **vol. 309 (2005)**, p. 272, doi:10.1126/science.1113523.

[77] V. G. Dubrovskii, G. E. Cirlin, I. P. Soshnikov, A. A. Tonkikh, N. V. Sibirev, Y. B. Samsonenko, and V. M. Ustinov, 'Diffusion-induced growth of GaAs nanowhiskers during molecular beam epitaxy: Theory and experiment', *Phys. Rev. B*, **vol. 71 (2005)(20)**, 205325.

[78] J. B. Hannon, S. Kodambaka, F. M. Ross, and R. M. Tromp, 'The influence of the surface migration of gold on the growth of silicon nanowires', *Nature*, **vol. 440 (2006)**, pp. 69–71, doi:10.1038/nature04574.

[79] L. Jensen, M. Bjoerk, S. Jeppesen, A. Persson, B. Ohlsson, and L. Samuelson, 'Role of surface diffusion in chemical beam epitaxy of InAs Nanowires', *Nano Lett.*, **vol. 4 (2004)(10)**, pp. 1961–1964, doi:10.1021/nl048825k.

[80] J. Johansson, C. P. T. Svensson, T. Martensson, L. Samuelson, and W. Seifert, 'Mass Transport Model for Semiconductor Nanowire Growth', *J. Phys. Chem. B*, **vol. 109 (2005)**, pp. 13567–13571, doi:10.1021/jp051702j.

[81] J. Johansson, B. A. Wacaser, K. A. Dick, and W. Seifert, 'Growth related aspects of epitaxial nanowires', *Nanotechnology*, **vol. 17 (2006)**, p. S335, doi:10.1088/0957-4484/17/11/S21.

[82] A. Persson, M. Larsson, S. Stenström, B. Ohlsson, L. Samuelson, and L. Wallenberg, 'Solid-phase diffusion mechanism for GaAs nanowire growth', *Nat. Mater.*, **vol. 3 (2004)**, pp. 677–681, doi:10.1038/nmat1220.

[83] M. C. Plante and R. R. Lapierre, 'Growth mechanisms of GaAs nanowires by gas source molecular beam epitaxy', *J. Cryst. Growth*, **vol. 286 (2006)(2)**, p. 394, doi: 10.1016/j.jcrysgro.2005.10.024.

[84] F. M. Ross, J. Tersoff, and M. C. Reuter, 'Sawtooth Faceting in Silicon Nanowires', *Phys. Rev. Lett.*, **vol. 95 (2005)(14)**, pp. 146104–4, doi:10.1103/PhysRevLett.95.146104.

[85] W. Seifert, M. Borgstrom, K. Deppert, K. A. Dick, J. Johansson, M. W. Larsson, T. Martensson, N. Skold, C. Patrik T. Svensson, and B. A. Wacaser, 'Growth of one-dimensional nanostructures in MOVPE', *J. Cryst. Growth*, **vol. 272 (2004)(1-4)**, pp. 211–220, doi:10.1016/j.jcrysgro.2004.09.023.

[86] J. Kikkawa, Y. Ohno, and S. Takeda, 'Growth rate of silicon nanowires', *Appl. Phys. Lett.*, **vol. 86 (2005)(12)**, pp. 123109–3, doi:10.1063/1.1888034.

[87] K. A. Dick, K. Deppert, T. Martensson, B. Mandl, L. Samuelson, and W. Seifert, 'Failure of the Vapor-Liquid-Solid Mechanism in Au-Assisted MOVPE Growth of InAs Nanowires', *Nano Lett.*, **vol. 5 (2005)(4)**, pp. 761–764, doi:10.1021/nl050301c.

[88] R. Dingle, K. SHaklee, R. Leheny, and R. Zetterstrom, 'Stimulated Emission and Laser Action in Gallium Nitride', *Appl. Phys. Lett.*, **vol. 19 (1971)(1)**, pp. 5–7, doi: 10.1063/1.1653730.

[89] W. Han, S. Fan, Q. Li, and Y. Hu, 'Synthesis of Gallium Nitride Nanorods Through a Carbon Nanotube-Confined Reaction', *Science*, **vol. 277 (1997)(5330)**, pp. 1287–1289, doi:10.1126/science.277.5330.1287.

[90] M. Yoshizawa, A. Kikuchi, M. Mori, N. Fujita, and K. Kishino, 'Growth of Self-Organized GaN Nanostructures on Al2O3(0001) by RF-Radical Source Molecular Beam Epitaxy', *Jpn. J. Appl. Phys.*, **vol. 36 (1997)**, pp. L459–L462, doi: 10.1143/JJAP.36.L459.

[91] M. A. Sanchez-Garcia, E. Calleja, E. Monroy, F. J. Sanchez, F. Calle, E. Munoz, and R. Beresford, 'The effect of the III/V ratio and substrate temperature on the morphology and properties of GaN- and AlN-layers grown by molecular beam epitaxy on Si(111)', *J. Cryst. Growth*, **vol. 183 (1998)(1-2)**, p. 23.

[92] E. Calleja, M. Sanchez-Garcia, F. Sanchez, F. Calle, F. Naranjo, E. Munoz, S. Molina, A. Sanchez, F. Pacheco, and R. Garcia, 'Growth of III-nitrides on Si(111) by molecular beam epitaxy. Doping, optical, and electrical properties', *J. Cryst. Growth*, **vol. 201-202 (1999)**, pp. 296–317, doi:10.1016/S0022-0248(98)01346-3.

[93] S. Nakamura, T. Mukai, and M. Senoh, 'Candela-class high-brightness InGaN/AlGaN double-heterostructure blue-light-emitting diodes', *Appl. Phys. Lett.*, **vol. 64 (1994)(13)**, pp. 1687–1689.

[94] S. Nakamura, M. Senoh, S. ichi Nagahama, N. Iwasa, T. Yamada, T. Matsushita, H. Kiyoku, and Y. Sugimoto, 'InGaN-Based Multi-Quantum-Well-Structure Laser Diodes', *Jpn. J. Appl. Phys.*, **vol. 35 (1996)**, pp. L74–L76, doi:10.1143/JJAP.35.L74.

[95] F. Ponce and D. Bour, 'Nitride-based semiconductors for blue and green light-emitting devices', *Nature*, **vol. 386 (1997)**, pp. 351–359, doi:10.1038/386351a0.

[96] S. Nakamura, 'The Roles of Structural Imperfections in InGaN-Based Blue Light-Emitting Diodes and Laser Diodes', *Science*, **vol. 281 (1998)(5379)**, pp. 956–961, doi:10.1126/science.281.5379.956.

[97] P. J. Pauzauskie and P. Yang, 'Nanowire photonics', *Materials Today*, **vol. 9 (2006)(10)**, pp. 36–45, doi:10.1016/S1369-7021(06)71652-2.

[98] T. Zywietz, J. Neugebauer, and M. Scheffler, 'Adatom diffusion at GaN (0001) and (0001) surfaces', *Appl. Phys. Lett.*, **vol. 73 (1998)(4)**, pp. 487–489, doi: 10.1063/1.121909.

[99] M. Ding, H. Kim, and A. I. Akinwande, 'Observation of valence band electron emission from n-type silicon field emitter arrays', *Appl. Phys. Lett.*, **vol. 75 (1999)(6)**, pp. 823–825, doi:10.1063/1.124525.

[100] E. I. Givargizov, 'Ultrasharp tips for field emission applications prepared by the vapor–liquid–solid growth technique', *J. Vac. Sci. Technol., B*, **vol. 11 (1993)(2)**, pp. 449–453, doi:10.1116/1.586882.

[101] F. C. K. Au, K. W. Wong, Y. H. Tang, Y. F. Zhang, I. Bello, and S. T. Lee, 'Electron field emission from silicon nanowires', *Appl. Phys. Lett.*, **vol. 75 (1999)(12)**, pp. 1700–1702, doi:10.1063/1.124794.

[102] E. C. Heeres, E. P. A. M. Bakkers, A. L. Roest, M. Kaiser, T. H. Oosterkamp, and N. de Jonge, 'Electron emission from individual indium arsenide semiconductor nanowires', *Nano Lett.*, **vol. 7 (2007)(2)**, pp. 536–540, doi:10.1021/nl062554r.

[103] E. I. Givargizov, A. N. Kiselev, L. N. Obolenskaya, and A. N. Stepanova, 'Nanometric tips for scanning probe devices', *Appl. Surf. Sci.*, **vol. 67 (1993)(1-4)**, pp. 73–81, doi:10.1016/0169-4332(93)90297-O.

[104] S. D. Franceschi, J. A. van Dam, E. P. A. M. Bakkers, L. F. Feiner, L. Gurevich, and L. P. Kouwenhoven, 'Single-electron tunneling in InP nanowires', *Appl. Phys. Lett.*, **vol. 83 (2003)(2)**, pp. 344–346, doi:10.1063/1.1590426.

[105] J. van Dam, S. de Franceschi, E. Bakkers, and L. Kouwenhoven, 'Elektronica met nanodraden', *Nederlands tijdschrift voor natuurkunde*, **vol. 69 (2003)(7)**, pp. 240–243.

[106] Y. Cui, Q. Wei, H. Park, and C. M. Lieber, 'Nanowire Nanosensors for Highly Sensitive and Selective Detection of Biological and Chemical Species', *Science*, **vol. 293 (2001)(5533)**, pp. 1289–1292, doi:10.1126/science.1062711.

[107] F. Patolsky, B. P. Timko, G. F. Zheng, and C. M. Lieber, 'Nanowire-based nanoelectronic devices in the life sciences', *Mrs Bulletin*, **vol. 32 (2007)(2)**, pp. 142–149.

[108] X. Duan, Y. Huang, Y. Cui, J. Wang, and C. M. Lieber, 'Indium phosphide nanowires as building blocks for nanoscale electronic and optoelectronic devices', *Nature*, **vol. 409 (2001)(6816)**, pp. 66–69, doi:10.1038/35051047.

[109] M. Gudiksen, L. Lauhon, J. Wang, D. Smith, and C. Lieber, 'Growth of nanowire superlattice structures for nanoscale photonics and electronics', *Nature*, **vol. 415 (2002)**, p. 617, doi:10.1038/415617a.

[110] M. H. M. van Weert, O. Wunnicke, A. L. Roest, T. J. Eijkemans, A. Y. Silov, J. E. M. Haverkort, G. W. 't Hooft, and E. P. A. M. Bakkers, 'Large redshift in photoluminescence of p-doped InP nanowires induced by Fermi-level pinning', *Appl. Phys. Lett.*, **vol. 88 (2006)(4)**, 043109.

[111] S. C. Erwin, L. Zu, M. I. Haftel, A. L. Efros, T. A. Kennedy, and D. J. Norris, 'Doping semiconductor nanocrystals', *Nature*, **vol. 436 (2005)(7047)**, pp. 91–94, doi: 10.1038/nature03832.

[112] Y. Wang, V. Schmidt, S. Senz, and U. Gosele, 'Epitaxial growth of silicon nanowires using an aluminium catalyst', *Nature Nanotechnology*, **vol. 1 (2006)(3)**, pp. 186–189, doi:10.1038/nnano.2006.133.

[113] B. Mandl, J. Stangl, T. Martensson, A. Mikkelsen, J. Eriksson, L. Karlsson, G. Bauer, L. Samuelson, and W. Seifert, 'Au-Free Epitaxial Growth of InAs Nanowires', *Nano Lett.*, **vol. 6 (2006)(8)**, pp. 1817–1821, doi:10.1021/nl060452v.

[114] U. Goesele, 'How clean is too clean?', *Nature*, **(2006)**, doi:10.1038/nature04609.

[115] A. L. Roest, M. A. Verheijen, O. Wunnicke, S. Serafin, H. Wondergem, and E. P. A. M. Bakkers, 'Position-controlled epitaxial III-V nanowires on silicon', *Nanotechnology*, **vol. 17 (2006)(11)**, pp. S271–S275, doi:10.1088/0957-4484/17/11/S07.

[116] E. P. A. M. Bakkers, J. A. V. Dam, S. D. Franceschi, L. P. Kouwenhoven, M. Kaiser, M. Verheijen, H. Wondergem, and P. V. D. Sluis, 'Epitaxial growth of InP nanowires on germanium', *Nat. Mater.*, **vol. 3 (2004)**, p. 769?773, doi:10.1038/nmat1235.

[117] M. A. Verheijen, G. Immink, T. de Smet, M. T. Borgstrom, and E. P. A. M. Bakkers, 'Growth kinetics of heterostructured GaP-GaAs nanowires', *J. Am. Chem. Soc.*, **vol. 128 (2006)(4)**, pp. 1353–1359, doi:10.1021/ja057157h.

[118] A. Kosiorek, W. Kandulski, P. Chudzinski, K. Kempa, and M. Giersig, 'Shadow Nanosphere Lithography: Simulation and Experiment', *Nano Lett.*, **vol. 4 (2004)(7)**, pp. 1359–1363, doi:10.1021/nl049361t.

[119] M. Sander and L.-S. Tan, 'Nanoparticle Arrays on Surfaces Fabricated Using Anodic Alumina Films as Templates', *Adv. Funct. Mater.*, **vol. 13 (2003)(5)**, pp. 393–397, doi:10.1002/adfm.200304290.

[120] T. Bogart, S. Dey, K.-K. Lew, S. Mohney, and J. Redwing, 'Diameter-Controlled Synthesis of Silicon Nanowires Using Nanoporous Alumina Membranes', *Adv. Mater.*, **vol. 17 (2005)(1)**, pp. 114–117, doi:10.1002/adma.200400373.

[121] K.-K. Lew and J. M. Redwing, 'Growth characteristics of silicon nanowires synthesized by vapor-liquid-solid growth in nanoporous alumina templates', *J. Cryst. Growth*, **vol. 254 (2003)(1-2)**, pp. 14–22, doi:10.1016/S0022-0248(03)01146-1.

[122] T. Martensson, P. Carlberg, M. Borgstrom, L. Montelius, W. Seifert, and L. Samuelson, 'Nanowire Arrays Defined by Nanoimprint Lithography', *Nano Lett.*, **vol. 4 (2004)(4)**, pp. 699–702, doi:10.1021/nl035100s.

[123] P. Mohan, J. Motohisa, and T. Fukui, 'Controlled growth of highly uniform, axial/radial direction-defined,individually addressable InP nanowire arrays', *Nanotechnology*, **vol. 16 (2005)(12)**, pp. 2903–2907, doi:10.1088/0957-4484/16/12/029.

[124] P. Mohan, J. Motohisa, and T. Fukui, 'Realization of conductive InAs nanotubes based on lattice-mismatched InP/InAs core-shell nanowires', *Appl. Phys. Lett.*, **vol. 88 (2006)(1)**, pp. 013110–3, doi:10.1063/1.2161576.

[125] P. Mohan, J. Motohisa, and T. Fukui, 'Fabrication of InP/InAs/InP core-multishell heterostructure nanowires by selective area metalorganic vapor phase epitaxy', *Appl. Phys. Lett.*, **vol. 88 (2006)(13)**, pp. 133105–3, doi:10.1063/1.2189203.

[126] J. Noborisaka, J. Motohisa, and T. Fukui, 'Catalyst-free growth of GaAs nanowires by selective-area metalorganic vapor-phase epitaxy', *Appl. Phys. Lett.*, **vol. 86 (2005)(21)**, pp. 213102–3, doi:10.1063/1.1935038.

[127] J. Noborisaka, J. Motohisa, S. Hara, and T. Fukui, 'Fabrication and characterization of freestanding GaAs/AlGaAs core-shell nanowires and AlGaAs nanotubes by using selective-area metalorganic vapor phase epitaxy', *Appl. Phys. Lett.*, **vol. 87 (2005)(9)**, pp. 093109–3, doi:10.1063/1.2035332.

[128] L. Yang, J. Motohisa, J. Takeda, K. Tomioka, and T. Fukui, 'Size-dependent photoluminescence of hexagonal nanopillars with single InGaAs/GaAs quantum wells fabricated by selective-area metal organic vapor phase epitaxy', *Appl. Phys. Lett.*, **vol. 89 (2006)(20)**, pp. 203110–3, doi:10.1063/1.2372710.

[129] H. Ng, J. Han, T. Yamada, P. Nguyen, Y. Chen, and M. Meyyappan, 'Single Crystal Nanowire Vertical Surround-Gate Field-Effect Transistor', *Nano Lett.*, **vol. 4 (2004)(7)**, pp. 1247–1252, doi:10.1021/nl049461z.

[130] T. Bryllert, L.-E. Wernersson, T. Löwgren, and L. Samuelson, 'Vertical wrap-gated nanowire transistors', *Nanotechnology*, **vol. 17 (2006)(11)**, pp. S227–S230, doi:10.1088/0957-4484/17/11/S01.

[131] J. Goldberger, A. Hochbaum, R. Fan, and P. Yang, 'Silicon Vertically Integrated Nanowire Field Effect Transistors', *Nano Lett.*, **vol. 6 (2006)(5)**, pp. 973–977, doi:10.1021/nl060166j.

[132] V. Schmidt, H. Riel, S. Senz, S. Karg, W. Riess, and U. Gösele, 'Realization of a Silicon Nanowire Vertical Surround-Gate Field-Effect Transistor', *Small*, **vol. 2 (2006)**, p. 85, doi:10.1002/smll.200500181.

[133] E. D. Minot, F. Kelkensberg, M. van Kouwen, J. A. van Dam, L. P. Kouwenhoven, V. Zwiller, M. T. Borgstrom, O. Wunnicke, M. A. Verheijen, and E. P. A. M. Bakkers,

'Single quantum dot nanowire LEDs', *Nano Lett.*, **vol. 7 (2007)(2)**, pp. 367–371, doi: 10.1021/nl062483w.

[134] M. Law, L. E. Greene, J. C. Johnson, R. Saykally, and P. Yang, 'Nanowire dye-sensitized solar cells', *Nat. Mater.*, **vol. 4 (2005)(6)**, pp. 455–459, doi:10.1038/nmat1387.

[135] J. R. Arthur, 'Molecular beam epitaxy', *Surf. Sci.*, **vol. 500 (2002)**, pp. 189–217.

[136] H. Lüth, *Solid Surfaces, Interfaces and Thin Films*, Springer Verlag (2001).

[137] E. Hellman, D. Buchanan, and C. Chen, 'Nucleation of AlN on the (7x7) reconstructed Si(111) surface', *MRS Internet Journal of Nitride Semiconductor Research*, **vol. 3 (1998)(43)**, pp. 1–7.

[138] F. Semond, Y. Cordier, N. Grandjean, F. Natali, B. Damilano, S. Vezian, and J. Massies, 'Molecular Beam Epitaxy of group-III nitrides on silicon substrates: Growth, properties and device applications', *Phys. Status Solidi A*, **vol. 188 (2001)(2)**, pp. 501–510.

[139] T. Zywietz, J. Neugebauer, and M. Scheffler, 'The adsorption of oxygen at GaN surfaces', *Appl. Phys. Lett.*, **vol. 74 (1999)(12)**, pp. 1695–1697, doi:10.1063/1.123658.

[140] J. Neugebauer, T. K. Zywietz, M. Scheffler, J. E. Northrup, H. Chen, and R. M. Feenstra, 'Adatom Kinetics On and Below the Surface: The Existence of a New Diffusion Channel', *Phys. Rev. Lett.*, **vol. 90 (2003)(5)**, p. 056101, doi: 10.1103/PhysRevLett.90.056101.

[141] A. Kikuchi, M. Kawai, M. Tada, and K. Kishino, 'InGaN/GaN Multiple Quantum Disk Nanocolumn Light-Emitting Diodes Grown on (111) Si Substrate', *Jpn. J. Appl. Phys.*, **vol. 43 (2004)(12A)**, pp. L1524–L1526, doi:10.1143/JJAP.43.L1524.

[142] K. A. Bertness, A. Roshko, N. A. Sanford, J. M. Barker, and A. V. Davydov, 'Spontaneously grown GaN and AlGaN nanowires', *J. Cryst. Growth*, **vol. 287 (2006)(2)**, p. 522, doi:10.1016/j.jcrysgro.2005.11.079.

[143] R. K. Debnath, R. Meijers, T. Richter, T. Stoica, R. Calarco, and H. Luth, 'Mechanism of molecular beam epitaxy growth of GaN nanowires on Si(111)', *Appl. Phys. Lett.*, **vol. 90 (2007)(12)**, 123117, doi:10.1063/1.2715119.

[144] S. J. Kwon, 'Theoretical Analysis of Non-Catalytic Growth of Nanorods on a Substrate', *J. Phys. Chem. B*, **vol. 110 (2006)**, p. 3876, doi:10.1021/jp056252+.

[145] R. J. Meijers, *Herstellung III-N-basierender Halbleiterschichten und Heterostrukturen im Hinblick auf mögliche Spinelektronik-Anwendungen*, Master's thesis, RWTH Aachen, Germany (2004).

[146] O. Ambacher, M. S. Brandt, R. Dimitrov, T. Metzger, M. Stutzmann, R. A. Fischer, A. Miehr, A. Bergmaier, and G. Dollinger, 'Thermal stability and desorption of Group III nitrides prepared by metal organic chemical vapor deposition', *J. Vac. Sci. Technol., B*, **vol. 14 (1996)(6)**, pp. 3532–3542, doi:10.1116/1.588793.

[147] X. H. Zheng, Y. T. Wang, Z. H. Feng, H. Yang, H. Chen, J. M. Zhou, and J. W. Liang, 'Method for measurement of lattice parameter of cubic GaN layers on GaAs (0 0 1)', *J. Cryst. Growth*, **vol. 250 (2003)(3-4)**, pp. 345–348, doi:10.1016/S0022-0248(02)02465-X.

[148] E. Bauer and J. H. van der Merwe, 'Structure and growth of crystalline superlattices: From monolayer to superlattice', *Phys. Rev. B*, **vol. 33 (1986)(6)**, pp. 3657–3672.

[149] A. Krost and A. Dadgar, 'GaN-based optoelectronics on silicon substrates', *Materials Science and Engineering B*, **vol. 93 (2002)(1-3)**, p. 77, doi:10.1016/S0921-5107(02)00043-0.

[150] T. Stoica and L. Vescan, 'Misfit dislocations in finite lateral size $Si_{1-x}Ge_x$ films grown by selective epitaxy', *J. Cryst. Growth*, **vol. 131 (1993)(1-2)**, pp. 32–40, doi:10.1016/0022-0248(93)90393-B.

[151] P. M. Bridger, Z. Z. Bandic, E. C. Piquette, and T. C. McGill, 'Correlation between the surface defect distribution and minority carrier transport properties in GaN', *Appl. Phys. Lett.*, **vol. 73 (1998)(23)**, pp. 3438–3440, doi:10.1063/1.122790.

[152] S. J. Rosner, E. C. Carr, M. J. Ludowise, G. Girolami, and H. I. Erikson, 'Correlation of cathodoluminescence inhomogeneity with microstructural defects in epitaxial GaN grown by metalorganic chemical-vapor deposition', *Appl. Phys. Lett.*, **vol. 70 (1997)(4)**, pp. 420–422, doi:10.1063/1.118322.

[153] M. A. Reshchikov and H. Morkoc, 'Luminescence properties of defects in GaN', *J. Appl. Phys.*, **vol. 97 (2005)(6)**, 061301, doi:10.1063/1.1868059.

[154] F. Calle, F. J. Sánchez, J. M. G. Tijero, M. A. Sánchez-García, E. Calleja, and R. Beresford, 'Exciton and donor - acceptor recombination in undoped GaN on Si(111)', *Semicond. Sci. Technol.*, **vol. 12 (1997)(11)**, pp. 1396–1403, doi:10.1088/0268-1242/12/11/011.

[155] N. Thillosen, K. Sebald, H. Hardtdegen, R. Meijers, R. Calarco, S. Montanari, N. Kaluza, J. Gutowski, and H. Lüth, 'The State of Strain in Single GaN Nanocolumns As Derived from Micro-Photoluminescence Measurements', *Nano Lett.*, **vol. 6 (2006)(4)**, pp. 704 – 708, doi:10.1021/nl052456q.

[156] A. Kikuchi, K. Yamano, M. Tada, and K. Kishino, 'Stimulated emission from GaN nanocolumns', *Phys. Status Solidi B*, **vol. 241 (2004)(12)**, pp. 2754–2758, doi:10.1002/pssb.200405103.

[157] K. Bertness, N. Sanford, J. Barker, J. Schlager, A. Roshko, A. Davydov, and I. Levin, 'Catalyst-Free Growth of GaN Nanowires', *J. Electron. Mater.*, **vol. 35 (2006)(4)**, pp. 576–580.

[158] L. Cerutti, J. Ristic, S. Fernandez-Garrido, E. Calleja, A. Trampert, K. H. Ploog, S. Lazic, and J. M. Calleja, 'Wurtzite GaN nanocolumns grown on Si(001) by molecular beam epitaxy', *Appl. Phys. Lett.*, **vol. 88 (2006)(21)**, 213114.

[159] R. Meijers, R. Calarco, N. Kaluza, H. Hardtdegen, M. v. Ahe, H. Bay, H. Lüth, M. Buchmeier, and D. Bürgler, 'Epitaxial growth and characterization of Fe thin films on wurtzite GaN(0 0 0 1)', *J. Cryst. Growth*, **vol. 283 (2005)(3-4)**, pp. 500–507, doi: 10.1016/j.jcrysgro.2005.06.004.

[160] G. Mula, B. Daudin, C. Adelmann, and P. Peyla, 'MBE Growth Of GaN Films In Presence Of Surfactants: The Effect Of Mg And Si', in *MRS Fall Meeting Conference Proceedings* (1999) .

[161] J. Neugebauer, 'Surfactants and antisurfactants on group-III-nitride surfaces', *Phys. Status Solidi C*, **vol. 0 (2003)(6)**, pp. 1651–1667.

[162] T. Myers, A. Ptak, L. Wang, and N. Giles, 'Magnesium and Beryllium Doping During rf-Plasma MBE Growth of GaN', in *Proceedings of the International Workshop on Nitride Semiconductors*, Institute of Pure and Applied Physics Conference Series 1 (2000) pp. 451–454.

[163] M. A. L. Johnson, J. D. Brown, N. A. El-Masry, J. J. W. Cook, J. F. Schetzina, H. S. Kong, and J. A. Edmond, 'Molecular beam epitaxy growth and properties of GaN, InGaN, and GaN/InGaN quantum well structures', *J. Vac. Sci. Technol., B*, **vol. 16 (1998)(3)**, pp. 1282–1285, doi:10.1116/1.590000.

[164] G. M. Dalpian and J. R. Chelikowsky, 'Self-Purification in Semiconductor Nanocrystals', *Phys. Rev. Lett.*, **vol. 96 (2006)(22)**, 226802.

[165] U. Kaufmann, M. Kunzer, M. Maier, H. Obloh, A. Ramakrishnan, B. Santic, and P. Schlotter, 'Nature of the 2.8 eV photoluminescence band in Mg doped GaN', *Appl. Phys. Lett.*, **vol. 72 (1998)(11)**, pp. 1326–1328, doi:10.1063/1.120983.

[166] M. Leroux, N. Grandjean, B. Beaumont, G. Nataf, F. Semond, J. Massies, and P. Gibart, 'Temperature quenching of photoluminescence intensities in undoped and doped GaN', *J. Appl. Phys.*, **vol. 86 (1999)(7)**, pp. 3721–3728, doi:10.1063/1.371242.

[167] E. Dimakis, G. Konstantinidis, K. Tsagaraki, A. Adikimenakis, E. Iliopoulos, and A. Georgakilas, 'The role of nucleation temperature in In-face InN-on-GaN(0001) growth by plasma-assisted molecular beam epitaxy', *Superlattices Microstruct.*, **vol. 36 (2004)**, pp. 497–507, doi:10.1016/j.spmi.2004.09.010.

[168] V. Y. Davydov, A. A. Klochikhin, V. V. Emtsev, F. Bechstedt, A. V. Mudryi, and E. E. Haller, 'Reply to 'Comment on 'Band Gap of InN and In-Rich $In_xGa_{1-x}N$ Alloys (0.36 $< x < 1$)'', *Phys. Status Solidi B*, **vol. 233 (2002)**, pp. R10–R11, doi:10.1002/1521-3951(200210)233:3<R10::AID-PSSB999910>3.0.CO;2-E.

[169] J. Grandal, M. Sánchez-García, F. Calle, and E. Calleja, 'Morphology and optical properties of InN layers grown by molecular beam epitaxy on silicon substrates', *Phys. Status Solidi C*, **vol. 2 (2005)(7)**, pp. 2289–2292, doi:10.1002/pssc.200461571.

[170] M. C. Johnson, C. J. Lee, E. D. Bourret-Courchesne, S. L. Konsek, S. Aloni, W. Q. Han, and A. Zettl, 'Growth and morphology of 0.80 eV photoemitting indium nitride nanowires', *Appl. Phys. Lett.*, **vol. 85 (2004)(23)**, pp. 5670–5672, doi:10.1063/1.1831563.

[171] T. Matsuoka, H. Okamoto, M. Nakao, H. Harima, and E. Kurimoto, 'Optical bandgap energy of wurtzite InN', *Appl. Phys. Lett.*, **vol. 81 (2002)(7)**, pp. 1246–1248, doi:10.1063/1.1499753.

[172] Y. Saito, H. Harima, E. Kurimoto, T. Yamaguchi, N. Teraguchi, A. Suzuki, T. Araki, and Y. Nanishi, 'Growth Temperature Dependence of Indium Nitride Crystalline Quality Grown by RF-MBE', *Phys. Status Solidi B*, **vol. 234 (2002)(3)**, pp. 796–800, doi:10.1002/1521-3951(200212)234:3<796::AID-PSSB796>3.0.CO;2-H.

[173] K. M. Yu, Z. Liliental-Weber, W. Walukiewicz, W. Shan, J. W. Ager, III, S. X. Li, R. E. Jones, E. E. Haller, H. Lu, and W. J. Schaff, 'On the crystalline structure, stoichiometry and band gap of InN thin films', *Appl. Phys. Lett.*, **vol. 86 (2005)(7)**, 071910, doi:10.1063/1.1861513.

[174] A. A. Klochikhin, V. Y. Davydov, V. V. Emtsev, A. V. Sakharov, V. A. Kapitonov, B. A. Andreev, H. Lu, and W. J. Schaff, 'Manifestation of the equilibrium hole distribution in photoluminescence of n-InN', *Phys. Status Solidi B*, **vol. 242 (2005)(4)**, pp. R33–R35, doi:10.1002/pssb.200510007.

[175] C. H. Liang, L. C. Chen, J. S. Hwang, K. H. Chen, Y. T. Hung, and Y. F. Chen, 'Selective-area growth of indium nitride nanowires on gold-patterned Si(100) substrates', *Appl. Phys. Lett.*, **vol. 81 (2002)(1)**, pp. 22–24, doi:10.1063/1.1490636.

[176] T. Tang, S. Han, W. Jin, X. Liu, C. Li, D. Zhang, C. Zhou, B. Chen, J. Han, and M. Meyyapan, 'Synthesis and characterization of single-crystal indium nitride nanowires', *J. Mater. Res.*, **vol. 19 (2004)(2)**, pp. 423–426, doi:10.1557/JMR.2005.0049.

[177] T. Yodo, H. Yona, H. Ando, D. Nosei, and Y. Harada, 'Strong band edge luminescence from InN films grown on Si substrates by electron cyclotron resonance-assisted molecular beam epitaxy', *Appl. Phys. Lett.*, **vol. 80 (2002)(6)**, pp. 968–970.

[178] J. Zhang, B. Xu, F. Jiang, Y. Yang, and J. Li, 'Fabrication of ordered InN nanowire arrays and their photoluminescence properties', *Phys. Lett. A*, **vol. 337 (2005)(1-2)**, pp. 121–126, doi:10.1016/j.physleta.2005.01.048.

[179] J. Zhang, L. Zhang, X. Peng, and X. Wang, 'Vapor?solid growth route to single-crystalline indium nitride nanowires', *J. Mater. Chem.*, **vol. 12 (2002)**, pp. 802 – 804, doi:10.1039/b111270h.

[180] A. G. Bhuiyan, A. Hashimoto, and A. Yamamoto, 'Indium nitride (InN): A review on growth, characterization, and properties', *J. Appl. Phys.*, **vol. 94 (2003)(5)**, pp. 2779–2808, doi:10.1063/1.1595135.

[181] V. Davydov and A. Klochikhin, 'Electronic and vibrational states in InN and $In_xGa_{1-x}N$ solid solutions', *Semiconductors*, **vol. 38 (2004)(8)**, pp. 861–898, doi: 10.1134/1.1787109.

[182] C. Stampfl, C. G. Van de Walle, D. Vogel, P. Krüger, and J. Pollmann, 'Native defects and impurities in InN: First-principles studies using the local-density approximation and self-interaction and relaxation-corrected pseudopotentials', *Phys. Rev. B*, **vol. 61 (2000)(12)**, pp. R7846–R7849, doi:10.1103/PhysRevB.61.R7846.

[183] K. A. Dick, K. Deppert, M. W. Larsson, T. Martensson, W. Seifert, L. R. Wallenberg, and L. Samuelson, 'Synthesis of branched 'nanotrees' by controlled seeding of multiple branching events', *Nat. Mater.*, **vol. 3 (2004)**, pp. 380–384, doi:10.1038/nmat1133.

[184] K. A. Dick, K. Deppert, T. Martensson, W. Seifert, and L. Samuelson, 'Growth of GaP nanotree structures by sequential seeding of 1D nanowires', *J. Cryst. Growth*, **vol. 272 (2004)(1-4)**, pp. 131–137, doi:10.1016/j.jcrysgro.2004.09.004.

[185] K. A. Dick, K. Deppert, L. S. Karlsson, W. Seifert, L. R. Wallenberg, and L. Samuelson, 'Position-Controlled Interconnected InAs Nanowire Networks', *Nano Lett.*, **vol. 6 (2006)(12)**, pp. 2842–2847, doi:10.1021/nl062035o.

[186] K. A. Dick, K. Deppert, M. W. Larsson, W. Seifert, L. R. Wallenberg, and L. Samuelson, 'Height-controlled nanowire branches on nanotrees using a polymer mask', *Nanotechnology*, **vol. 18 (2007)(3)**, pp. 035601–, doi:10.1088/0957-4484/18/3/035601.

[187] Wikipedia, 'Cleanroom', definition in Wikipedia, the free encyclopedia (2007), `http://en.wikipedia.org/wiki/Cleanroom`.

[188] T. Richter, *Galliumnitrid-Nanodrähte und deren Charakterisierung*, Master's thesis, RWTH Aachen, Germany, Institut für Schichten und Grenzflächen (ISG-1), Forschungszentrum Jülich GmbH (2005).

[189] Z. Qin, Z. Chen, Y. Tong, X. Ding, X. Hu, T. Yu, and G. Zhang, 'Study of Ti/Au, Ti/Al/Au, and Ti/Al/Ni/Au ohmic contacts to n-GaN', *Appl. Phys. A: Mater. Sci. Process.*, **vol. 78 (2004)(5)**, pp. 729–731, doi:10.1088/0268-1242/11/10/002.

[190] A. C. Schmitz, A. T. Ping, M. A. Khan, Q. Chen, J. W. Yang, and I. Adesida, 'Schottky barrier properties of various metals on n-type GaN', *Semicond. Sci. Technol.*, **vol. 11 (1996)(10)**, p. 1464, doi:10.1088/0268-1242/11/10/002.

[191] R. Calarco, M. Marso, T. Richter, A. I. Aykanat, R. Meijers, A. v.d. Hart, T. Stoica, and H. Lüth, 'Size-dependent Photoconductivity in MBE-Grown GaN-Nanowires', *Nano Lett.*, **vol. 5 (2005)(5)**, pp. 981–984, doi:10.1021/nl0500306.

[192] A. Rose, 'Space-Charge-Limited Currents in Solids', *Physical Review*, **vol. 97 (1955)(6)**, pp. 1538–1544, doi:10.1103/PhysRev.97.1538.

[193] M. Marso, 'private communication', .

[194] M. Kočan, A. Rizzi, H. Lüth, S. Keller, and U. K. Mishra, 'Surface Potential at as-Grown GaN(0001) MBE Layers', *Phys. Status Solidi B*, **vol. 234 (2002)**, p. 773, doi: 10.1002/1521-3951(200212)234:3<773::AID-PSSB773>3.0.CO;2-0.

[195] I. Mahboob, T. D. Veal, C. F. McConville, H. Lu, and W. J. Schaff, 'Intrinsic Electron Accumulation at Clean InN Surfaces', *Phys. Rev. Lett.*, **vol. 92 (2004)(3)**, 036804, doi:10.1103/PhysRevLett.92.036804.

[196] I. Mahboob, T. D. Veal, L. F. J. Piper, C. F. McConville, H. Lu, W. J. Schaff, J. Furthmuller, and F. Bechstedt, 'Origin of electron accumulation at wurtzite InN surfaces', *Phys. Rev. B*, **vol. 69 (2004)(20)**, 201307, doi:10.1103/PhysRevB.69.201307.

[197] R. Calarco and M. Marso, 'GaN and InN nanowires grown by MBE: A comparison', *Appl. Phys. A: Mater. Sci. Process.*, **vol. 87 (2007)(3)**, pp. 499–503, doi: 10.1007/s00339-007-3871-6.

List of publications

Parts of this work have already been published:

A part of Chapter 5 is published in:

Debnath, R. K.; Meijers, R.; Richter, T.; Stoica, T.; Calarco, R. & Luth, H. (2007), 'Mechanism of molecular beam epitaxy growth of GaN nanowires on Si(111)', *Applied Physics Letters* **90**(12), 123117.

A part of Chapter 6 is published in:

Meijers, R.; Richter, T.; Calarco, R.; Stoica, T.; Bochem, H.; Marso, M. & Lüth, H. (2006), 'GaN-nanowhiskers: MBE-growth conditions and optical properties', *Journal of Crystal Growth* **289**(1), 381–386.

A part of Chapter 8 is published in:

Stoica, T.; Meijers, R.; Calarco, R.; Richter, T. & Lüth, H. (2006), 'MBE growth optimization of InN nanowires', *Journal of Crystal Growth* **290**, 241–247.

Stoica, T.; Meijers, R.; Calarco, R.; Richter, T.; Sutter, E. & Lüth, H. (2006), 'Photoluminescence and Intrinsic Properties of MBE-Grown InN Nanowires', *Nano Letters* **6**(7), 1541–1547.

The contact preparation and electrical measurements in Sec. 9.3, Sec. 9.4 and Sec. 9.5 have been described in:

Richter, T. (2005),'Galliumnitrid-Nanodrähte und deren Charakterisierung', Master's thesis, RWTH Aachen, Germany.

Calarco, R.; Marso, M.; Richter, T.; Aykanat, A. I.; Meijers, R.; v.d. Hart, A.; Stoica, T. & Lüth, H. (2005), 'Size-dependent Photoconductivity in MBE-Grown GaN-Nanowires', *Nano Letters* **5**(5), 981–984.

Calarco, R. & Marso, M. (2007), 'GaN and InN nanowires grown by MBE: A comparison', *Applied Physics A: Materials Science & Processing* **87**(3), 499–503.

Other publications:

Buchmeier, M.; Bürgler, D. E.; Grünberg, P. A.; Schneider, C. M.; Meijers, R.; Calarco, R.; Raeder, C. & Farle, M. (2006), 'Anisotropic FMR-linewidth of triple-domain Fe layers on hexagonal GaN(0001)', *Physica Status Solidi (a)* **203**(7), 1567 – 1572.

Calarco, R.; Marso, M.; Meijers, R.; Richter, T.; Aykanat, A.; Stoica, T. & Lüth, H. (2004), 'GaN Nanocolumns on Si(111) Grown by Molecular Beam Epitaxy', *ASDAM 2004 - Conference Proceedings, 5th International Conference on Semiconductor Devices and Microsystems*, 9–12.

Cavallini, A.; Polenta, L.; Rossi, M.; Richter, T.; Marso, M.; Meijers, R.; Calarco, R. & Lüth, H. (2006), 'Defect Distribution along Single GaN Nanowhiskers', *Nano Letters* **6**(7), 1548–1551.

Meijers, R.; Calarco, R.; Kaluza, N.; Hardtdegen, H.; Ahe, M. v.; Bay, H.; Lüth, H.; Buchmeier, M. & Bürgler, D. (2005), 'Epitaxial growth and characterization of Fe thin films on wurtzite GaN(0001)', *Journal of Crystal Growth* **283**(3-4), 500–507.

Milekhin, A.; Meijers, R.; Richter, T.; Calarco, R.; Montanari, S.; Lüth, H.; Sierra, B. A. P. & Zahn, D. R. T. (2006), 'Surface enhanced Raman scattering by GaN nanostructures obtained by bottom-up and top-down approaches', *Journal of Physics: Condensed Matter* **18**, 5825–5834.

Milekhin, A. G.; Meijers, R.; Richter, T.; Calarco, R.; Lüth, H.; Sierra, B. A. P. & Zahn, D. R. T. (2006), 'Surface enhanced Raman scattering by GaN nanocolumns', *Physica Status Solidi (c)* **3**(6), 2065 – 2068.

Sebald, K.; Gutowski, J.; Thillosen, N.; Montanari, S.; Meijers, R.; Calarco, R.; Kaluza, N. & Lüth, H. (2006), 'Microphotoluminescence studies on single GaN nanocolumns', *Materials Research Society Symposium Proceedings* **892**, 805–810.

Sutter, E.; Sutter, P.; Calarco, R.; Stoica, T. & Meijers, R. (2007), 'Assembly of ordered carbon shells on GaN nanowires', *Applied Physics Letters* **90**(9), 093118.

Thillosen, N.; Sebald, K.; Hardtdegen, H.; Meijers, R.; Calarco, R.; Montanari, S.; Kaluza, N.; Gutowski, J. & Lüth, H. (2006), 'The State of Strain in Single GaN Nanocolumns As Derived from Micro-Photoluminescence Measurements', *Nano Letters* **6**(4), 704 – 708.

Cavallini, A.; Polenta, L.; Rossi, M.; Stoica, T.; Calarco, R.; Meijers, R. J.; Richter, T. & Lüth, H. (2007),'Franz-Keldysh effect in GaN nanowires', accepted for publication in Nano Letters.

Calarco, R.; Meijers, R. J.; Debnath, R. K.; Stoica, T.; Sutter, E. & Lüth, H. (2007),'Nucleation and growth of GaN nanowires on Si(111) performed by molecular beam epitaxy', submitted to Nano Letters.

Acknowledgments

Now that this thesis is almost finished an important part still remains to be written. I am grateful to all the people who have contributed to this work in direct or indirect manner. First of all I would like to thank Prof. Hans Lüth for giving me the opportunity to work in his institute and his compelling enthusiasm for interesting physical questions. I really appreciate his clear reasoning, which have made difficult things much easier to understand. I am also indebted to Prof. Gernot Güntherodt for kindly accepting to referee this work. Our new institute director, Prof. Grützmacher is thanked for supporting this work in its final stages.
Great appreciation goes of course to Raffaella for carefully reviewing this work and kindly accepting me in her group. I am grateful for the confidence she had in me and giving me the freedom to explore many aspects of our treasured nanowires. She found a good balance between showing me how to work independently and being there when needed. Even though, as an experimentalist, I like to do measurements she has showed me the importance and value of putting your thoughts in the form of a paper.
Despite the many problems we have had with our MBE, Karl-Heinz somehow always knew where to get parts or who to ask if we could not fix the problem ourselves. I am also thankful for our fruitful cooperation producing many interesting samples. I enjoyed our non-scientific discussions, especially during the major soccer championships.
Words cannot describe my full gratitude for the contributions of Jakob and Thomas during my three years as a PhD student in Jülich. I really appreciate all the hard work Thomas has done regarding the electrical measurements, despite many difficulties, that helped to get a better understanding of these tiny nanocrystals. Your 'interesting' emails have helped getting rid of frustration about yet another machine, which was not working. Jakob, you have been somewhat like me 'daytime family' helping me through difficult times and I could not have wished for a better roommate!
Toma seems to have an answer for all questions and even though I did not always understand them immediately, you have helped me a lot to extend my knowledge about many interesting phenomena. Thank you very much for that. I would also like to thank Lili Vescan even though she left soon after I came. Your systematic and logical way of thinking have been an example for me.
Debnath and Jegan, I really enjoyed working with you and appreciate all the work you have done. I learned a lot from our discussions. Debnath, I am still amazed of the perfection of your SEM images.
Michel, every time you amaze me again with your extensive knowledge and interesting views on life. I really enjoyed our trip to Bologna. It was one of the nicest business trips I have had. Thank you very much for that!
Michael Indlekofer has showed me many times that there seems to be a Green's function for every problem. Thank you for all your help especially also for 'tuning' the German summary.
Sergio, Katharina, Christian, Denny and Vitaliy, somehow you always produced a smile on

my face, wether it is related to the superior qualities of Linux or just some other stuff. You helped me feel at home in Jülich.
Irene and Andrea seem to have an answer for every administrative problem you can think of and besides that you are also two great personalities.
I would like to express my gratitude to Anna Cavallini and her group in Bologna, especially Laura and Marco for our fruitful cooperation, which has and still does produce interesting results and publications. I'll never forget the Italian spirit, which is really unique.
Eli Sutter has supplied us with a huge number of high quality TEM images. We have learned a lot about the nanowire growth from your images and therefore I am grateful.
The people of Philips and AMOLF in Eindhoven, especially Erik Bakkers, Jaime Gomez Rivas, Silke Diedenhofen and Gabriele Vecchi, I thank for interesting discussions on nanowires and hope we will learn more about their optical properties in the near future.
I want to thank Matthias Buchmeier and Daniel Bürgler for the pleasant cooperation and the magnetic measurements on the Fe samples, which eventually did not become a part of this thesis, but produced some nice publications.
I am grateful to Simone Montanari for introducing me to the cleanroom and his positive attitude convincing me there is a solution to every problem.
Nicoleta has provided us with some excellent GaN samples and helped with AFM measurements. Thank you very much for that and for being a pleasant office neighbour.
I thank Angela Rizzi and her group at the University of Göttingen, in particular Marco Bertelli and Jörg Malindretos for interesting discussions on nitrides.
It was also a real pleasure to get to know Martin and Martina Kočan and wish them all the best in Australia.
I thank Prof. D. Zahn and Alexander Milekhin in Chemnitz for Raman measurements.
I thank Mr. Bochem and Elke for many high quality SEM images and CL measurements and W. Reichert and Martina v.d. Ahe for XRD measurements. I also thank Nicolas Thillosen for PL and Andreas Mück for SIMS measurements. I am grateful to Steffi Bunte, Jana Mohr and the rest of the cleanroom team for their support in processing samples and the large number of wafers and samples Steffi and Jana have cut perfectly. Klaus Wambach and Karl Nicol have often helped with their experience to solve MBE related problems. Thanks a lot.
I want to thank Thomas Schäpers, Mihail Lepsa, Arno Förster, Jürgen Moers, Martin Mikulics, Hilde Hardtdegen, Roger Steins, Michael Goryl, Gero Heidelberger and Mr. Crecelius for contributing to this work in various ways.
I thank the administrative team for adequately taking care of administrative issues as well as the people from the mechanical and electrical workshop for solving various problems. The people at the ZEL I thank for developing the software to automate the MBE. I also valued the support and the expertise of the people at the 'Zentralbibliothek'.
The time in Aachen and in Kerkrade would have been less interesting without Maarten, Pim, Tim and Floris. Thanks guys for a nice time. Hopefully we will have the chance to go to 'Epen' for many years to come.
I am deeply grateful to my family for giving me the opportunity to pursue my goals, for believing in me and always giving me their full support as well as solving all kinds of problems.
My newly won family I want to thank for making me feel at home from the first day.
Marjolyn, at the beginning of this thesis you have become a very important part of my life and have always been a great support and believed in me. I am deeply grateful for being the permanent sunshine in my life.

Curriculum Vitae

Personal Details

Name:	Meijers
First Name:	Ralph Joseph
Date of Birth:	April 27th, 1977
Place of Birth:	Kerkrade, The Netherlands
Citizenship:	Dutch

Education

09.1983 - 07.1989	Primary School in Kerkrade, The Netherlands
09.1989 - 06.1995	Atheneum 'Antonius Doctor College', Kerkrade, The Netherlands
10.1995 - 09.1998	RWTH Aachen, Mathematics
10.1997 - 03.2004	RWTH Aachen, Physics, degree 'Diplom-Physiker'
05.2004 - 05.2007	Research Centre Jülich, PhD student Physics
30.08.2007	Final Examination, PhD degree in Physics

Work experience

03.2003 - 07.2007	Research Centre Jülich, research assistant
09.2007 - present	ASML Netherlands, R&D engineer